EPR Spectroscopy as a Tool for the Elucidation of Non-Covalent Structuring Principles in Complex Soft Matter

Dissertation

zur Erlangung des Grades

“Doktor der Naturwissenschaften”

im Promotionsfach Chemie

am Fachbereich Chemie, Pharmazie und Geowissenschaften

der Johannes Gutenberg-Universität Mainz

Dennis Kurzbach

geboren in Rüsselsheim

Mainz 2013

Dekan:

1. Berichterstatter:

2. Berichterstatter:

Tag der mündlichen Prüfung: 21.3.2013

Table of Content

Introduction 1

1. Fundamentals of EPR Spectroscopy 5

1.1 Introduction to EPR Spectroscopy 5

2. Correlated Electrostatic Interactions as Structuring Principle of Supramolecular Assemblies 31

2.1 Highly Defined Colloid-Like Ionic Clusters Through Self-Assembly in Solution. 32

2.2 DNA-Condensation with Spermine Dendrons: Interactions in Solution, Charge Inversion, and Morphology Control 35

2.3 Summary 44

3. Dendronized Polymers as Molecular Transporters 47

3.1 Assessing the Solution Shape and Size of Charged Dendronized Polymers Using Double Electron-Electron Resonance. 49

3.2 Loading and Release Capabilities of Charged Dendronized Polymers. 53

3.3 Load-Collapse-Release Cascades of Amphiphilic Guest Molecules in Charged Dendronized Polymers through Spatial Separation of Non-Covalent Forces 61

3.4 Summary 68

4. The Nanoscale Collapse Behavior of Alkylene Oxide-Based Thermoresponsive Polymers 72

4.1 The Phase Behavior of Pluronic Triblock Copolymers 73

4.2 How Structure-Related Collapse Mechanisms Determine Nanoscale Inhomogeneities in Thermoresponsive PPO-co-PG and PEO-co-PDEGA 79

4.3 Impact of Amino-Functionalization on the Response of Poly(ethylene oxide) to pH-Sensitivity 91

4.4 Conclusion 95

5. The Phase Transition of Genetically Encoded Elastin-Like Polypeptides 100

5.1 A Highly Cooperative Phase Transition in Genetically Encoded Polymers Revealed by EPR Spectroscopy 101

6. The Conformational Space of Intrinsically Disordered Proteins 108

6.1 Cooperatively Folded Conformational Substates in Osteopontin 109

6.2 Conformational Adaptions of Osteopontin upon Heparin Binding 113

6.3 Structural Response of Intrinsically Disordered BASP1 to pH Variation 116

7. Summary and Outlook 116

Appendix 130

A2. Correlated Electrostatic Interactions as Structuring Principle of Supramolecular Assemblies 130

A2.1 Highly Defined Colloid-Like Ionic Clusters Through Self-Assembly in Solution. 130

A2.2 DNA-Condensation with Spermine-Dendrimers: Interactions in Solution, Charge Inversion, and Morphology Control 132

A3. Dendronized Polymers as Molecular Transporters 138

A3.1 Assessing the Solution Shape and Size of Charged Dendronized Polymers Using Double Electron Electron Resonance. 138

A3.2 Loading and Release Capabilities of Charged Dendronized Polymers. 139

A3.3 Counterion-Induced Condensation of Charged Dendronized Polymers 149

A4. The Nanoscale Collapse Behavior of Alkylene Oxide-Based Thermoresponsive Polymers 151

4.1 The Phase Behavior of Pluronic Triblock Copolymers 151

A4.2 How Structure-Related Collapse Mechanisms Determine Nanoscale Inhomogeneities in Thermoresponsive PEO-co-PDEGA and PPO-co-PG 153

A4.3 Impact of Amino-Functionalization on the Response of Poly(ethylene oxide) to pH-Sensitivity 158

A5. The Phase Transition of Genetically Encoded Elastin-Like Polypeptides 161

A5.1 A Highly Cooperative Phase Transition in Genetically Encoded Polymers Revealed by EPR Spectroscopy 161

A6. The Conformational Space of Intrinsically Disordered Proteins 165

A6.1 Cooperatively Folded Conformational Substates in Osteopontin 165

A6.2 Conformational Adaptions of Osteopontin upon Heparin Binding 168

A6.3. Structural Response of Intrinsically Disordered BASP1 to pH Variation 169

Introduction

At the beginning of the 21st century there is a growing need for novel materials. Energy storage, therapeutics and microelectronics illustrate only three examples out of many issues that scientists try to tackle with so-called responsive molecular and supramolecular compounds. In this context the notion of 'response' refers to a property of a substance that allows for dynamic adaption to changes in environmental conditions. Heat-dependent changes in molecular conformation or a pH-dependent degree of hydration are prominent examples for responsiveness. In the course of the development of novel materials researchers have started to intensively explore *non-covalent interactions* between *polymers* as keys to responsive behavior.[1, 2] The term non-covalent interaction includes a lot of forces, which give rise to interaction energies on the order of thermal energy at room temperature (k_BT = 4.1·10^{-21} J). Hence, they are weak when compared to covalent chemical bonds. Examples are hydrogen bonding or Van-der-Waals interaction. Also less explored non-covalent forces, like π-π interaction or depletion forces have drawn increasing attention throughout the recent past.[1, 2] Due to the limited strength of non-covalent forces also rather small changes in environmental conditions can change the force equilibrium in a given system and trigger versatile adaptions of a responsive polymer.

Frequently, it is a subtle interplay between non-covalent forces and classic thermodynamic factors that leads to the emergence of responsive properties of materials. Entropic losses might counteract a collapse of a system due to non-covalent attraction among its constituents or favorable solvent-polymer interaction might interfere with an envisioned self-assembly of solutes. Especially entropic contributions to molecular interaction energies are almost omnipresent.

Functional, stimuliresponsive polymers (in this context a stimulus is, e.g., a change in temperature or pH) are considered as highly promising candidates for future applications in many fields of natural and life sciences. Applications in drug and molecular delivery,[3-7] tissue engineering, molecular sensing and chemical catalysis are currently highly discussed.[8, 9] Envisaged compounds embrace a wide spectrum of molecular structures, ranging from simple synthetic polymers, via hydrogels, to biomimetic and complex biological structures.[8, 10-17] For a purposeful application of a responsive polymer, however, one has to fully understand the interplay among different non-covalent forces that leads to (desired) adaptions to environmental changes or restructuring of a polymer. The force equilibrium between the non-covalent forces that dominate the configuration of a given system in a given state are in this thesis referred to as *interaction profile* or *pattern*. Understanding these profiles allows for controlled tuning of the response of functional polymer-based systems to external stimuli. This is widely regarded to be of high importance for the controlled application of any kind of functional material.

Responsiveness of a polymer-based system to external stimuli is also intriguing from a physicochemical point of view. Changes in environmental conditions often lead to conformational rearrangements of the polymers on several length scales. Restructuring of the molecular world frequently triggers tremendous effects on macroscopic length scales. Even the emergence of only smallest inhomogeneities in an otherwise homogeneous polymer solution might lead to macroscopic clouding and drastically increased viscosity through crosslinking of chains. The underlying mechanisms and non-covalent interaction profiles are often challenging to understand and hence foster academic interest with the aim to elucidate the forces that govern molecular behavior. The development of models that make the prediction of structural response possible may allow for a directed

design of a system for a particular application.[18] Understanding the effects of non-covalent forces in soft matter such as nanophase separation, host-guest interaction or self-assembly may be utilized in order to purposefully construct polymer-based materials. This might turn out to be necessary for solving 21st century challenges. However, scientists have only just begun to develop concepts to describe the complicated interaction patters that underlie structuring principles in state-of-the-art responsive soft matter. E.g. the macroscopic phase behavior of amphiphilic copolymers might be heuristically describable through hydrophilic-hydrophobic balances. Yet, as I will show in the course of this thesis the mechanisms behind phase transitions of amphiphilic polymers entail complex conformational rearrangements on several length scales; comprising nano-, meso- and macrophase-separation. Stimuli-triggered phase separation is thereby only one example of responsive materials' behavior.

This thesis aims at connecting structural and functional changes of complex soft matter systems with their molecular interaction profiles. It addresses the problem of elucidating non-covalent forces as structuring principle of mainly polymer-based systems in solution. The structuring principles of a wide variety of complex soft matter types will be analyzed. In many cases this will be done by exploring conformational changes upon the exertion of external stimuli. The central question throughout this thesis will be how a certain non-covalent interaction profile leads to condition-dependent structuring of a polymeric system.

To answer this question, electron paramagnetic resonance (EPR) spectroscopy was chosen here as the main experimental technique for the investigation of the structure principles of polymers. EPR is an intrinsically local technique, which is sensitive to unpaired electrons. This means that with EPR one detects only the local surroundings or environments of molecules that carry an unpaired electron. Non-covalent forces are normally effective on length scales of a few nanometers and below. Thus, EPR is excellently suited for their investigations.[19] It allows for detection of interactions on length scales ranging from approx. 0.1 nm up to 10 nm. However, restriction to only one experimental technique likely leads to only incomplete pictures of complex systems. Therefore, the studies presented in the following are frequently augmented with further experimental and computational methods in order to yield more comprehensive descriptions of the systems chosen for investigation.

In general, the field of responsive polymers is very vast. Therefore, I chose to investigate selected systems of varying complexity to find out what their structuring principles are and how different non-covalent forces dominate the conformational space of these systems. They are representative for synthetic, biomimetic and biological structures. Every investigated system is dominated by a certain non-covalent interaction profile. This categorization in terms of interaction profiles will reach from mere electrostatics over interplay between hydrogen bonds and hydrophobic attraction to the complex profiles of biomimetic and biological soft matter (see Figure 1).

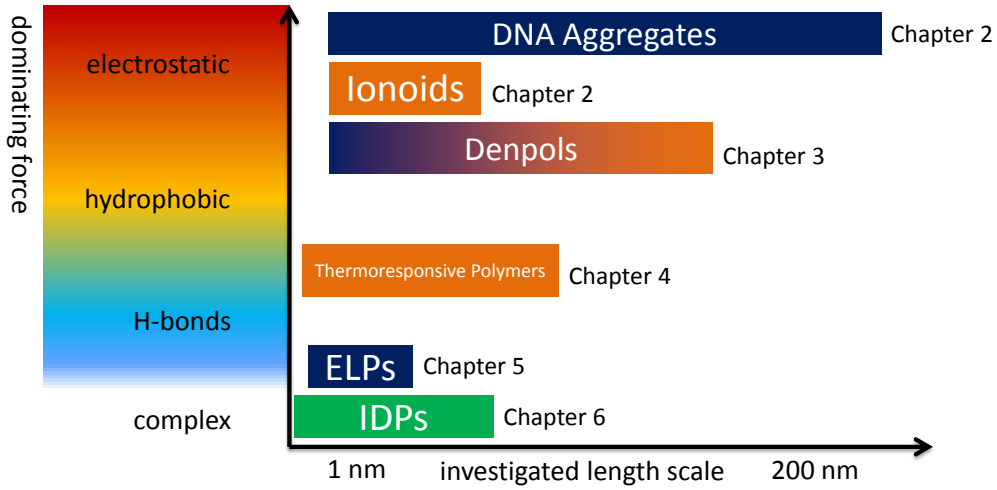

Figure 1. Schematic classification of the investigated systems, according to the force dominating a system and the investigated length scale. Orange indicates synthetic systems, dark blue biomimetic ones and green biological matter.

I will start in **Chapter 2** by introducing non-covalent interaction profiles with two examples based on correlations among electrostatic forces. The first example shall introduce correlation effects in non-covalent interaction profiles as structuring principles in *Ionoids*. These are colloid-like ionic clusters that occur in solutions of macrocyclic cations and small divalent counterions. Ionoids feature a well-defined, monodisperse size despite a quite mobile interior. These structures represent the first observation of structuring due to electrostatic correlations between low-molecular building blocks. In the second example electrostatic correlations will be exploited to condense DNA by multivalent counterions. It will be shown how the combination of EPR and transmission electron microscopy (TEM) yields insights into the way charged dendrons affect the morphology of DNA condensates and how these are influenced by stimuli like temperature or ionic strength.

These two examples shall demonstrate that non-covalent forces, especially Coulombic ones, can have structuring effects on soft matter on several length scales; between ionic building blocks of polymeric structures and between polyelectrolytes themselves. Building on this, I will proceed by showing how electrostatic structuring principles can be combined with hydrophobic ones, which adds a further degree of complexity to the notion of an interaction profile. This will be subject of **Chapter 3** at the example of host-guest interactions in so-called dendronized polymers (denpols). It will be shown that higher generations of charged denpols have a size and shape independent of their environment and that their surface can be decorated with ionic guests.[20] This is done by means of double electron-electron resonance spectroscopy (DEER) that allows for the determination of interspin distances up to a few nanometers. Subsequently it will be demonstrated that the interior of denpols can be loaded with fatty acid derivatives (up to 2.2 guest molecules per dendron unit). The arrangement of the guest compounds inside the denpols is elucidated by a novel application of DEER (mixed isotopologues for spectral selection). Release of guest compounds from denpols can be triggered by varying the solution pH or by increasing concentrations of surfacing ions. Finally, knowledge about DNA condensation will be combined with knowledge about loading of charged denpols leading to the concept of twofold packing of guests – firstly through host-guest interaction and secondly through condensation of the hosts. This gives rise to *load-collapse-release cascades* through exploitation of spatially separated non-covalent interaction profiles in denpols.

In **Chapter 4** the focus will be shifted from electrostatics in dendronized polymers to thermoresponsive alkylene oxide-based materials, whose structuring principles are based on hydrogen bonds and counteracting hydrophobic interactions. It will be shown that the temperature-induced collapse or inverse temperature transition of poly(ethylene oxide)-poly(propylene oxide)-poly(ethylene oxide) (PEO-PPO-PEO) block copolymers proceeds via nanoscale inhomogeneities. I.e., their phase transition is preceded by a collapse of nanoscopic regions that cannot be detected by macroscopic techniques, but can easily be explored by intrinsically local EPR. Nanoscale inhomogeneities are frequently encountered during the thermal collapse of thermoresponsive polymers. PPO-co-PG (poly(propylene oxide)-co-poly(glycidol)) and PEO-co-PDEGA (poly(ethylene oxide)-co-poly(N,N-diethyl glycidyl amine)) of different topology and architecture all exhibit this property. The collapse mechanism in dependence of hydrophilic-hydrophobic balance and topology of all these polymers will be elucidated and it will be demonstrated how one can control the occurrence of a certain type of nanoscale inhomogeneity in combination with a specific phase transition mode by selecting a particular combination of polymer properties.

Chapter 5 will complementarily elucidate the temperature-dependent phase behavior of elastin-like polypeptides (ELPs). ELPs are based on the primary Val-Pro-Gly-Xaa-Gly sequence found in tropoelastin (Xaa is a guest residue of any amino acid except Pro). The phase transition, as governed by changes in hydrogen bonding patterns (from ELP-solvent to ELP-ELP H-bonds) and in configurational entropy, is dependent on factors like chain length, mean hydropathy of the polymers and concentration, but primarily on the primary Val-Pro-GLy-Xaa-Gly sequence. By tuning the guest residue composition different types of nanoscale phase behaviors can be achieved. Such, ELPs are the first (and so far only) class of compounds that is shown to feature a first-order inverse phase transition on nanoscopic length scales.

Finally, this thesis will address complex biological systems, namely intrinsically disordered proteins (IDPs), in **Chapter 6**. These proteins lack defined secondary and tertiary structure and hence have much in common with random-coil polymers. However, I will show that the conformational space of the IDPs Osteopontin (OPN), a cytokine involved in metastasis of several kinds of cancer, and BASP1 (brain acid soluble protein one), a protein associated with neurite outgrowth, is governed by a subtle interplay between electrostatic forces, hydrophobic interaction, system entropy and hydrogen bonds. Such, IDPs can even sample cooperatively folded structures, which have so far only been associated with globular proteins. This study of IDPs demands for reassessment of the classic order vs. disorder scheme of structural biology. The EPR approach to IDPs gives further rise to highly detailed data about how structural adaptions of IDPs compensate for varying solution conditions and entropic loses through ligand binding. Such insights into structuring principles of IDPs might help to understand their versatile functions in eukaryotic life.

1. Fundamentals of EPR Spectroscopy

1.1 Introduction to EPR Spectroscopy

The term electron paramagnetic resonance (EPR) spectroscopy (also electron spin resonance or electron magnetic resonance) summarizes a set of methods and experimental techniques based on resonance of unpaired electron spins in external magnetic fields. (Commonly the notion of 'spins' is equivocally used with 'unpaired electrons'.) Owing to the restricted magnitude of the magnetic moment, μ, of an electron spin EPR is sensitive towards length scales of a few nanometers. It is therefore the method of choice for the elucidation of structuring principles of soft matter on molecular lengths scales. Since EPR is a magnetic resonance technique, it is based on the energetic splitting of spin states upon exposition of a paramagnetic sample to a static, external magnetic field. Subsequent irradiation of electromagnetic waves yields information about a sample through its interaction with the incident waves. EPR is sensitive to the individual responses of different paramagnetic centers in a sample. It is consequently an intrinsically local technique. This implies that one always detects the superposition of all paramagnetic centers in a sample and never the ensemble average. Detectable interactions of an unpaired electron with its surrounding range from ~0.1 nm (Fermi-contact interaction) to ~10 nanometers (dipolar coupling between unpaired electrons).[21] The spectrum of applications is huge, but mostly interactions between electrons and surrounding nuclei, between two electrons or effects of molecular motion and environment on the line-shape of a spectrum contains the desired information.[22] In the context of a certain molecular system (and frequently in combination with other experimental techniques) interpretation of this limited number of detected entities can lead to highly sophisticated and useful information. In the following, the basic physics behind EPR spectroscopy and the most important experimental techniques will be introduced together with frequently used molecules that comprise paramagnetic centers.

1.1.1 Historical Sketch of EPR Spectroscopy

EPR spectroscopy is a technique that essentially detects electron spins by exploiting the ability of unpaired electrons to absorb certain types of irradiation if exposed to appropriately strong magnetic fields. Stern and Gerlach[23] discovered in 1921 that an unpaired electron features an intrinsic magnetic moment, called spin, which can populate two discrete quantum mechanical states: $M_s = +1/2$ and $M_s = -1/2$. This magnetic moment later was related to the angular momentum by Uhlenbeck and Goudsmit[24] via the gyromagnetic ratio γ_e (in the following bold symbols denote vectors and matrices):

$$\boldsymbol{\mu} = \gamma_e \hbar \boldsymbol{S} = -g_e \beta_e \boldsymbol{S} \quad (1.1.1)$$

$$\gamma_e = \frac{q}{2m} \quad (1.1.2)$$

$\boldsymbol{S}$ is the electron spin operator, β_e the Bohr magneton, q the charge of the electron and m its mass. g_e is the so-called g-value of the free electron (g_e ≈ 2.002331). It will be discussed in detail in Section 1.1.2. If exposed to a magnetic field, $\boldsymbol{B}$, an electron spin can populate two energy levels, according to $M_s = +1/2$ and $M_s = -1/2$, separated by an energy $\Delta U(B)$:

$$\Delta U(B) = h\nu = \Delta M_s g \beta_e B \quad (1.1.3)$$

If the energy $h\nu$ of an incident electromagnetic wave fulfills the above equation for a certain value of $\boldsymbol{B}$ (i.e., if the resonance condition is met), a spin-containing sample can absorb parts of the incident electromagnetic wave and an EPR spectrum can be detected. This absorption was achieved technically first by Zavoisky.[25] Subsequently, Frenkel[26] interpreted this field-dependent absorption as an EPR spectrum.

After the end of World War II EPR techniques rapidly developed because of the pronounced availability of microwave systems operating at approx. 9.4 GHz (X-band), which are well-suited for application in EPR. These systems were originally developed for use in RADAR tracking.[22] At first, all improvements focused on continuous-wave (CW) EPR and interpretation of corresponding spectra. Major contributions can be attributed to Abragam, Bleaney, Pryce and Van Vleck.[22, 27] Pulse EPR, which does not rely on the continuous irradiation of microwaves but on sequences of short microwaves pulses, did not develop much until the 1980s, although pulse and Fourier-Transform techniques were already known from nuclear magnetic resonance (NMR) spectroscopy.[28] Fast microwave components and sufficiently fast digital electronics, however, were still missing and only the groups of W.B. Mims and Yu. D. Tsvetkov were effectively working on pulse EPR.[21] It was not until 1987 that the first commercially available pulse EPR spectrometer was introduced by Bruker.[29] From 1990 on also high-field pulse EPR evolved significantly, pioneered by Ya. S. Lebedev. In 1996 also devices operating at 94 GHz (W-band) became commercially available.[30] Today EPR has developed to a full-grown experimental technique that makes it possible to perform a vast variety of experiments, reaching from fast analytical detection of paramagnetic substances to complicated nanoscale distance measurements.

1.1.2 The Motion of Spins

In the following the method of EPR spectroscopy will be introduced in detail. The general behavior of electron spins in and their interactions with magnetic fields will be described first. Afterwards the CW EPR experiment and the most important pulse EPR experiments will be described in parallel with a quantum mechanical description of spin dynamics.

Spin Dynamics

EPR spectroscopy is usually applied to solution- or solid-state samples containing a large ensemble of spins. Thus, an electromagnetic wave (in most cases microwaves) irradiated towards a paramagnetic sample in an external, static magnetic field does not only interact with one spin system, but with many. For a typical sample the number of interacting spins exceeds 10^{10}; constituting a so-called *spin ensemble*. Consequently, a macroscopic net magnetization per unit volume, M_0, i.e., the sum of the magnetic moments μ of i spins is detected:

$$\boldsymbol{M_0} = \frac{1}{V}\sum_{i=1}^{N} \boldsymbol{\mu_i} \quad (1.1.4)$$

$\boldsymbol{\mu}$ is related to the energy of a spin-system by:

$$\boldsymbol{\mu} = -\frac{U(\boldsymbol{B},\boldsymbol{S})}{\boldsymbol{B^T}} \quad (1.1.5)$$

(Throughout this thesis the transpose of a matrix $\boldsymbol{X}$ will be denotes as $\boldsymbol{X^T}$.) As described by eq. 1.1.5 it depends on the spin-systems' magnetic moment and hence on the energetic state of the ensemble spins in a magnetic field, $\boldsymbol{B}$, if the resonance condition (eq. 1.1.3) is met.

An ensemble of spins in a static, homogeneous magnetic field exists in a dynamic equilibrium, according to the fundamental principles of electrodynamics. This means that the net magnetization, $\boldsymbol{M}$, is time-dependent since it precesses with the frequency of the magnetic field:[31]

$$\frac{d\boldsymbol{M}}{dt} = \gamma_e \boldsymbol{M} \times \boldsymbol{B} \quad (1.1.6)$$

Defining $\boldsymbol{B}$ to run along an axes z (the quantification axis), one obtains for the time-dependent magnetization in direction of the Cartesian principal axes:

$$\frac{dM_x}{dt} = \gamma_e B M_y \;\rightarrow\; M_x = M_\perp^0 \cos \omega_B t \quad (1.1.7)$$

$$\frac{dM_y}{dt} = \gamma_e B M_x \;\rightarrow\; M_y = M_\perp^0 \sin \omega_B t \quad (1.1.8)$$

$$\frac{dM_z}{dt} = 0 \;\rightarrow\; M_z = M_z^0 \quad (1.1.9)$$

$M_\perp^0$ denotes magnetization perpendicular to z. $\boldsymbol{M}$ precesses around $\boldsymbol{B}$ with the so-called Larmor frequency $\omega_B = -\gamma_e B$. For a more precise description of spin dynamics, one has to take relaxation effects into account, too. At a particular energy difference between the two spin states, $M_s = |\alpha\rangle = +1/2$ and $M_s = |\beta\rangle = -1/2$, their population is determined by a Boltzmann distribution:

$$\frac{n_\alpha}{n_\beta} = \exp\left(-\frac{\Delta U(B)}{k_B T}\right) \quad (1.1.10)$$

If an incident microwave perturbs the equilibrium distribution of a spin system by energy dU_0 at a time t_0 the populations of the spin states change and the system gains additional energy, relative to the equilibrium state. Instantaneously, the spin system starts to exponentially lose this extra energy to its surrounding. The time-dependence of this process can be described by:[22]

$$dU = dU_0 \exp\left[\frac{-(t - t_0)}{\tau_1}\right] \quad (1.1.11)$$

Starting at a time t_0 the amount of lost energy after the time t is essentially dependent on τ_1, which denotes the longitudinal relaxation time. By definition this is the time needed for $\Delta n = n_\beta - n_\alpha$ to change by $\left[\Delta n_{t\rightarrow\infty} - \Delta n_{t=t_0}\right][1 - e^{-1}]$. τ_1 applies primarily to M_z, since $\boldsymbol{B}$ is quantified along this axis. Such, transverse contributions to $\Delta U(B)$ in eq. 1.1.10 can be neglected. The transverse relaxation time, τ_2, applies for M_x and M_y. The physical reasons behind τ_2 is primarily ascribed to loss of coherence between spins due to spin flip-flop processes, proceeding with a rate:[21]

$$\frac{1}{\tau_2} = \frac{1}{\tau_2'} + \frac{1}{2\tau_1} \quad (1.1.12)$$

$$\frac{1}{\tau_2'} = \left(\frac{g\beta_e}{\hbar}\right)^2 B^2 \tau_c \quad (1.1.13)$$

Eq. 1.1.12 and 1.1.13 are only valid in the so-called Redfield limit. Eq. 1.1.13 only applies for random field relaxation. Other mechanisms are relevant for nitroxides (cf. Section 1.2). This means that states comprising couplings between spins and their surrounding must be short-lived compared to the time scale of electron-spin relaxation.[32, 33]

τ_c is (for spherical molecules) the rotational correlation time. For isotropic, Brownian motion it amounts to:

$$\tau_c = \frac{1}{6D_r} \quad (1.1.14)$$

This will be discussed below. D_r is the diffusion coefficient of rotational motion. Beforehand, the introduction of magnetization of a relaxing spin system will be completed since it can be described conveniently using τ_1 and τ_2. By including longitudinal and transverse relaxation the so-called Bloch equations that describe the entire motion of precessing spins in a steady magnetic field, $\boldsymbol{B}$ (frequently also denoted $\boldsymbol{B_0}$), can be set up:

$$\frac{dM_x}{dt} = \gamma_e\left(BM_y - B_1 \sin(\omega t)M_z\right) - \frac{M_x}{\tau_2} \quad (1.1.15)$$

$$\frac{dM_y}{dt} = \gamma_e(B_1 \cos(\omega t)M_z - BM_x) - \frac{M_y}{\tau_2} \quad (1.1.16)$$

$$\frac{dM_z}{dt} = \gamma_e\left(B_1 \sin(\omega t)M_x - B_1 \cos(\omega t)\, M_y\right) - \frac{M_z - M_z^0}{\tau_1} \quad (1.1.17)$$

ω is the frequency of the microwave $\boldsymbol{B_1}$ that initially perturbs the equilibrium of the spin system. $\boldsymbol{B_1}$ is an oscillating magnetic field, perpendicular to $\boldsymbol{B}$, which induces the energy difference dU_0 (see eq. 1.1.11) and hence an initial change in energy level population, as depicted in Figure 1.1.1. In a typical EPR experiment $\boldsymbol{B_1}$ refers to a microwave that is irradiated onto a sample. The absorption of $\boldsymbol{B_1}$ through paramagnetic centers in the sample gives rise to an EPR spectrum.

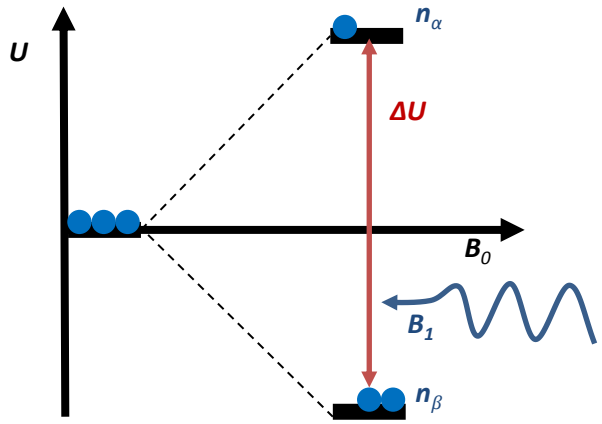

Figure 1.1.1. Sketch of a spin system in a magnetic field $\boldsymbol{B_0}$. $\boldsymbol{B_1}$ induces a transition from the β to α state.

Quantification of Molecular Motion

One cannot describe the dynamics of spins in a magnetic field without taking into account the rotational diffusion of the spin-carrying compounds (in most cases radical molecules). Their dynamics affect the relaxation processes of excited spins since Their rotational diffusion affects τ_2 because the unpaired electrons' environment is effectively rotated. This can be described by an integration over rotational autocorrelation functions, $\rho(t)$:

$$\tau_c = \int_{t=0}^{t=\infty} \rho(t)dt \quad (1.1.18)$$

$\rho(t)$ formally describes the autocorrelation of Wigner-rotation matrix elements, which is an eigenfunction of the Hamiltonian of spherosymmetrical problems:[34]

$$\rho(t) = \langle D_{l,m,n}(\Omega(t)) | D_{l,m,n}(\Omega(t=0)) \rangle \quad (1.1.19)$$

$D_{l,m,n}(\Omega(t))$ denotes a Wigner-matrix element, which is dependent on the orientation $\Omega(t)$ of the spin-carrying compound, where l denotes the order of the spherical harmonic.[34, 35] Most generally, the distribution of orientations, $P(\Omega, t)$, can be described by the time-dependent Smoluchowski equation:[36]

$$\frac{d}{dt}P(\Omega, t) = -\Gamma_\Omega P(\Omega, t) \quad (1.1.20)$$

Γ_Ω denotes the time-independent rotational motion operator. For the case of isotropic Brownian motion Γ_Ω can be described by a random walk on the surface of a sphere:

$$\Gamma_\Omega = -D_r \nabla_\Omega^2 \quad (1.1.21)$$

∇ is the del operator. By inserting eq. 1.1.21 in eq. 1.1.20 it can be shown that:

$$\rho(t) = \exp[-tD_r l(l+1)] \quad (1.1.22)$$

D_r is the Stokes-Einstein coefficient for spherical rotational motion. Inserting eq. 1.1.22 into eq. 1.1.18 and applying the Stokes-Einstein equation finally yields (for $l = 2$, which applies to tensors describing anisotropic interaction in the spin Hamiltonian):

$$\tau_c = \frac{4\pi R_h}{3k_B T} \quad (1.1.23)$$

where R_h is the rotational hydrodynamic radius of the spin-carrying species. In EPR spectroscopy, however, spins often do not rotate isotropically, but rotate slowly around one axes of the molecular frame, while they rotate fast around the others. Schneider and Freed have developed a theory that can account for such anisotropic motion. They showed that the coefficient for rotational motion can be expressed as:[36]

$$\boldsymbol{D}_r = \begin{bmatrix} D_\perp & & \\ & D_\perp & \\ & & D_\parallel \end{bmatrix} \quad (1.1.24)$$

$D_\perp$ can account for the diffusion around the two fast principal axes x, y and $D_\parallel$ can account for the rotation around the slow axis z. Note that there are even more sophisticated models for complex motion like the MOMD (macroscopic order microscopic disorder) or SRLS (slowly relaxing local structure) model.[37, 38]

1.1.3 Magnetic Interactions and the Spin Hamiltonian

It is convenient to express the energy levels of a spin system in terms of a spin Hamiltonian, which summarizes all effective, magnetic interactions that can influence the energetic state of a spin system. The typical effective, time-independent Hamiltonian of a spin $\boldsymbol{S}$ has the form:

$$\mathcal{H}_0 = \mathcal{H}_{EZ} + \mathcal{H}_{ZFS} + \mathcal{H}_{hf} + \mathcal{H}_{NQ} + \mathcal{H}_{e-e} \quad (1.1.25)$$

From left to right the different elements of the Hamiltonian denote the electron-Zeeman (EZ) interaction, the zero-field splitting (ZFS), the hyperfine (hf) interaction, the nuclear-quadrupole (NQ) interaction and the electron-electron (e-e) interaction. The elements not only interactions of $\boldsymbol{S}$ with external magnetic fields and other electrons are taken into account, but also dipolar and Fermi-type interactions of a nuclear spin $\boldsymbol{I}$ with $\boldsymbol{S}$. This hyperfine coupling of free electrons with surrounding nuclei is an inevitable feature of EPR spectra, since it is practically an omnipresent phenomenon. Note that the eigenfunctions of spin Hamiltonians are (wave) functions of the electron spin. Thus, they are integrable and H_0 spans a Hilbert space with dimensionality d_H, describing the number of energy levels of all participating spins J_k:

$$d_H = \prod_k (2J_k + 1) \quad (1.1.26)$$

In the following the different contributions to the effective Hamiltonian will be discussed in detail.

Electron-Zeeman Interaction

The electron-Zeeman Hamiltonian H_{EZ} describes the interaction of electron spins with an external magnetic field. If the electron-Zeeman interaction is much larger than all other interactions, the so-called high-field approximation holds. This means that all terms of the spin Hamiltonian can be neglected, which are not aligned along the quantification axis, z. For practically applied fields the high field-approximation is usually valid and the electron-Zeeman Hamiltonian can therefore be expressed as:

$$\mathcal{H}_{EZ} = \frac{\beta_e}{\hbar} \boldsymbol{B}^T \boldsymbol{g} \boldsymbol{S} \quad (1.1.27)$$

$\boldsymbol{g}$ denotes the effective g-value of the spin system. It can be expressed as a diagonalized 3x3 matrix with principal values g_{xx}, g_{yy} and g_{zz}. The g-matrix in return is dependent on contributions from spin-orbit coupling of excited spin-states $|m\rangle$:[21]

$$\boldsymbol{g} = g_e \boldsymbol{\delta_{ij}} + 2 \sum_k \sum_{m \neq 0} \frac{\lambda_k \langle m | \boldsymbol{L}_{ki} | 0 \rangle \langle 0 | \boldsymbol{L}_{kj} | m \rangle}{E_0 - E_m} = g_e \boldsymbol{\delta_{ij}} + \boldsymbol{2} \lambda_k \boldsymbol{\Lambda} \quad (1.1.28)$$

$\boldsymbol{\delta_{ij}}$ denotes the Kronecker delta. The admixture of the orbital angular momentum thus is inversely proportional to the difference between the energies of the ground and excited state, $E_0 - E_m$. λ_k is the spin-orbit-coupling constant of the *kth* atom. $\boldsymbol{L}$ is the angular momentum operator and the indices *i-j* run over the coordinate system axes x, y and z.

g_e, the g-value of the free electron, is fundamental proportionality constant. Its value is approx. 2.002331. It relates the magnetic moment of the free electron to the Bohr magneton and the spin state:

$$\boldsymbol{\mu_s} = g_e \beta_e \frac{\boldsymbol{S}}{\hbar} \quad (1.1.29)$$

Such, the spin magnetic moment is – neglecting minor corrections through quantum electrodynamics – twice as large as its angular momentum.

Dipole-Dipole Interaction

Electron spins can interact through space with each other since they are the quantum mechanical analogue to classic magnetic dipoles. In the point dipole approximation, the dipolar coupling energy between two spins $\boldsymbol{S_1}$ and $\boldsymbol{S_2}$ is characterized by the dipolar coupling Hamiltonian:

$$\mathcal{H}_{dd} = \boldsymbol{S_1^T D S_2} = \frac{\mu_o}{r^3 4\pi\hbar}\boldsymbol{g_1 g_2}\beta_e^2\left[\boldsymbol{S_1^T S_2} - \frac{3}{r^2}\left(\boldsymbol{S_1^T r}\right)\left(\boldsymbol{S_2^T r}\right)\right] \quad (1.1.30)$$

Here $\boldsymbol{r}$ is the vector connecting the two electron spins. r denotes its magnitude. In the principal axes system, $\boldsymbol{D}$ can be expressed as:

$$\boldsymbol{D} = \frac{\mu_o}{r^3 4\pi\hbar}\boldsymbol{g_1 g_2}\beta_e^2\begin{pmatrix}-1 & & \\ & -1 & \\ & & 2\end{pmatrix} = \begin{pmatrix}-\omega_{dd} & & \\ & -\omega_{dd} & \\ & & 2\omega_{dd}\end{pmatrix} \quad (1.1.31)$$

Obviously, the dipolar coupling tensor $\boldsymbol{D}$ is of axial symmetry and traceless. ω_{dd} is the dipolar coupling frequency:

$$\omega_{dd}(\theta_{12}, r) = \frac{\mu_o}{r^3 4\pi\hbar}\boldsymbol{g_1 g_2}\beta_e^2(3\cos^2\theta_{12} - 1) \quad (1.1.32)$$

Here, θ_{12} is the angle between the magnetic field $\boldsymbol{B_0}$ and the axis connecting the two spins $\boldsymbol{S_1}$ and $\boldsymbol{S_2}$ (see Figure 1.1.2). From eq. 1.1.32 it is evident that the dipolar coupling intensity obeys an r^{-3} dependence. This will become very important throughout the course of this thesis since this relation is essential for nanoscale distance measurement.

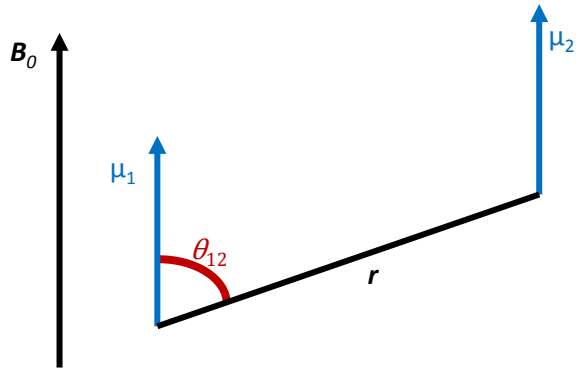

Figure 1.1.2. Two dipolarly coupled spins with magenetic moments, μ_1 abd μ_2 are depicted schematically. The angle between the $\boldsymbol{B}_0$ field and the vector connecting the two moments, θ_{12}, is shown in red. Note that, if the two magnetic moments did not align along $\boldsymbol{B_0}$, the dieder angle Φ would have to be taken into account, too.

Exchange Interaction

If two spins come spatially close together and their orbital functions overlap weakly, their interaction can no longer be described by mere dipolar coupling. Instead the so-called exchange coupling tensor $\boldsymbol{J}$ is employed to describe the energetic contribution due to orbital overlap. The corresponding Hamiltonian is:[22]

$$\mathcal{H}_{exch} = \sum_{ij} J_{ij} S_{1i} S_{2j} = \frac{1}{2}\left(\boldsymbol{S_1^T J S_2} + \boldsymbol{S_2^T J^T S_1}\right) \quad (1.1.33)$$

In this case $\boldsymbol{J}$ has the form of a 3x3 matrix and takes also through-space interactions (Coulomb potentials) into account.[22] However, it is the isotropic part of $\boldsymbol{J}$, which is important for most applica-

tions in the realm of EPR. If anisotropic exchange interactions can be neglected, $J_{iso} = tr(\boldsymbol{J})/3$ can be approximated in terms of molecular orbitals of the two exchanging electrons $\Psi(1)$ and $\Psi(2)$:[22]

$$J_{iso} = -2\left\langle \Psi_\alpha(1)\Psi_\beta(2)\left|\frac{e^2}{4\pi\varepsilon_0 r}\right|\Psi_\alpha(2)\Psi_\beta(1)\right\rangle \quad (1.1.34)$$

and

$$\mathcal{H}_{exch,iso} = J_{iso}\boldsymbol{S}_1^T\boldsymbol{S}_2 \quad (1.1.35)$$

Subscript α and β denote the spin state. Such, J_{iso} essentially represents an overlap integral of the two wave functions $\Psi(1)$ and $\Psi(2)$. It is important to note that the total magnetic interaction energy between two electrons, as described by an electron-electron coupling frequency ω_{e-e} can now be expressed as $\omega_{e-e} = \omega_{dd} + J_{iso}$ and, consequently, $H_{e-e} = H_{exch} + H_{dd}$ applies.

Zero-Field Splitting

If a spin system consists of more than one electron and the different spins couple strongly (e.g. in high-spin complexes of transition metals), the system can be described conveniently by a group spin $\boldsymbol{S} > 1/2$. In such a case the energy levels of the system are non-degenerate, even in the absence of an external magnetic field. This is denominated as zero-field splitting. The corresponding Hamiltonian can be written as:

$$\mathcal{H}_{ZFS} = \boldsymbol{S^T D S} \quad (1.1.36)$$

The tensor $\boldsymbol{D}$, however, is not necessary of axial symmetry as in the case of mere dipolar interaction. For i individual spins the group spin, $\boldsymbol{S}$, amounts to $\sum_i \boldsymbol{S_i}$. Yet, for nearly all systems presented in this thesis $\boldsymbol{S} = 1/2$ applies (except for Mn^{2+} in Chapter 2) and the zero-field splitting term, $\mathcal{H}_{ZFS}$, can be neglected, when an effective spin Hamiltonian is set up.

Hyperfine Interaction

The term hyperfine (hf) interaction summarizes all interactions between an electron spin and surrounding nuclear spins. A general hf Hamiltonian ($\mathcal{H}_{hf}$) consists of an isotropic ($\mathcal{H}_F$) and an anisotropic part ($\mathcal{H}_{DD}$). The former describes Fermi-type, the latter dipolar interactions. Both can be summarized by a hyperfine coupling tensor $\boldsymbol{A}$:[22]

$$\boldsymbol{A} = a_{iso}\mathbf{1} + \frac{\boldsymbol{gT}}{g_e} \quad (1.1.37)$$

And for i coupled nuclei one obtains:

$$\mathcal{H}_{hf} = \sum_{i=1}^{N} \boldsymbol{S}^T\boldsymbol{A}_i\boldsymbol{I_i} = \mathcal{H}_F + \mathcal{H}_{DD} \quad (1.1.38)$$

$\mathbf{1}$ denotes the identity matrix. The factor g/g_estems from admixtures of spin-orbit coupling to the dipolar hyperfine interaction. a_{iso} describes the isotropic Fermi-contact interaction in cases where a singly occupied molecular orbital (SOMO) overlaps with a coupling nucleus. Since only spherical orbitals have finite spin densities > 0 at the locus of the nucleus, $\langle\Psi(0)^*|\Psi(0)\rangle$, contact interaction in most cases is closely related to unpaired electrons in s-type orbitals. Such, this type of interaction is non-directed and hence, isotropic. In general one can state that the higher the spin density at a nucleus, the higher the Fermi contact interaction:

$$a_{iso} = \frac{2\mu_0}{3\hbar} g_e \beta_e g_n \mu_n \langle \Psi(0)^* | \Psi(0) \rangle \quad (1.1.39)$$

From a_{iso} one can calculate the spin population in an s orbital, ρ_s:

$$\rho_s = \frac{a_{iso} g_e}{a_0 g_{iso}} \quad (1.1.40)$$

a_0 denotes the isotropic hyperfine coupling constant one would observe for a pure s-electron.[22, 39]

The traceless dipolar coupling tensor $\boldsymbol{T}$ describes the anisotropic part of the hf Hamiltonian:

$$\boldsymbol{T} = \frac{\mu_0}{4\pi\hbar} g_e \beta_e g_n \mu_n \left\langle \Psi_0 \left| \frac{3 r_i r_j - \boldsymbol{\delta_{ij}} r^2}{r^5} \right| \Psi_0 \right\rangle \quad (1.1.41)$$

Ψ_0 is the wave function of the SOMO, hence the orbital function of the unpaired electron. r_i and r_j are components of the electron-nucleus vector in a molecular framework. (As in the case of eq. 1.128, the indices *i-j* run over the coordinate system axes x, y, z.)

For protons $\boldsymbol{T}$ can conveniently be described if the point-dipole approximation is taken into account. This implies that it is possible to approximate the spin density, ρ_k, of a coupling nucleus, N, which is more than 0.25 nm away from the electron spin, as a point-like. $\boldsymbol{T}$ can then be written as:

$$\boldsymbol{T} = \frac{\mu_0}{4\pi\hbar} g_e \beta_e g_n \mu_n \sum_{k \neq N} \rho_k \frac{3 \boldsymbol{n_k} \boldsymbol{n_k^T} - \mathbf{1}}{R_k^3} \quad (1.1.42)$$

$\boldsymbol{n_k}$ denotes the unity vector along the axes connecting the nucleus of the proton with the hyperfine coupling nucleus (connecting vector: R_k).

Nuclear Quadrupole Interaction

Nuclei with $I > 1/2$ feature non-spherical charge symmetry. Thus, they have a magnetic quadrupolar moment. The nuclear quadrupole interaction Hamiltonian can be represented by:

$$\mathcal{H}_{NQ} = \boldsymbol{I}^T \boldsymbol{P} \boldsymbol{I} = P_x I_x^2 + P_y I_y^2 + P_z I_z^2 \quad (1.1.43)$$

The right-hand site of the above equation is valid only in a principal axes frame. In such a case, the quadrupolar interaction can be expressed as:

$$P_z = \frac{e^2 q Q}{2I(I-1)\hbar} \quad (1.1.44)$$

Furthermore an asymmetry parameter, η, describes the "deviation of the field gradient from uniaxial symmetry about z":[22]

$$\eta = \frac{P_x - P_y}{P_z} \qquad |P_z| \geq |P_y| \geq |P_x| \quad (1.1.45)$$

$|e|q$ describes the maximal electric field gradient affecting the nuclear magnetic moment. $|e|Q$ describes the electric shape of the nucleus. Such, the quadrupolar coupling $|e^2 q Q e^{-1}|$ is dependent on the electric shape and chemical environment of the nucleus. E.g. a highly symmetrically substituted ^{14}N-nucleus ($I = 1$), does only lead to very weak quadrupolar coupling, since $|e|q$ becomes zero at the locus of the nucleus.[40]

Nuclear-Zeeman and Dipolar Nuclear Interaction

In analogy to the electron-Zeeman and the dipolar interaction between two electrons, the nuclear-Zeeman and the dipolar nuclear interaction describe the interaction between a nucleus and an external magnetic field and between several nuclei, respectively. However, in EPR applications these interactions are too weak to be observed. Yet, nuclear-Zeeman interactions can affect resonance frequencies of nuclei, when observed indirectly by EPR spectroscopy (see Section 1.1.6).

1.1.4 Continuous Wave EPR

The most common EPR technique is continuous wave (CW) EPR. This technique features constant microwave irradiation ($\boldsymbol{B_1}$) combined with a field-sweep of the external magnetic field ($\boldsymbol{B_0}$). If at some field strength the resonance condition is met (eq. 1.1.3) the microwave field is absorbed and one detects an absorption line. The shape of the line (i.e. splitting, line-width etc.) encodes information about the effective spin Hamiltonian. The advantage of CW EPR is that also very fast relaxing spin systems with very short τ_1 and τ_2 are detectable. Many of these systems cannot be accurately detected by means of pulsed techniques as in modern NMR spectroscopy. Mathematically, the absorption of $\boldsymbol{B_1}$ can be described by the Bloch equations. These yield the change in magnetization of a spin system in dependence of incident irradiation. If at a certain field strength the resonance condition is met for sufficiently long irradiation of $\boldsymbol{B_1}$ the spin system's magnetization reaches a steady state, different from the equilibrium state. The steady-state solutions for the Bloch equations are:

$$M_{x\Phi} = -M_z^0 \frac{\gamma_e B_1 (\omega_B - \omega)\tau_2^2}{1 + (\omega_B - \omega)^2\tau_2^2 + \gamma_e^2 B_1^2 \tau_1 \tau_2} \quad (1.1.46)$$

$$M_{y\Phi} = -M_z^0 \frac{\gamma_e B_1 \tau_2}{1 + (\omega_B - \omega)^2\tau_2^2 + \gamma_e^2 B_1^2 \tau_1 \tau_2} \quad (1.1.47)$$

$$M_{z\Phi} = -M_z^0 \frac{1 + (\omega_B - \omega)\tau_2^2}{1 + (\omega_B - \omega)^2\tau_2^2 + \gamma_e^2 B_1^2 \tau_1 \tau_2} \quad (1.1.48)$$

$M_{x\Phi}$, $M_{y\Phi}$ and $M_{z\Phi}$ denote the magnetization in a coordinate frame that rotates around the z axes with the frequency ω (cf. section on the motion of spins in magnetic fields).[22] $M_{z\Phi}$, the so-called longitudinal magnetization, tends to be large compared to $M_{x\Phi}$ and $M_{y\Phi}$ and cannot be detected with conventional experimental setups. Usually a low power microwave source is used for CW EPR so that eq. 1.1.46-48 can be expressed as

$$M_{x\Phi} = -M_z^0 \frac{\gamma_e B_1 \Omega_s \tau_2^2}{1 + \Omega_s^2 \tau_2^2} \quad (1.1.49)$$

$$M_{y\Phi} = -M_z^0 \frac{\gamma_e B_1 \tau_2}{1 + \Omega \tau_2^2} \quad (1.1.50)$$

$$M_{z\Phi} = -M_z^0 \frac{1 + \Omega_s \tau_2^2}{1 + \Omega \tau_2^2} \quad (1.1.51)$$

$$\Omega_s = \omega_B - \omega \quad (1.1.52)$$

since $B_1 << \Omega_s$. In this case one could detect both the magnetizations, in x and y direction, by a quadrature-detection scheme.[21] However, this is commonly only done for pulse applications. Note that $M_{x\Phi}$ and $M_{y\Phi}$ are phase shifted by 90° so that the detected signal, *V*, becomes complex:

$$V = -M_{y\Phi} + iM_{x\Phi} \quad (1.1.53)$$

Here, M_y corresponds to a Lorentzian absorption line, while the imaginary part, M_x, corresponds to a dispersion line (Figure 1.1.3).

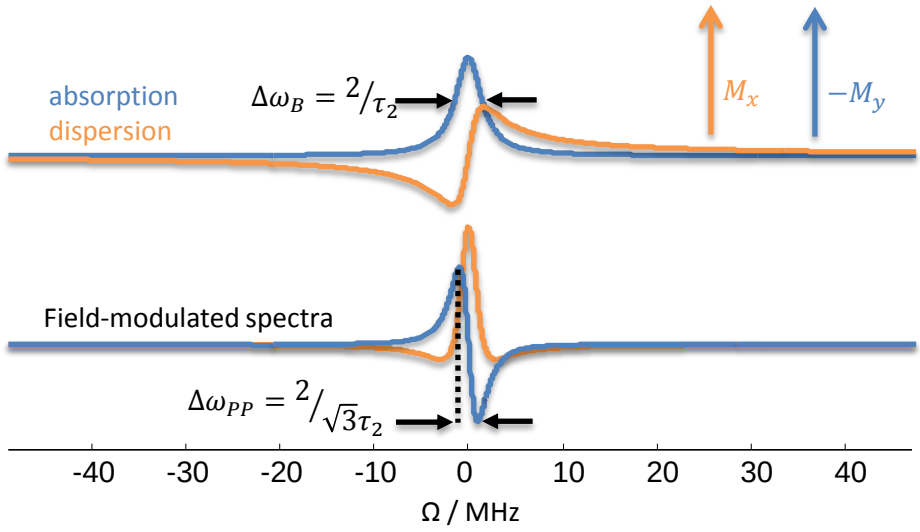

Figure 1.1.3. Lorentzian absorption and dispersion line, as calculated from eq. 1.1.49 and 1.1.50 (top) and the corresponding CW EPR signal (bottom). Note that the CW EPR signal corresponds to the first derivative of the absorption and dispersion line.

In the case of homogeneous line broadening the Lorentzian line-shape is characterized by the full width of the line at half its maximum (FWHM), which corresponds to a frequency range of $\Delta\omega_B = 2/\tau_2$. This line width can primarily be attributed to life-time broadening. This means, the finite life time of coherent, transverse electron states (described by τ_2) leads to small uncertainties in the resonance frequency.[41] In cases of inhomogeneous broadenings stemming from non-resolved hyperfine couplings the line-shape can feature significant Gaussian contributions. This yields an overall Voigt line.[22] Additionally, in a real CW EPR experiment the static magnetic field is modulated with a frequency of typically 100 kHz and the signal is detected in a phase sensitively way with respect to the modulation frequency. This reduces the detected band-width of frequencies and minimizes the signal-to-noise (SNR) ratio. (Usually, detector diodes are sensitive to a very broad band-width.) As a consequence the actually detected signal appears as the first derivative of the absorption line. In such a case the peak-to-peak line-width is given by: $\Delta\omega_{PP} = 2/(\sqrt{3}\tau_2)$. From Figure 1.1.3 it is evident how the microwave irradiation $\boldsymbol{B_1}$ is absorbed at a given offset frequency leading to an EPR spectrum.

1.1.5 Quantum Mechanical Description of Spin Ensembles

For many applications of EPR, e.g., for nanoscale distance measurements, one has to apply certain pulse sequences in order to extract the desired information. For such pulsed EPR experiments the classical treatment of a spin ensemble can no longer be applied – as in the description of CW EPR – since this cannot account for the interactions in multi-spin systems. Hence, before proceeding with the description of pulse EPR the quantum mechanical treatment of spin ensembles has to be introduced. In a quantum mechanical picture a single spin can populate two distinct states, $|\alpha\rangle$ and $|\beta\rangle$, corresponding to $M_s = +1/2$ and $M_s = -1/2$. The wave function of such a single spin is given by: $|\Psi\rangle = c_\alpha|\alpha\rangle + c_\beta|\beta\rangle$. c_α and c_β are normalization coefficients.[21] The probability to find a spin a

state $|\alpha\rangle$ or $|\beta\rangle$ is $\left|c_{\alpha/\beta}\right|^2$. In a so-called pure state that is constituted of *N* spins featuring a constant phase difference (so-called coherence) the spin system can be expressed by a single wave function $|\Psi\rangle^N$. Any other state can be described by a superposition of i sub-ensembles of pure states with probability p_i and wave function $|\Psi_i\rangle$. The magnetization of any spin system at any moment can be expressed in terms of the normalization coefficients:[21]

$$M_x = \frac{-g_e\beta_e N}{2V}\sum_i p_i\left(c_\alpha^{(i)^*}c_\beta^{(i)} + c_\alpha^{(i)}c_\beta^{(i)^*}\right) = \frac{-g_e\beta_e N}{2V}\overline{|c_\alpha||c_\beta|\cos\Delta\varphi} \quad (1.1.54)$$

$$M_y = \frac{ig_e\beta_e N}{2V}\sum_i p_i\left(c_\alpha^{(i)^*}c_\beta^{(i)} - c_\alpha^{(i)}c_\beta^{(i)^*}\right) = \frac{-g_e\beta_e N}{2V}\overline{|c_\alpha||c_\beta|\sin\Delta\varphi} \quad (1.1.55)$$

$$M_z = \frac{-g_e\beta_e N}{2V}\sum_i p_i\left(c_\alpha^{(i)} - c_\beta^{(i)}\right) \quad (1.1.56)$$

V denotes the total volume of the overall system and $\Delta\varphi$ the phase difference between the α- and the β-spin state. The horizontal bar indicates the ensemble average. Note that for a single pure state $i = 1$. The coefficients $\overline{\left|c_{\alpha/\beta}\right|^2}$, $\overline{c_\alpha^* c_\beta}$ and $\overline{c_\alpha c_\beta^*}$ then constitute the so-called density matrix $\boldsymbol{\sigma}$ of a system of non-coupled spins:

$$\boldsymbol{\sigma} = \begin{pmatrix} \overline{|c_\alpha|^2} & \overline{c_\alpha^* c_\beta} \\ \overline{c_\alpha c_\beta^*} & \overline{\left|c_\beta\right|^2} \end{pmatrix} \quad (1.1.57)$$

A spin system is entirely described by the density matrix. Its diagonal elements correspond to the populations of the spin states, while the off-diagonal elements quantify the coherences perpendicular to the quantification axis. Thus, the difference in diagonal elements is proportional to longitudinal magnetization, while the magnitude of the off-diagonal elements is proportional to transverse magnetization. The above description, however, is only valid for non-interacting spin ensembles. For systems with two coupled spin systems (e.g. $\boldsymbol{S} = 1/2$ and $\boldsymbol{I} = 1/2$) and a Hilbert-Space dimension of $\mathrm{d_H} = 4$ (see eq. 1.1.26), it can be shown that the density matrix becomes:[21]

$$\boldsymbol{\sigma} = \sum_{\mathrm{i}=1}^{\mathrm{n}} \mathrm{p_i}|\Psi_\mathrm{i}\rangle\langle\Psi_\mathrm{i}| = \sum_{kl}\overline{c_l^* c_k}|\mathrm{l}\rangle\langle\mathrm{k}| \quad (1.1.58)$$

$\langle k|$ and $|l\rangle$ denote the basis states of the Hilbert space and $l = 1$ has been assumed for the second equality. Note that for any observable A the expectation value[42] can be calculated as $\langle A\rangle = tr\{A\sigma\}$. This is of importance for the calculation of detectable magnetizations by means of the product-operator formalism, which will be introduced below. A schematic representation of the four-level density matrix (corresponding to two coupled spins) is shown in Figure 1.2.4.

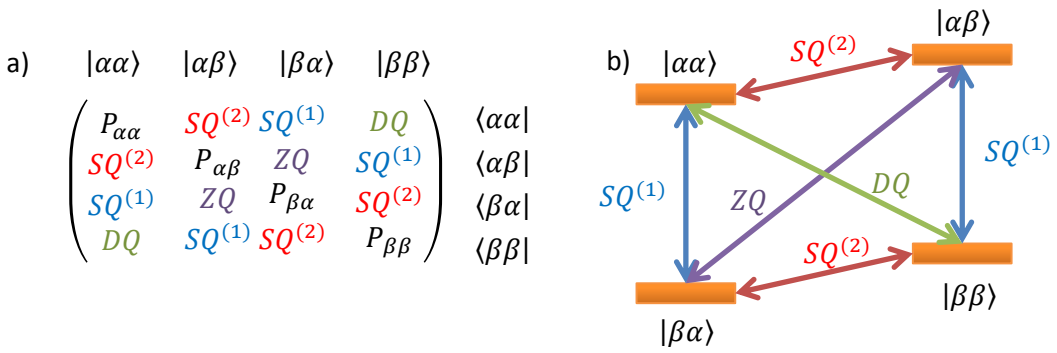

Figure 1.1.4. a) The density matrix elements of a coupled two-spin system. Diagonal elements (black) correspond to the populations of the energy levels depicted in b). ZQ, denotes zero-quantum coherences, SQ single-quantum coherences, DQ double-quantum coherences and P populations. b) Energy level diagram of a coupled two-spin system.

Time Evolution of Spins Systems

Considering a spin system and neglecting relaxation effects, the time-evolution of eq. 1.1.58 can be expressed by that of constituting states, which are described by the wave function $|\Psi_k\rangle$:[21]

$$\boldsymbol{\sigma}(t) = \sum_k \mathrm{p_k} |\Psi_k\rangle\langle\Psi_k| \quad (1.1.59)$$

Applying the time-dependent Schrödinger equation to eq. 1.1.59 one derives the Liouville-von Neumann equation:

$$\frac{d\sigma}{dt} = -i \sum_k p_k (\mathcal{H}|\Psi_k\rangle\langle\Psi_k| - |\Psi_k\rangle\langle\Psi_k|\mathcal{H}) = -i(\mathcal{H}\boldsymbol{\sigma} - \boldsymbol{\sigma}\mathcal{H}) = -i[\mathcal{H}(t), \boldsymbol{\sigma}(t)] \quad (1.1.60)$$

The Liouville-von Neumann equation can be considered a quantum mechanical analogue of the Bloch equations. It can readily be solved when the Hamiltonian is time independent over a sufficiently long period of time. In such a case formal integration yields:

$$\boldsymbol{\sigma}(t) = exp\big(\boldsymbol{U}(t)\boldsymbol{\sigma}(t=0)\boldsymbol{U}^{\dagger}\big) \quad (1.1.61)$$

$$\boldsymbol{U}(t) = \exp(-i\mathcal{H}t) \quad (1.1.62)$$

The exponential operator $\boldsymbol{U}(t)$ is called a propagator, because it "propagates the density operator in time",[21] via unitary transformation corresponding to a rotation in Hilbert-space. If the spin-system undergoes significant changes during an experiment, it is convenient to divide its time evolution of the spin system into intervals of constant $\boldsymbol{U}(t)$. In such a case the expectation value of any desired observable can be calculated at any time by applying the respective propagators (density operator formalism):

$$\langle A\rangle = \mathrm{Tr}\{\boldsymbol{U}_n \dots \boldsymbol{U}_2\boldsymbol{U}_1\boldsymbol{\sigma}(t=0)\boldsymbol{U}_1^{\dagger}\boldsymbol{U}_2^{\dagger} \dots \boldsymbol{U}_n^{\dagger}\boldsymbol{A}\} \quad (1.1.63)$$

Product Operator Formalism

For larger spin systems the application of the whole density matrix operator might become difficult. It is therefore convenient to decompose $\boldsymbol{\sigma}$ into a set of $d_L = d_H^2$ orthogonal basis sets, which span a Liouville space. The exemplary spin system $\boldsymbol{S} = 1/2\,, \boldsymbol{I} = 1/2$ can be expressed in a basis set of the Liouville space by:[21]

$$\{\boldsymbol{A_1}, \boldsymbol{A_2}, \dots, \boldsymbol{A_n}\} = \{\boldsymbol{S_x}, \boldsymbol{S_y}, \boldsymbol{S_z}, \boldsymbol{1}\} * \{\boldsymbol{I_x}, \boldsymbol{I_y}, \boldsymbol{I_z}, \boldsymbol{1}\} \quad (1.1.64)$$

$\boldsymbol{S_{x,y,z}}$ and $\boldsymbol{I_{x,y,z}}$ denote Cartesian spin operators that quantify the spin angular momentum in x, y, and z direction. Normalizing eq. 1.1.64 yields:

$$\{\boldsymbol{A_1}, \boldsymbol{A_2}, \dots, \boldsymbol{A_{16}}\}$$
$$= \left\{\frac{1}{2}\boldsymbol{1}, \boldsymbol{S_x}, \boldsymbol{S_y}, \boldsymbol{S_z}, \boldsymbol{I_x}, \boldsymbol{I_y}, \boldsymbol{I_z}, 2\boldsymbol{S_xI_x}, 2\boldsymbol{S_xI_y}, 2\boldsymbol{S_xI_z}, 2\boldsymbol{S_yI_x}, 2\boldsymbol{S_yI_y}, 2\boldsymbol{S_yI_z}, 2\boldsymbol{S_zI_x}, 2\boldsymbol{S_zI_y}, 2\boldsymbol{S_zI_z}\right\} \quad (1.1.65)$$

Each of these 16 base vectors can be considered an element of the overall density-matrix operator. In contrast to the density operator formalism, the advantage of the product operator formalism is that it can be applied to systems with any number of spins. To apply the product operator formalism to EPR, one has to determine how an operator ***A*** evolves under another operator ***B*** into a state **C**:

$$e^{-i\varphi \boldsymbol{B}}\boldsymbol{A}e^{\varphi \boldsymbol{B}} = \boldsymbol{C} \text{ or } \boldsymbol{A} \xrightarrow{\varphi \boldsymbol{B}} \boldsymbol{C} \quad (1.1.66)$$

φ corresponds in most cases to either a flip angle due to a microwave pulse or an amplitude of an interaction described by the Hamiltonian. Thus, considering a spin system to be in an equilibrium state with the magnetization quantified along $-\boldsymbol{S_z}$ (see eq. 1.1.70) and applying a microwave pulse that rotates the magnetization by $\pi/2$ around the x axes, one finds:

$$\boldsymbol{\sigma}_{eq} = -\boldsymbol{S_z} \xrightarrow{(\pi/2)\boldsymbol{S_x}} \boldsymbol{S_y} \quad (1.1.67)$$

Hence, the microwave pulse transfers magnetization from polarization in –z direction to coherence in y direction. Further it can be shown that, as long as all terms of the Hamiltonian commute, multiple operations can be expressed as:[21]

$$\boldsymbol{A} \xrightarrow{\varphi_1 \boldsymbol{B}_1} \xrightarrow{\varphi_2 \boldsymbol{B}_2} \dots \xrightarrow{\varphi_n \boldsymbol{B}_n} \boldsymbol{C}_n \quad (1.1.68)$$

1.1.6 Pulsed EPR

With the product operator formalism and the quantum mechanical description of time-dependent spin ensembles one can describe pulse EPR experiments concisely. Considering a spin system in its equilibrium state, the polarization in terms of the spin density operator, $\boldsymbol{\sigma}_{eq}$, can be expressed as:

$$\boldsymbol{\sigma}_{eq} = \frac{\exp(-\mathcal{H}_0 \hbar/kT)}{\mathrm{Tr}[\exp(-\mathcal{H}_0 \hbar/kT)]} \quad (1.1.69)$$

Assuming the electron-Zeeman interaction to dominate the spin Hamiltonian in the high-temperature (i.e. $\Delta U(B) \ll k_B T$) and high-field limit one can state that $\mathcal{H}_0 \cong \omega \boldsymbol{S_z} \ll k_B T$. Applying this approximation to eq. 1.1.69 and performing a series expansion the density matrix in the equilibrium state can be expressed as:

$$\boldsymbol{\sigma}_{eq} = \boldsymbol{1} - \frac{\hbar\omega}{k_B T}\boldsymbol{S_z} \quad (1.1.70)$$

Hence, in its equilibrium state the magnetization is quantified along the –z axes of the laboratory frame. A microwave pulse will disturb this equilibrium. Such a pulse is characterized by its duration, τ_p, and intensity. The effective influence of a pulse on the magnetization can be described by a nutation frequency, ω_{nut}. The magnetization is flipped by an angle β_i around axes i by a microwave pulse of length τ_p:

$$\beta_i = \omega_{nut}\tau_p \quad (1.1.71)$$

The Primary Echo

Consider a $\pi/2$ microwave pulse. It transfers the equilibrium magnetization to coherence like shown in eq. 1.1.67. In a rotating frame coordinate system the different packages of coherent spins will start immediately to precess with their offset frequency Ω_S (see eq. 1.1.52) around the magnetic-field quantification axes. Differences in Ω_S stem from slightly different local environments of the different spins in a system. Thus, every spin has a different resonance frequency. Assuming now that the coherence evolves for a time interval τ every package of coherent spins gains a phase according to their specific offset frequency such that:[21]

$$\boldsymbol{S_y} \xrightarrow{\tau\Omega_S \boldsymbol{S_z}} \cos(\tau\Omega_S)\boldsymbol{S_y} - \sin(\tau\Omega_S)\boldsymbol{S_z} \quad (1.1.72)$$

After the time τ the magnetization is spread in the x-y plane like depicted in Figure 1.1.5. One can refocus the magnetization by applying a π-pulse around the x axis. After waiting for another period of length τ the magnetization becomes:

$$\cos(\tau\Omega_S)\boldsymbol{S_y} - \sin(\tau\Omega_S)\boldsymbol{S_z} \xrightarrow{\pi \boldsymbol{S_x}} -\cos(\tau\Omega_S)\boldsymbol{S_y} - \sin(\tau\Omega_S)\boldsymbol{S_z} \xrightarrow{\tau\Omega_S \boldsymbol{S_z}} -\boldsymbol{S_y} \quad (1.1.73)$$

Thus, ideally all magnetization is refocused after 2τ in –y direction. The time-dependent detection of this magnetization yields the so-called primary echo of the electron spins or "electron spin echo" (ESE). Since every spin package has a slightly different offset frequency that depends on the direct environment of the respective spins, one can gain information about the chemical surrounding of an unpaired electron through its ESE.[43]

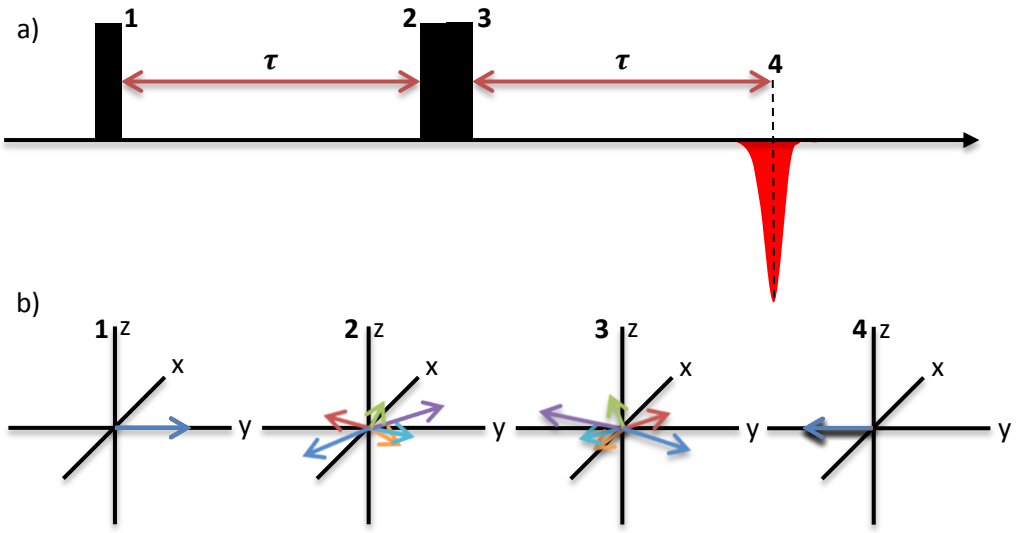

Figure 1.1.5. a) The pulse sequence for the primary echo. The first pulse flips the equilibrium magnetization by an angle of $\pi/2$. The second π-pulse inverts the phase of coherences generated by the first pulse. b) Schematic depiction of the evolution of different spin packages with different offset frequencies during the primary echo sequence.

An ESE can be analyzed by 1D Fourier transformation.[21] Such, one can transform the echo from the time domain into the frequency domain and analyze the different offset frequencies precisely. Since the spin packages develop under the full effective Hamiltonian every interaction summarized by $\mathcal{H}_0$ (see eq. 1.1.25) is represented by the ESE. However, many interactions like weak hyperfine cou-

plings are often not well resolved in an ESE, such that one has to exploit more complex pulse sequences for their elucidation. The most important sequences will be introduced in the following.

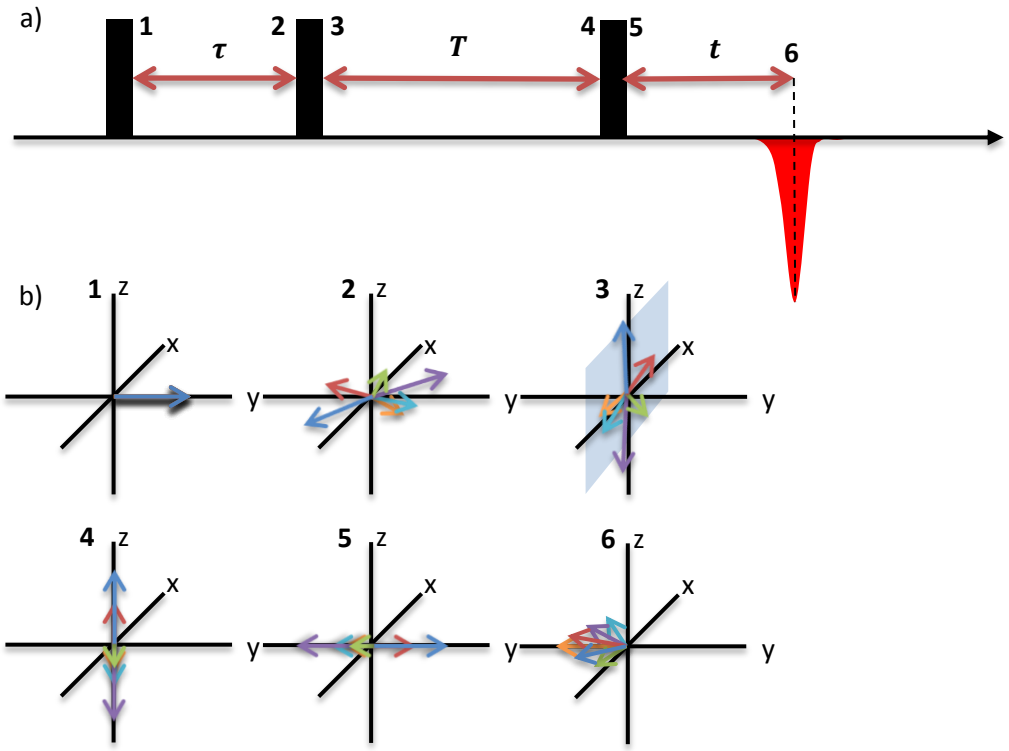

Figure 1.1.6. a) The pulse sequence for a stimulated echo. All three pulses are $\pi/2$ pulses. b) Evolution of the magnetization of different spin packages with different offset frequencies during the three-pulse experiment. Note how the magnetization refocuses only partially in –y direction at point of time 6.

Stimulated Echo

The stimulated echo constitutes the basis for many high-sensitivity experiments. The stimulated echo sequence consists of three $\pi/2$-pulses. The time interval between the second and the third pulse, t, must not equal the interval between the first and the second pulse, τ. In fact, usually $T \gg \tau$. The evolution of the density matrix can be calculated according to eq. 1.1.66 and 1.1.68:[21]

$$\boldsymbol{\sigma}_{eq} = -\boldsymbol{S_z} \xrightarrow{(\pi/2)\boldsymbol{S_x}} \xrightarrow{\tau\Omega_S\boldsymbol{S_z}} \xrightarrow{(\pi/2)\boldsymbol{S_x}} \xrightarrow{t\Omega_S\boldsymbol{S_z}} \xrightarrow{(\pi/2)\boldsymbol{S_x}} \xrightarrow{\tau\Omega_S\boldsymbol{S_z}} \boldsymbol{\sigma}_{echo} \quad (1.1.74)$$

Performing the calculation steps given in eq. 1.1.74, the density matrix after the third pulse can be shown to be:

$$\boldsymbol{\sigma}(\boldsymbol{\tau}+\boldsymbol{T}+\boldsymbol{t}) = -\frac{1}{2}\left[\cos\left(\Omega_S(t-\tau)\right)+\cos\left(\Omega_S(t+\tau)\right)\right]\boldsymbol{S_y} + \frac{1}{2}\left[\sin\left(\Omega_S(t-\tau)\right)+\sin\left(\Omega_S(t+\tau)\right)\right]\boldsymbol{S_x} \quad (1.1.75)$$

Note that only magnetization in x and y direction is taken into account in eq. 1.1.75, although for long τ_2 there would be a significant contribution in z-direction. In practice the transverse relaxation is much faster than the longitudinal relaxation (due to the energy conservation in spin flip-flop process) such that during the period T the x- and y components of the magnetization vanish and after the third pulse only x and y components significantly contribute to the stimulated echo (as shown in Figure 1.1.6). Note that due to the evolution during T the magnetization is not completely refocused in the –y direction. Thus, one loses approx. half of the echo intensity, compared to the primary

echo, yet much longer evolution periods are possible, since magnetization is stored in z-direction during t and hence only decays with τ_1 (instead of with τ_2). Longer evolution times are often necessary for the detection of interactions that oscillate with relatively small frequencies. A sufficiently long time periods has to be observed covering at least half an oscillation.

Two-Pulse ESEEM

For a spin system with coupled $\boldsymbol{S} = 1/2$ and $\boldsymbol{I} = 1/2$ the primary echo sequence creates nuclear coherences, which interfere with the electron spin echo. The first $\pi/2$-pulse creates electron coherence according to $SQ^{(1)}$ (see Figure 1.1.4), but due to the hyperfine interaction the density matrix evolves under the Hamiltonian $\Omega_S \boldsymbol{S_z} + \boldsymbol{S_z^T A I_z} + \boldsymbol{B S_z I_x} + \omega_I \boldsymbol{S_z}$ ($\boldsymbol{S_i}$ denotes the spin operator for a particular direction of the principal coordinate frame, $i = x, y, z$) during the waiting period τ (neglecting nuclear Zeeman interaction). The second term of this Hamiltonian leads to the population of coherences between the electron spin and nuclear spin. The second π pulse inverts the coherence, like in the case of the primary echo, yet additionally ZQ and DQ become populated if the spin system evolves under influences of hyperfine coupling. As a consequence, the transverse magnetization refocuses with an τ-dependent intensity of:[21]

$$V_{2p}(\tau) = \mathrm{Tr}\left(\boldsymbol{\sigma S_y}\right) = 1 - \frac{k}{4}\left[2 - 2\cos(\omega_\alpha \tau) - 2\cos\left(\omega_\beta \tau\right) + 2\cos(\omega_+ \tau) + 2\cos(\omega_- \tau)\right] \quad (1.1.76)$$

With a modulation-depth parameter of:

$$k = \left(\frac{\boldsymbol{B}\omega_I}{\omega_\alpha \omega_\beta}\right)^2 \quad (1.1.77)$$

Here, $\boldsymbol{B} = (\boldsymbol{A}_\parallel - \boldsymbol{A}_\perp)\sin\theta\cos\theta$ for axial $\boldsymbol{A}$. Such, by detecting the echo intensity as a function of τ one can extract the nuclear modulation frequencies $\omega_\alpha, \omega_\beta, \omega_+$and ω_- from the echo intensity envelope. This experiment is referred to as electron spin echo envelope modulation (ESEEM) spectroscopy. ω_α and ω_β denote the absolute values of the nuclear modulation frequencies of the two transitions $SQ^{(2)}$ (see Figure 1.1.4 b)). In eq. 1.1.76 $\omega_+ = |\omega_\alpha| + |\omega_\beta|$ and $\omega_- = |\omega_\alpha| - |\omega_\beta|$. Note that for the case of negligible anisotropy of the hyperfine interaction the modulation frequencies depend on the hyperfine splitting and the nuclear-resonance frequency as:

$$\omega_\alpha = \left|\omega_I + \frac{A}{2}\right| \quad \omega_\beta = \left|\omega_I - \frac{A}{2}\right| \quad (1.1.78)$$

Three-Pulse ESEEM and HYSCORE

Since the nuclear-combination frequencies $\omega_+$and ω_- complicate spectra and do not yield relevant information their contributions to an echo can be supressed by splitting the second π-pulse of the two-pulse ESEEM sequence into two $\pi/2$-pulses. For the three-pulse experiment the envelope modulation of the echo is given by the following equation as can be shown by propagating the respective product operators:[21]

$$V_{3p}(t) = 1 - \frac{k}{4}\Big\{\left[1 - \cos\left(\omega_\beta \tau\right)\right]\left[1 - \cos\left(\omega_\alpha (t+\tau)\right)\right] + \left[1 - \cos(\omega_\alpha \tau)\right]\left[1 - \cos\left(\omega_\beta (t+\tau)\right)\right]\Big\} \quad (1.1.79)$$

Thus, by detecting the echo intensity as a function of t (as defined in Figure 1.1.6 a)) one can extract the modulation frequencies of different nuclei interacting with a detected spin from three-pulse ESEEM time traces. The shape of an ESEEM time trace is shown in Figure 1.1.7 a) for coupling of a

nucleus with 4 MHz nuclear frequency and a hyperfine coupling constant of 40 MHz calculated from eq. 1.1.79. Fourier transformation of the time trace yields the frequency domain spectrum, depicted in Figure 1.1.7 b). ω_α and ω_β appear as peaks centered around ω_I and separated by A (see eq. 1.1.78).

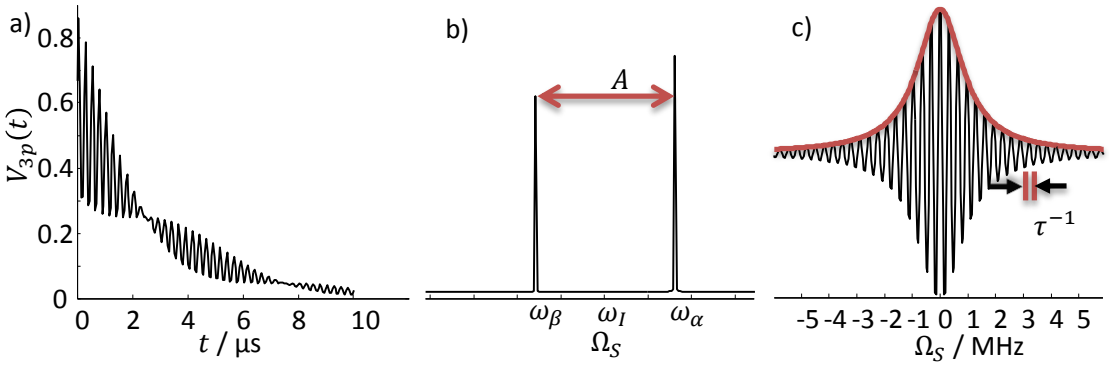

Figure 1.1.7. a) A 3p-ESEEM time-trace modulated with ω_α and ω_β. b) Frequency domain after Fourier transformation of the time trace depicted in a). c) A polarization grating. The wave length of the modulation is dependent on the time τ. The smaller τ, the higher the resolution of the grating.

If there are many different nuclei interacting with one electron spin it is often difficult to assign the two modulation frequencies to a certain nucleus. To circumvent this problem, one can add an unselective π-pulse between the second and the third pulse to the stimulated echo sequence, in order to perform so-called hyperfine sublevel correlated (HYSCORE) spectroscopy. A set of coherences populated on a certain transition after the second pulse is thereby transferred to another transition. Sweeping t_1 and t_2 (as defined in Figure 1.1.8 a)) yields two 3p-ESEEM time domain traces. By a 2D Fourier transformation one ends up with a two-dimensional spectrum that features cross peaks located at ω_α in the one dimension and ω_β in the other. In the case of weak coupling, i.e. $|\omega_I| > |A/2|$ the cross peaks are centred around $|\omega_I|$ and separated by A in both dimension. In the case of $|\omega_I| < |A/2|$ the cross-peaks are centred around $A/2$ and separated by $2|\omega_I|$ (see Figure 1.1.8 b)). Thus, one can easily assign a modulation frequency to a certain nucleus and simultaneously extract the hyperfine interaction strength from a HYSCORE spectrum, also if many nuclei contribute to the hf spectrum. Note that contributions of quadrupolar couplings can significantly complicate the appearance of HYSCORE spectra. For the simplest case of $\boldsymbol{I} = 1$ quadrupolar interactions typically shift the nuclear frequency of a nucleus to $\omega_I + (2M_I + 1)A$ and the cross peaks split along the main diagonal by $3P_z$ around the nuclear frequency. Hence, the interpretation of HYSCORE spectra can become quite difficult, but yields a lot of information about the hyperfine and quadrupolar interaction of an electron spin with its surrounding. With HYSCORE spectroscopy one is able to resolve even weak hyperfine interactions that cannot be observed in a CW EPR or ESE spectrum since they are covered in the inherent line width of the corresponding signals.

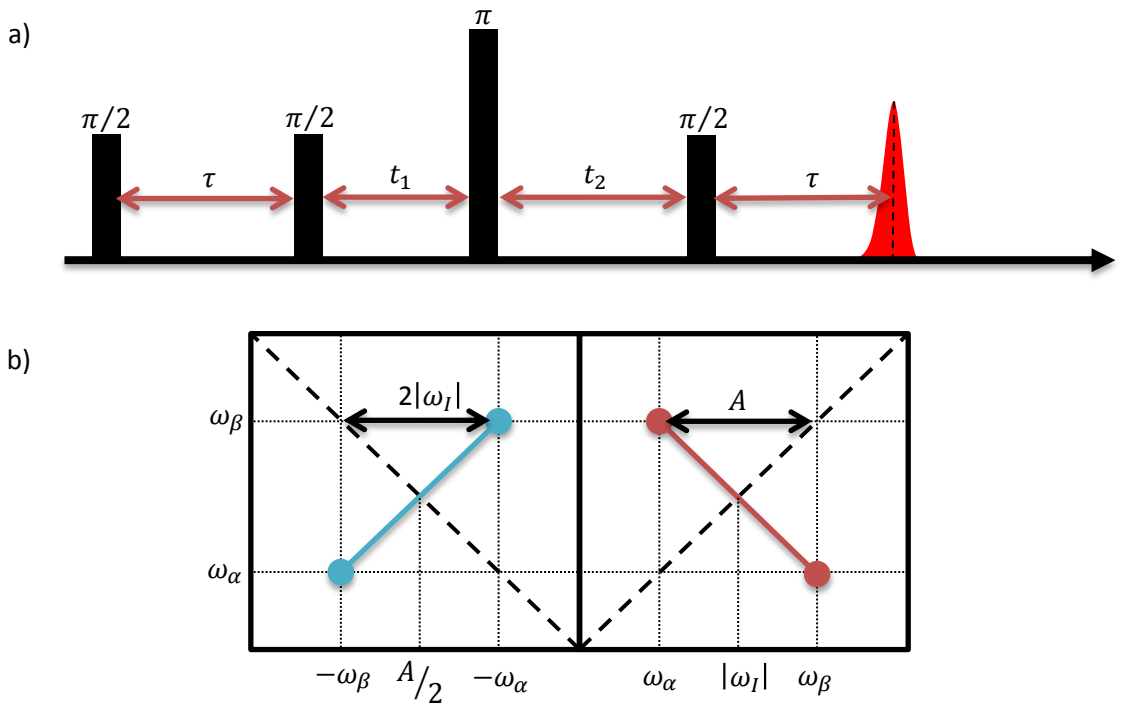

Figure 1.1.8. a) Pulse sequence for a HYSCORE experiment, during which t_1 and t_2 are varied. b) Schematic HYSCORE spectrum after 2D FT of the time domain data. The red line indicates the appearance of the spectrum in the weak coupling case of $|\omega_I| > |A/2|$ (right). The blue line indicates the appearance of the spectrum in the strong coupling case of $|\omega_I| < |A/2|$ (left).

Note that blind spots are an inseparable feature of 3p-ESEEM and HYSCORE. Since the mathematical description of the envelope of the time trace contains a $1 - \cos(\omega_{\alpha,\beta}\tau)$ term, the modulation vanishes if $\omega_{\alpha,\beta} = n\,2\pi/\tau$ with $n = 1,2,3 \ldots$ Hence, in order to detect the complete hyperfine pattern one has to repeat 3p-ESEEM and HYSCORE experiments with different values of τ and sum up the respective spectra.

DEER

The dipolar interaction between two electron spins can be observed with the double electron-electron resonance (DEER) experiment. This technique is of high importance for this thesis. It is frequently utilized to extract the distance between two unpaired electrons from the strength of their dipolar coupling, described by ω_{DD}. As stated in eq. 1.1.32, ω_{DD} is related to the interspin distance by an r^{-3} dependence. In practice one can gain distance information in the range from approx. 1.5 nm to 8 nm with DEER. To observe the dipolar interaction between electron spins, one creates a refocused echo (on so-called observer spins) that is modulated with the dipolar coupling frequency between the observer spins and surrounding ones. One achieves this modulation by flipping non-observed spins (pump spins) during the time evolution of echo sequence (see Figure 1.1.9), typically at resonance frequencies clearly separated from those of the observer spins. This is done by applying an additional π-pulse with a frequency different from the observer frequency (see Figure 1.1.9). The observed spins (underlying the refocused echo) "feel" the subsequent changes in local magnetic fields as a consequence of the flipping of the pump spins. The echo becomes modulated with ω_{DD}. The pulse sequence is given in Figure 1.1.9 a). τ_1 is kept constant, while t is varied. The normalized echo intensity with respect to t is given by:[21]

$$V_{DEER}(r,t) = 1 - \int_0^{2\pi} \sin\theta_{12}\,\lambda(1 - \cos(\omega_{DD}t))d\theta_{12} \quad (1.1.80)$$

θ_{12} is defined in Figure 1.1.2. λ is an experimental constant that denotes the percentage of spins flipped by the pump π-pulse. It is connected to the average number of spins, $\langle n \rangle$, coupled to a single observer spin by:

$$\langle n \rangle = 1 - \frac{\ln(1-\Delta)}{\lambda} \quad (1.1.81)$$

Δ denotes the modulation depth of a renormalized DEER time trace, which is the signal decay at $t \to \infty$ (Figure 1.1.9 b)). The maximum distance that can be detected depends on the evolution time of the spin-system τ_2, since $r_{max} \approx (\hbar\gamma\pi^{-1}\tau_2)^{1/3}$. The minimum distance is determined by the length of the pump pulse, τ_p: $r_{min} \approx \left(2\hbar\gamma^2\pi^{-1}\tau_p\right)^{1/3}$.[44]

Note that in practice raw time traces of DEER stem from the product of the signal contributions of pump and observer spins and of a homogeneous distribution of distant spins and spin pairs. (The latter is commonly denominated as 'DEER background') Depending on the dimensionality, d, of the system the homogeneous distribution is described by:

$$V_{DEER}^{hom} = exp\left(-\tau_{relax}^{-1}\lambda c_{pump} t^{d/3}\right) \quad (1.1.82)$$

τ_{relax}^{-1} depends on d. λc_{pump} denotes the concentration of excited pump spins. The raw time domain data is typically divided by the background contribution to allow for extraction of interspin distances exclusively between pump and observer spins. Since in practice distance distributions (as opposed to single interspin distances) characterize a system the DEER signal can be expressed in terms of a distance distribution, $P(r)$, and of a Kernel function, $K(r,t)$:

$$V_{DEER}(r,t) = ln\frac{V(t)}{V(0)} = \int_{r_{min}}^{r_{max}} K(r,t)P(r)dr \quad (1.1.83)$$

$$K(r,t) = -\lambda\left(1 - \int_0^{\pi/2} \cos(\omega_{DD}(\theta_{12},r)t)\sin\theta_{12}\, d\theta_{12}\right) \quad (1.1.84)$$

$P(r)$ is a distance distribution between pump and observer spins. This expression of the DEER signal is the most convenient for computational processing of time domain data.

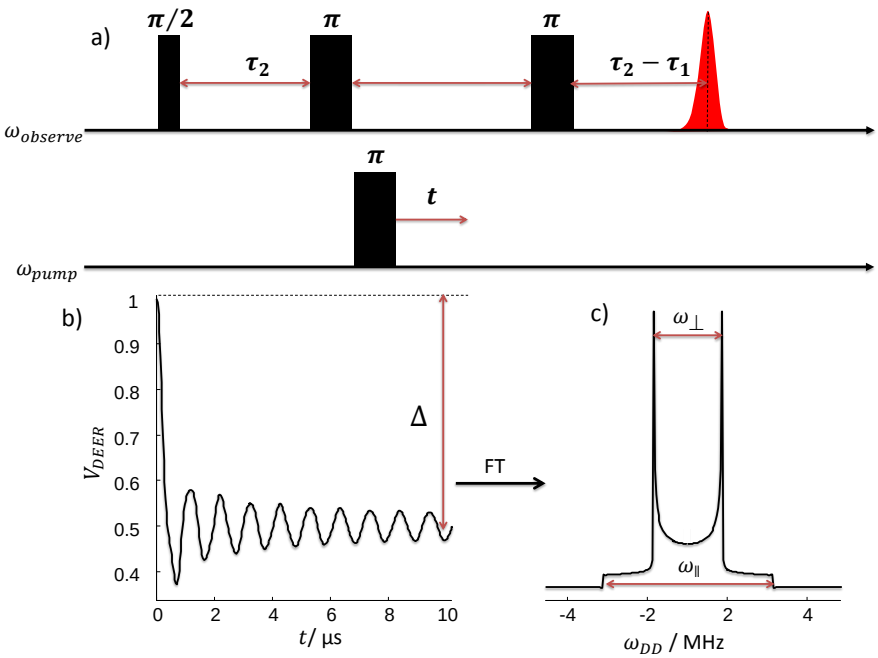

Figure 1.1.9. a) Pulse sequence for DEER experiments. b) Schematic DEER time trace. Δ denotes the modulation depth as given in eq. 1.1.81. c) Fourier transformation of the time trace in b) yields the dipolar spectrum (Pake pattern). The inner maxima are separated by $\omega_{\perp}$, which corresponds to the dipolar coupling frequency at $\theta_{12} = \pi$. The outer shoulders are separated by $\omega_{\parallel}$, which corresponds to the dipolar coupling frequency at $\theta_{12} = 0$.

By fitting the time domain data (Figure 1.1.9 b)) with a certain distance distribution, $P(r)$, one extracts distance information from DEER time traces. This can be achieved either with a predefined model (like a Gaussian distance distribution) or following a model-free employing, e.g., the Tikhonov regularization.[45] However, since the extraction of distance information from DEER data is a moderately ill-posed inverse problem reliable, model-free distance information can only be obtained when clear-cut modulations are present in the time trace.

1.2 Nitroxides

Here, frequently used paramagnetic compounds and numerical techniques to interpret their corresponding spectra will be introduced. The most abundant spin-carrying molecular systems used for EPR are nitroxide-based spin labels or spin probes. These feature an N-O moiety that comprises an unpaired electron. The most important nitroxides for this thesis are summarized in Chart 1.2.1. The depicted molecules are predominantly used as molecular tracers that interact non-covalently with a system of interest. However, by chemical attachment a nitroxide can also be fixed at a certain position of, e.g., a macromolecule, such that one exactly knows its position. The latter is a so-called spin labeling approach, while one speaks of a spin probing apprioach in the former case.

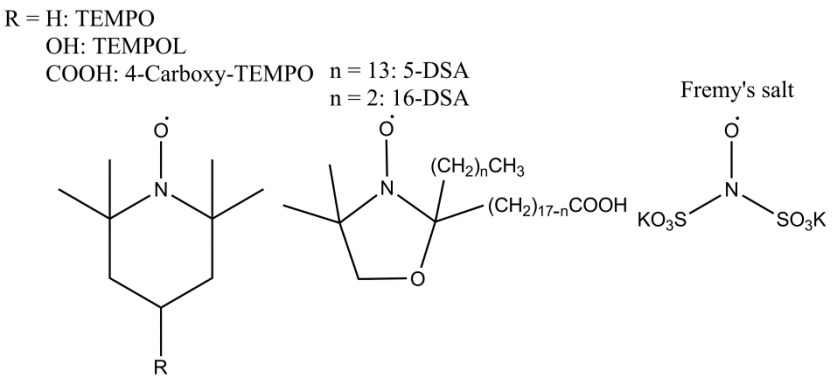

Chart 1.2.1. The most important nitroxides for this thesis and their molecular structures. The abbreviations denote: TEMPO: (2,2,6,6-Tetramethylpiperidin-1-yl)oxyl; TEMPOL: 4-hydroxy- (2,2,6,6-Tetramethylpiperidin-1-yl)oxyl; 4-HBT: 4-hydroxybenzoyl-(2,2,6,6-Tetramethylpiperidin-1-yl)oxyl; DSA: 4,4-dimethyl-oxazolidine-N-oxyl stearic acid. Fremy's salt will be abbreviated as FS in the following.

From an energetic point of view the most important interaction in a nitroxide is the coupling between the ^{14}N ($I = 1$) nucleus of the N-O group and the unpaired electrons with each other and with an external magnetic field. Evaluating the effective Hamiltonian (neglecting quadrupolar interactions; eq. 1.1.85) leads to the energy diagram depicted in Figure 1.1.10.

$$\mathcal{H}_{eff} = \frac{\beta_e}{\hbar}\boldsymbol{B}^T\boldsymbol{g}\boldsymbol{S} + \frac{\beta_n g_n}{2\hbar}\boldsymbol{B}^T\boldsymbol{I} + \boldsymbol{S}^T\boldsymbol{A}_i\boldsymbol{I}_i \quad (1.2.1)$$

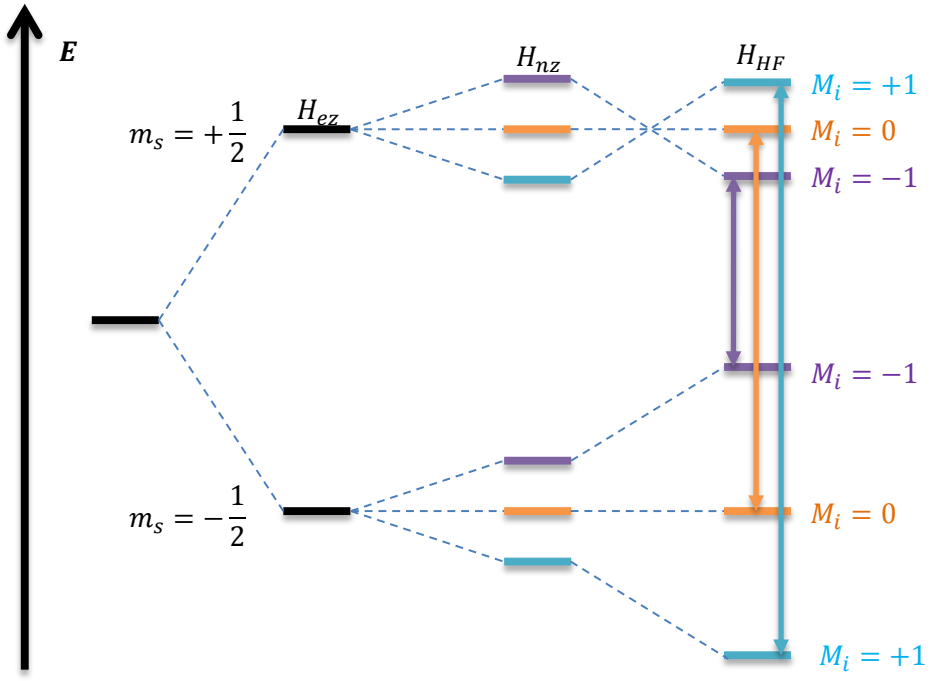

Figure 1.2.1. Typical energy diagram of a nitroxide radical. (Quadrupolar interactions are neglected.)

Three allowed transitions with $\Delta M_s = 1$ and $\Delta M_i = 0$ are typically detected by EPR measurements on nitroxides (arrows in Figure 1.2.1). The g value of a typical nitroxide is only slightly anisotropic, i.e. orientation dependent. For X-band frequencies (approx. 9.4 GHz) as used primarily throughout this thesis usually all orientations are detected simultaneously at a given field strength. Only at higher frequencies (e.g., W-band: approx. 94 GHz) the g-anisotropy can be resolved. In contrast to g, the absolute value of the hyperfine interaction between the nitrogen nucleus and the electron spin

of a nitroxide is strongly orientation dependent, such that hyperfine selection can already be achieved at X-band. (This is necessary for DEER in order to spectrally select distinct observer and pump spins.) The commonly used molecular frame of a nitroxide and the corresponding hyperfine interactions are depicted in Figure 1.1.11. Along the x and y direction the hyperfine splitting is rather weak (~10-12 MHz) and thus not resolved at X-band, but in z direction coupling constants between 40 MHz and 50 MHz are typically detected.

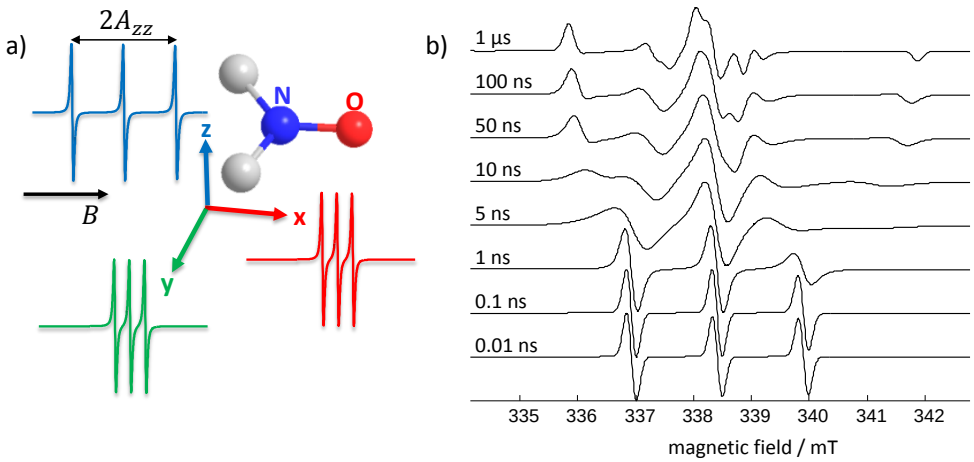

Figure 1.2.2. a) The nitroxide molecular framework and corresponding fast-tumbling, orientation-selective CW EPR spectra. b) CW EPR spectra of a nitroxide for different values of τ_c

Much information can be extracted from CW EPR spectra of a nitroxide. The rotational mobility of a spin-probe or label can be evaluated by analysis of the line shape. At high rotational mobility, i.e., $\tau_c < 0.5\ ns$, all orientations are averaged. With decreasing rotational mobility this averaging gradually diminishes until a solid-state spectrum is reached at $\tau_c \geq 1\ \mu s$ (see Figure 1.2.2 b)). Such, by analysis of the line shape one can determine the rotational correlation time of a nitroxide. Note that the rotational diffusion must not necessarily be isotropic, as described in eq. 1.1.23 and 1.1.24.

Of special interest for this thesis is the information contained in the g-tensor and the magnitude of hyperfine interaction. These parameters report the polarity of the environment of a nitroxide. As the polarity increases, the probability of the unpaired electron to be found close to the nitrogen nucleus increases, since zwitterionic resonance structures become more favorable compared to neutral ones (see Figure 1.2.3). Hence, the hf interactions are stronger in polar than in apolar environments and coupling constants increase. Furthermore, the probability of hydrogen bond formation at the oxygen atom often increases with polarity of a nitroxide's surrounding. As a consequence the isotropic g-value becomes smaller because of changes in spin-orbit coupling (see eq. 1.1.28).

Nitroxides are generally quite sensitive to environmental influences. If a system provides polar and apolar environments simultaneously, a nitroxide can be distributed between them. Such, a partitioning gives rise to a spectral contrast between a species A in the polar regions and a species B located in the apolar regions as shown in Figure 1.2.3. Throughout this thesis species A will refer to a nitroxide in a polar region and species B will refer to a nitroxide in an apolar. The spectral contribution of the two species to an experimental spectrum, $\boldsymbol{S_{exp}}$, can be expressed as mole fractions of species A and B: $\boldsymbol{S_{exp}} = \chi_A \boldsymbol{S_A} + (1-\chi_A)\boldsymbol{S_B}$. $\chi_B = 1 - \chi_A = n_B / \sum_{i=1} n_i$ is a relative measure of the hydrophobic volume present in a system. With nitroxides that partition between different environments in one can detect the occurrence of apolar cavities of any kind. It should be noted that the

hyperfine tensor of the effective spin Hamiltonian (eq. 1.1.25) is completely independent of the g tensor, which describes the field position of the spectrum at a given frequency. g typically shifts to lower field positions with increasing hydrophobicity of an unpaired electron's environment. Hence, as depicted in Figure 1.2.3 c), the most prominent effects can be observed at the high-field line of a nitroxide spectrum, where A- and g-shifts add up. By analysis of simple CW EPR spectra of a nitroxide one can obtain information about its partitioning coefficients and the polarity of its environment.

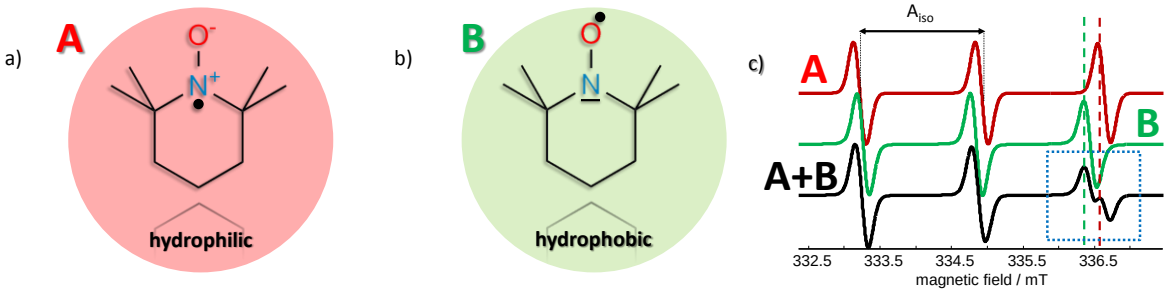

Figure 1.2.3. Origin of the spectral components of CW EPR spectra of TEMPO in a (nano-)phase separated system. a) Mesomeric structure of TEMPO in a hydrophilic environment. The unpaired electron is predominantly localized at the nitrogen atom. b) Mesomeric structure of TEMPO in a hydrophobic environment. The unpaired electron is predominantly localized at the oxygen atom. c) Spectral components: stemming from TEMPO in a hydrophilic environment (A; red); stemming from TEMPO in a hydrophobic environment (B; green); combined, bimodal spectrum (A+B; black). The dashed lines mark the differences between the high-field transitions of species A and B. a_{iso} approximately corresponds to the separation of the zero crossings of two lines of a TEMPO CW EPR spectrum. The blue marked region of the spectrum (high-field transition) shows the most prominent effects.

Probe vs. Label

The advantage of a spin probe over a spin label is that one does not alter the system by chemical attachment of the nitroxide and hence does not risk a change of the system's properties. Yet, one cannot imply the exact position of the nitroxide for the interpretation of EPR data. Labels are typically used for DEER since it is often necessary to know the nitroxides' positions in order to reasonably interpret distance information. Such, the choice between label and probe crucially depends on the desired information. Using a probe one has to be aware that the individual properties of different spin probes (Chart 1.2.1) give rise to different information. As an example, large spin probes cannot enter apolar cavities in polar surroundings that are below a certain size. Only if the apolar domains are of a certain threshold size, the respective spin probes can enter them in sizeable amounts. Smaller, amphiphilic spin probes can also detect smallest apolar cavities, yet they distribute (partition) between the solvent and the cavities, while very hydrophobic probes are likely to enter the cavities (if large enough) quantitatively. Thus, strongly hydrophobic spin probes have higher propensities than small amphiphiles to enter large hydrophobic nanodomains quantitatively and to penetrate their interior more deeply. The fraction of spin probes inside hydrophobic cavities is crucial for CW EPR. Only if sizable fractions of a probe have entered a cavity, the spectral contribution of the incorporated species is large enough to be detected as a significant spectral component (see Figure 1.2.3 c)). The choice of the probe therefore depends crucially on the system of interest, since the balance between polarity of the cavities and hydrophilicity of the probe, as well as the probe size have to be taken into account.

Spectral Simulations of CW EPR Spectra

Since it is only in very rare cases possible to extract all spectral information from a CW EPR spectrum by eye, most spectra that were recorded throughout this thesis were analyzed by means of numerical spectral simulations. All spectral simulations were performed with home-written programs in MATLAB (The MathWorks, Inc.) employing the EasySpin toolbox for EPR spectroscopy.[46] They are based on the quantum mechanical calculation of resonance fields by evaluating the effective Hamiltonian (eq. 1.1.85) for a certain set of spectral parameters (primarily hyperfine tensor, g tensor and line-width) at a certain microwave frequency. For the calculation of the resonance fields EasySpin uses the Breit-Rabi expression.[46] Simulations of CW EPR spectra in fluid solution were either performed by using a model based on the slow-motion theory developed by Schneider and Freed, or by using a model based on the fast-motion theory developed by Freed and Fraenkel as implemented in EasySpin.[36] These simulations can account for the effect of rotational diffusion in a wide $\boldsymbol{D}$-regime.[36] If intending to simulate a spectrum in the slow tumbling regime the stochastic Liouville-von Neumann equation (eq. 1.1.60) can be solved in the eigenbasis of the diffusion tensor by EasySpin. Such, contributions of anisotropic τ_cs to the line width are taken into account (eq. 1.1.12 – 1.1.24). In the isotropic limit this is not necessary, since the isotropic rotation of the radicals leads to an averaging of all spectral parameters over all orientations. In the fast motion regime small differences in line intensity are treated as small perturbations of the effective spin Hamiltonian.

References and Notes

[1] D. A. Walker, B. Kowalczyk, M. O. d. l. Cruz, B. A. Grzybowski, *Nanoscale* **2011**, *3*, 1316.
[2] K. J. M. Bishop, C. E. Wilmer, S. Soh, B. A. Grzybowski, *Small* **2009**, *5*, 1600.
[3] P. Bawa, B. Pillay, Y. E. Choonara, L. C. d. Toit, *Biomed. Mater.* **2009**, *4*, 022001.
[4] D. Schmaljohann, *Advanced Drug Delivery Reviews* **2006**, *58*, 1655.
[5] C. d. l. H. Alacrón, S. Pennadam, C. Alexander, *Chem. Soc. Rev.* **2005**, *34*, 276.
[6] E. S. Gil, S. M. Hudson, *Prog. Polym. Sci.* **2004**, *29*, 1173.
[7] A. Chilkoti, M. R. Dreher, D. E. Meyer, *Advanced Drug Delivery Reviews* **2002**, *54*, 1093.
[8] B. Obermeier, F. Wurm, C. Mangold, H. Frey, *Angew. Chem. Int. Ed.* **2011**, *50*, 7988.
[9] M. J. N. Junk, U. Jonas, D. Hinderberger, *Small* **2008**, *4*, 1485.
[10] D. Roy, J. N. Cambre, B. S. Sumerlin, *Prog. Polym. Sci.* **2010**, *35*, 278.
[11] C. Weber, R. Hoogenboom, U. S. Schubert, *Progess in Polymer Science* **2012**, *37*, 686.
[12] L. A. Lyon, Z. Meng, N. Singh, C. D. Sorrell, A. S. John, *Chem. Soc. Rev.* **2009**, *38*, 865.
[13] S. Ganta, H. Devalapally, A. Shahiwala, M. Amiji, *Journal of Controlled Release* **2008**, *126*, 187.
[14] Y. Zhou, D. Yan, W. Dong, Y. Tian, *J. Phys. Chem. B* **2007**, *111*, 1262.
[15] R. Liu, M. Fraylich, B. R. Saunders, *Colloid. Polym. Sci.* **2009**, *287*, 627.
[16] J.-F. Lutz, A. Hoth, *Macromolecules* **2006**, *39*, 893.
[17] J.-F. Lutz, Ö. Akdemir, A. Hoth, *J. Am. Chem. Soc.* **2008**, *128*, 13046.
[18] C.-A. Palma, M. Cecchini, p. Samori, *Chem. Soc. Rev.* **2012**, *41*, 3713.
[19] G. Martini, L. Ciani, *Phys. Chem. Chem. Phys.* **2008**, *11*, 211.
[20] B. Z. Zhang, R. Wepf, K. Fischer, M. Schmidt, S. Besse, P. Lindner, B. T. King, R. Sigel, P. Schurtenberger, Y. Talmon, Y. Ding, M. Kroger, A. Halperin, A. D. Schluter, *Angew Chem Int Edit* **2011**, *50*, 737.
[21] A. Schweiger, G. Jeschke, "*Principles of pulse electron paramagnetic resonance*", Oxford University Press, New York, 2001.
[22] J. A. Weil, J. R. Bolton, J. E. Wertz, "*Electron Paramagnetic Resonance - Elementary Theory and Practical Applications*", John Wiley & Sons Inc., New York, 1994.
[23] W. Gerlach, O. Stern, *Z. Phys.* **1921**, *8*, 110.
[24] G. E. Uhlenbeck, S. Goudsmit, *Naturwissenschaften* **1925**, *13*, 953.

[25] E. Zavoisky, *J. Phys. U.S.S.R.* **1945**, *9*, 245.
[26] J. Frenkel, *L. Phys. USSR* **1945**, *9*, 299.
[27] N. F. Ramsey, *Bull. Magn. Reson.* **1985**, *7*, 94.
[28] R. R. Ernst, W. A. Anderson, *Rev. Sci. Instrum.* **1966**, *37*, 93.
[29] K. Holczer, D. Schmalbein, *Bruker Report* **1987**, *1*, 22.
[30] P. Höfer, G. G. Maresch, D. Schmalbein, K. Holczer, *Bruker Report* **1996**, *142*, 15.
[31] G. E. Pake, T. L. Estle, "*The Physical Principles of Electron Paramagnetic Resonance*", Benjamin Reading, MA, 1970.
[32] R. R. Sharp, *J. Chem. Phys.* **1990**, *15*, 6921.
[33] A. G. Redfield, *IBM Journal* **1957**, 19.
[34] A. H. Beth, B. H. Robinson, "*Biological Magnetic Resonance Vol. 8 - Spin Labeling - Theroy and Application*", Plenum Press, New York, 1989.
[35] A. R. Edmonds, "*Anular Momentum in Quantum Mechanics*", Princeton University Press, Princeton, 1960.
[36] D. J. Schneider, J. H. Freed, "*Biological Magnetic Resonance Vol. 8 - Theory and Applications*", Plenum Press, New York, 1989.
[37] E. Meirovitch, J. H. Freed, *J. Phys. Chem.* **1984**, *88*, 4995.
[38] A. Polimeno, J. H. Freed, *J. Phys. Chem.* **1995**, *99*, 10995.
[39] D. Hinderberger, R. P. Pikorski, M. Goenrich, R. K. Thauer, A. Schweiger, J. Harmer, B. Jaun, *Angew. Chem. Int. Ed.* **2006**, *118*, 3684.
[40] C. H. Townes, *J. Phys. Chem.* **1949**, *17*, 782.
[41] P. W. Atkins, "*Physikalische Chemie*", Wiley-VCH, Weinheim, 2001.
[42] J. J. Sakurai, "*Modern Quantum Mechanics*", Addison-Wesley, Reading, 1994.
[43] For this thesis pulse experiments are only applied to freeze quenched solutions at cryogenic temperatures.
[44] Y. D. Tsvetkov, A. D. Milov, A. G. Maryasov, *Russ. Chem. Rev.* **2008**, *77*, 487.
[45] G. Jeschke, A. Koch, U. Jonas, A. Godt, *J Magn Reson* **2002**, *155*, 72.
[46] S. Stoll, A. Schweiger, *J. Magn. Reson.* **2006**, *178*, 42.

2. Correlated Electrostatic Interactions as Structuring Principle of Supramolecular Assemblies

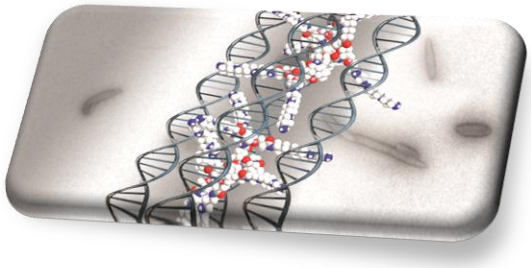

Many societal challenges at the beginning 21st century involve an apparent and growing need for functional materials and novel ways for their synthesis and assembly. Materials researchers rose to this challenge by utilization of non-covalent structuring principles for the design of supramolecular objects. Such, a plethora of self-assembling building blocks for the bottom-up construction of new types of polymers and nanostructures has enjoyed increasing popularity in the recent past.[1-3] Supramolecular materials like foldamers, surface films, nanoparticles etc. are created by exploitation of non-covalent interaction profiles[4] that can be systematically tuned in order to lead to a systematic arrangement of nanoscale building blocks.[5-11] In this section it is my aim to introduce these structuring effects to the reader and to show how they can be exploited for the bottom-up construction of novel, smart materials.

To start with, I will focus on interaction patterns that are dominated by electrostatics – in particular by long-range correlated electrostatic interactions. This notion is here understood to comprise correlations that act in solutions on length scales beyond the Bjerrum length.[12] Although short-range correlations are well-known from classic crystallography, long-range electrostatic correlations have so far only been discussed in the context of densely charged polyelectrolytes. Here long-range correlations will be shown, to the best of my knowledge for the first time, to yield non-trivial, non-random (thermal) behavior even of low-molecular ionic building blocks in supramolecular assemblies. This will be demonstrated for solutions of small multivalent ions. The latter self-assemble under right conditions into colloid-like ionic clusters of defined size and a nonetheless quite mobile interior. These assemblies are coined *Ionoids*. At the example of Ionoids it is shown how an intrinsically non-directed force like electrostatic attraction/repulsion can act as structuring principle of a, from small building blocks bottom-up constructed, defined 'polyelectrolyte'.

The second half of this chapter will be concerned with supramolecular assemblies of larger polyelectrolytes – i.e., with highly defined assemblies of DNA, so-called DNA-condensates. The focus of this second study will lie on counterion interactions and solution conditions, since these two factors predominantly affect the structuring of DNA assemblies. In this context, highly charged dendritic counterions are shown to be exploitable to control size, charge and morphology of DNA-dendriplexes because they adopt electrostatically correlated liquid-like phases on the DNA surfaces.

2.1 Highly Defined Colloid-Like Ionic Clusters Through Self-Assembly in Solution.

This study is intended to contribute to the search for new polymers constructed through non-covalent molecular forces. It is based on the idea of supramolecular or even polymer-like structures through self-assembly of small ionic monomers, merely formed from intrinsically non-directed electrostatic and solvent interactions.[13-15] To achieve this aim, it was made use of a recently highlighted, multi-cationic molecular box ($\mathbf{1}^{4+}$; Figure 2.1.1 a)), developed by Sessler and co-workers, which has already been applied in self-assembly applications of metal-organic rotaxane frame-works.[16] $\mathbf{1}^{4+}$ seems to facilitate structure generation through self-assembly, indicated by e.g. the surprising ability to build supramolecular necklaces due to incorporation of electron-rich aromatic guest molecules.[17, 18] However, not being focused on such short-ranged interactions here, but on new applications of long-ranged electrostatic forces at the nanoscale (for a recent review see Walker et al. 2011[12]), $\mathbf{1}^{4+}$ was combined with small di-anionic salts: $(KSO_3)_2CH_2$ ($\mathbf{2}^{2-}$) and $(KSO_3)_2NO$ ($\mathbf{3}^{2-}$, or Fremy's salt in later chapters) to generate a defined assembly of cations and anions in solution. The molecular structures of all used compounds are shown in Figure 2.1.1. However, self-assembly as a consequence of electrostatic attraction between small, ionic building blocks is complex to describe qualitatively as well as quantitatively, since not only Coulombic forces, but also entropy changes due to counterion release, solvation of ions, depletion forces etc., contribute to the total free energy of a system.[12] Therefore, a central question in any application of solution-based ionic self-assembly is: does any kind of ordered arrangement of the ionic building blocks take place?[19, 20] Intuitively one would assume the distribution of ions in solution to be of random, rather homogeneous nature.

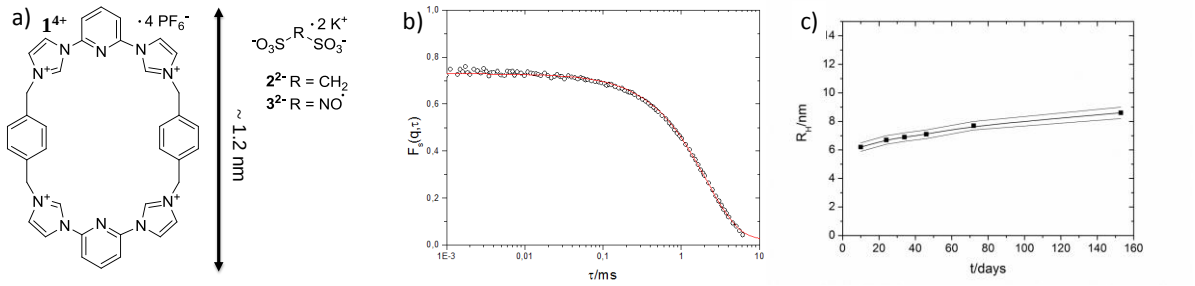

Figure 2.1.1. a) Molecular structure of $\mathbf{1}^{4+}$ (left) and $\mathbf{2}^{2-}$ / $\mathbf{3}^{2-}$ (top right). b) A typical monoexponential fit of an autocorrelation function gained from DLS on $\mathbf{2}^{2-}/\mathbf{1}^{4+}$ Ionoids. c) Hydrodynamic radii of the $\mathbf{2}^{2-}/\mathbf{1}^{4+}$ Ionoids plotted versus time, as derived from DLS measurements. t = 0 days refers to the date of initial preparation. The upper and lower lines indicate error estimates derived from the fits of the autocorrelation functions.

In the following dynamic light-scattering (DLS) data is presented that clearly illustrate that mixtures of low concentrations of anionic $\mathbf{2}^{2-}$ and cationic $\mathbf{1}^{4+}$ self-assemble in solution to highly defined, monodisperse ionic clusters. In this special case the distribution of ions in solution is therefore not trivial at all, but well-ordered due to long-range electrostatic correlations. Performing molecular dynamics (MD) and Monte Carlo (MC) simulations the internal constitution of the ionic clusters was further elucidated. The simulations also show how a long-ranged order may be induced by electrostatic correlations of the cationic macrocycles. MD and MC indicate that the monodisperse objects that are formed through these correlations are constituted of relatively loosely bound ions. The ions nonetheless occupy certain fixed coordinates in the clusters for at least orders of nanoseconds.[21][22] The reliability of the computational data is additionally supported by DEER spectroscopy data. Taking long-ranged (DLS, MC) and molecular (MD, DEER) insights together, this section demonstrates, to the best of my knowledge for the first time, that size-controlled self-assembly of small ions in

solution is possible through electrostatic interaction. The so-formed objects can be regarded as loosely bound ion-based colloids, thus the name *Ionoids* was proposed already.[21] These Ionoids are peculiar since they result from ion-ion correlations of moderately charged constituents at low concentrations, while long-range electrostatic correlations have so far only been discussed in the context of highly charged macroions (see Section 2.2).[23-25]

2.1.1 Results and Discussion

Dynamic light scattering experiments were performed on a system containing $\mathbf{2}^{2-}/\mathbf{1}^{4+}$, prepared in a ratio of 3 mM : 1 mM in DMSO/ 88 % glycerol 1:1. The data were kindly provided by Nane Pfaffenberger from the Lab of PD Dr. Wolfgang Schärtl from the University of Mainz.[26] The measurements revealed, after an initial period of several days where no correlation could be detected, monodisperse small objects in the solution. The fit of one correlation function measured at a scattering angle of 90° is depicted in Figure 2.1.1 b). Note the monoexponential nature of this fit, which indicates monodispersity of the aggregates in the solution. The intercept of the correlation function is unusually low due to the small signal-to-noise ratio < 3. I.e., the scattered intensity from the pure solvent mixture is nearly 40% of the overall scattered intensity. Since in the absence of $\mathbf{2}^{2-}$ no correlation were found at all for solutions of $\mathbf{1}^{4+}$, but only the DLS signature of the pure solvent mixture, it is at hand to deduce that the small, monodispers objects stem from self-assembly of $\mathbf{2}^{2-}$ and $\mathbf{1}^{4+}$. The hydrodynamic radius, R_H, of the $\mathbf{2}^{2-}$-$\mathbf{1}^{4+}$ clusters is quite small, i.e. 6.2 nm ± 0.2 nm 10 days after sample preparation. A slow growth (+ 2 nm after 140 days; see Figure 2.1.1 c)) can be observed, fostering an analogy with charge-stabilized colloids. It is important to note that all correlation functions measured over time can be fitted by a single exponential decay and that the resulting diffusion coefficient is independent of the scattering angle, which underlines the monodispersity in aggregate size. Thus, one can conclude that the $\mathbf{2}^{2-}$ molecules bring together 3-4 (estimated from the size of approx. 6-7 nm) $\mathbf{1}^{4+}$ molecules in an extraordinarily uniform manner.

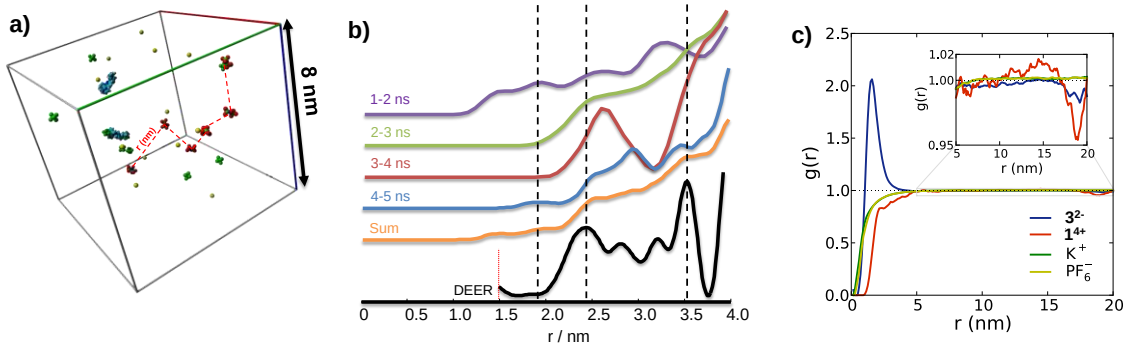

Figure 2.1.2. a) Snapshot after 2 ns of MD of the system $\mathbf{3}^{2-}/\mathbf{1}^{4+}$ 6:2. b) Pair correlation function of $\mathbf{3}^{2-}$ molecules gained from MD simulation of the system $\mathbf{3}^{2-}/\mathbf{1}^{4+}$ 6:2, summed up over different time-intervals. The overall distance distribution is shown in yellow. Note that over time certain maxima in the distributions appear frequently, as indicated by the dashed lines. The black distribution depicts the distances gained from DEER on the same system. c) The Monte-Carlo derived radial distribution function for $\mathbf{3}^{2-}$ (blue), calculated for 2 $\mathbf{1}^{4+}$ and 6 $\mathbf{3}^{2-}$ molecules. The box size was 26^3 nm^3. As can be seen, there are no distinct maxima in the distance distribution. The $\mathbf{1}^{4+}$-$\mathbf{1}^{4+}$ distribution (red) reveals a long-range correlation at approx. 15 nm.

To support the reliability of the DLS data and to elucidate the internal constitution of the ionic clusters, all-atom MD simulations were conducted corresponding to the system $\mathbf{3}^{2-}$: $\mathbf{1}^{4+}$ = 6:2. All simulations reports herein are kindly provided by Dr. Daniel Kattnig. Details are given in reference [21]. In order to check the reliability of the MD simulations they are supplemented with DEER data. To this end $\mathbf{2}^{2-}$ was replaced by paramagnetic $\mathbf{3}^{2-}$. (This change may have an influence on special inter-

actions in the Ionoids, yet long-range electrostatic interactions remain unchanged.)[27] Starting from a random distribution of all molecules the system was equilibrated for 0.2 ns and subsequently trajectories for 8 ns were extracted with the aim of calculating the radial distribution function, g(r), of $\mathbf{3}^{2-}$. Figure 2.1.2 a) shows a snapshot of the simulation after 2 ns. Figure 2.1.2 b) depicts the radial distance distribution of $\mathbf{3}^{2-}$ summed up over 8 ns of simulation and over different time intervals of 1 ns. Prominent features in the overall g(r) at 1.9 nm, 2.4 nm, 3.5 nm are observable. Thus, the distribution of $\mathbf{3}^{2-}$ in the simulated system is far from being random. Also the distributions summed up in each case over 1 ns of simulation indicate favored population of distinct $\mathbf{3}^{2-}$-distances in the $\mathbf{3}^{2-}/\mathbf{1}^{4+}$ system. It is astonishing at first sight that maxima in g(r) in Figure 2.1.2 b) occur with a spacing of approx. 0.5 nm, indicating a periodic arrangement of the spin probes.

Yet, although the inner constitution of the $\mathbf{3}^{2-}$-$\mathbf{1}^{4+}$ aggregates could be assessed with MD, the global size of the so formed aggregates cannot be deduced from the simulation and compared with R_H, because of a box-size of only 8^3 nm^3. Therefore, Monte-Carlo (MC) simulations with a box-size of 26^3 nm^3 were conducted to elucidate the individual cluster size. These simulations include electrostatic potentials as well as excluded volume effects. However, MC simulation shows that due to mere electrostatic interactions and excluded volume no distinct short-range association takes place (see Figure 2.1.2 c)). Yet, the simulations do reveal a surprising long-range correlation of $\mathbf{1}^{4+}$ at about 15 nm, suggesting a defined size of the observed ionic clusters and electrostatic and excluded volume effects to be essential for the formation of the observed ionic clusters. This assumption is supported by the fact that the experimentally determined radius (6.2 nm – 8.2 nm) and the radius suggested by the MC simulations (R ≈ 7.5 nm) are in good agreement. Yet, the distinct $\mathbf{3}^{2-}$-$\mathbf{3}^{2-}$ distances, as gained from MD, seem to be a consequence of additional entropic or solvent effects, next to mere electrostatics.

To further support the reliability of the computational data a DEER experiment was performed on a freeze-quenched $\mathbf{3}^{2-}$/ $\mathbf{1}^{4+}$ system to extract the experimental distance distribution of $\mathbf{3}^{2-}$. The resulting distance distribution is depicted in Figure 2.1.2 b) in black (bottom). It shows the population of all $\mathbf{3}^{2-}$-$\mathbf{3}^{2-}$ distances of 6 mM $\mathbf{3}^{2-}$ molecules around 2 mM $\mathbf{1}^{4+}$ molecules and can directly be compared with the g(r) gained from MD. Taking into account that the simulation features significantly higher concentrations than the experimentally measured system (the $\mathbf{1}^{4+}$ concentration was three times higher than in the experiment to increase the speed of calculation) and the restricted number of simulated $\mathbf{1}^{4+}$ and $\mathbf{3}^{2-}$ molecules, the simulation-derived and the experimental distribution are overall in reasonable agreement. However, there are no distinct dipolar modulations observable in the DEER time traces (see Appendix A2.1.1). Hence, the extracted distances (by Tikhonov regularization) have to be treated with caution. Yet, since they are clearly indicative of non-homogenous/non-random distributions of $\mathbf{3}^{2-}$ and in addition are even in reasonably good agreement with the simulated distributions, one can assume that the distances extracted from the MD simulation resemble the internal organization of the Ionoids to a large degree. Thus, the molecular arrangement depicted in Figure 2.1.2 a) can be regarded as a representative snapshot of the distribution of ions in an Ionoid. Since the distribution of molecules does not change too much over time, it is at hand to assume that the $\mathbf{1}^{4+}$ molecules are forced into a short-distance arrangement, in order to minimize the potential electrostatic energy of the whole system.

The divalent $\mathbf{3}^{2-}$ molecules may be acting as 'ionic glue' between the $\mathbf{1}^{4+}$ macrocycles. In doing so, the positions of local maxima in the distance distribution, as derived from the MD simulation, do not vary significantly over time. This means that the covered conformational ensemble seems to be relatively small. Once $\mathbf{3}^{2-}$ is 'trapped' in an ensemble it remains at a certain position for at least sev-

eral nanoseconds. CW EPR data at room temperature heavily support this hypothesis: the $\mathbf{3}^{2-}$ probes still rotate relatively freely, although their rotational mobility is slightly restricted when small amounts of $\mathbf{1}^{4+}$ are added to a $\mathbf{3}^{2-}$ solution (see Appendix A2.1.2 for the CW EPR spectra and corresponding spectral simulations). At the same time, $\mathbf{3}^{2-}$ molecules still favor certain coordinates in the Ionoids, because of electrostatic attraction to $\mathbf{1}^{4+}$ and repulsion among themselves. It is likely that the combination of larger organic and small, yet doubly charged, inorganic building blocks is necessary for the emergence of ordered ionic assemblies, which persist in solution over time. Also solvent effects may play a role, since DMSO is known to feature anomalous properties, because of self-association.[28] Taking all the experimental and computational data into account, one can conclude that the self-assembled objects feature a defined radius, although, on a molecular scale their interior seems to not be strongly fixed: 'Gluing' $\mathbf{3}^{2-}$-molecules can still rotate relatively undisturbed. Yet, on the supramolecular scale certain, defined coordinates inside the aggregates are preferentially populated for at least some nanoseconds. The position of the 'glue', hence, is not arbitrary. From a physico-chemical point of view it is highly intriguing that an intrinsically non-directed force like electrostatic attraction/repulsion leads to the formation of highly defined nanoscopic objects. One can even control the initial size of the self-assembled Ionoids precisely and keep them stable in solution for months. Thus, by choosing the right ions and counterions their distribution in solution is not, like one would expect intuitively for electrolyte solutions, more or less homogeneous.[28, 29] Contrary, they do assemble into discrete arrangements, as it has been observed for macroions, e.g. for DNA,[30, 31] already years ago.

2.2 DNA-Condensation with Spermine Dendrons: Interactions in Solution, Charge Inversion, and Morphology Control

Going beyond long-range correlations between small molecules, a typical example for electrostatic correlation in the regime of non-crystalline soft matter is the assembly of counterions on the surface of a densely charged polyelectrolyte. In recent literature reports, especially aggregation of polyelectrolytes due to interactions with multivalent counterions has received ample attention, not at least because of its importance for biological systems like DNA-histone complexes.[32-36] Frequently, it was found that a subtle interplay between hydrophobic polymer backbone and charged side groups dominates the response of a polyelectrolyte to varying concentrations of multivalent counterions.[32] An understanding of this response will also be of importance for the following chapter about charged dendronized polymers, since interaction profiles among these are similarly dominated by an interplay between electrostatic and hydrophobic interaction.

A special case of counterion-induced polyelectrolyte aggregation is the packing of DNA strands into dense and structured aggregates, a phenomenon known as DNA condensation (not to be confused with Manning-type condensation of counterions[37-39]). It has been subject to numerous studies in the past, primarily due to potential applications in non-viral gene delivery.[31] In this context, packing of DNA into spatially well-defined objects (coined condensates) is important, since this prevents large-scale aggregation of DNA and precipitation in vivo, which would suspend DNA-functionality. (For reviews see e.g. references [40, 41].) Different types of artificial condensation agents, e.g. small complexes like hexaammine cobalt(III) or stiff aromatic dendrons have already been successfully applied to condense DNA into defined objects.[42, 43] Also, much attention has been focused on spherical cationic dendrimers, since their affinity to form complexes with DNA (so called dendriplexes) can be controlled by a variety of external stimuli like pH or ionic.[43-49] DNA particles formed by complexation with positively charged dendrimers can either exist as amorphous aggregates or as

highly structured condensates with a definite shape, such as toroids or rods. Toroids are in most cases the favored structure. Rods often only constitute transition states towards toroids or exist in small concentrations next to other (toroidal) structures. Extreme conditions that favor kinking of DNA strands may facilitate the occurrence of rods, but generally they are rather rare.[50, 51]

The interaction between multivalent cations and highly negatively charged polyelectrolytes like DNA has also been addressed by theoreticians and theories have been developed about the net charge of double stranded (ds-)DNA and charge inversion due to presence of highly charged counterions. A promising descriptive approach with large explanatory potential is the formation of highly correlated liquid phases of counterions (condensation agents) on the surface of macroions.[52, 53] Also polyelectrolyte counterions have been under investigation and it has been shown that charge properties can be described with a correlation based theory in this case, too, by fractionization of the polymer charge.[54]

From an experimental point of view, a lot of techniques (e.g. EM, DLS, CD or UV[42, 45, 47, 55, 56]) have been applied to determine the structure of DNA condensates, but EPR spectroscopy has so far not been established in the field of DNA condensation, although it was used before once to determine interactions between DNA and starburst dendrimers.[48] Yet, its popularity for the investigation of drug delivery systems has grown in recent years.[57]

In the present section an approach is presented using spin-labeled spermine dendrons, originally (without spin label) developed by Smith and co-workers,[44] to investigate the biomimetic interaction between 884 bp ds-DNA and cationic dendrons by means of CW EPR. Figure 2.2.1 depicts the spin-labeled generation two dendron (SL-G2 throughout this thesis) that was used to condensation agent. Furthermore, it will be demonstrated how one can exploited small amounts of EPR active Mn^{2+} ions to reveal information about the state of SL-G2/DNA dendriplexes and about the net charge of formed condensates or aggregates. In combination with TEM measurements a detailed picture of the complexation of DNA strands with condensation agents in solution and in the solid state is gained. It will be shown that correlation effects have inevitably to be taken into account when explaining this picture.

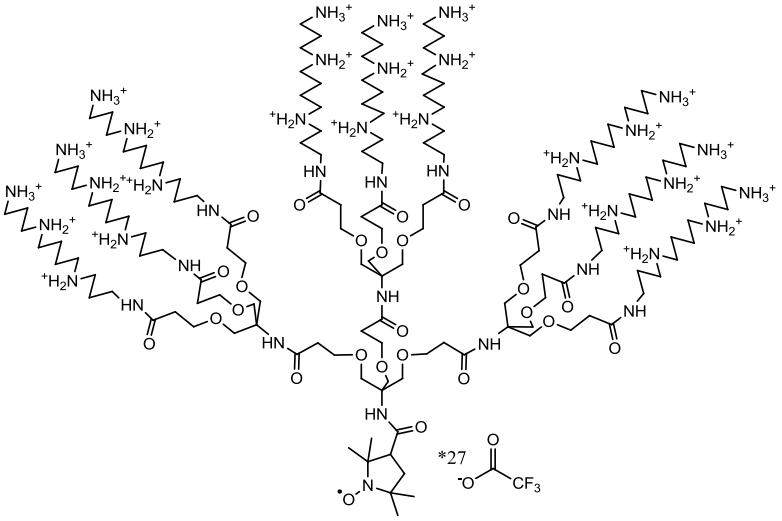

Figure 2.2.1. Structure of the spin-labeled Newkome-type dendron SL-G2 used for EPR tracking of polyelectrolyte condensation.

2.2.1 Results

In Figure 2.2.2 a) the CW EPR spectra are shown for buffered solutions (pH 7.4) of SL-G2 and 884 bp ds-DNA at different charge ratios (cr). The cr is defined as the ratio of the overall concentration of positive charges of the dendron to the concentration of the negative charges of the DNA phosphate groups. For all cr values given a net charge of +27, i.e., quantitative protonation of the ammonium groups at pH 7.4, is assumed per SL-G2 molecule. However, one has to be are aware of the fact that primarily the peripheral ammonium groups will interact with the DNA. The overall nucleotide concentration typically was 2.3 mM.

From comparison of the CW EPR line shape of SL-G2 in mere buffer with the line shapes at cr = 0.35 – 2.30 it can be clearly deduced that DNA presence significantly affects the spectra (Figure 2.2.2 a)). The line broadening at cr > 0 is a consequence of electrostatic attachment of the dendrons to DNA and subsequently restricted rotational freedom. This can be deduced from previous EPR work on counterion attachment (or "condensation" according to Manning[37-39]) to polyions.[15, 58] Spectral simulations support this scenario, too. They indicate a slower rotational motion of SL-G2 in the presence than in the absence of DNA. While the rotational correlation time for the mere SL-G2 is found to be $\tau_c \approx 3$ ns, for SL-G2 in presence of DNA one finds $\tau_c \approx 15$ ns (see Appendix A2.2.5). These values clearly allow for distinction of DNA-bound and free SL-G2 dendrons. From the fact that the rotational correlation time τ_c of site bound SL-G2 remains constant under all experimental conditions, one can deduce that it stays condensed throughout all experiments presented here. This further justifies quantification of the two species in terms of mole fractions.

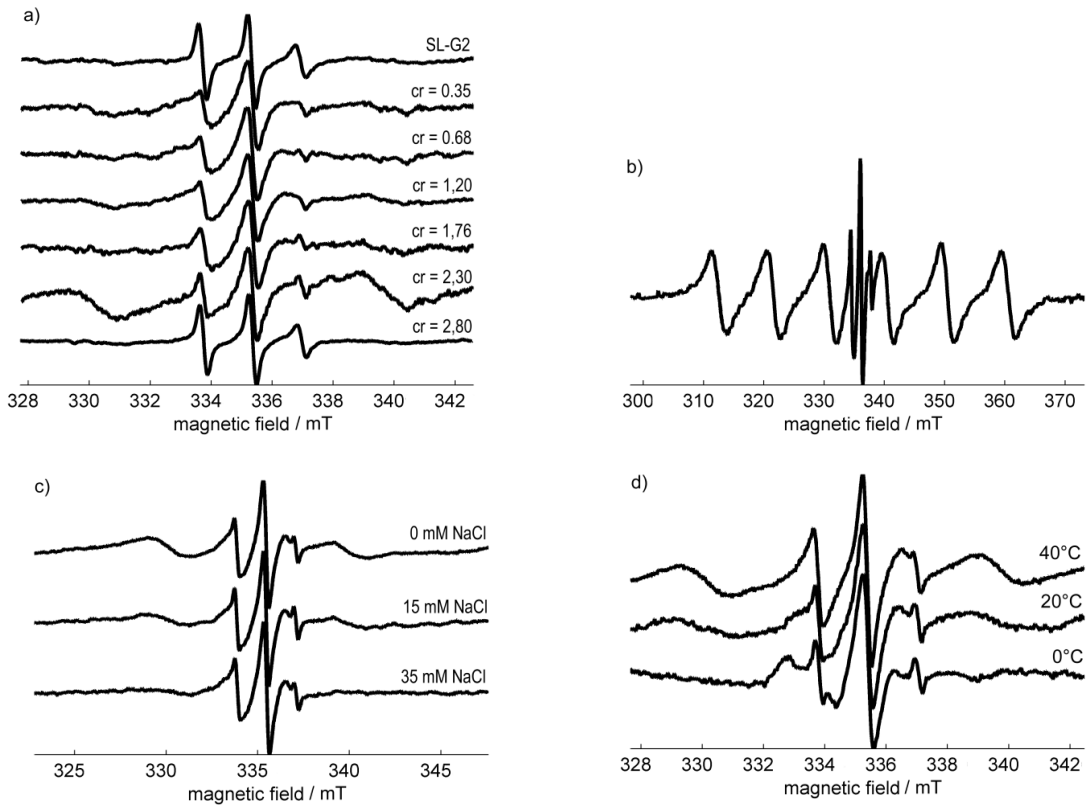

Figure 2.2.2 a) X-band (microwave frequency: ~9.4 GHz) CW EPR spectra of SL-G2 / DNA mixtures at different charge ratios. At cr = 2.30 two broad lines, stemming from Mn^{2+} cations appear. b) Wide sweep CW EPR spectrum of SL-G2 / DNA mixture at cr = 2.3. The six Mn^{2+}-lines as well as the three lines of the nitroxide based spin probe SL-G2 are visible.c) CW ESR spectra of SL-G2 / DNA (cr = 2.3) mixtures at different NaCl concentrations. d) CW EPR spectra of SL-G2 / DNA mixtures at different temperatures. With increasing temperature the Mn^{2+} lines gain intensity (cr = 2.3).

Nearly all CW EPR spectra of SL-G2 in DNA solutions show contributions of free and bound species. With increasing cr the contribution of the free species to the overall spectrum increases. Only at cr = 2.80 solemnly the free species is detectable. In all other cases the contribution of the slow species dominates as can be seen from the spectra in Figure 2.2.2. Interestingly, at cr = 2.30 two additional broad lines at 330 mT and 340 mT appear next to the nitroxide spectrum. Scanning with a broader sweep width reveals that these lines can be traced back to Mn^{2+} cations (see Figure 2.2.2 b)) that had been added after co-dissolving the synthesized DNA. Mn^{2+} has an electron group spin of $S = 5/2$ and a nuclear spin of $I = 5/2$. Since only the $M_S = -1/2 \rightarrow M_S = +1/2$ transition is observable at the moderate X-band frequencies used here, only the six ^{55}Mn hyperfine lines appear and the two detected with the small sweep range in Figure 2.2.2 stem from the $M_I = \pm 1/2$ transitions. For all the EPR spectra depicted in Figure 2.2.2 the Mn^{2+} concentration was constantly 0.5 mM, but only at a charge ratio between 2 and 2.5 Mn signatures are clearly detectable.

Adding small concentrations of monovalent salts like sodium chloride to a sample at cr = 2.3 leads the disappearance of the Mn^{2+} lines (see Figure 2.2.2 c)). Contrary, increasing temperature intensifies the Mn^{2+} contributions (see Figure 2.2.2 d)). Signals stemming from SL-G2 remain unchanged in both cases.

Spectral simulations of the overall spectra are obtained by adding weighted spectral contributions from the fast and slow SL-G2 species. These weights are a direct measure of the mole fractions χ_i of the condensed and "free" species. It should be noted that it is quite difficult to obtain exact values for χ_i in cases of relatively broad EPR lines from spectral simulations at the present level of noise in the spectra. However, for different cr values one can obtain approximate mole fractions $\chi_{condensed} \approx 0.7$ for cr = 0.35-1.20, $\chi_{condensed} \approx 0.5$ for cr = 1.76, $\chi_{condensed} \approx 0.4$ for cr = 2.30 and $\chi_{condensed} < 0.1$ for cr = 2.80. (For the simulations see Appendix A2.2.6.)

To complement CW EPR data the condensates' / aggregates' morphology was observed at different charge ratios and salt concentrations with transmission electron microscopy (TEM). Corresponding micrographs are presented in Scheme 2.2.1. At a charge ratio of 2.3 dendriplexes constitute rod-like condensates of a typical length of 300 nm. Adding 35 mM NaCl to a rod-containing solution leads primarily to large aggregates of rods and toroids. Tenfold dilution of the samples atof 35 mM NaCl leads to thin and flexible fibers and some thin toroids, while in the case without extra salt no changes in aggregate morphology could be detected. Varying the charge ratio by decreasing or increasing the amount of SL-G2 in the solution leads to aggregates of undefined morphology (Scheme 2.2.1 left-hand side).

The appearance of the Mn^{2+} signal in the CW EPR spectra at cr = 2.3 can therefore be correlated with the appearance of well-defined rod-like structures, as detected by TEM. This is true also for tenfold dilute samples. The rod-like condensate morphology is not affected by dilution, hence the Mn^{2+} signal does not disappear.

For data on interaction between DNA and other generations of condensation agents (SL-G0 and SL-G1) see reference [59]. Depending on the dendron generation, striking differences in solution behavior and condensation efficiency can occur as a consequence of a generation-dependent charge density.[46, 56, 60]

2.2.2 Discussion

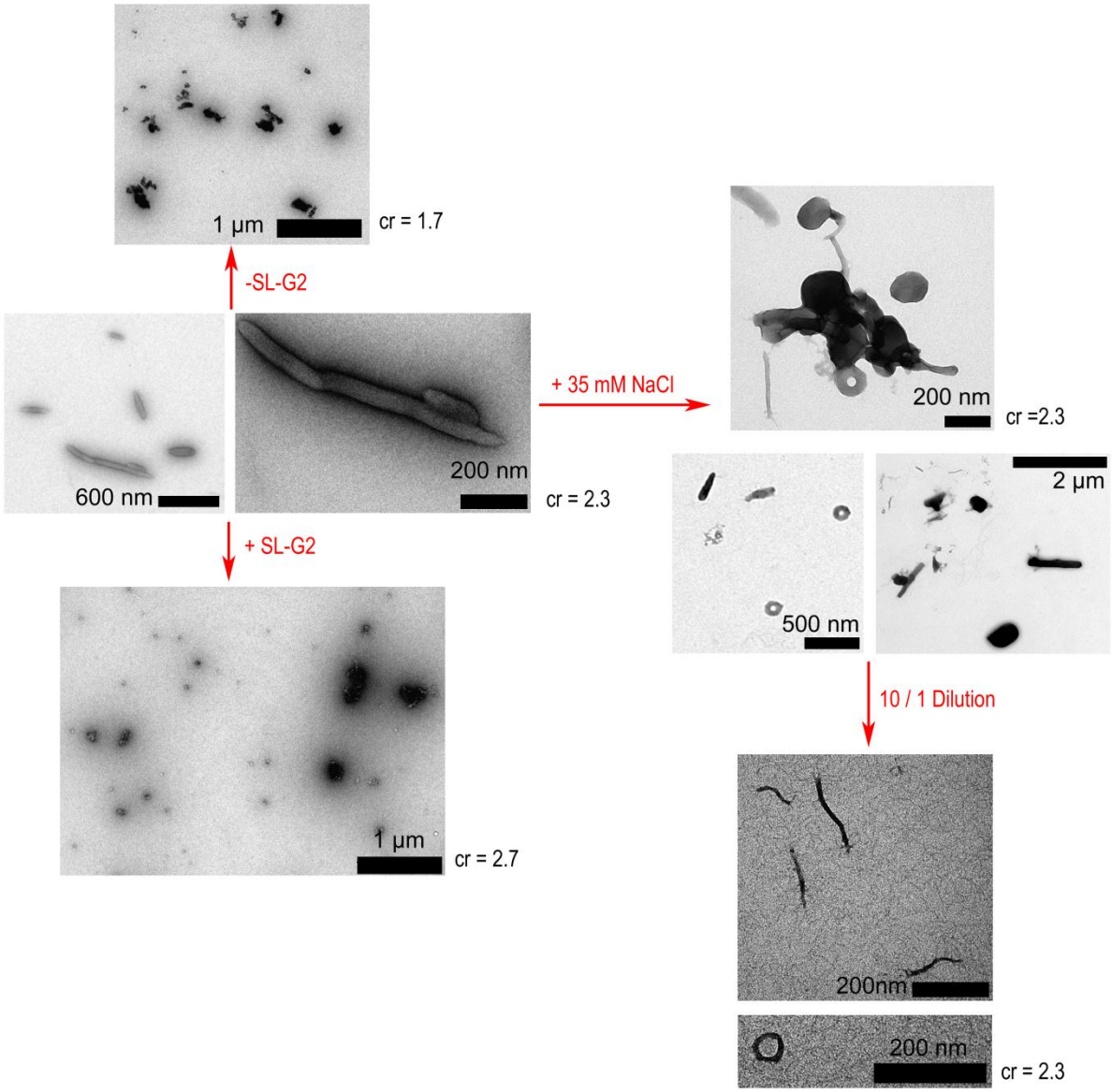

Scheme 2.2.1: Transmission electron micrographs of DNA condensates and aggregates. The scheme should be read as follows: At cr = 2.3 the dendriplexes are rod-shaped, as depicted on the left hand side in the center. Decreasing the charge ratio by reducing the SL-G2 concentration leads to undefined aggregates (top left). Increasing the charge ratio leads to aggregates of undefined shape as well (bottom left). When the ionic strength of the solution is increased by addition of 35 mM NaCl, the rods at cr = 2.3 partially transform to toroids. The rods and toroids aggregate and mainly large assemblies of different rods and toroids can be detected (right hand side, center). When the solution at cr = 2.3 and 35 mM NaCl is diluted tenfold, the aggregates disappear and mainly thin worm-like structures and some thin toroids are formed. Note that dilution in the case without NaCl does not lead to a significant change in morphology.

Correlation of TEM and EPR Data

Mn^{2+} CW EPR signatures (one can view Mn^{2+} as a second spin probe) can only be detected at cr = 2.3, i.e., if rods appear in the TEM micrographs. This is also true for a wide range of concentrations (0.23 mM – 2.3 mM; see Appendix A2.2.4).

The disappearance of the manganese signal after addition of 35 mM NaCl at cr = 2.3 can empirically be correlated with the partial transformation of the rods into toroids and clustering of these into larger objects. In the presence of NaCl only a few “single” condensates can be observed in the transmission electron micrographs (see Scheme 2.2.1, center). Variations in concentration under

NaCl conditions do not lead to any changes in the CW EPR spectra. Therefore the transformation of the larger clusters into fibers upon dilution cannot be followed by EPR.

At charge ratios clearly different from 2.3 only undefined aggregates can be observed with TEM. In this case also no Mn^{2+} signal is observable with CW EPR. Yet, the decreased rotational mobility of SL-G2, compared to the freely rotating species, still is indicative of DNA-SL-G2 interactions that trigger DNA aggregation.

Concluding, presence of Mn^{2+} EPR signatures is strictly correlated with rod-like condensate morphologies for the present system. Unfortunately there are no micrographs available of the DNA / SL-G2 system at elevated temperatures, but since the Mn^{2+} signal increases with rising temperature one could speculate that the formed rods remain stable up to body temperature. As will be shown in the next section, the state of the Mn^{2+} ions can be regarded as site-bound, as long as they don't give rise to an EPR signal.[61] In return, the detection of an Mn^{2+} signal indicates divalent ions that are not strongly site-bound to DNA.

Taking all the data together, one can determine the morphology of the investigated system by conventional CW EPR spectroscopy. Interestingly, no significant changes in the CW EPR spectral shape could be observed after longer waiting periods (even after days, although the signal intensity decreases notably). This indicates that the formed dendriplexes are at least metastable. By correlating the EPR data with TEM data it becomes obvious that simple CW EPR yields an elegant method to quickly detect the morphology (and charge, as will be inferred below) of DNA condensates/aggregates.

Charge Inversion and NaCl Dependence

The most striking finding in the CW EPR spectra is the occurrence of the Mn^{2+} lines at cr = 2.3 (see Figure 2.2.2 b)). Since Mn^{2+} acetate added to a buffered solution of pure DNA does not exhibit any EPR activity one can conclude that Mn^{2+} interacts strongly with DNA. The densely packed negative charges on the DNA strands strongly attract the positively charged Mn^{2+} ions leading to site-binding. The resulting decrease in rotational Mn^{2+} mobility comes along with strong line broadening. Broadening of Mn^{2+} signals beyond detection is documented[61] and can be reproduced for the present case by spectral simulation when using τ_c values of ~1 ns.[62] Thus, it is reasonable to assume that in buffered solutions of DNA the Mn^{2+} ions are strongly attached to DNA double strands. This changes with increasing concentrations of SL-G2. As expected from simple Manning-type considerations of counterion attachment[15, 37-39, 58] the multiple charged SL-G2 (see Figure 2.2.1) competes with cations of lower charge for attachment to the DNA strands. Condensation of part of the counterions to the chain is energetically favoured, if the Manning parameter (linear charge density) is greater than the inverse of the counterion valence ($\xi \geq z^{-1}$).[37, 39] Condensation of Mn^{2+} to the DNA leads to the following scenario: The overall concentration of Mn^{2+} was 0.5 mM. Such, ~1.3 mM negative DNA charges still compensate for other counterions at a nucleotide concentration of 2.3 mM (assuming complete compensation of 1 mM negative DNA charges by the Mn^{2+} ions). Most of the counterions can be expected to be monovalent. At lower cr SL-G2 will compete with these first.

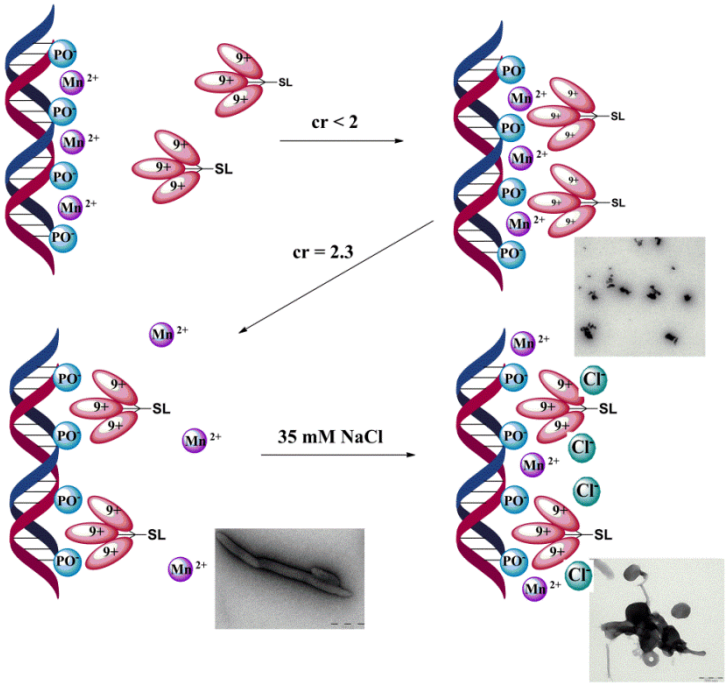

Scheme 2.2.2. A sketch of the molecular scale picture that arises from the EPR data and theories of counterion condensation together with corresponding TEM micrographs. The red ellipses marked with 9+ represent one arm of SL-G2 with 3 spermine groups.

At cr = 2.3 the SL-G2 concentration is high enough such that divalent cations are expelled, too (Scheme 2.2.2, lower left side), as judged from CW EPR. There are two possible and not mutually exclusive explanations for the expelling of small counterions of low valence due to increasing SL-G2 concentrations:

A) The Mn^{2+} ions are expelled due to an increase in the system's entropy. When n/2 Mn^{2+} counterions are released from the polymer strand by a n times positive charged SL-G2 denrimer the overall amount of molecules in the solution is raised from 2 to (4 + 3n)/2, when the trifluoroacetic acetate (TFA) counterions of SL-G2 are taken into account, too.[63],[64]

B) Due to charge inversion of the DNA strands at cr 2.3 the net charge is switched from negative to positive such that the Mn^{2+} ions experience a repulsive force and are released from the condensed state.[53, 65] Several arguments support the assumption of an inverted DNA charge:

1) The increase in Mn^{2+} signal intensity with rising temperature is in accordance with the theory of charge inversion due to correlation holes, which can be regarded as "mirror" images of counterion charge on the polyelectrolyte. This theory predicts that for a concentration, c_s, of counterions with charge Z in the bulk solution the inverted charge is given by $Q^* = \varepsilon_0 \varepsilon r k_B T \ln(c_s/c_0)/Ze$, with c_0 being the counterion concentration at the isoelectric point (exact charge cancellation).[53] Thus, Q^* increases, when T increases and more Mn^{2+} ions are expelled, when $c_s > c_0$. This is in good agreement with the experimentally determined temperature-dependence of the CW EPR spectra (Figure 2.2.2 d)). The fact that the Mn^{2+} signal disappears when sodium chloride is added seems to contradict charge inversion through correlation holes, because monovalent ions provide Debye-Hückel screening with a decay length of $\kappa^{-1} = (2e^2 c_s/\varepsilon_0 \varepsilon k_B T)^{1/2}$. Therefore, charge inversion should become stronger with increasing c_s, since the charging energy of the polyelectrolyte is screened much stronger than the correlation energy of the condensed SL-G2 ions. However, increasing inverted charge through addition of monovalent counterions is predicted only for small c_s. This is not

the case here. The NaCl concentrations used are at least one order of magnitude higher than the nucleotide or SL-G2 concentration.[53][66][67]

2) At such high concentrations of monovalent salt the net charge of the formed condensates is affected, because monovalent ions condense on the SL-G2 counterions and thereby hamper charge inversion of the whole condensate. This has been shown before.[68] As a consequence, the repulsive force on the Mn^{2+} ions decreases (see Scheme 2.2.2, lower right side). This assumption is also consistent with the fact that the rods formed at cr = 2.3 in the absence of NaCl transform into larger aggregate due to screened like-charge repulsion at 35 mM NaCl in the bulk solution. This is evident from reports on intercomplex aggregation at high concentrations of free condensation agents.[55]

3) Further information can be gained from the fact that rods are formed only at cr = 2.3, in the absence of NaCl. Note that rods are rarely observed and frequently constitute transition states en route to toroids.[40, 51, 69] Here, the rods can be observed even after days (see Scheme 2.2.1, center). For rod-like structures to appear, normally sharp kinks in the rather rigid DNA are needed, which requires that the double helix is locally destabilized, such that DNA strands can fold back.[50] This is not the case here: from the micrographs presented in Scheme 2.1.1 the average rod length can be estimated to be around 300 nm, which remarkably is the length of a fully streched 884 bp ds-DNA (counting one base pair as 0.34 nm, 884 bp DNA is 300.56 nm long[70]) Therefore it seems unlikely that the DNA molecules fold back to generate rod-like structures. A parallel assembly of strands is more plausible.[71]

Studies with dendrimers like PAMAM (poly(amido amine)) or PPI (poly(propylene imine)) showed that DNA dendriplexes can experience a structural instability at the isoelectric point. When DNA charge becomes inverted condensates can undergo phase transitions into hexagonal or square phases, which consist of parallel ordered DNA and intercalated dendrimers.[41, 72] Since PAMAM and PPI dendrimers are relatively similar to SL-G2 this phase transition is a viable explanation for the rod-like structures in this study, too.

Concluding, the rods presented in Scheme 2.2.1 are very likely charge inverted dendriplexes of parallely ordered, stretched DNA strands.

Due to this and the observed response to temperature- and NaCl concentration-variations that matches the theoretically predicted behavior, it is reasonable to assume that charge inversion is actually responsible for the observed expelling of the Mn^{2+} ions. Of course, an increase in the overall entropy likely plays a particular role, too, but it alone could not account for all the observed phenomena.

Charge Ratio Dependence

It intuitively appears reasonable to assign the appearance of defined, rod-like structures to precisely defined (isoelectric) conditions, since DNA condensation theory predicts a lot of factors – apart from the mere electrostatic interaction between DNA and condensation agent – to be responsible for the formation of well-defined structures (e. g. solvent-DNA interactions, surface potential, etc.).[40] Variation of only one parameter can initially lead to the formation of undefined aggregates.[44] The above argumentation can also account for the fact that highly structured condensates appear only at a cr around 2.3 together with the manganese signal in the CW EPR spectra, while other charge ratios lead to undefined aggregates. Rod-like condensates appear at the isoelectric point (around cr 2.3) in this scenario, where the complexes' charge is exactly cancelled through counterions. At charge ratio ≠ 2.0 – 2.5, where undefined aggregates are observable the net charge of the dendri-

plexes would hence be (non-compensated) negative or (strongly inverted) positive charge. Thus, higher net charge of the complexes would be the reason for the undefined aggregates to appear, because short-ranged attractive interactions, which favor S- or H-phase structures[72] are screened by like-charges of the complexes.

Assuming the above literature-based deduction to be correct one is able with conventional CW EPR is suitable for the precise location of the onset of charge inversion of DNA.

Monovalent Salt Dependence upon Dilution

Thin fibers and toroids are formed at cr = 2.3 through tenfold dilution of NaCl-containing samples. The thick rods formed without NaCl in the solution at cr = 2.3 remain stable upon dilution (cf. Scheme 2.2.1). Tenfold dilution of the original cr = 2.3 solutions, with and without additional NaCl indicate that the interaction between SL-G2 and DNA in individual complexes is not affected by diluting, since the nitroxide signal remains unchanged (see Appendix A2.2.5). Therefore, the dilution-triggered structural adaptions observed by TEM have to be correlated with interactions between dendriplexes and not with changes in SL-G2 coordination. Under salt free conditions the manganese signal remains constant. This is a clear indication that the condensates remain in a rod-like shape and their charge remains inverted. However, in the presence of NaCl the aggregates as well as the thicker rods and toroids at the original nucleotide concentration of 2.3 mM disintegrate upon dilution to form thin fibers and Mn^{2+} is consequently not observable. Remarkably, the presence of low-valent salt is assumed to lead to larger and thicker toroids in other studies.[73] However, in these cases toroid formation was based on a nucleation and growth mechsnism, while in the case presented here already formed aggregates disintegrate.

The thin fibers formed after dilution are not confined to a certain length, but exist at lengths between approx. 100 nm and 200 nm. Furthermore, the rods are not perfectly linear anymore, but resemble worm-like chains[74], since the TEM data indicate particular bending of all the condensates.

Two factors can account for the described behavior upon dilution:

1) NaCl seems to affect the dendriplex superstructures first. Since the SL-G2-nitroxide signal remains (as inferred from the CW EPR spectra) unchanged, the interaction between SL-G2 and the DNA is not affected. It seems plausible to assume a screening of electrostatic interactions between the dendriplexes only.

2) The fact that the thin fibers have lengths shorter than that of the used DNA but are definitively thicker than a single double helix indicates back-folding. This is well-documented for stiff polyelectrolytes that self-fold in order to avoid unfavorable solvent exposure.[75] Therefore, a kinking of the DNA has to be taken into account, which is necessary for back folding. Literature reports indicate that the degree of hydration of the DNA strands is crucial for kinking of the strands, because the B-form of the DNA has to be destabilized for sharp fold-backs (a ds-DNA molecule can bend 90° at maximum).[50]

Since the repulsive interaction between the condensates at cr = 2.3 is most-likely screened by 35 mM NaCl, one may speculate that repulsive interactions between dendriplex segments are screened, too. This assumption is supported by theoretical approaches, which predict condensation of the monovalent ions onto the dendron surface.[31] This consequently leads to a screening of the dendron charge and reduced dendriplex persistence lengths. Such, self-folding and kinking of the DNA may be possible. Also, the high charge density (27 positive charges) of the dendrons is confined

to a relatively small patch of the DNA molecules. This may well destabilize the double-helix B-form and can desolvate it. This explanation also accounts for the fact that in absence of NaCl no transformation from rods to fibers can be observed, because charges on the dendriplex surfaces prevent back-folding.

2.3 Summary

Altogether, this section presents experimental and computational evidence for the formation of electrostatically self-assembled supramolecular structures in solution. The complexity of phenomena that can arise from correlated non-covalent interaction profiles at nanoscopic length scales could be demonstrated during the case study of DNA condensation and of Ionoids.

Ionoids are nano-assemblies that have a well-defined size and molecules in their interior populate transiently certain fixed positions, while retaining rotational freedom. Ionoids can possibly open new routes towards the design and self-assembly of novel materials, by exploiting electrostatic interactions between small molecules, which has not attracted much attention in this field of research so far. In addition, these nano-objects are intriguing from a theoretical point of view, since long-range electrostatic correlations in solution have been postulated, but not yet been observed directly for low-molecular electrolytes (unlike macroions). Here such correlations lead to the emergence of unexpected structuring phenomena.[76, 77] From the slow but steady size-increase over the course of two months (see Figure 2.1.1 c)) one may even speculate that Ionoids could be some sort of solvated precursor for precipitation or even crystallization nuclei. More experimental evidence would be needed to further substantiate such a picture, which currently is a mere speculation. The responsiveness of Ionoids towards stimuli like concentration, solvent-mixture or charge ratio may also become interesting in the course of the search for new responsive materials.

When 884 bp ds-DNA is condensed into densely packed aggregates or condensates by the spermine terminated SL-G2 dendron a high structural diversity can be observed. The different structures heavily depend on the charge ratio between positively charged ammonium groups of the dendron and negatively charged phosphate groups of the DNA and on the concentration of monovalent co-solutes. As many, partly counteracting interactions are responsible for the shape of DNA condensates or aggregates a large morphology band width is not unexpected. Yet, all morphological transitions can be explained consistently by correlated electrostatic interactions. From EPR and TEM a molecular scale picture can be inferred, as it is depicted in Scheme 2.2.2. Conventional CW EPR allows a closer look at the local environment of the paramagnetic molecules. TEM gives a complementary, global view on the morphology of the formed condensates and aggregates. Thus, one can gain a very detailed picture of the system, ranging from the underlying molecular interactions in solution to the morphology of the solid condensates. From this, one is able to control the condensate morphology in a very precise manner.

The reader should now have an idea of the possibilities concerning macromolecular morphology and phase control that arise from tuning non-covalent interaction profiles. The following section about dendronized polymers will further exploit this possibility.

References and Notes

[1] J. M. Lehn, *Rep. Prog. Phys.* **2004**, *67*, 249.

[2] G. M. Whitesides, B. Grzybowski, *Science* **2002**, *295*, 2418.
[3] J. M. Lehn, *Top Curr Chem* **2012**, *322*, 1.
[4] K. J. M. Bishop, C. E. Wilmer, S. Soh, B. A. Grzybowski, *Small* **2009**, *5*, 1600.
[5] B. M. Rosen, C. J. Wilson, D. A. Wilson, M. Peterca, M. R. Imam, V. Percec, *Chem. Rev.* **2009**, *109*, 6275.
[6] H. Juwarker, K.-S. Jeong, *Chem. Soc. Rev.* **2010**, *39*, 3664.
[7] J. C. Huie, *Smart Mater. Struct.* **2003**, *12*, 264.
[8] C. F. J. Faul, M. Antonietti, *Adv. Mater.* **2003**, *15*, 673.
[9] Y. Tezuka, *Chem. Rev.* **2005**, *5*, 17.
[10] F. Gröhn, *Macromol. Chem. Phys.* **2008**, *209*, 2295.
[11] R. M. Capito, H. S. Azevedo, Y. S. Velichko, A. Mata, S. I. Stupp, *Science* **2008**, *319*, 1812.
[12] D. A. Walker, B. Kowalczyk, M. Olvera de la Cruz, B. A. Grzybowski, *Nanoscale* **2011**, *3*, 1316.
[13] D. Kurzbach, M. N. Reh, D. Hinderberger, *ChemPhysChem* **2011**, *12*, 3566.
[14] J. Heller, H. Elgabarty, B. Zhuang, D. Sebastiani, D. Hinderberger, *J. Phys. Chem. B* **2010**, *114*, 7429.
[15] D. Hinderberger, H. W. Spiess, G. Jeschke, *Europhysics Letters* **2005**, *70(1)*, 102.
[16] H.-Y. Gong, B. M. Rambo, W. Cho, V. M. Lynch, M. Oh, J. L. Sessler, *Chem. Commun.* **2011**, *47*, 5973.
[17] H.-Y. Gong, B. M. Rambo, E. Karnas, V. M. Lynch, J. L. Sessler, *Nature Chemistry* **2010**, *2*, 406.
[18] A. I. Share, A. H. Flood, *Nature Chemistry* **2010**, *2*, 349.
[19] R. M. Fuoss, *Trans. Faraday Soc.* **1934**, *30*, 967.
[20] P. Zhu, X. You, L. R. Pratt, K. D. Papadopoulos, *J. Chem. Phys.* **2011**, *134*, 054502.
[21] D. Kurzbach, D. R. Kattnig, N. Pfaffenberger, W. Schärtl, D. Hinderberger, *ChemistryOpen* **2012**, *1*, 211.
[22] All simulated data was kindly provided by Dr. Daniel Kattnig and details on how these simulations were performed can be found in reference 21.
[23] J. E. Sader, D. Y. C. Chan, *Langmuir* **2000**, *16*, 324.
[24] I. Rouzina, V. A. Bloomfield, *J. Phys. Chem.* **1996**, *100*, 9977.
[25] M. Patra, M. Karttunen, M. T. Hyvönen, E. Falck, I. Vattulainen, *J. Phys. Chem. B* **2004**, *108*, 4485.
[26] Note that for these measurements the exact concentration of $\mathbf{2}^{2-}$ within the light scattering sample is difficult to determine, since the solubility of the pure component $\mathbf{2}^{2-}$ is only 3 mM in the used solvent mixture.
[27] Note that the concentration in the simulations was three times higher than in the DEER measurements, to reduce the computation time.
[28] A. K. Adya, O. N. Kalugin, M. N. Volobuev, Y. V. Kolesnik, *Mol. Phys.* **2001**, *99*, 835.
[29] O. N. Kalugin, A. K. Adya, M. N.Volobuev, Y. V. Kolesnik, *PCCP* **2003**, *5*, 1536.
[30] V. A. Bloomfield, *Biopolymers* **1997**, *44*, 269.
[31] C. Dufès, I. D. Uchegbu, A. G. Schätzlein, *Adv. Drug Delivery Rev.* **2005**, *57*, 2177.
[32] Q. Liao, A. V. Dobrynin, M. Rubinstein, *Macromolecules* **2006**, *39*, 1920.
[33] H. Schiessel, P. Pinucs, *Macromolecules* **1998**, *31*, 7953.
[34] C. L. Cooper, P. L. Dubin, A. B. Kayitmazer, S. Turksen, *Curr. Opinion Coll. Interf. Sci.* **2005**, *10*, 57.
[35] P.-Y. Hsiao, *J. Chem. Phys.* **2006**, *124*, 044904 1.
[36] A. V. Dobrynin, M. Rubinstein, *Prog. Polym. Sci.* **2005**, *30*, 1049.
[37] G. S. Manning, *J. Chem. Phys.* **1969**, *51*, 934.
[38] G. S. Manning, *J. Chem. Phys.* **1969**, *51*, 924.
[39] G. S. Manning, *Acc. Chem. Res.* **1979**, *12*, 443.
[40] V. A. Bloomfield, *Biopolymers* **1997**, *44*, 269.
[41] C. Dufès, I. D. Uchegbu, A. G. Schätzlein, *Adv. Drug Deliv. Rev.* **2005**, *57*, 2177.
[42] S. He, P. G. Arscott, V. A. Bloomfield, *Biopolymers* **2000**, *53*, 329.
[43] Z. B. Shifrina, N. V. Kuchkina, P. N. Rutkevich, T. N. Vlasik, A. D. Sushko, V. A. Izumrudov, *Macromolecules* **2009**, *42*, 9548.
[44] M. A. Kostiainen, J. G. Hardy, D. K. Smith, *Angew. Chem. Int. Ed.* **2005**, *44*, 2556.

[45] A. M. Carnerup, M.-L. Ainalem, V. Alfredsson, T. Nylander, *Langmuir* **2009**, *25*, 12466.
[46] M.-L. Ainalem, A. M. Carnerup, J. Janiak, V. Alfredsson, T. Nylander, K. Schillén, *Soft Matter* **2009**, *5*, 2310.
[47] K. Fant, E. K. Esbjörner, P. Linclon, B. Nordén, *Biochemistry* **2007**, *47*, 1732.
[48] M. F. Ottaviani, F. Furini, A. Casini, N. J. Turro, S. Jockusch, D. A. Tomalia, L. Messori, *Macromolecules* **2000**, *33*, 7842.
[49] M. Piest, J. F. J. Engbersen, *J. Control. Release* **2010**, *148*, 83.
[50] P. G. Arscott, C. Ma, J. R. Wenner, V. A. Bloomfield, *Biopolymers* **1995**, *36*, 345.
[51] J. Haley, P. Kabiru, Y. Geng, *Mol. BioSyst.* **2010**, *6*, 249.
[52] V. I. Perel, B. I. Shklovskii, *Physica A* **1999**, *274*, 446.
[53] A. Y. Grosberg, T. T. Nguyen, B. I. Shklovskii, *Rev. Mod. Phys.* **2002**, *74*, 329.
[54] T. T. Nguyen, B. I. Shklovskii, *Physica A* **2002**, *310*, 197.
[55] D. Störkle, S. Duschner, N. Heimann, M. Maskos, M. Schmidt, *Macromolecules* **2007**, *40*, 7998.
[56] V. A. Kabanov, V. G. Sergeyev, O. A. Pyshkina, A. A. Zinchenko, A. B. Zezin, J. G. H. Joosten, J. Brackman, K. Yoshikawa, *Macromolecules* **2000**, *33*, 9587.
[57] G. Martini, L. Ciani, *PCCP* **2009**, *11*, 211.
[58] D. Hinderberger, H. W. Spiess, G. Jeschke, *J. Phys. Chem. B* **2004**, *108*, 3698.
[59] D. Kurzbach, C. Velte, G. Kizilsavas, P. Arnoldt, D. Hinderberger, *Soft Matter* **2011**, 7, 6695.
[60] P. Welch, M. Muthukumar, *Macromolecules* **2000**, *33*, 6159.
[61] M. F. Ottaviani, F. Montalti, M. Romanelli, N. J. Turro, D. A. Tomalia, *J. Phys. Chem.* **1996**, *100*, 11033
[62] D. Hinderberger, H. W. Spiess, G. Jeschke, *Macromolecules* **2002**, *35*, 9698
[63] The net charge of SL-G2 is +27, but the effective charge responsible for the condensation process is primarely located on the outer sphere of the dendrimer, therefore we refer to a n times positive charged dendron at this point.
[64] M. J. N. Junk, W. Li, A. D. Schlüter, G. Wegner, H. W. Spiess, A. Zhang, D. Hinderberger, *Angew. Chem. Int. Ed.* **2010**, *122*, 5818.
[65] A. V. Kabanov, V. A. Kabanov, *Bioconjugate Chem.* **1995**, *6*, 7.
[66] It should be mentioned that most of the theoretical studies concerning counterion condensation and charge inversion focus on point charges or spheres as counterions, and it has been shown that the phenomenon of charge inversion induced by correlation holes is also applicable for positive polymers. Thus charge inversion has to be taken into account whether one treats SL-G2 as a sphere of a radius r or considers the different spermine moieties as hyperbranched cationic oligomer/polymers.
[67] For such high c_s values one expects a decrease in binding energy of SL-G2 to the DNA strands, but from Figure 2.2.2 c) it can be deduced that the rotational mobility of the spin label is not affected by c_s (SL-G2 remains bound to the DNA strands at even higher concentrations) Thus, there is no evidence for a reduction in SL-G2 binding energies.
[68] M. Tanaka, A. Y. Grosberg, *J. Phys. Chem.* **2001**, *115*, 567.
[69] I. D. Vilfan, C. C. Conwell, T. Sarkar, N. V. Hud, *Biochemistry* **2006**, *45*, 8174.
[70] R. Knippers, "*Molekulare Genetik*", 6 edition, Thieme, StuttgartNew York, 1995.
[71] It should be noted, that the buffer concentration (250 mM) is relatively high compared to the concentrations of nucleotides, condensation agent etc. and hence could affect the system. Yet, the buffer concentration resembles physiological conditions, is constant throughout all experiments and effects due to the trizma base can be regarded as constant and present in vivo.
[72] H. M. Evans, A. Ahmad, K. Ewert, T. Pfohl, A. Martin-Herranz, R. F. Bruinsma, C. R. Salfinya, *Phys. Rev. Lett.* **2003**, *91*, 075501.
[73] C. C. Conwell, I. D. Vilfan, N. V. Hud, *PNAS* **2003**, *100*, 9296.
[74] M. Rubinstein, R. Colby, "*Polymer Physics*", Oxford University Press, New York, 2003.
[75] W. Zhuang, E. Kasemi, Y. Ding, M. Kröger, A. D. Schlüter, *Adv. Mater.* **2008**, *20*, 3204.
[76] P. Gonzalez-Mozuelos, J. M. Mendez-Alcaraz, *Phys. Rev. E* **2001**, *63*, 021201.
[77] V. Vlachy, *Annu. Rec. Phys. Chem.* **1999**, *50*, 145.

3. Dendronized Polymers as Molecular Objects and Transporters

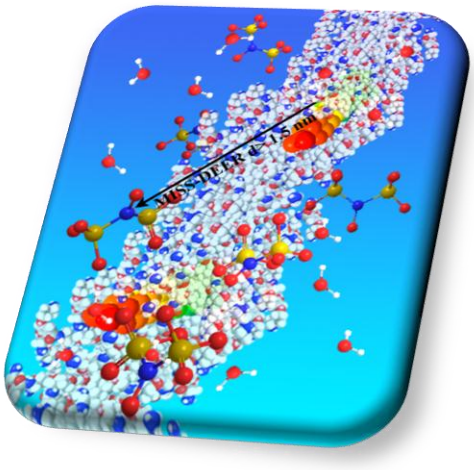

In the previous chapter effects of mere electrostatics on shape and size of macromolecules and molecular assemblies have been introduced. Here, interaction profiles with an additional degree of complexity are in the focus. This chapter is dedicated to *electrostatic and hydrophobic* interactions that simultaneously dominate interaction profiles in charged dendronized polymers (denpols). In particular, their solution structure and potential use for future molecular delivery applications is addressed.

Denpols are macromolecules that bear dendron-side chains on every repeat unit (see Figure 3.1). The arising sterical constraints render denpols quite rigid. For high generation of the dendritic side chains the resulting repulsion may be even large enough to lead to shape persistence and amazingly high persistence length.[1] Therefore, denpols can geometrically be approximated as nanoscopic cylinders. Recently, considerable stiffness has been reported for a neutral generation 5 species with a persistence length of $l_p \approx 30$ nm.[2] This denpol even largely maintains its cross-section geometry when deposited on a solid substrate.[3] Because of this shape persistence, denpols attracted recent attention as *molecular objects*. This term refers to nanostructured objects that exhibit a persistent shape, independent of their immediate environment, and that have a well-defined envelope.[3, 4] Such, for molecular objects the solution structure is obliged to not differ significantly from its solid state structure. For most macromolecules, even biomacromolecules, a striking difference between liquid- and solid-state conformations is observed. E.g., it was recently shown by DEER spectroscopy that even for the well-folded protein human-serum albumin (HSA), the solution structure differs significantly from the crystal structure.[5-7]

For the present study Dr. Baozhong Zhang from the group of Prof. Dr. A. Dieter Schlüter from the ETH Zürich provided denpols whose terminal layer (the cylindrical outermost shell) carries positively charged ammonium groups. The denpols are based on a poly(methacrylate) backbone. Electrostatic and steric repulsion among the dendritic side chains both contribute to the stiffness of the denpols. The number of dendron-branching units, n, determines the number of terminal groups per dendron-side chain as 2^n.[3, 8, 9] Due to the unique structure of peripherally charged denpols they mimic

the properties of biological membranes to a certain degree. The charged cylinder envelope surrounds a layer of dense organic, hydrophobic structure. This arrangement is reminiscent of phospholipid bilayers or vesicles. Such, interaction between denpols and amphiphiles can be observed that resemble comparable interactions in real biological systems.[10] Also the molecular weight of higher generations of denpols can be compared to the weight of biological macromolecules.[3] Denpols represent the first class molecules with molecular precision[11] to possess such a high weight.

In the following, the morphological behavior of denpols and its implications for their interaction with guest molecules will be presented. First influences of peripheral charge on shape persistence will be investigated with DEER on Fremy's salt (abbreviated FS in the following) guests (see Figure 3.1.1) that self-assemble on the denpol's cylindrical surface. Secondly, the large loading capacity of denpols as a consequence of their persistent shape will be assessed. This is done by applying a novel, for this purpose developed DEER application. Finally, it will be shown how a concept of a *load-collapse-release cascade* (comprising guest uptake, subsequent condensation of the host compounds and guest release from the condensates) can be realized with charged denpols to achieve dense guest-compound packing. This last section combines the first two as well as Section 2.2. Internal loading of denpols is combined with self-assembly of salts on the denpols' surface, leading to (DNA-)condensation-like collapse behavior.

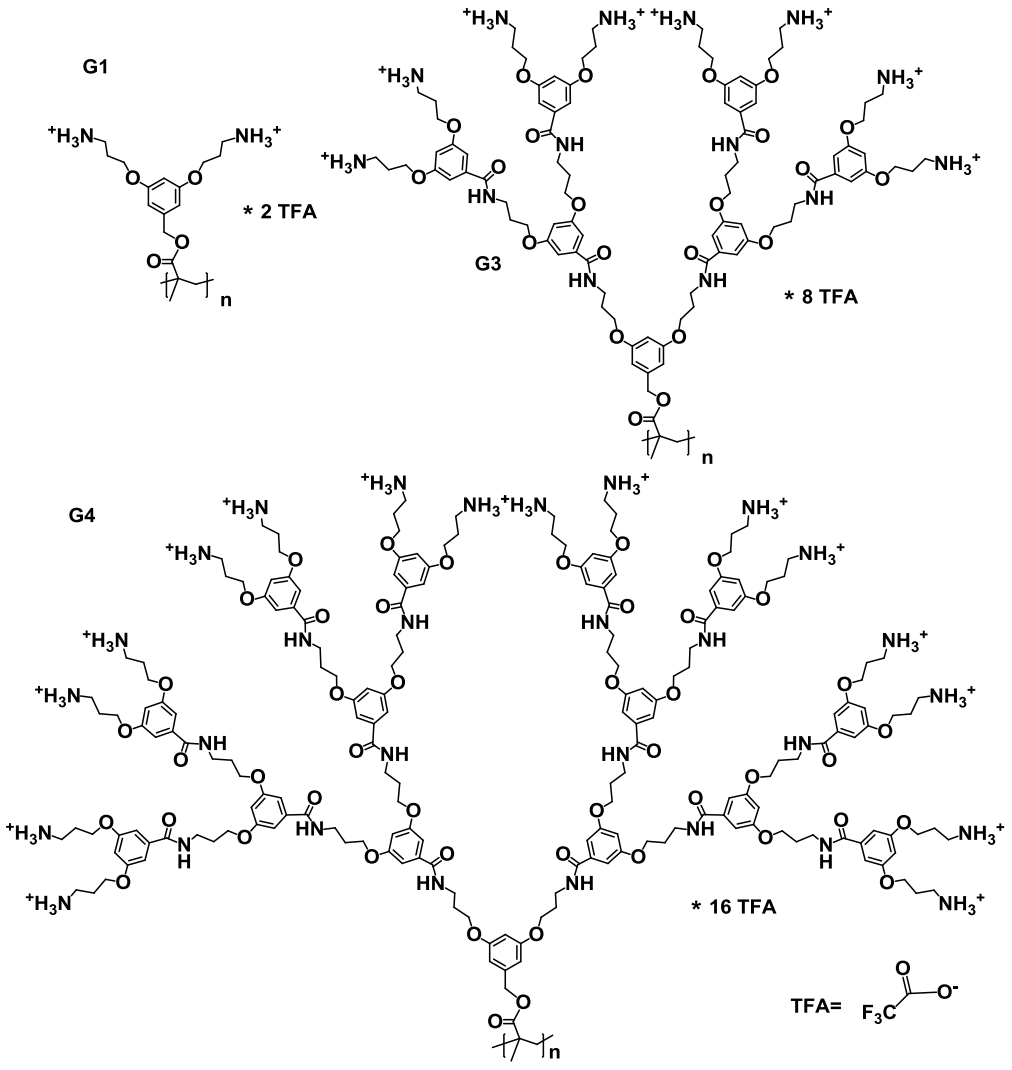

Figure 3.1. Molecular structure of the denpols de-PG1, de-PG3 and de-PG4.

3.1 Assessing the Solution Shape and Size of Charged Dendronized Polymers Using Double Electron-Electron Resonance.

Peripherally charged denpols are expected to exhibit pronounced shape persistence due to sterical as well as electrostatic repulsion between their dendritic side chains. Yet, it is questionable which dendron generation, G, is at least necessary to achieve a shape that is constant and independent of the denpols' local environment. To answer this question their solution size has to be assessed and compared with solid-state sizes. To this end, DEER spectroscopy[12] is utilized in the following to determine the solution-state size (thickness) of the cylinders defined by the charged periphery of denpols of different generations. The claim that conventional PMA is rendered into a cylindrical molecular object by attaching charged, high-generation dendrons to each of its main chain repeat units is substantiated by showing that morphological differences between the solid and solution state (cylinder diameter) vanish with growing side chain generation. Furthermore, it is demonstrated that DEER on dianionic spin probes, which self-assemble close to the surface of cationic denpols (site-directed spin probing), is an indirect and yet precise method to determine the effective spatial constitution and diameter of these large, charged objects in solution.

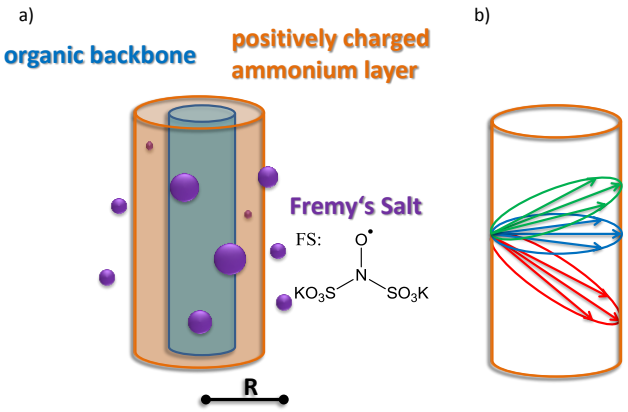

Figure 3.1.1. a) Sketch of the coordination of FS on the cylindrical surface of the dendronized. b) Possible distances between two spin on the surface of a cylinder. The red, blue and green ellipses represent only three of an infinite number of possible orientations.

3.1.1 Results and Discussion

To elucidate the size of a denpol in solution in dependence of its side-chain generation an indirect approach is followed here. The distance distribution of spin probes on the surface of the denpols (see Figure 3.1.1) is determined and fitted with an analytical model to yield the size of the cylinder defined by the denpols envelope. To gain distance distributions by DEER spectroscopy spin labels are usually covalently attached to well-defined positions of a molecule (e.g., of a protein).[13, 14] While this spin-labeling approach is in principle not out of question for studying denpols, comparable and even more heuristic insights can be achieved relying on self-assembly of the doubly negatively charged spin probe Fremy's salt (see Figure 3.1.1) at the denpol's ammonium surface layer of high positive charge density.

To achieve such insights it is important to show first that FS actually does coordinate to the denpols' surfaces: Room temperature CW EPR measurements on 2 mM solutions of Fremy's Salt containing 1wt % of denpols show that the line width and the rotational mobility, represented by the rotational correlation time, τ_c, of the spin probes increase notably if FS is in solution with denpols as compared to a pure solution of FS in water (see Appendix Figure A3.1.1). Judging from what is known from

Section 2.2, this suggests that the FS molecules are indeed electrostatically bound to the surface of the denpols under investigation.[15]

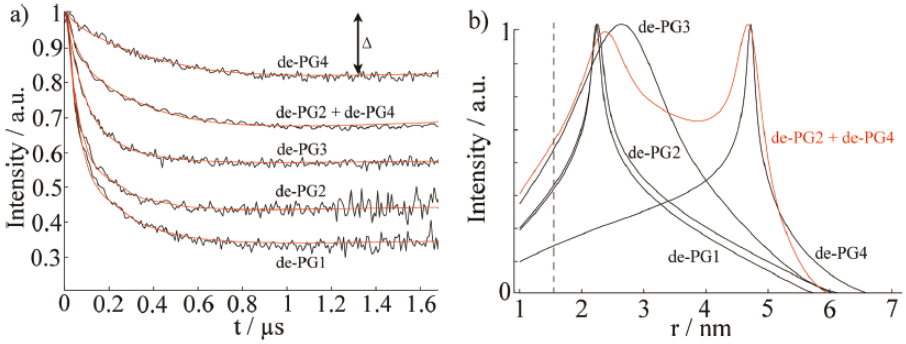

Figure 3.1.2. a) The normalized time traces, i.e., form factors, of the dipolar evolution for FS coordinated to denpols of different generations. The red lines indicate the fits of the experimental time traces (black lines) based on cylindrical distributions of FS. b) Distance distributions of spins in denpol solutions containing Fremy's Salt. The distributions were calculated from the fits of the experimental time traces, presented in a). The red line represents the bimodal distribution determined for a mixture of de-PG2 and de-PG4. The dotted line indicates the minimal, by DEER detectable distance, r_{min}.

This is substantiated by HYSCORE[16, 17] data that show that the electron spin of the unpaired electron of FS is significantly coupled to at least one ^{14}N nucleus in the surrounding of the probe (see Appendix A3.1). This suggests that a large fraction of FS is adsorbed at the ammonium surface potentially building ion pairs. In the CW EPR experiments it was not observed that FS breaches the dense peripheral ammonium layer of the denpols. Indeed, the isotropic hyperfine coupling constant of the nitoxide moiety of FS was constant at a value representative for an aqueous environment (36.7±0.1 MHz). Thus, FS does not penetrate the internal space of the denpols at a significant concentration, but exclusively binds to their surface. It has been shown earlier that FS binds transiently (contact time < 1ns) with only one of its sulfonate groups to polycations. This is typically indicated by characteristic CW EPR line patterns. Since the CW spectra recorded during this study resemble these characteristic patterns[15, 18] one can safely assume that FS binds with only one sulfonate group to dendronized polymers (see Appendix A3.1). Therefore, a restructuring of the denpol surfaces due to a 'bridging' effect between ammonium groups is not expected. Bridging between two different denpol chains is unlikely, too. The transient nature of the coordination of FS does not allow for stable connections between two polymer chains.

Previous AFM studies indicate that in the solid state the diameter of the denpols PG1-4[19] grows with increasing generation; PG-1 is approx. 0.8 nm thick and PG-4 about 4 nm (tapping heights on mica; note that PG refers to denpols with BOC-protected peripheral amines, while de-PG refers to the deprotected analogues).[3, 6] Since one can detect distances between approx. 1.5 and 8 nm with DEER, one may determine the solution diameter of the denpols, which might be difficult to assess by other means or would involve high efforts (e.g. expensive neutron scattering).[20, 21]

Figure 3.1.2 a) depicts the time traces of the dipolar evolution for FS ions self-assembled on the surface of denpols of different generations. Also shown are fits (red traces) based on a physical model that assumes a uniform distribution of the probes on the surface of a cylinder (described below). A very important, experimentally accessible parameter here is the modulation depth, Δ, of the time traces (see Figure 3.1.2 a)), which depends on the number of coupled spins *n* (see Section 1.1.6 on DEER and eq. 1.1.81).[22] In Figure 3.1.2 a) it can be observed that Δ and, hence, n, too, decreases with increasing generation of the dendritic side chains, which is in line with the concurrent

increase of the surface accessible to the probes (and a corresponding decrease of the surface concentration). Table 3.1.1 summarizes n and Δ for the investigated samples. The maximum number of coupled spins (observed for de-PG1) is 2.41, which is low enough for multispin artifacts to be negligible.[23]

Table 3.1.1. Radii gained from DEER measurements with Fremy's salt as spin probe (solution state) and from AFM tapping height (solid state) are listed for all generations investigated during this work. The ratio R_{DEER} / R_{AFM} indicates the differences between the size of the denpols in the solution and solid state.

	de-PG1	de-PG2	de-PG3	de-PG4
R_{DEER} (nm)	0.8 ± 0.2[a]	0.8 ± 0.2[a]	1.0 ± 0.3	2.1 ± 0.4
R_{AFM} (nm)	0.2 ± 0.1	0.5 ± 0.1	1.1 ± 0.1	2.0 ± 0.4
R_{DEER}/R_{AFM}	4.5 ± 0.1	4.5 ± 0.1	0.9 ± 0.2	1.1 ± 0.4
Δ	0.64	0.54	0.42	0.16
n	2.41	2.07	1.75	1.24

[a]Values represent the lower distance limit of DEER.

According to the shell factorization model, introduced by Jeschke et. al.,[24] the normalized time-domain DEER signal (Figure 3.1.2 a)) is related to the distance distribution, $P(r)$ (Figure 3.1.2 b), by a convolution-type integral equation as described in Section 1.1.6 on DEER. While in principle $P(r)$ could be determined by the regularization approach, a simple geometrical model from the outset is assumed instead and tested against the experimental time traces. This approach alleviates issues related to the uniqueness of the solution for $P(r)$, which often hamper regularization approaches.[25]

Given the highly constrained molecular shapes of the dendronized polymers, it is assumed that the FS-spin probes are distributed independently and uniformly on the lateral surface of circular cylinders. Indeed, from steric considerations and the fact that the persistence lengths, l_p, of the neutral denpol analogues are 5 – 10 nm,[3, 6] de-PG1 to de-PG4 may be regarded as stretched on a length scale up to 10 nm. An analytic expression for the distance distribution $P(r)$ for two points on the lateral surface of a cylinder was provided by Dr. Daniel Kattnig (see reference [26] for the complete derivation). It can be compactly expressed as:

$$P(r) = \frac{2r}{L^2\pi}\left(\frac{L}{R}F(\varphi|k^2) - 2\sin^{-1}(k\sin\varphi)\right)\Big|_{\varphi=\Re\cos^{-1}\left(\frac{L}{r}\right)}^{\Re\sin^{-1}(k^{-1})} \quad (3.1.1)$$

Here, F denotes the incomplete elliptical integral of the first kind. $\Re$ is the real part and $k = r/2R$. Dimensionless units with radius $R = 1$ are chosen and the cylinder height is denoted by L.

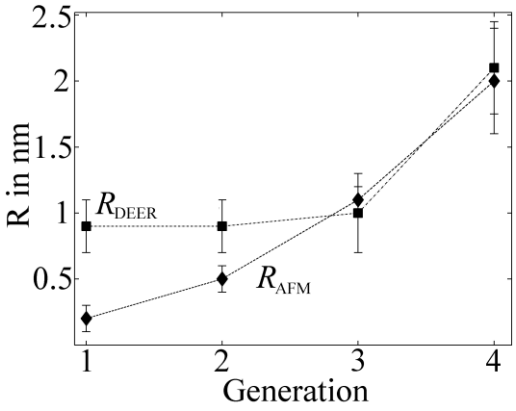

Figure 3.1.3. Radii of the different generations of dendronized polymers determined from solution and solid-state measurements plotted versus denpol generation. Values marked R(DEER) stem from analysis of the data presented in Figure 3.1.2 and are representative for the size of the molecules in solution (filled squares). Values marked R(AFM) stem from AFM tapping heights of the protected denpols PG1-4 and are representative for the size in the solid state (filled diamonds). Error bars were calculated by subtracting the measured from the corrected radii (for details see reference [26]).

Fits of DEER time traces based on eq. 3.1.1 yield the distance distribution of FS on the cylindrical surface formed by the dendronized polymers (see Figure 3.1.2 b)). The two essential fitting parameters are the radius (diameter) of the cylinder, R_{DEER}, and the length L. In line with the expected persistence lengths, all values for L in the fits amount to ~7 nm. This distance can be regarded as the upper limit of the presented DEER experiments, as these are limited by the length of the recorded time traces. In return, this indicates that on DEER-length scales denpols essentially behave as stiff rods. The most probable distance R_{DEER} of $P(r)$, after correction of the finite size of the probes and their thermal motion (see below), corresponds to the diameter of the effective cylinder and hence to the approximate thickness of the denpols, too. Note that for size-diameter determination it is not necessary that the surface of the denpols is completely covered with FS ions. With a concentration of positive charges of 28.8 mM (corresponding to 1 wt% de-PG4) and 4 mM negative charges of FS in the solution, at maximum 13.8 % of the denpol charges can be covered with FS. However, since the contact of FS with the surface denpol is transient and only a fraction of FS is bound to the denpol surface at a given moment of time. A statistical distribution and hence a detectable mean value of distances between spin probes in every direction on the surface is nonetheless sufficient to extrapolate and extract the size information from DEER time traces by eq. 3.1.1. The obtained (corrected) denpol radii are graphically depicted in Figure 3.1.3 and listed in Table 3.1.1 together with the radii determined on basis of the AFM tapping heights (R_{AFM}) from denpols with protected terminal amines on mica.[3] The latter can be considered the radii of the neutral denpol analogues in the solid state since the samples are dried on a mica surface during the preparation process. Some phenomena that might influence data gained by AFM and DEER should be noted: 1) AFM is known to underestimate heights of objects on surfaces. 2) DEER measurements are based on electrostatic self-assembly of FS hence one has to take into account that not all of the spin probes are fixed to the surface of the cylinders. Thermal motion leads to a radial distribution of spin probes in the electrostatic potential around the cylinder.[18] Therefore, the radii of the denpols as determined from the DEER time traces are expected to be shifted to larger values. One can correct for these effects by determining the distance distribution of the FS anions at the surface of the polycations (see reference [26]). This correction is based on the non-linear Poisson-Boltzmann equation.

Recall that for DEER the minimally detectable distance r_{min} depends on the pump-pulse length τ_p. For τ_p = 12 ns, r_{min}≈1.6 nm (uncorrected) can be estimated,[27] which is in good agreement with ear-

lier experimental findings[28] and the lower distance bound determined by the cylinder model presented in this study (R_{DEER} = 0.8 nm, which corresponds to a distance of 1.6 nm). The limited excitation bandwidth of the DEER pump pulse precludes the detection of short distances between two spins. This explains why R_{DEER} appears to be equal for generation 1 and 2, although the modulation depth differs significantly.

Self-backfolding and 3D network formation has been reported for charged dendronized polymers,[29] which could also lead to aberrations of R_{DEER} from the actual solution radius of the molecules. However, no indications for such phenomena were found during the investigations as fitting the data to bimodal distributions always yields results similar to fitting to monomodal distribution. These cautioning words notwithstanding, R_{DEER} can be expected to represent a good approximation of the actual radii of the dendronized polymers in solution.[3]

To further test the reliability of the used model DEER on mixtures of de-PG2 and de-PG4 was performed. The data were fitted with a bimodal distribution based on two cylinders. The time trace is shown in Figure 3.1.2 a), the distance distribution is shown red in Figure 3.1.2 b). The (uncorrected) radius obtained for de-PG2 is 1.2 nm and for de-PG4 2.4 nm. These values are in good agreement with radii determined from samples containing only the respective individual denpols. The mixture contained equal masses of both of the denpols. Such, 45 % of the ammonium groups present in the system belong to de-PG4 and 55% to de-PG2. 44% of the distribution in Figure 3.1.2 b) can be traced back to FS on the surface of de-PG2, while 56% stem from FS on de-PG4. Taking into account that the surface charge density of de-PG2 is smaller compared to de-PG4 on can deduce that the de-PG2 - FS attraction is also weaker than that between de-PG4 and FS. Thus, the experimentally determined fractions are in good agreement with the physico-chemical expectations. Hence, it is reasonable to assume that a cylindrical shell model is robust and appropriate for analyzing the distribution of molecules on the surface of dendronized polymers and for determining the radius of a particular denpol generation.

Both, R_{DEER} and R_{AFM} increase with increasing denpol generation (cf. Table 3.1.1 and Figure 3.1.3). The solid-state radii of the generation 1 and 2 denpols fall short of the corresponding solution radii, because of the insensitivity of DEER to low distances. Furthermore, the exceptionally small solid state radius of only 0.2 nm for PG1 might indicate some significant contraction on mica. For generations 3 and 4, R_{DEER}/R_{AFM} approaches unity, i.e., the radius in solution approaches that of the solid state. This finding suggests that highly derivatized and branched denpols in solution may be regarded as molecular objects. While the term molecular object has been discussed in the context of a generation 5 denpol,[3] the data shown here substantiate that even the charged, lower generations, de-PG3 and de-PG4, fulfill the requirements of this concept. Apparently, steric and electrostatic repulsion between monomer units inhibits a change in structure or compaction upon drying. For generations of charged denpols >3 the molecules are apparently forced into an expanded conformational state.

3.2 Loading and Release Capabilities of Charged Dendronized Polymers.

Higher generations of charged denpols adopt expanded, shape-persistent conformations in solution. This property gives rise to large internal cavities inside the denpols due to “free” space in their dendritic architecture.[7] Hence, a large loading capacity for small guest molecules can be expected. The present section therefore addresses the internal packing of denpols with small amphiphilic spin

probes. In this context it should be noted that the monomeric precursors of denpols, dendrons, constitute a well-studied class of hosting structures. They have the ability to host and selectively release guest molecules upon external stimuli.[30, 31] A prominent early example is Meijer's "particle in the dendritic box" from 1994.[32, 33] Spherical dendrimers with peripheral amino acid units are loaded up with either the EPR probe 3-carboxy proxyl or with dye molecules such as Rose Bengal, which can selectively be liberated. (For selected other approaches see references [34-45]). The loading capacity was determined by EPR and UV spectroscopy, respectively. It remained unclarified, however, where inside the dendrimers the guest molecules were located. Particularly, it could not be excluded that they would preferentially be positioned in the outermost shell. In contrast to dendrons, the loading capacity of denpols and their applicability for molecular transport has only just begun to be investigated.[46] Yet, such endeavors are of interest because there is a growing need for host-guest complexes between macromolecular host systems and small amphiphilic guest molecules, due to many potential applications in targeted delivery, polymer therapeutics, molecular sensing etc.[47-49] In this respect, denpols may feature promising properties. Due to the enormous sterical crowding of the side-group dendrons, the generation-dependent and tunable thickness of denpols should allow for adjusting the capability to incorporate guests. Controlling factors include the total available volume (free space between dendron branches) in the guest swollen state and Flory's χ parameter between guest and host.[2] Because of a linear dependence of the maximum diameter of denpols on generation and an exponential dependence of the density on generation,[50] there is no simple prediction of the loading capacity of denpols for different generations. It may well be that the capacity passes through a maximum. A further complication is that the highly branched structure of denpols could result in a steric barrier towards uptake of molecules with shapes that do not fit into the interior whereas other structurally more compatible molecules may well be incorporated even if they happen to have a higher molar mass. Because of their potentially enormous interior, the term 'nanocontainer' has already been applied to denpols. [51, 52]

In Section 3.1 the size and phase behavior of denpols has been assessed through *site-directive spin-probing* by measuring interactions of self-assembled guest molecules on the surface of a denpol. This approach will be expanded in this section. CW EPR and DEER, both in combination with site-directive spin-probing,[26] is performed on two isotope-labeled nitroxide probes, ^{15}N-Fremy's salt and ^{14}N-DSA (4,4-dimethyl-oxazolidine-N-oxyl stearic acid; see Figure 3.2.1 and Chart 1.2.1), to characterize and quantify the uptake of the DSA fatty acid derivatives into peripherally charged denpols of different generations. Fatty acids are well suited model compounds for amphiphilic guest molecules. They will be shown to be incorporated into denpols like they are into biological membranes. This is a consequence of the denpols constitution with a charged periphery that surrounds an interior of hydrophobic organic dendrons. That is to say, the denpols' topology resembles the constitution of, e.g., vesicles of phospholipids, where the charged phosphate groups surround an assembly of alkyl chains. In this regard, the charged denpols thus act as artificial, membrane-mimicking objects.

3.2.1 CW EPR - Incorporation of DSA into Denpols

When the nitroxide spin-labeled fatty acid DSA (see Figure 3.2.1), is added to aqueous denpol solutions, CW EPR can be employed to detect the uptake of this probe by the denpols, since the incorporation/binding leads to changes in rotational motion of the fatty acids and in the polarity of their environment.[53, 54] Here two types of DSA derivatives are used: 5-DSA, where the spin label is attached close to the carboxylate head group of the stearic acid and 16-DSA, where the spin label is located at the end of the hydrophobic tail (see Figure 3.2.1 a)). Since CW EPR is an intrinsically local

magnetic resonance technique, one can exclusively monitor the head or the tail environment of DSA by varying the labeling position. Spectral simulations were employed to yield a) the exact hyperfine tensors of the spin Hamiltonian and b) the rotational correlation time of the spin labels.[54, 55] The corresponding spectra for solutions of de-PG1-4 (1 wt %) containing 1 mM DSA are shown in Figure 3.2.1 b) and c) (the ratios of DSA molecules to denpol-monomeric units in these solutions are: de-PG1: 0.06 / de-PG2: 0.13 / de-PG3: 0.27 / de-PG4: 0.56).

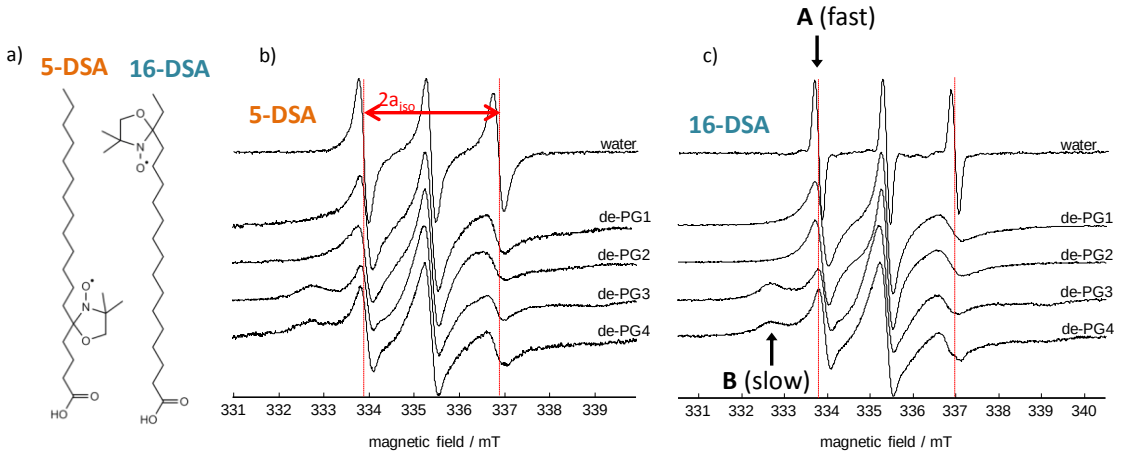

Figure 3.2.1. a) Molecular structures of 5-DSA and 16-DSA (carrying a DOXYL spin label at different positions along the alkyl chain). b) CW EPR spectra of 5-DSA, in presence of 4 different generations of denpols, and free 5-DSA in water (top). The dashed red lines indicate twice the isotropic hyperfine coupling between the ^{14}N nucleus and the electron spin of the DOXYL group. c) CW EPR spectra of 16-DSA in presence of the different denpol generations and free 16-DSA in water (top). A and B indicate prominent features of the spectral contributions of the two types of DSA (see text for details).

When DSA is dissolved in the presence of denpols of any generation, one notices a clear-cut decrease of τ_c, compared to the free spin probe in water, giving rise to asymmetric CW EPR spectra (see spectral component A in Figure 3.2.1 b) and c)). This indicates a restricted mobility and a strong interaction of DSA with the denpols and is in good agreement with earlier studies on DSA binding to macromolecules.[53, 56, 57] When either de-PG3 or de-PG4 are co-dissolved with DSA, two distinct spectral components are detectable for both (5-, 16-) labeling positions. Besides the asymmetric component A**,** present also in the de-PG1 and de-PG2, a more slowly rotating spectral component B becomes apparent. Note that the clear spectral separation between the two species indicates that there are two distinct DSA species, which both feature significantly slower rotational motion than freely dissolved DSA. In the following the more prominent species, A, will be discussed first and species B afterwards.

From CW EPR one can infer that out of 1 mM all of the DSA probes interact with 1 wt% denpols in aqueous solution, since no freely rotating DSA in aqueous environment is detected (see Section 3.2.3; for other of DSA/denpol ratios). To test if the bound spin probes are indeed located inside the denpols and are not just dispersed on their surface (only this justifies the notion 'loading of denpols') one needs to inspect their hfc constants (a_{iso}). Concerning species A these are significantly smaller for solutions of DSA and denpols than for DSA in neat water. This indicates a hydrophobic environment of the DOXYL reporter groups (see Appendix Figure A3.2.6) in the presence of denpols. The simplest explanation for this is a hydrophobic interaction with the side-groups scaffoldings of the denpols. Since the denpols in solution are shape-persistent molecular objects (as shown in the previous section)[26] one can think of the DSA molecules as being stuck inside the cylinder defined by the denpols' charged envelope.[58]

The hfc values of the DSA species A decrease with increasing denpol generation (see Appendix Table A3.2.2 and Figure A3.2.6), indicating that the water accessibility of the hydrophobic backbone of de-PGs decreases with rising generation. The experienced environmental polarity[59] is lower for 5-DSA than for 16-DSA for all generations smaller than four. At G = 4 hfc values for both, 5-DSA and 16-DSA are similar and resemble pentane solutions. Note that there are conflicting views concerning radial density profile of denpols. One report sees a density increase with growing distance from the polymer backbone,[60] while another, more recent molecular dynamics study in vacuum arrives at a constant profile, which is caused by backfoldings.[61] This report states that a more or less constant inner density results from backfoldings, because water is a poor solvent for the strongly hydrophobic interior of the denpols PG1-4. However, taking also the ammonium layer of de-PG1-4 into account, an equilibrium between electrostatic forces expanding the denpols and forces leading to their collapse would appear as structuring principle. In agreement with the results from Section 3.1,[26] this may also lead to shape persistence. In line with the assumed electrostatic expansion, the DSA hfcs and τ_cs here suggest a slightly increasing polymer density with increasing radial distance. Certain backfolding cannot be excluded. Nonetheless, an ordered incorporation of the fatty acids into the denpols can be deduced from the monotone generation-dependence of the spectral parameters.

Intuitively, the incorporation of DSA into denpols could be similar to the incorporation of fatty acids into layers of ionic surfactants or phospholipids: the polar carboxy group of DSA points towards the charged surface of the layer and the hydrophobic tail of DSA is arranged along the internal hydrophobic scaffolding.[57, 58, 62] It is commonly acknowledged that fatty acids in such a layer are relatively mobile.[63, 64] Judging from the still relatively small τ_c-values (relatively high rotational mobility, but still slower dynamics than free DSA), the same conclusion can be drawn for the DSA-species A here (see Figure 3.2.1 and Appendix A3.2.6).[65] τ_c of 5-DSA increases steadily from 9.5 ns to 12.5 ns with generation, while it decreases steadily from 10.0 ns to 6.25 ns for 16-DSA. These values are in good agreement with the picture drawn above: The binding of the carboxylate terminus leads to a slow-down of the 5-DSA-DOXYL group's local rotational mobility and the effect increases with the bulkiness at the ammonium layer. The 16-DSA probes gain mobility as the denpols size increases leading to more internal free space. Also the tendency of collapse of the interior is increasingly counteracted by the growing electrostatic repulsion among the ammonium head groups.

In contrast to DSA species A, the more immobilized DSA species B, which occurs in the spectra of de-PG3- and 4-containing samples, is stronger immobilized. Since there is no exchange between both species observable on the EPR time scale of 10^{-5} - 10^{-9} s, one can safely state that there are two distinct, long-lived types of binding modes of DSA inside the higher-generation denpols. Unfortunately, it is very difficult to gain precise hfc values for the slow species B from spectral simulations of the room temperature two-component CW EPR spectra (at X-band frequencies in the slow tumbling regime) due to effects of rotational anisotropy on the line shape. Yet, DSA species B can be approximated with the same hyperfine tensor as used for the spectral simulation of species A. Only τ_c needs to be longer. The simulated hf tensor might, however, not coincide precisely with the actual hyperfine interaction of species B. Several effects, which could explain the slower rotation species B, such as bending of the alkyl chains of DSA or an inhomogeneous distribution of DSA inside the higher generation denpols cannot be ruled out. Yet, the sum of all information obtained from CW EPR allows for the deduction of one likely explanation: Species B only occurs in high-generation denpols and can be simulated with the same hfc- and g-values as species A. In addition, with increasing DSA content of the solutions its spectral contribution increases relative to the contribution of species A (see Appendix Figures A3.2.4 and A3.2.5 for all CW EPR spectra). Thus, it is reasonable to assume that in de-PG3 and 4 a second type of "binding site" can be occupied by DSA, probably as a conse-

quence of the crowded ammonium groups. In this scenario a partially denser packing of DSA inside the denpols would lead to the slow-down in rotation of the DOXYL-labels of species B. Further, it cannot be detected when DSA is neutralized through methylation (see Appendix Figure A3.2.12 for the CW EPR spectra). This indicates that species B depends, like A, on electrostatic binding of the DSA carboxylate group to the denpols' ammonium layer. Concluding, it is likely that species A as well as species B are bound in a similar way to de-PG3 and 4, differing only in packing or scaffolding density. (Note that methylated DSA is still incorporated in sizeable amounts into the denpols indicating that the binding is primarily of a hydrophobic nature. Yet, a deprotected carboxylate group of DSA might be crucial for an ordered orientation of the probes.)

3.2.2 MISS-DEER - Assembly and Orientation of DSA in Denpols

To gain deeper insights into the arrangement of DSA within the denpols, an effective DEER-based method was developed to characterize the separation of the DOXYL reporter groups from the charged surface of the denpols.

DEER is employed in an unusual manner here. It is combined with spin probing and selective isotope labeling.[26, 66-69] The main aim is to test the hypothesis that DSA species A and B are incorporated into denpols like fatty acids are incorporated into layers of ionic surfactants or liposomes. To this end, mixtures of ^{14}N and ^{15}N isotope-labeled nitroxides are used, which are spectrally well separated. Besides spectral selectivity, one achieves spatial selectivity as the different isotope-labeled nitroxides are located at different regions of a denpol: FS is exclusively assembled on the denpol surface and DSA exclusively in the denpol interior. Such a distinction of nanoscopic interior and exterior is an intrinsic property of molecular objects, since their definition implies a well-defined envelope and solvent interface. DEER measurements between ^{15}N-FS self-assembled on the cylindrical surface of the denpols (cf. Section 3.1) and ^{14}N-DSA incorporated into their interior, allows for selectively detecting the distance between the two NO isotopologues. This approach is called MISS-DEER (mixed isotopologues for spectral separation).[70] It is inspired by Jeschke and co-workers who have already applied isotopologue-selective DEER in a different manner. They provide methods for separating ^{14}N-^{14}N from ^{15}N-^{15}N-distances in mixtures of ^{14}N-^{14}N and ^{15}N-^{15}N labeled bi-radicals and in the outlook of their paper suggest the use of mixed-isotopologue samples for DEER.[69] A further, similar approach was presented by Grotz et al. The authors detected DEER signals due to a single nitrogen vacancy in a diamond and external TEMPO molecules.[71] Note that for the determination of the guest molecule concentration and distribution in spherical micelles other DEER-based techniques than MISS-DEER might be superior.[72-75]

For the present study de-PG4 was chosen as model host. It was tested first that the incorporation of DSA into this denpol is not significantly affected by the FS spin probes on its surface (see section 3.1 and Appendix Figure A3.2.8). From the CW EPR spectra one can deduce that no large-scale rearrangement of the guests takes place (and in return that FS still electrostatically binds to the denpols). Yet, it cannot be excluded that electrostatic screening of the ammonium layer by FS will lead to a slightly different binding mode of DSA. In particular, it is expected that FS and the carboxylate group of DSA avoid each other at the surface due to like charges and consequently a slightly denser packing of DSA at the central longitudinal axis of the denpols may arise. For 16-DSA FS actually leads to a broader line width in the ESE spectrum of the mixture than in the spectra of the single components (see Appendix Figure A3.2.2).

Nevertheless, due to the combination of slightly different hyperfine and electron Zeeman (g-) values of FS and DSA and the selective isotope labeling, the ^{14}N- and ^{15}N-based nitroxides can in any case

spectroscopically be well addressed separately (by microwave pulses) even if both species are present in the system (see Figure 3.2.2 a) and Appendix Figure A3.2.2). Pumping the FS spins on the surface of the cylindrical denpol and observing the subsequent effect on the DSA probes by MISS-DEER yields the ^{15}N-^{14}N (FS-DSA) coupling. Note that due to the lower distance boundary of the DEER of ~1.6 nm (see section 3.1.1) measurements with de-PG3 or lower generations cannot reliably be analyzed since already the de-PG3 diameter is only approx. 2 nm.[68],[76] Possible contributions of ^{14}N-^{14}N (DSA-DSA) couplings to the MISS-DEER data were eliminated by dividing the original experimental time traces by time traces obtained from reference measurements, to yield contributions exclusively from ^{14}N-^{15}N dipolar coupling. The procedure is explained in detail in Appendix A3.2.6. The background-corrected, ^{14}N-^{15}N dipolar evolution of the spin echo intensity is depicted in Figure 3.2.2 b).

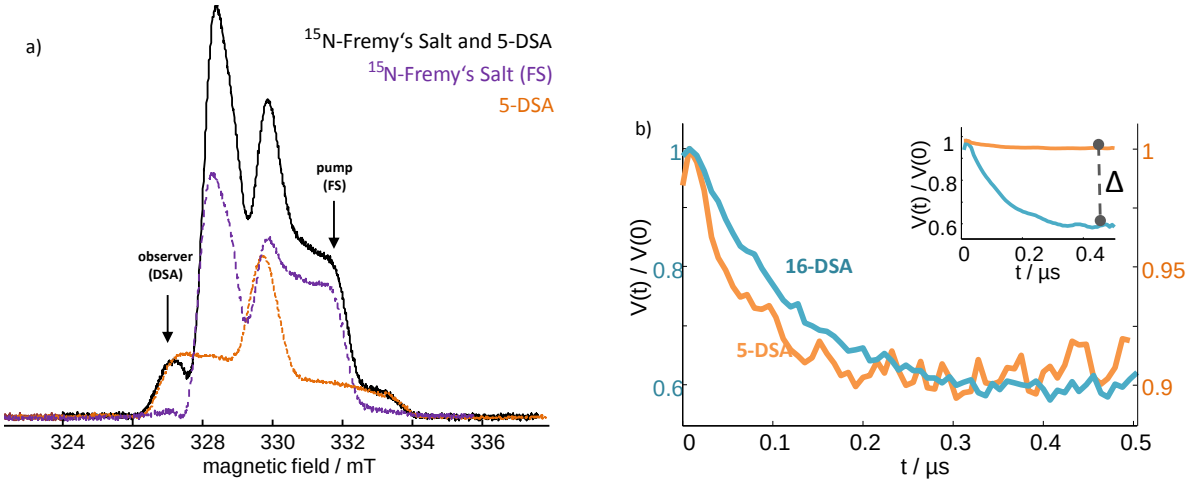

Figure 3.2.2. a) ESE-detected field-swept spectra of ^{15}N-FS, (^{14}N-)5-DSA and their mixture self-assembled with de-PG4. The field position of the observer pulse in the MISS-DEER experiment and the field position of the pump-pulse are marked with arrows. b) Normalized and long pass-filtered MISS-DEER time traces, V(t), based on the dipolar coupling between ^{15}N-FS and ^{14}N-5-DSA (orange) or ^{14}N-16-DSA (blue). Note the different scales for the 5- and 16-DSA trace. The inset at the top shows the unscaled traces. 5-DSA exhibits a significantly smaller modulation depth.

The faster initial decay of the re-normalized 5-DSA trace in Figure 3.2.2 b), compared to the 16-DSA trace, indicates shorter distances from the ^{15}N-FS-probes to the labeling site of 5-DSA than to the labeling site of 16-DSA. Yet, it will here be refrained from a more detailed analysis of the time domain data or the ensuing distance distributions. The analysis simply focuses on the fact that there is a striking difference in modulation depth between the two time traces: FS-16-DSA: 0.4, FS-5-DSA: < 0.1. This difference is a clear indication for an arrangement of DSA in higher generation denpols that resembles the schematic view depicted in Figure 3.2.3 (reminiscent of the fatty-acid incorporation into membranes). Remember that the lower distance boundary of the MISS-DEER experiments is 1.6 nm.[26, 68] The average distance between FS in the periphery of de-PG4 and the surface layer of de-PG4 is around 0.34 nm, as is shown in reference [26]. The maximum distance from the carboxylate group of 5-DSA to the unpaired electron spin of 5-DSA is approx. 0.7 nm, as derived from simple structural considerations. For 16-DSA the maximal distance between spin and the terminal carboxylate group is approx. 1.9 nm. Since 0.34 nm + 0.7 nm < 1.6 nm, the above derived membrane analogy is fully supported by the MISS-DEER data: It is likely that a considerable number of spins does not contribute to the overall DEER signal in the case of 5-DSA since the head group of DSA is close to the FS layer on the surface of the denpols. This causes the small modulation depth. In contrast for 16-DSA, the distance between the FS layer and the DOXYL group is long enough such that contribu-

tions to the MISS-DEER time traces are not suppressed (always assuming that the stearic acids are fully extended). This leads to the higher modulation depth.

Hence, from the design of the MISS-DEER experiment and from the much smaller Δ for 5-DSA than for 16-DSA one can deduce in a binary manner (FS-DOXYL distance <1.6 nm or >1.6nm) that a significant part of the DSA-probes is incorporated with the carboxylate group towards the charged ammonium surface of the denpols and with their hydrophobic tail towards the interior. This is in agreement with the intuitive picture that there is an attraction between the polar, anionic carboxylate group of DSA and the cationic ammonium layer of the denpols and that the hydrophobic tail of DSA associates with the dendron side chains of the denpols.

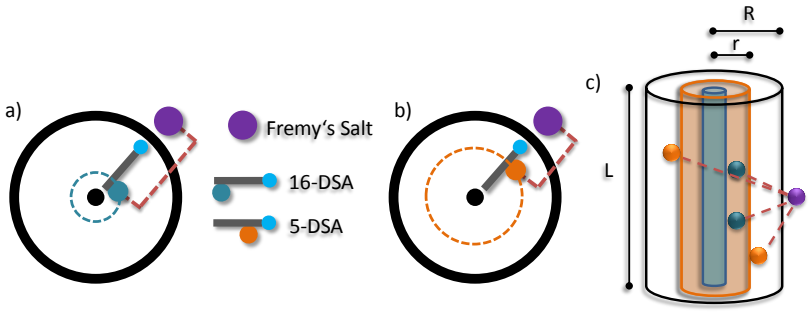

Figure 3.2.3. Suggested incorporation of a) 16-DSA and b) 5-DSA into the denpol cross-section (indicated by the black circle) as well as a three dimensional model (c)). The blue and orange spots indicate the positions of the 5- and 16-DSA-DOXYL groups (contained cylinders of radius r), the violet ones the location of ^{15}N-FS on the surface of the cylinder (radius R) and the light blue ones mark the carboxylate groups of DSA. The distance/dipolar coupling between the ^{14}N and the ^{15}N-bearing nitroxides detected by DEER is indicated by the dashed, red lines. Note that the indicated coupling sketched in a) and b) represents the shortest possible distance.

It should be noted that effects due to spectral orientation selection could play a role, too. The orientations excited by the applied pump and observer pulses are similar for both cases (see Appendix Figure A3.2.3). Such, in terms of orientation selection alone, the difference in modulation depth could only derive from preferred orientations of the labels with respect to the magnetic field. This certainly is possible. The DOXYL group of 5-DSA could have a slight yet particular preference for certain orientations with respect to the peripheral ammonium layer of de-PG4[73] while this may not be the case for 16-DSA. In such a case, the relative number of coupled DSA spins excited by ^{15}N-FS-spins would be smaller for 5-DSA than for 16-DSA. However, the difference in rotational mobility, which can be regarded as an indirect measure for the number of populated orientations of a spin-probe, between 5- and 16-DSA is not very high ($\tau_{c,5\text{-DSA}}$ = 12.50 ns / $\tau_{c,16\text{-DSA}}$ = 6.25 ns). Thus, it is unlikely that orientation selection is responsible for the large difference in modulation-depth, depicted in Figure 3.2.2 b), even if upon freeze quenching well defined orientational relations are overpopulated. Furthermore, even for strong orientation selectivity only very weak effects on the modulation depth are expected at X-band frequencies.[77]

However, one cannot claim for sure that all of the probes are arranged as described above, since it remains unsolved if the sketched arrangement is true for both DSA species, A and B. A heterogeneous distribution of DSA inside de-PG3 and 4 might as well be possible. But, as argued above, a similar arrangement for species A and B, differing only in packing density, should be considered to be most likely.

It should furthermore be noted that in fact an arrangement as shown in Figure 3.2.3 is unlikely for lower-generation denpols (de-PG1 and 2) since their radii are simply not large enough. Yet, judging from the hfc value (Section 3.2.1) and the rotational correlation times it is plausible to assume that the carboxylate group is still attached to the ammonium layer of the denpols and that the tail is surrounded by the hydrophobic denpol scaffolding. However, the exact alignment in lower generation denpols remains elusive and is probably more complicated than for higher generation denpols.

3.2.3 Determination of Loading Capacities

The maximum amount of DSA that can be loaded into the different generations of denpols can be quantified since increasing the ratio DSA / denpol leads to the detection of free, quickly rotating DSA probes in the system above a certain DSA concentration. This point can be determined by CW EPR and spectral simulations. As long as no free DSA species is needed to simulate a CW EPR spectrum at a certain ratio of DSA to denpol monomer concentration one can safely assume that DSA is quantitatively incorporated into the respective denpol. The determined loading capacity increases – as expected – with rising generation, since the space available for incorporation of DSA in the organic interior of the denpols becomes larger. Anticipating the loading capacity of a denpol is complicated since different types of guest molecules may exhibit drastically different modes of incorporation. In fact, maxima of uptake capacities may be reached at different generations. Here, the maximum loading that was achieved with fatty acid derivatives here exceeds 2.20 DSA molecules per de-PG4 repeat unit (which only corresponds to a ~15% increase in mass: 5651 g/mol of a denpol-monomer unit vs. 2.2 · 384.5 g/mol = 845.9 g/mol DSA). For the other three generations one obtains: de-PG1: > 0.06, de-PG2: > 0.26, de-PG3: > 0.57 DSA molecules per repeat unit (see Appendix A3.2.3 for details on the determination of this values and Figures A3.2.4 and A3.2.5). Hence, the loading capacity of the charged dendronized polymers used in this study seems to increase exponentially with the denpol generation. It seems reasonable that with increasing generation also the number of binding or intercalation sites for DSA increases exponentially together with the number of ammonium groups of the denpol monomers. The loading capacity as a function of the denpol generation G, Φ(G), increases as exp(λG) and with λ = 1.27 (red diamonds and line in Figure 3.2.4). Using the denpol radii, as determined by AFM tapping heights, to estimate the denpol volume,[51] a linear relation between Φ(G) and the cylinder volume can be found. This is shown in Appendix Figure A3.2.7. Both, loading capacity and the denpols volume increase faster than 2^G and remarkably similar with generation (Figure 3.2.4*,* red and blue diamonds and lines). Not taking the collapse or swelling of the denpol interior into account, one could assume that Φ is proportional to the denpol mass per repeat unit. In this case, Φ would be expected to asymptotically increase as exp(λG), with $\lambda \approx \ln(2) \approx 0.69$. Contrary to this expectation, one finds λ = 1.27, i.e., the capacity increases almost with the square of the exponential G-dependence that is predicted from monomer mass alone. In terms of functional groups, on average 0.029 carboxylate groups of DSA are bound to one ammonium group of de-PG1, 0.066 in the case of de-PG2, 0.068 in the case of de-PG3 and 0.139 in the case of de-PG4. Hence, approx. every seventh ammonium group of de-PG4 is connected to a DSA-probe. It appears that a rather specific interaction between the amphiphilic fatty acids and the hydrophobic interior as well as hydrophilic ammonium layer of the denpols facilitates the uptake of more than two fatty acids per de-PG4 repeat unit. This assumption is supported by data on the uptake of the hydrophobized probe molecules, methylated 16-DSA. This uncharged 16-DSA methyl ester can only be incorporated in every third monomer of de-PG4. Hence, the loading capacity is drastically reduced if the ligand lacks specific binding of the carboxylate moiety to the ammonium layer of the denpols (for all corresponding data see Appendix Figure A3.2.7 and 12).

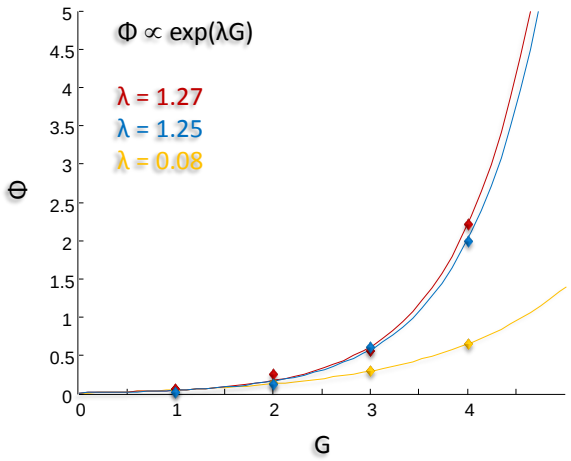

Figure 3.2.4. The loading capacity of DSA molecules per denpol-monomer, Φ, versus denpol generation, G. The experimentally determined values are marked as blue diamonds, values from AFM tapping heights of the uncharged denpol PG1-4 are marked as red diamonds and values calculated from the monomer mass of the different denpol generations are marked as yellow diamonds. The corresponding solid lines represent exponential fits to the data of the form exp(λG). The λ values are given at the top left.

3.2.4 Release of DSA

The peripheral ammonium layer of the denpols also opens a route towards release of the incorporated guest molecules. By increasing solution pH, the surface is charge-neutralized. This leads to less favorable hosting parameters and release of fatty acids from the host. As CW EPR studies show (see Appendix Figure A3.2.11), approximately 60 % of the DSA guests are released from the denpols when the pH is raised from 7 to 14. Co-dissolution of hydrophobic monovalent salt like the imidazolium-based ionic liquid BmimBF$_4$ (1-Butyl-3-methylimidazolium tetrafluoroborate) even leads to the release of more than 90 % of the guest molecules. These released DSA probes show the spectral signature of freely rotating DSA and are marked in Appendix Figure A3.2.11. A future use of denpols as molecular transporter therefore seems possible.

3.3 Load-Collapse-Release Cascades of Amphiphilic Guest Molecules in Charged Dendronized Polymers through Spatial Separation of Non-Covalent Forces

In Section 2.2 it was demonstrated how non-covalent interaction patterns between polyelectrolytes and multivalent counterions can appear as structuring principle in DNA condensation. These interaction patterns were shown to be influenced by solution conditions as temperature and ionic strength, allowing for control over condensate morphology and size. The concept of controlled polyelectrolyte condensation will here be expanded to denpols.

As shown in the Section 3.2, charged denpols are capable of hosting a very large number of guest molecules due to “free” space in their dendritic architecture.[7, 50, 51] This leads to dense guest molecule packing of one guest per ~1.5 nm^3.[78] This number reflects the pronounced molecular loading capacity of state-of-the-art polymeric host systems. Ever larger amounts of guest molecules concentrated in small volumes are especially desirable from a polymer therapeutics point of view, in order to render extensive drug transport with only small amounts of carrier molecules possible.[79] Thus, motivated by the aim of optimizing packing densities in molecular transporters a concept of a two-step packing technique is developed here. This technique in principle allows for transport of large drug amounts through body fluid within very small carrier volumes. In a first step the denpols are

loaded with guest molecules and in a second step controlled aggregation of the already loaded denpol hosts themselves is triggered. This yields mesoscopic vesicles of densely packed molecular carriers. This "packing sequence" is possible because higher generations of denpols can be considered molecular objects, as shown in Section 3.1.[4, 26, 51] This denpol feature allows for spatial separation of different types of non-covalent interactions: If the surface of a molecular object (a denpol) is charged, it gives rise to electrostatic interactions with external ionic species, which cannot breach the charged periphery (see Section 3.1). Simultaneously, the organic, internal dendron scaffolding can be subject to distinct hydrophobic interactions, well-separated from influences of electrostatic interaction with surrounding ions (see Section 3.2).[26] Thus, the charged, shape-persistent denpol envelope should allow for surface coordination of small multivalent ions and charge screening leading to controlled aggregation (as known from DNA condensation)[80] of the denpols, while their interior is separately loaded with other guest molecules through hydrophobic interaction. In the following, I will show that this "spatially separating non-covalent interactions"-approach can successfully be applied to denpol/amphiphile host-guest complexes. Such, controlled aggregation and mesoglobule formation of amphiphile-loaded denpols without drastically influencing the guest-denpol interaction is achieved.[81] This finally leads to the desired increase in local guest concentrations and by augmentation with release possibilities to a *load-collapse-release cascade.*

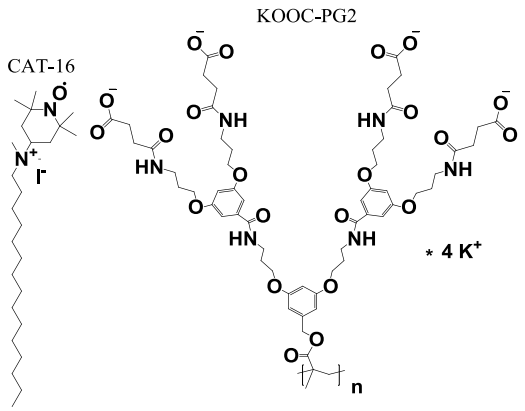

Figure 3.3.1. Chemical structure of KOOC-PG2 and CAT-16.

3.3.1 Results and Discussion

For the realization of a *load-collapse-release cascade* de-PG3 and an anionic generation 2 denpol, KOOC-PG2,[82] which is carboxylate-terminated (see Figure 3.3.1), were chosen as model compounds. For tracing incorporation of guest molecules in denpols and denpol aggregates, CW EPR on two spin-labeled amphiphiles was empolyed. Acidic 16-DSA, as introduced in Section 3.2, is used to load cationic de-PG3 – DSA binds primarily through hydrophobic interaction to the denpols, as evident from the data on methylated DSA (see Appendix A.3.2.6) – and cationic CAT-16 (4-(N, N-dimethyl-N-hexadecyl)amino-(2,2,6,6-Tetramethylpiperidin-1-yl)oxyl iodide) is used to study the loading of anionic KOOC-PG2 (see Figure 3.3.1). In principle fluorescence techniques could also allow for monitoring and following of guest compound incorporation into denpols, even on single-molecule level. Yet, rotational motions of a probe molecule on a sub-nanosecond time scale can easily be quantified by means of CW EPR.[83] Such, also minor environmental influences that do not strongly influence a probe's rotational mobility can be observed. Fluorescence probing techniques are in the majority of cases sensitive for the nanosecond time scale only.[84] For the exact elucidation of larger micellar configurations fluorescence spectroscopy might nonetheless be superior to CW EPR.[85]

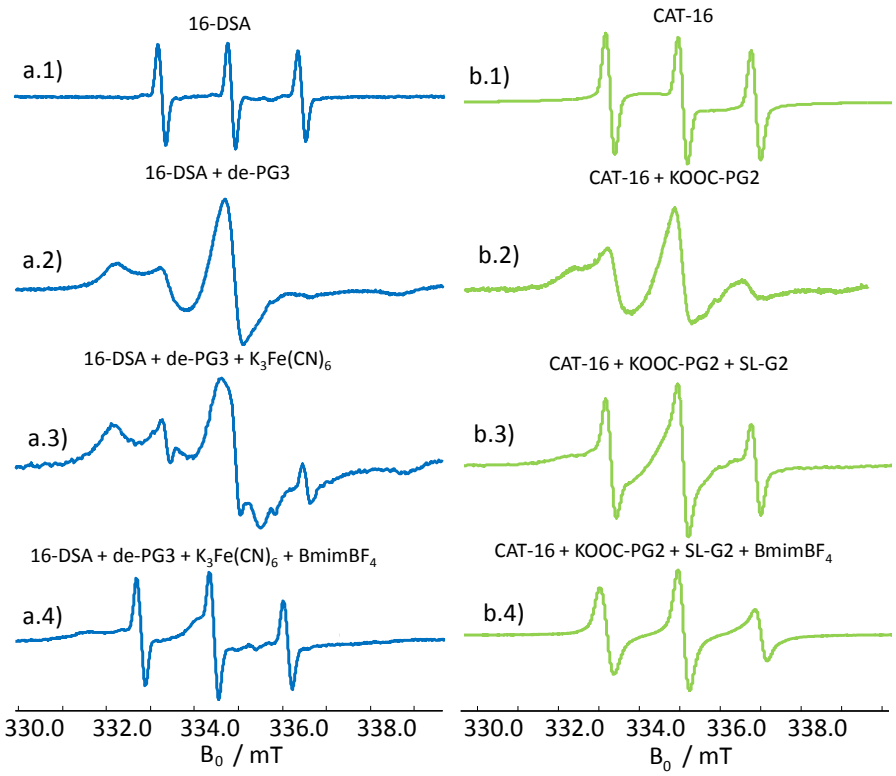

Figure 3.3.2. CW EPR monitoring of 1mM (a.1)) 16-DSA and (b.1)) CAT-16 spin probes in aqueous solution, and incorporated in 1 wt% de-PG3 (a.2)), and KOOC-PG2 (b.2)) respectively. Spectra for aggregation of de-PG3 by K_3FeCN_6 (a.3) and KOOC-PG2 by SL-G2 (b.3) at cr = 1 are also shown. Adding 20 v/v% of $BmimBF_4$ leads to almost quantitative release of the probes from their denpol hosts (a.4 and b.4). Note that if both, CAT-16 and SL-G2, are present in a system one nearly exclusively detects CAT-16 due to its much higher concentration.

If 10 mg/mL de-PG3 are added to 1 mM solutions of 16-DSA the probes are incorporated quantitatively by the denpols (see previous section). The same is true for 10 mg/mL KOOC-PG2 in 1 mM solutions of CAT-16. In both cases, free probes in aqueous environment (sharp lines; see Figure 3.3.2 a.1) and b.1)) cannot be detected by means of CW EPR (Figure 3.3.2 a.2) and b.2)). This indicates spontaneous uptake and high binding affinities between the amphiphiles and the denpols. Approx. every fourth dendron unit is loaded with an amphiphile at the concentrations used here. After quantitative probe uptake it is tested next whether multiple, simultaneous host-guest interactions can be exploited in charged denpols for an aggregation/condensation of already loaded denpols. This should lead to increased local guest concentrations.

Loading and Aggregation of de-PG3

The extended persistent structure of peripherally charged molecular objects like de-PG3 gives rise to a spatial separation of macromolecular regions in which different types of non-covalent forces are predominantly active. Ions in the surrounding solution only interact electrostatically with the charged surface of de-PG3 while guest compounds like 16-DSA interact predominantly with its internal hydrophobic scaffolding. Thus, electrostatic guest interactions on the surface are separated from internal hydrophobic interactions. Both types of host-guest interactions should not significantly interfere with each other. Concerning electrostatic interactions it was already shown in Section 3.1 that FS only transiently coordinates to de-PG3's surface.[26] To achieve permanent electrostatic binding of ions to the denpol's ammonium layer and permanent surface guest attachment the 3:1 electrolyte $K_3Fe(CN)_6$ was dissolved into solutions of 16-DSA-loaded de-PG3. The threefold charged $Fe(CN)_6^{3-}$ is expected to give rise to permanent surface coordination.[86] Assuming all of the ammonium groups to be charged at pH 7 and complete dissociation of $K_3Fe(CN)_6$, one finds at a charge

ratio (cr) of 0.5 (meaning that the total charge concentration for trivalent $Fe(CN)_6^{3-}$ is half the ammonium concentration) that TEM micrographs are identical to those of de-PG3 in the absence of $Fe(CN)_6^{3-}$ ions (see Figure 3.3.3 a), left and Appendix A3.2). Only after further increasing the K_3FeCN_6 concentration, to reach a cr of 1, one finds that de-PG3 forms mesoglobules (see Figure 3.3.3 a), center).[87]

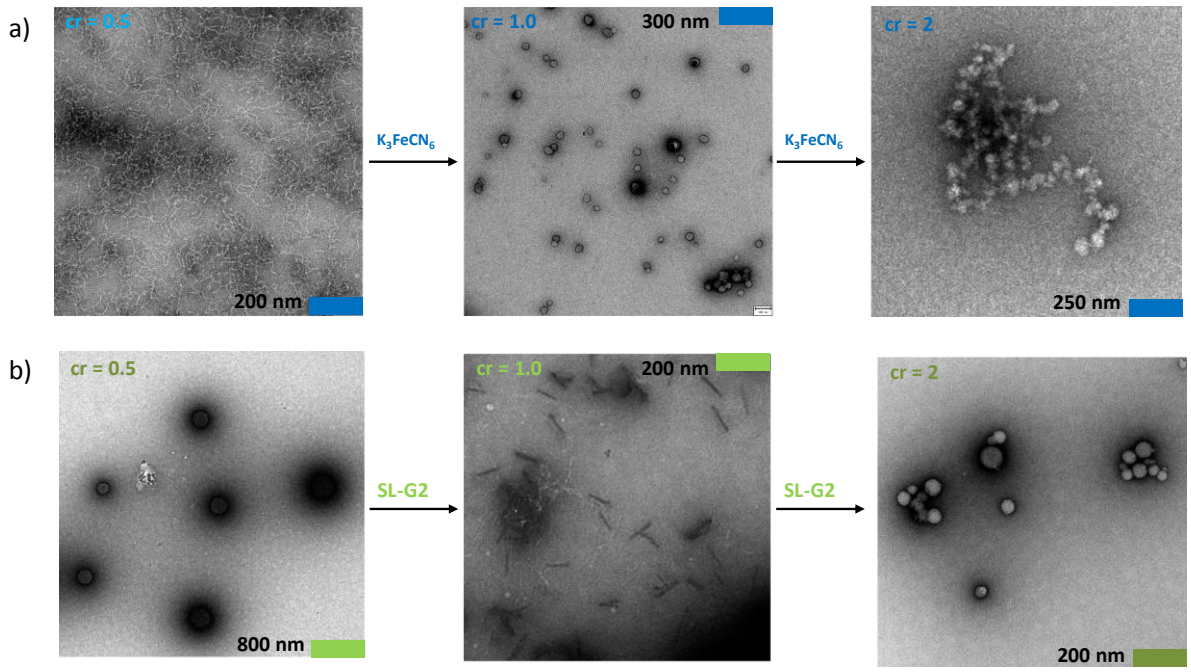

Figure 3.3.3. a) TEM micrographs of de-PG3 at different concentrations of $K_3Fe(CN)_6$. At cr = 0.5 stretched, linear structures are observed while at cr = 1 defined globular objects are formed. At cr = 2 pearl-necklace-type structures can be observed. b) TEM micrographs of KOOC-PG2 at different concentrations of SL-G2. At cr = 0.5 defined globules with varying radii appear. At cr = 1 rod-like condensates and at cr = 2 globules can be observed, which partially cluster in aggregates of several globules.

The screening of the positively charged surface layer of de-PG3 by counterion condensation of the multivalent anions leads to poor solvent conditions for the denpols and subsequently to their aggregation. Due to the restricted diameter of the mesoglobules of approx. 30 to 50 nm they are likely composed of approx. two densely packed denpol molecules, as judged from simple volume considerations. Note that de-PG3 can only be surely regarded as molecular objects in the non-condensed state since counterion condensation alters the surface charge density and reduces electrostatic repulsion between the dendron-side groups. Judging from the globular shape of the denpol aggregates, the formation of ion pairs is even likely to render denpols rather flexible. However, if the different non-covalent interactions are still spatially separated in a collapsed, non-molecular object state guest amphiphiles will remain incorporated in the aggregates and a loss in persistence length is of minor importance for the present purpose.

During the collapse and the aggregation of de-PG3 the 16-DSA probes remain largely bound in the denpols, as judged from the spectrum in Figure 3.3.2 a.3). Normalized signal double integrals yield spectral contributions of less than 3 % for the free and more than 97 % for the bound species. Thus, to a very large degree the 16-DSA probes remain inside the denpols during aggregation. Because of this, one may state that a “twofold packing” of the 16-DSA probes is possible with de-PG3; first by incorporation into the dendritic scaffolding of individual denpols and second by packing of the host structures themselves. The underlying physical reason for this is given by the different types of attractive interactions between de-PG3 and the two different guest molecules that are spatially sev-

ered and separately addressable. The interaction is mostly hydrophobic between 16-DSA and the denpol's interior and mostly electrostatic between $Fe(CN)_6^{3-}$ and the denpol's surface. Spatially separated from the former, only the latter interaction is responsible for triggering aggregation/condensation. Considering that approx. 0.25 DSA probes are bound per de-PG3 repetition unit (see Appendix A3.2.3 for details on the calculation) and that every polymer chain consists of approx. 1000 repeat units,[88] one can estimate that around 500 guest molecules can be incorporated into a 20 - 50 nm large mesoglobule of two denpols.

Table 3.3.1. Selected parameters of the system 16-DSA/de-PG3.

	16-DSA	**16-DSA/de-PG3**	**16-DSA/de-PG3/ K_3FeCN_6**
χ[a]	1.0	0.0	< 0.03
Aggregate Size	-	-	cr = 0.5: n/a cr = 1: 30-50 nm cr = 2: > 250 nm

[a] χ denotes the mole fraction of freely rotating 16-DSA.

If the concentration of $Fe(CN)_6^{3-}$ is further increased to a cr of 2 the mesoglobules aggregate to form larger structures as shown in Figure 3.3.3. a) on the right. Note that the aggregate morphology could be influenced by the drying process during TEM sample preparation. Thus, the different shapes and sizes depicted in Figure 3 generally might not exactly represent the wet state. However, for the present purpose, which is to show whether aggregates form or not, the TEM data in Figure 3.3.3 is sufficient and one can clearly discern between non-aggregated (Figure 3.3.3 a) left) and aggregated (Figure 3.3.3 a) center and right) states. Furthermore, despite drying effects the data allow for feasible approximations of the aggregate size with respect to the cr. No changes in the fraction of free guest molecules are observed when the cr is increased from 1 to 2. This observation can be traced back to the fact that in denpols electrostatic and hydrophobic interactions are spatially separated and that only the former is strongly affected by counterion condensation. Hence constant fractions of incorporated 16-DSA are expected since the fatty acid derivative binds primarily through hydrophobic interactions to the denpols (although electrostatics do play a certain role in orientation of DSA, as shown in the previous section).

Loading and Condensation of KOOC-PG2

Table 3.3.2. Selected parameters of the system CAT-16/KOOC-PG2.

	CAT-16	CAT-16/KOOC-PG2	**CAT-16/KOOC-PG2/SL-G2**
χ[a]	1.0	0.0	~0.5
Aggregate Size	-	-	cr = 0.5: 200-700 nm cr = 1: 60-150 nm cr = 2: 40-100 nm

[a] χ denotes the mole fraction of freely rotating 16-DSA.

In nature polyelectrolyte condensation/aggregation phenomena similar to the aggregation of de-PG3[89, 90] can be observed, too, e.g. in packing of DNA around histones.[91] In analogy to ds DNA, charged denpols also feature rather long persistence lengths[51] and high charge densities.[26] In Chapter 2 the investigation of interactions between positively charged spermine dendrons (SL-G2) and ds DNA was presented together with the morphologies of the solid-state structures of DNA

condensates that result from dendriplex formation.[92] Building on this, it is tested here whether the (like DNA) negatively charged denpol KOOC-PG2 exhibits condensation behavior comparable to DNA, due to similar charge and persistence length.

In analogy to Chapter 2 SL-G2 is used as condensation agent (see Figure 3.3.4 a)). Subsequent to quantitative incorporation of CAT-16 probes in every fourth dendron unit of KOOC-PG2 in aqueous solution (as monitored by CW EPR; see Figure 3.3.2 b.2)), SL-G2 is co-dissolved in order to coordinate to the denpol's carboxylate-surface layer.

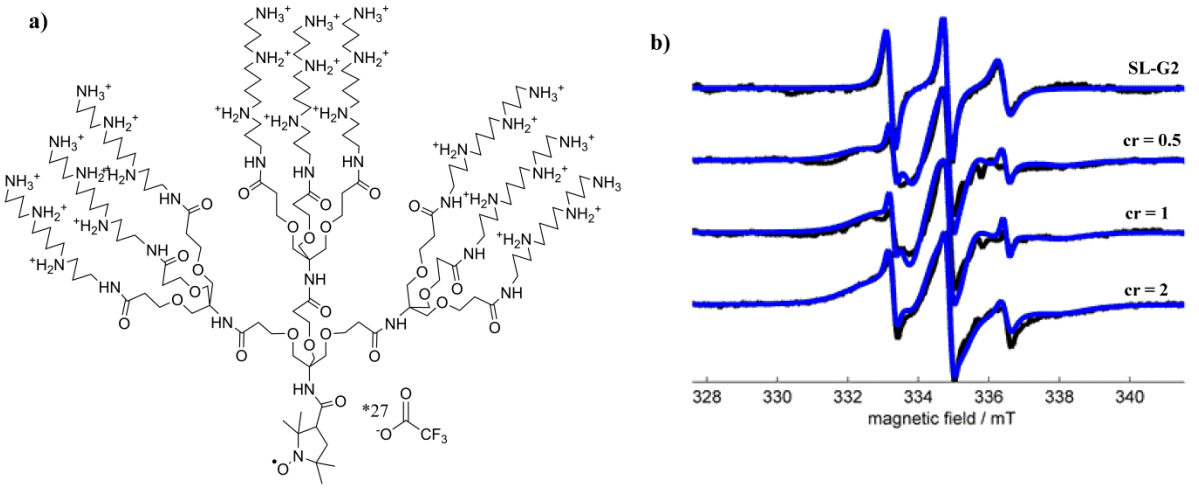

Figure 3.3.4. a) Molecular structure of SL-G2. b) CW-EPR of the free SL-G2 (top) and of SL-G2 and KOOC-PG2 at cr = 0.5, 1 and 2 at X-band (~9.4 GHz). As can be seen a large fraction of the SL-G2 dendrons give rise to very broad lines in the presence of KOOC-PG2, showing that SL-G2 binds to the dendronized polymer. From spectral simulations it can be deduced that spin exchange ferqeuncies increase continuously with increasing cr. Simulation parameters: **g** = [2.0089 2.0044 2.0029] for all species; **A** = [4.5 4.5 39.5] MHz for the fast, solvent exposed species and **A** = [4.5 4.5 38.5] MHz for the slow one. ω_{ex} = 0 MHz for cr = 0.5, $\omega_{ex} \approx$ 0.5 MHz for cr = 1 and $\omega_{ex} \approx$ 10 MHz for cr = 2.

In Figure 3.3.4 b) the CW EPR spectra of SL-G2 are shown for the unbound (top) and bound (cr = 0.5, 1 and 2) state are shown. From spectral simulations (superimposed in blue) one can extract that the spin exchange frequency, ω_{ex}, increases with rising cr. This indicates that the local concentration of SL-G2 increases, as expected, with the cr due to ever denser packing of condensation agents on the denpols' surface.[93] The consequently differing number of charge neutralized carboxylate groups leads to cr-dependent aggregate sizes of KOOC-PG2 dendriplexes. In the dry state TEM reveals that this system displays properties differing from those of the de-PG3/$Fe(CN)_6^{3-}$ system. Globules of diameters notably varying between approx. 200 nm and 700 nm exist already at cr = 0.5 (see Figure 3.3.3 b)). At cr = 1, rod-like structures with a length between ~60 nm and 150 nm can be observed. Their diameter is between ~20 nm and 40 nm. Recall that SL-G2 also leads to the formation of rod-like condensates through dendriplex formation with DNA (cf. Section 2.2.2).[92] Thus, KOOC-PG2 partly mimics the condensation behavior of DNA. In both cases SL-G2 complexes appear as rod-like structure in TEM micrographs – likely as a consequence of similarly high charge density and stiffness. It is noteworthy that the thickness of the KOOC-PG2/SL-G2 rods inversely scales with their length. Hence, short rods are thicker than long rods, which may indicate a 'back-folded' constitution. At cr = 2 smaller globular structures – with a diameter of ~40-100 nm – appear, which partially aggregate into bundles of three to ten globules (analogously, also complexation of ds DNA with SL-G2 leads to the formation of rod-like condensates only in a confined cr range).[92]

Although one needs to be cautious concerning aggregate morphologies derived from solid-state TEM, certain parallels between DNA- and KOOC-PG2-aggregates are nonetheless apparent. However, the appearance of rods of confined length and diameter from KOOC-PG2 solutions with SL-G2 at a cr of 1 is unexpected. Chains of denpols that are aligned in parallel are needed to form such types of condensates through electrostatic interaction between condensation agents and polyelectrolytes in solution. This is typically observed only for polyelectrolytes with persistence length longer than ~15 nm.[80, 94]

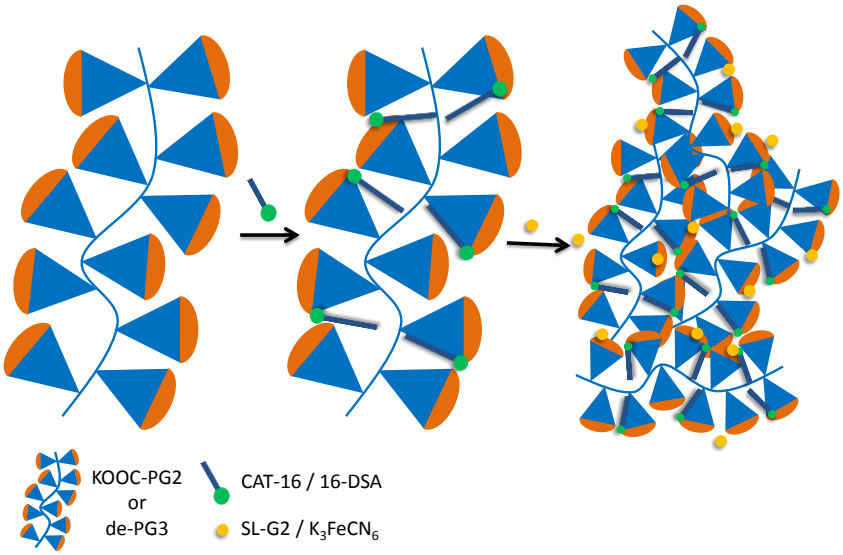

Figure 3.3.5. Schematic depiction of twofold packing of guest amphiphiles in denpol-based hosting structures. In the first step the amphiphiles (CAT-16/16-DSA) accumulate in the dendritic scaffolding of the denpols. In the second step the denpol hosting structures themselves cluster due to screening of the peripheral charge by multivalent counterions (SL-G2/$FeCN_6^{3-}$). The orange patches indicate the charged outer periphery of the denpols de-PG3 and KOOC-PG2. Note that the figure does not represent the release of CAT-16/16-DSA due to counterion condensation.

Release of Guest-Amphiphiles

For a host-guest system to be regarded as a possible candidate for molecular transport applications, the guest incorporation has to be reversible. In the present case guest release is possible through adding 20 v/v% of $BmimBF_4$ to the host-guest complexes. This yields nearly quantitative guest release – in accordance with the results from Section 3.2.4 – after incorporation into denpols and even after their counterion-induced aggregation (see Figure 3.3.2 a.4) and b.4)).[78] This observation can be explained as follows: Firstly, due to its amphiphilic character $BmimBF_4$ yields a very favorable environment for 16-DSA and CAT-16, such that solvation of the amphiphiles in the solvent mixture water/$BmimBF_4$ becomes favorable compared to denpol incorporation.[78] Secondly, $BmimBF_4$ can penetrate the dense layer of ammonium/carboxylate groups on the denpols' surfaces due to its charged and simultaneously apolar nature. Such, $BmimBF_4$ is able to screen attractive interactions between guest amphiphiles and a denpols at its periphery as well as in the dendritic interior. After adding $BmimBF_4$, the solutions still remain turbid, indicating that the denpol aggregates do not fully re-dissolve. Thus, a *load-collapse-release* cascade is realized with charged denpols. In Figure 3.3.5 the 'packing sequence' is schematically depicted that was realized for small amphiphilic guests in dendronized polymer-based hosting systems.

It should be noted that in the case of CAT-16 loading of KOOC-PG2 one observes a significant amount of the probes (about 50%, see Figure 3.3.2 b.3)) being released from the hosts already through SL-G2-coordination. This is not the case for 16-DSA and de-PG3. This can be explained when

assuming that the interaction between CAT-16 and KOOC-PG2 is based more on electrostatics than the interaction between 16-DSA and de-PG3.[78] Since the aggregation agents (SL-G2 and K_3FeCN_6) reduce the denpols' surface charge this leads to stronger destabilizing effects on the internal host guest interaction between CAT-16 and KOOC-PG2 than between 16-DSA and de-PG3. Thus, for the *load-collapse-release* cascade for very dense packing of guest compounds in molecular transport systems, the de-PG3/16-DSA system appears to be better suited than KOOC-PG2/CAT-16, since less guest molecules are released upon condensation.

For loading of de-PG3 with 16-DSA and subsequent aggregation through $Fe(CN)_6^{3-}$ one yields around $2 \cdot 10^3$ probes per μm^3, six fold the initial bulk concentration, as estimated from a globule radius of 50 nm and 500 guests per globule.

3.4 Summary

In Section 3.1 a simple geometrical model is presented to indirectly determine the thickness of a cylindrical nano-sized object in solution. This was achieved through analysis of the distribution of spin probes self-assembled in the electrostatic potential of the surface of a peripherally charged denpol. This approach leads to the manifestation of the idea of charged dendronized polymers (even as low as generation 3) as molecular objects with an environment-independent, persistent shape. In particular, DEER measurements showed that the size of ammonium-terminated denpols in solution becomes similar to the size in the solid state as the generation grows. In the special case of ammonium-terminated denpols addressed here, Fremy's salt as negatively charged spin probe could fortuitously be applied. A correction accounting for the thermal motion of the probe in the electrostatic potential is necessary, though. Spin labeling of the periphery still remains an option, although this approach may be comparably cumbersome with respect to both, time and costs. In addition, it is subject to the risk that the shape of the molecular object is actually changed by the probe or its linker. In conclusion, DEER in combination with site-directed spin probing is a fast and precise alternative for the determination of the size of nanoscopic objects in solution. [95, 96]

In Section 3.2 it is shown that not only the surface of denpols can be decorated with (FS) guest compounds. Dendronized polymers with a hydrophobic interior and a positively charged peripheral ammonium layer are also suited for internal incorporation of amphiphilic guest. To elucidate the orientation of the guest compounds a DEER experiment is developed in which different nitroxide isotopologues are selectively addressed (MISS-DEER). By exciting ^{15}N-Fremy's salt spin probes that self-assemble on the surface of the denpols and detecting the dipolar coupling to incorporated DSA guest molecules, additionally some light could be shed on the orientation of the DSA probes inside the denpols. Spin-labeled fatty acids are incorporated into the denpols in a specific way: The carboxylate group interacts with the outer charged shell of the cylindrical host while the hydrophobic tail aligns along the hydrophobic core. The DSA loading capacity of denpols as found from CW EPR scales exponentially with denpol generation. The highest generation denpol used, de-PG4, is able to incorporate approximately 2.2 DSA molecules per repeat unit. Thus, charged dendronized polymers appear as promising candidates for future applications in molecular transport. It remains to be seen which loading can be achieved with more hydrophobic guest molecules or higher generations than the currently available generation 5.[51]

Finally, in Section 3.3 external and internal host-guest interactions in de-PG3 and KOOC-PG2 denpols were combined to achieve a load-collapse-release cascade. Guest incorporation into denpols represents the first step of the realized packing cascade. The second step, a further increase in local

concentration of 16-DSA/CAT-16 can be accomplished if enough of the charges of the denpol hosts are screened by multivalent (Z > 2) ions that permanently attach to the denpols' surfaces. The guest-swollen denpols collapse from solution to form compact aggregates, as observable by TEM. Finally, in a third step nearly quantitative release of 16-DSA from de-PG3/$Fe(CN)_6^{3-}$ as well as of CAT-16 from KOOC-PG2/SL-G2 condensates can be triggered by increasing $BmimBF_4$ concentrations. The molecular object-like constitution of dendronized polymers allows for distinct simultaneous interaction with multiple binding partners due to spatially discernible non-covalent forces (peripheral electrostatics and internal hydrophobic interactions). Hence, these macromolecules represent versatile candidates for future transport applications not only because of their huge "empty" interior, but also because very dense, yet reversible, guest packing can be achieved.

References and Notes

[1] L. Shu, A. Schäfer, A. D. Schlüter, *Macromolecules* **2000**, *33*, 4321.

[2] M. Rubinstein, R. Colby, "*Polymer Physics*", Oxford University Press, New York, 2004.

[3] B. Zhang, R. Wepf, K. Fischer, M. Schmidt, S. Besse, P. Lindner, B. T. King, R. Sigel, P. Schurtenberger, Y. Talmon, a. et, *Angew. Chem. Int. Ed.* **2011**, *50*, 737.

[4] S. I. Stupp, S. Son, L. S. Li, H. C. Lin, M. Keser, *J. Am. Chem. Soc.* **1995**, *117*, 5212.

[5] M. J. N. Junk, H. W. Spiess, D. Hinderberger, *Angew. Chem. Int. Ed.* **2010**, *49*, 8755.

[6] Y. Guo, J. D. v. Beek, B. Zhang, M. Colussi, P. Walde, A. Zhang, M. Kröger, A. Halperin, A. D. Schlüter, *J. Am. Chem. Soc.* **2009**, *131*, 11841.

[7] A. D. Schlüter, J. P. Rabe, *Angew. Chem. Int. Ed.* **2000**, *39*, 864.

[8] L. Shu, A. D. Schlüter, *Macromolecules* **2000**, *201*, 239.

[9] W. Li, D. Wu, A. D. Schlüter, A. Zhang, *J. Poly. Sci. Part A* **2009**, *47*, 6630.

[10] J. Israelachvili, "*Intermolecular & Surface Forces*", Elsevier, London, 1991.

[11] Here molecular precision means thtat the exact position of every atom is known.

[12] A. Schweiger, G. Jeschke, "*Principles of pulse electron paramagnetic resonance*", Oxford University Press, New York, 2001.

[13] G. H. Bird, S. Pornsuwan, S. Saxena, C. E. Schafmeister, *ACS Nano* **2008**, *2*, 1857.

[14] O. Schiemann, P. Cekan, D. Margraf, T. F. Prisner, S. T. Sigurdsson, *Angew. Chem. Int. Ed.* **2009**, *48*, 3292.

[15] D. Hinderberger, H. W. Spiess, G. Jeschke, *J. Phys. Chem. B* **2004**, *108*, 3698.

[16] P. Höfer, A. Grupp, M. Mehring, *Chem. Phys. Lett.* **1986**, *132*, 279.

[17] D. Kurzbach, A. Sharma, D. Sebastiani, K. W. Klinkhammer, D. Hinderberger, *Chem. Sci.* **2011**, *2*, 473.

[18] D. Hinderberger, H. W. Spiess, G. Jeschke, *Europhys. Lett.* **2005**, *70(1)*, 102.

[19] I stick to the notation introdiuced by Schlüter and co-workers. Therefore, de-PG denotes deproteced, terminal amonnium groups.

[20] K. Schmidt-Rohr, A. Rawal, X.-W. Fang, *J. Chem. Phys.* **2007**, *126*, 054701.

[21] P. P. Borbat, J. H. Davis, S. E. Butcher, J. H. Freed, *J. Am. Chem. Soc.* **2004**, *126*, 7746.

[22] G. Jeschke, V. Chechik, P. Ionita, A. Godt, H. Zimmermann, J. Banham, C. R. Timmel, D. Hilger, H. Jung, *Appl. Magn. Reson.* **2006**, *30*, 473.

[23] G. Jeschke, M. Sajid, M. Schulte, A. Godt, *PCCP* **2009**, *11*, 6580.

[24] G. Jeschke, A. Koch, U. Jonas, A. Godt, *J. Magn. Reson.* **2002**, *155*, 72.

[25] P. G. Fajer, L. Brown, L. Song, "Practical Pulsed Dipolar ESR (DEER)", in *ESR spectroscopy in membrane biophysics*, M.A. Hemminga and L.J. Berliner, Eds., Springer, New York, 2007.

[26] D. Kurzbach, D. Kattnig, B. Zhang, A. D. Schlüter, D. Hinderberger, *J. Phys. Chem. Lett.* **2011**, *2*, 1583.
[27] Y. D. Tsvetkov, A. D. Milov, A. G. Maryasov, *Russ. Chem. Rev.* **2008**, *77*, 487.
[28] J. E. Banham, C. M. Baker, S. Ceola, I. J. Day, G. H. Grant, E. J. J. Groenen, C. T. Rodgers, G. Jeschke, C. R. Timmel, *J. Magn. Reson.* **2008**, *191*, 202.
[29] W. Zhuang, E. Kasemi, Y. Ding, M. Kröger, A. D. Schlüter, J. P. Rabe, *Adv. Mater.* **2008**, *20*, 3204.
[30] R. Esfand, D. A. Tomalia, *DDT* **2001**, *6*, 427.
[31] S. Svenson, D. A. Tomalia, *Adv. Drug Delivery Rev.* **2005**, *57*, 2106.
[32] J. F. G. A. Jansen, E. M. M. de Brabander-van den Berg, E. W. Meijer, *Science* **1994**, *266*, 1226.
[33] J. F. G. A. Jansen, E. W. Meijer, E. M. M. de Brabander-van den Berg, *J. Am. Chem. Soc.* **1995**, *117*, 4417.
[34] H. Namazi, M. J. Adeli, *Polymer* **3006**, *45*, 10788.
[35] H. Namazi, M. J. Adeli, Z. Zarnegar, S. Jafari, A. Dadkhah, A. Shukla, *Colloid. Polym. Sci.* **2007**, *285*, 1527.
[36] G. R. Newkome, K. K. Kotta, C. N. Moorefield, *Chem. Eur. J.* **2006**, *12*, 3726.
[37] H. Namazi, M. J. Adeli, *Polym. Sci. A: Polym. Chem.* **2005**, *43*, 28.
[38] C. M. Paleos, D. Tsiourvas, Z. Sideratou, L. Tziveleka, *Biomacromolecules* **2004**, *5*, 524.
[39] D. R. Vutukuri, S. Basu, S. Thayumanavan, *J. Am. Chem. Soc.* **2004**, *126*, 15636.
[40] I. Gitsov, K. R. Lambrych, V. A. Remnant, R. Pracitto, *J. Polym. Sci. A: Polym. Chem.* **2000**, *38*, 2711.
[41] D. M. Watkins, Y. Sayed-Sweet, J. W. Klimash, N. J. Turro, D. A. Tomalia, *Langmuir* **1997**, *13*, 3136.
[42] C. J. Hawker, K. L. Wooley, J. M. J. Fréchet, *J. Chem. Soc. Perkin. Trans.* **1993**, *1*, 1287.
[43] C. Liu, C. Gao, D. Yan, *Macromolecules* **2006**, *39*, 8102.
[44] G. R. Newkome, B. D. Woosley, E. He, C. N. Moorefield, R. Güther, G. R. Baker, G. H. Escamilla, J. Merrill, H. Luftmann, *Chem. Commun.* **1996**, 2737.
[45] G. R. Newkome, C. N. Moorefield, G. R. Baker, A. L. Johnson, R. K. Behera, *Angew. Chem. Int. Ed.* **1991**, *30*, 1176.
[46] J. M. Oliveira, A. J. Salgado, N. Sousa, J. F. Mano, *Prog. Polym. Sci.* **2010**, *35*, 1163.
[47] C. d. l. H. Alarcón, S. Pennadam, C. Alexander, *Chem. Soc. Rev.* **2005**, *34*, 276.
[48] B. Obermeier, F. Wurm, C. Mangold, H. Frey, *Angew. Chem. Int. Ed.* **2011**, *50*, 7988.
[49] A. Chilkoti, M. R. Dreher, D. E. Meyer, D. Raucher, *Adv. Drug Delivery Rev.* **2002**, *54*, 613.
[50] B. Zhang, R. Wepf, M. Kröger, A. Halperin, A. D. Schlüter, *Macromolecules* **2011**, *44*, 6785.
[51] B. Zhang, R. Wepf, K. Fischer, M. Schmidt, S. Besse, P. Lindner, B. T. King, R. Sigel, P. Schurtenberger, Y. Talmon, Y. Ding, M. Kröger, A. Halperin, A. D. Schlüter, *Angew. Chem. Int. Ed.* **2011**, *50*, 737.
[52] Z.-B. Zhang, Y.-H. Teng, W. Freas, D. K. Mohanty, *Macromol. Rapid Commun.* **2006**, *27*, 626.
[53] A. Caragheorgheopol, H. Caldararu, I. Dragutan, H. Joela, W. Brown, *Langmuir* **1997**, *13*, 6912.
[54] M. F. Ottaviani, G. Martini, L. Nuti, *Magn. Reson. Chem.* **1987**, *25*, 897.
[55] B. R. Knauer, J. J. Napier, *J. Am. Chem. Soc.* **1976**, *98*, 4395.
[56] M. J. N. Junk, H. W. Spiess, D. Hinderberger, *Angew. Chem. Int. Ed.* **2010**, *49*, 8755.
[57] W. L. Hubbell, H. M. McConell, *J. Am. Chem. Soc.* **1970**, *93*, 314.
[58] E. Szajdzinska-Pietek, R. Maldonado, L. Kevan, S. S. Berr, R. R. M. Jones, *J. Phys. Chem.* **1985**, *89*, 1547.
[59] Hydrophilicity here can be quantified as A_{iso}-$A_{iso,pentan}$/($A_{iso,water}$-$A_{iso,pentan}$).
[60] P. M. Welch, C. F. Welch, *Nano Letters* **2006**, *6*, 1922.

[61] O. Bertran, B. Zhang, A. D. Schlüter, A. Halperin, M. Kröger, C. Alemán, *RSC Adv.*, 2013, **3**, 126-140.
[62] G. Caminati, N. J. Turro, D. A. Tomalia, *J. Am. Chem. Soc.* **1990**, *112*, 8515.
[63] H. Schindler, J. Seelig, *J. Chem. Phys.* **1973**, *59*, 1841.
[64] G. H. Schnepel, D. Hegner, U. Schummer, *Biochimica et Biophysica Acta* **1974**, *397*, 67.
[65] Note that normally one can observe a clear difference in τ_c between 5- and 16-DSA, since the methylene chain becomes more rigid, the closer it is to the polar head group. In the case presented here, however, the difference between 5- and 16-DSA is small, which is why the picture of fatty acids in lipid bilayers or membranes may not be fully transferable to DSA in denpols.
[66] D. Hinderberger, H. W. Spiess, G. Jeschke, *Europhys. Lett.* **2005**, *70(1)*, 102.
[67] D. Hinderberger, H. W. Spiess, G. Jeschke, *Appl. Magn. Resonance* **2010**, *37*, 657.
[68] Y. D. Tsvetkov, A. D. Milov, A. G. Maryasov, *Russ. Chem. Rev.* **2008**, *77*, 487.
[69] G. Jeschke, H. Zimmermann, A. Godt, *J. Magn. Res.* **2006**, *180*, 137.
[70] D. Kurzbach, D. R. Kattnig, B. Z. Zhang, A. D. Schluter, D. Hinderberger, *Chem Sci* **2012**, *3*, 2550.
[71] B. Grotz, J. Beck, P. Neumann, B. Naydenov, R. Reuter, F. Reinhard, F. Jelezko, J. Wrachtrup, D. Schweinfurth, B. Sarkar, P. Hemmer, *New J. Phys.* **2011**, *13*, 055004.
[72] S. Ruthstein, D. Goldfarb, *J. Phys. Chem. C* **2008**, *112*, 7102.
[73] S. Ruthstein, A. Potapov, A. M. Raitsimring, D. Goldfarb, *J. Phys. Chem. B* **2005**, *109*, 22843.
[74] S. Ruthstein, A. M. Raitsimring, R. Bitton, V. Frydman, A. Godt, D. Goldfarb, *Phys. Chem. Chem. Phys.* **2009**, *11*, 148.
[75] B. E. Bode, R. Dastvan, T. Prisner, *J. Magn. Reson.* **2011**, *211*, 11.
[76] G. Jeschke, *ChemPhysChem* **2002**, *3*, 927.
[77] A. Marko, V. Denysenkov, D. Margraf, P. Cekan, O. Schiemann, S. T. Sigurdsson, T. F. Prisner, *J. Am. Chem. Soc.* **2011**, *133*, 13375.
[78] D. Kurzbach, D. R. Kattnig, B. Zhang, A. D. Schlüter, D. Hinderberger, *Chem. Sci.* **2012**, *3*, 2550.
[79] E. Cabane, X. Y. Zhang, K. Langowska, C. G. Palivan, W. Meier, *Biointerphases* **2012**, *7*.
[80] V. A. Bloomfield, *Biopolymers* **1997**, *44*, 269.
[81] J. Hu, T. Xu, Y. Cheng, *Chem. Rev.* **2012**, *112*, 3856.
[82] W. Zhuang, E. Kasemi, Y. Ding, M. Kröger, A. D. Schlüter, *Adv. Mater.* **2008**, *20*, 3204.
[83] D. Kurzbach, V. S. Wilms, M. Schömer, H. Frey, D. Hinderberger, *Macromolecules* **2012**, ***45***, 7535.
[84] D. D. Thomas, *Biophys. J.* **1978**, *24*, 439.
[85] F. M. Winnik, A. R. Davidson, G. K. Hamer, H. Kitano, *Macromolecules* **1992**, *25*, 1876.
[86] S. He, P. G. Arscott, V. A. Bloomfield, *Biopolymers* **2000**, *53*, 329.
[87] S. Bolisetty, C. Schneider, F. Polzer, M. Ballauff, W. Li, A. Zhang, A. D. Schluter, *Macromolecules* **2009**, *42*, 7122.
[88] Information provided by Dr. Baozhong Zhang.
[89] C.-I. Huang, M. O. d. l. Cruz, *Macromolecules* **2002**, *35*, 976.
[90] P. Gonzalez-Mozuelos, M. O. d. l. Cruz, *J. Chem. Phys.* **2003**, *118*, 4684.
[91] V. B. Teif, K. Bohnic, *Prog. Biophys. Mol. Biol.* **2011**, *108*, 208.
[92] D. Kurzbach, C. Velte, P. Arnold, G. Kizilsavas, D. Hinderberger, *Soft Matter* **2011**, *7*, 6695.
[93] J. A. Weil, J. R. Bolton, J. E. Wertz, "*Electron Paramagnetic Resonance - Elementary Theory and Practical Applications*", John Wiley % Sons Inc., New York, 1994.
[94] C. Dufès, I. D. Uchegbu, A. G. Schätzlein, *Advanced Drug Delivery Reviews* **2005**, *57*, 2177.
[95] M. J. N. Junk, U. Jonas, D. Hinderberger, *Small* **2008**, *4*, 1485.
[96] M. J. N. Junk, W. Li, A. D. Schlüter, G. Wegner, h. W. Spiess, A. Zhang, D. Hinderberger, *Macromol. Chem. Phys.* **2011**, 212, 1229.

4. The Nanoscale Collapse Behavior of Alkylene Oxide-Based Thermoresponsive Polymers

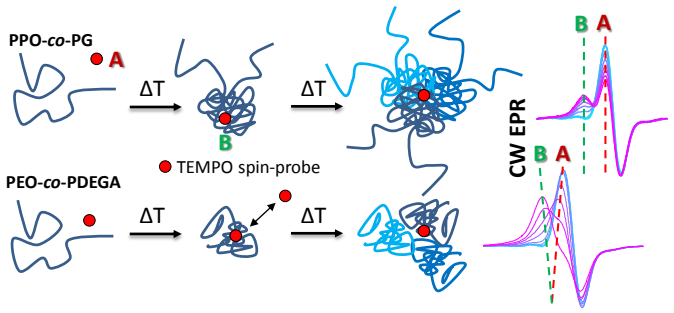

In this chapter the focus will be shifted from electrostatic and hydrophobic interactions to hydrogen bonds in equilibrium with hydrophobic interactions: In particular to the characterization of thermoresponsive polymers. These are macromolecules that exhibit a transition from a solution state to a non-solution, collapsed-chain state above a certain critical temperature, T_c. At this temperature stabilizing hydrogen bonds between polymers and solvent become weaker than hydrophobic the attraction among polymer chains, leading to dehydration and aggregation of the polymers.[1] Since solutions become turbid when a polymer aggregates or precipitates, this temperature is referred to as the cloud point. Often it is also denoted as the lower critical solution temperature (LCST). In parallel, in classical thermodynamics the abbreviation LCST denotes the *lowest* critical solution temperature at a given critical polymer concentration.[2] The denomination LCST therefore being ambiguous, I will use cloud point throughout this chapter. Since solutions of thermoresponsive polymers frequently become more ordered when surpassing T_c the term inverse phase transition is used commonly, too.

In the last 20 years, thermoresponsive polymers and their phase behavior have been investigated intensively in numerous fields of science[3-7] emphasizing their potential applications in drug delivery, tissue engineering and other scientific areas.[3-5] The versatility of thermoresponsive polymers relies on the fact that their composition, their chemical structure, their topology and their molecular weight can affect their phase transition behavior and cloud points significantly.[8-13] [14-21] E.g., a high fraction of hydrophilic comonomers may lead to stable hydration shells and high T_cs. On the contrary, T_c is generally shifted to lower temperatures by introduction of hydrophobic comonomers.[19, 22-28] According to Winnik and co-authors, alone in 2008, over 700 publications have been issued on poly-N-isopropylacrylamide (PNiPAAm), the most investigated thermoresponsive polymer.[1] This large number mirrors the fascinating complexity of thermosensitive macromolecules drawing interest from physical, chemical, biological, and medical sciences.[5] In this chapter I focus on an aspect of thermoresponsive polymers that is intriguing from a physico-chemical point of view but that is also quite important for their application in host-guest applications: nanoscopic spatial inhomogeneities.

Nanoscopic spatial inhomogeneities occur during the temperature-induced collapse of a thermoresponsive polymer, typically at temperatures below T_c. In this particular context, they can be

considered as a nanoscopic cluster of polymer segments, i.e. a separate nanophase with an approximate size of 1 to 50 nm, as defined by Wunderlich.[29] This separate nanophase provides a less polar environment than an aqueous medium. A nanoscale inhomogeneity must not be mistaken for a microphase, which typically features strong surface effects.[29, 30] In contrast it merely denotes local, nanoscopic patches of collapsed polymer segments, unimers or aggregates of only a small number of chains inside an otherwise homogeneous system.

In this context, the term *dynamic inhomogeneity refers* to nanoscopic, collapsed polymer domains that undergo significant morphological changes with temperature. This phenomenon typically comes along with spin probe guest molecules exhibiting varying site exchange frequencies ($\omega_{exchange} > 10^7 s^{-1}$) in a certain, restricted temperature range. Here site exchange denotes probes diffusing between the aqueous phase of the medium and apolar cavities consisting of collapsed polymer segments.[31, 32] In contrast, inhomogeneities that do not feature such dynamic conformational adaptions to temperature can be considered as being *static*. Commonly, they do not feature changes in guest exchange frequencies.[32, 33][34]

EPR spectroscopy can deliver interesting and novel insights into local, static and dynamic properties of thermoresponsive systems.[31-33, 35-37] This is mainly due to two strong points: high sensitivity to quite small probes and a favorable observable timescale. Such, EPR spectroscopy allows for the detection of rather small nanoscale inhomogeneities in polymer solutions on the local level.[38-41] For instance, CW EPR can probe nanoscopic apolar cavities (inhomogeneities) even when these cavities are too small or too sparse to be detected by macroscopic methods (e.g. turbidimetry).[32, 33] This is possible, since from a_{iso} one can distinct apolar, polymer-rich domains in a system from purely aqueous environments.[42] Hence, CW EPR data provide exclusive and fast evidence for an increase of local polymer density through either aggregation or compaction of polymer strands. No other methodological approach is needed.

In this context on should keep in mind that particular analytical methods reveal specific molecular information that can often complement each other:[31-33] Macroscopic ensemble-averaging methods like dynamic light scattering (DLS) yield valuable information about transition temperatures and ranges, while intrinsically local methods like magnetic resonance or fluorescence spectroscopy can probe, e.g., micellar configurations. Hence, the combination of macroscopic and local methods can lead to a rather thorough understanding of thermoresponsive polymers.

In the present chapter it will be shown how *dynamic* and *static* inhomogeneities appear on EPR time scales (~10^{-5} s – 10^{-9} s) and which structural parameters of a polymer trigger the occurrence of a certain type of inhomogeneity. In particular, certain molecular and topological features and corresponding non-covalent interaction profiles will be correlated with a particular collapse mechanism that in turn proceeds via either dynamic or static inhomogeneities.

4.1 The Phase Behavior of Pluronic Triblock Copolymers

In the realm of thermoresponsive polymers poly(ethylene oxide)-poly(propylene oxide)-poly(ethylene oxide) or PEO-PPO-PEO triblock copolymers are, next to PNiPAAm, one of the most frequently investigated compounds. They are subject of numerous studies in the fields of chemistry,[43] physics[8] and medicine.[44] Beside their low toxicity and good availability, they form lyotropic phases in aqueous solution above T_c. This makes them interesting for a lot of applications. PEO-PPO-PEO tri-block copolymers (commercially available as Pluronic® or Poloxamers) consist of two

poly(ethylene oxide) blocks of equal length attached to both ends of a poly(propylene oxide) chain. Table 4.1.1 summarizes the molecular weights and relative PEO/PPO fractions of the Pluronics used in this study and explains the common notation.

It is commonly understood that micellization of Pluronics is caused by a deswelling of the PPO chain at moderate temperatures or high concentrations. The onset of the dehydration event can be shifted to lower temperatures and concentrations by increasing the relative proportion of PPO in a chain and/or the overall molecular weight.[43, 45-50] T_c is concentration dependent, such that a given T_c is correlated with at a certain critical micellization concentration (CMC). Published T_c and CMC values often vary drastically for almost every commercially available PEO-PPO-PEO triblock copolymer, depending on the methods employed.[8, 51] Therefore, a methodological reflection about the applied experimental technique is of particular importance. Large parts of this section will be dedicated to this aspect.

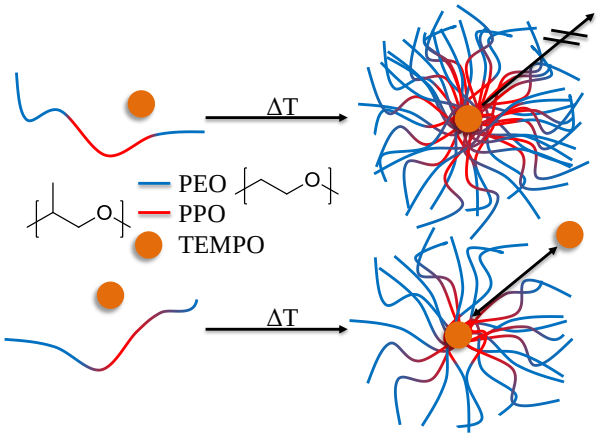

Scheme 4.1.1. Pluronics with high PEO content (top) form apolar cavities (drawn as micelle here) above T_c, which allow exchange of the TEMPO spin probes with the surrounding medium. Low PEO contents (bottom) lead to apolar cavities, in which enclosed species B appears static on the EPR timescale. PEO is drawn red and PPO is drawn blue.

For the present purpose, the investigation of the phase behavior of Pluronics, a spin probing approach was chosen, based on spectral contrast between probes in (nano-)phase separated systems. (see Section 1.2 and 3.1). The use of EPR spin probe techniques is a simple but highly efficient approach to investigate the micellization behavior of thermoresponsive polymers.

Table 4.1.1. Molecular weight and percentage of PEO per molecule of the Pluronics used.[a]

	L64	F68	P84	P105	F108	F127
M_w / g/mol	2900	8400	12600	4200	6500	14600
% PEO	40	80	40	50	80	70

[a]Pluronics are characterized by two or three numbers, whereby the last number indicates the percentage of PEO in a particular substance. The other numbers designate the molecular weight of the PPO chain (I.E. Pluronic F127 has a PEO fraction of 70% and the PPO chain a molecular weight of 4000 g/mol, in contrast Pluronic F68 consists of 80% PEO and the PPO chain has a molecular weight of 1750 g/mol).

Several EPR-based studies recently aimed at characterizing Pluronic-based systems, by means of spin probing.[33, 39, 52-56] In accordance with a chemist's intuition, primarily spin probes with strongly hydrophobic moieties, like end-labeled Pluronics have been employed. Thus, it was possible to in-

vestigate the constitution several lyotropic phases and these findings were largely in agreement with results gained with other methods.[57-61]

The aim of the present section is to show that the formation of nanoscopic inhomogeneities (the onset of the phase transition event) is often located well below previously published T_cs and that the type of occurring inhomogeneity depends on the Pluronics' PPO / PEO ratio. This is possible by using the quite small and amphiphilic spin probe TEMPO. The favorable partitioning coefficient of TEMPO between polar and apolar domains is exploited (between water and polystyrene: ~10^2, see reference [62]) to detect the very early occurrence of apolar polymer regions. In the following, dynamics of the inhomogeneities that occur during the thermal phase transition are addressed first and subsequently the micellization behavior is quantified.

4.1.1 Results and Discussion

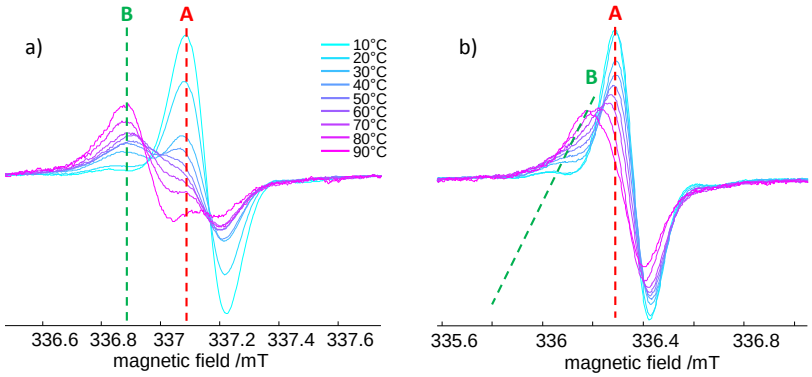

Figure 4.1.1. a) $M_i = -1$ transition line of 1 mM TEMPO solution in a 10 wt% of P105 from 10°C to 90°C. b) $M_i = -1$ transition line of 1 mM TEMPO in a 10 of wt% F108 from 10°C to 90°C. Dashed vertical lines serve as guide to the eye for following the shift of the high-field line of the species A and B. The exact positions of these lines (i.e. zero-crossings) are extracted from spectral simulations (see Appendix A4.1.1), since strong overlap renders a direct observation difficult.

Utilizing the combination of a favorable partitioning of TEMPO and its environmental sensitivity, aqueous solutions of selected Pluronic triblock copolymers of different length and hydrophilic/hydrophobic balance (see Table 4.1.1) are investigated. The focus is on 10 wt% solutions of Pluronics and 1 mM TEMPO. Regarding the overall phase behavior of Pluronics, all systems under investigation are in an isotropic phase regime at a polymer concentration of 10 wt % and ambient temperatures, but can undergo transitions into lyotropic, multiphase regions at elevated temperatures.[48]

Temperature Dependence

Figure 4.1.1 a) depicts the high-field transition line of the TEMPO spectrum ($M_i = -1$) in a 10 wt% aqueous solution of Pluronic P105. As described in Section 1.2 the high-field transition includes all information necessary for the interpretation of the spectra. Note that all series of measurements on Pluronics with a PEO fraction ≤ 50% (P105 / P84 / L64) show identical temperature-dependent changes of the high-field line shape. Hence, the discussion is restricted to P105 here, but representative for P84 / L64, too. (The complete spectra of all systems under investigation and the corresponding spectral simulations can be found in Appendix A4.1.1 and A4.1.2.) As indicated by the dashed vertical lines in Figure 4.1.1 a), the high-field line stemming from TEMPO species B in aggregates of P105 does not differ significantly in field position at different temperatures. Species B stems from incorporation of TEMPO in aggregates of the Pluronic above T_c, here above 20°C. The relative contribution of species B to the spectrum increases with rising temperature, indicating in-

creasing apolar volume in the system. From spectral simulations one can determine the hfc constant of species B. It remains constant at a value around 44 MHz. The average hfc value of the TEMPO species A is around 48 MHz. This difference of ~4 MHz translates to the polarity difference between water and chloroform. From the constant a_{iso} one can deduce also a constant polarity (with respect to temperature) inside the collapsed domains. Hence, they constitute static inhomogeneities, as no drastic conformational rearrangements take place with temperature.[33] For static inhomogeneities the exchange of the probes between the polar and the apolar environment, takes place – if at all – on time scales below those that can be resolved with conventional CW EPR at X-band ($\omega_{exchange} < 10^7$ s^{-1}).[26, 33, 57-58, 63]

Figure 4.1.1 b) depicts the evolution of the high-field line of TEMPO in a 10 wt% solution of F108. The depicted spectra are representative for all Pluronics with a PEO fraction ≥ 70% (F127 / F108 / F68). The contribution of the spectral component B increases with rising temperature. But in contrast to the constant field position described above, a shift of the line to higher fields can clearly be observed when the temperature is increased. This indicates a larger a_{iso} of species B at higher temperatures (see Figure 4.1.2 for the temperature-dependence of a_{iso}). At 90 °C the two lines of species A and B cannot be distinguished visually anymore. Spectral simulations, however, still enable one to differentiate the two lines. Note that the slight shift of species A at high temperatures to lower field is due to changes in hydration of TEMPO and is of universal nature. a_{iso} of species B increases from ~44 MHz to ~45.5 MHz with temperature and vice versa (Figure 4.1.2 b); note that hyperfine couplings of nitroxides normally decrease with rising temperature).[56, 64, 65][66]

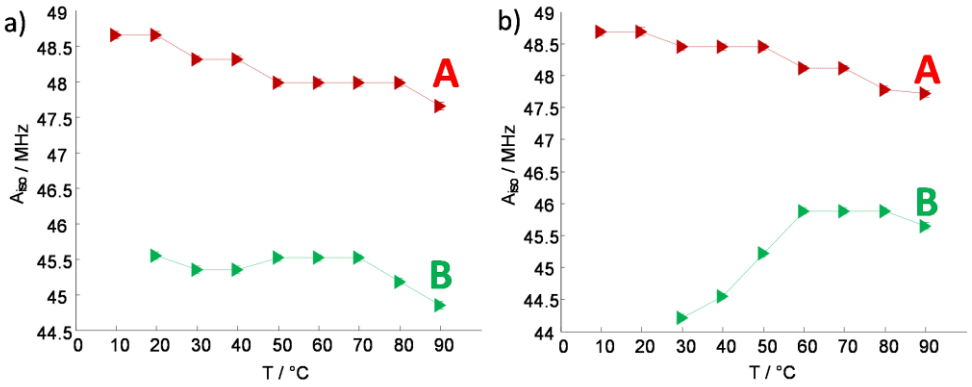

Figure 4.1.2. a) Isotropic hyperfine coupling values, a_{iso}, of the hydrophilic species A and the hydrophobic species B for P105 (representative for all Pluronics with a PEO content ≤ 50%) as a function of temperature. b) Isotropic hyperfine coupling values, a_{iso}, of the hydrophilic species A and the hydrophobic species B for F108 (representative for all Pluronics with a PEO content ≥ 70%).[52]

The shifting hyperfine coupling values of species A and B for F68, F108 and F127 with PEO ≥ 70% can only be explained by spin probes B exchanging ever faster between polar and apolar environments (on EPR timescales) with rising temperature (Figure 4.1.2 b)).[56] If the exchange frequency exceeds the observable regime and reaches the limit of fast exchange, ($\omega_{exchange} > 10^7$ s^{-1}) only one line at an averaged field position between the pure species A and B can be observed.[67] The exchanging spin probes come closer to the limit of fast exchange with increasing temperature due to increasing kinetic energy and the B line gains increasing contributions from species A (or TEMPO at the surface of a Pluronic aggregate). This leads to merging of the lines of species A and B. At 60°C, a_{iso} of species B for F68, F108 and F127 reaches a constant, averaged value since the resolv-

able timescale is underrun.[68] This is reasonable because TEMPO is preferentially located close to the interface of the polar and apolar regions.[33] Although the volume fraction of the aqueous environment is huge compared to the apolar regions, the TEMPO probes favor the latter, and their average duration of stay in the aqueous phase is short enough (<< 10^{-5} s) to allow for line averaging. Note that there is always a fraction of TEMPO probes that does not exchange at all and hence leads to detection of a species A in any regime of exchange.

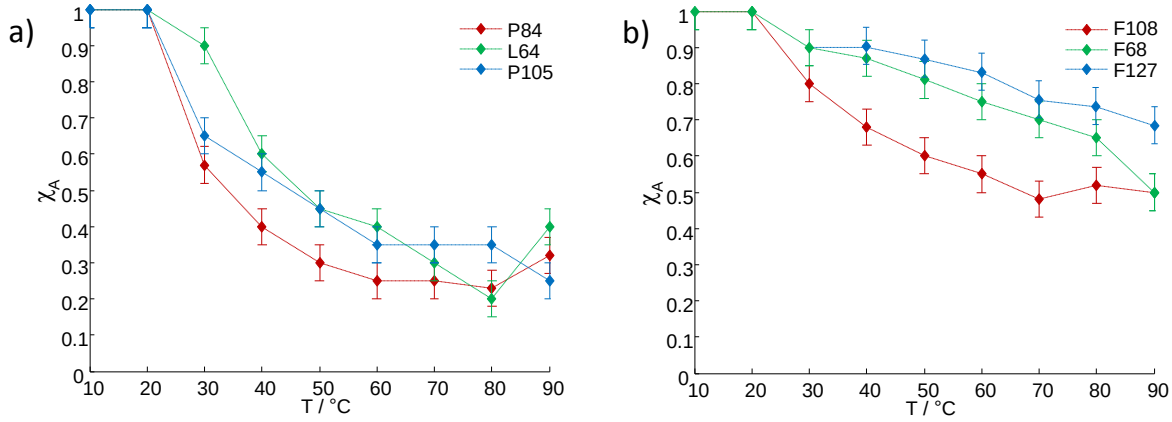

Figure 4.1.3. Mole fraction of spectral component A, χ_A, plotted vs. temperature for 10 wt% solutions of the different Pluronics investigated. The concentration of TEMPO in the solution was 1 mM. a) PEO contents ≤ 50% b) PEO content ≥ 70%.

Note that the shift in a_{iso} of species B could also be a consequence of changes in the Pluronic hosts' hydration states. Increasing hfc values hallmark a shift towards higher environmental polarity sensed by a probe. However, evidence for increasing polarity of Pluronic micelles' interior with rising temperature is not documented. In contrast, Pluronic micelles are commonly expected to be further dehydrated with increasing temperature or to become simply more apolar.[44] Therefore, the rationale based on spin probe exchange appears more appropriate in the present case.[69]

At this point the question arises why such dynamic guest exchange can only be observed for Pluronics with high PEO fractions, as depicted in Scheme 4.1.1 (bottom). Two factors may influence this phenomenon: the size of the micellar cores (1) and the amount of water inside them (2).

1) Increasing PEO block sizes result decreasing micellar core sizes and lower aggregation numbers.[43, 70] As an example, reported hydrophobic core radii[51] of Pluronic micelles are around 4.5 nm for PEO fractions of 50% and around 3.6 nm for 80%. Thus, the distance that has to be bridged by entrapped probes in order to exit the micellar core becomes shorter upon increasing PEO fractions. The micellar core size also strongly depends on the temperature. For instance, increasing the temperature by 30 K can result in a growth of 1 nm.[71] The (mean square) translational displacement of TEMPO, given by $\langle x^2 \rangle = 6 D_T \tau_T$, can be estimated to be in the range of $\sqrt{\langle x^2 \rangle} = 5.5 \pm 0.5\, nm$, when applying an average rotational correlation time τ_C of typically 0.2 ns, as gained from the spectral simulations. (D_T is the translational diffusion coefficient and τ_T is the characteristic translational diffusion time. For details of the calculations and the relation between τ_T and τ_c see Appendix A4.1.) Therefore, the range of the translational displacement may well allow TEMPO molecules to travel the distance from a micellar core's center to its outer boundary and across the interface to the PPO-poor region outside the core. This process will be faster for smaller cores facilitating site exchange for Pluronics of low PPO contents.

2) Higher fractions of water in the micellar cores may also play a crucial role. Pluronics with higher PEO fractions tend to host larger amounts of residual water and/or PEO in their micellar cores than Pluronics with lower PEO fractions.[70] Hence, it seems plausible that a less dense "packing" of the PPO-rich core gives rise to faster exchange rates of the spin probes due to less sterical restraints. However, an intuitively assumed deswelling of the core with increasing temperature cannot be excluded completely,[43, 46] but is unlikely, since it should lead to decreasing a_{iso} of species B. This is clearly not observed, neither for PEO fractions ≤ 50% nor for PEO fractions ≥ 70%. One could speculate that the core's composition, hence, remains mainly constant. Published data from fluorescence spectroscopy support this conclusion.[72]

Quantitative Analysis

In general, the mole fractions shown in Figure 4.1.3 mirror the behavior that can be expected from literature reports: With increasing temperature the mole fraction of species B, $\chi_B = 1-\chi_A$, increases due to an increasing number of collapsed PPO chains and volume of apolar regions. The temperature evolutions of the mole fractions for all Pluronics under investigation are shown in Figure 4.1.3. In all cases, the decrease of χ_A is spread over a wide temperature range ($\Delta T > 40$ °C). Pluronics with lower PEO fractions show steeper developments of the χ_A functions, since larger fractions of PPO yield more hosting space for TEMPO. It is noteworthy that the first appearance of species B can always be located between 20°C and 30°C, whereas published values indicate T_c values well above 30°C (e.g.: L64: 34.5 °C; F68: 33 °C for 10 wt% solutions) for some of the triblock copolymers investigated here.[8, 43] These values were mainly determined with macroscopic or ensemble-averaging methods like turbidimety or surface tension measurements.[8, 27, 51]

An intrinsically local method like CW EPR, utilizing a small, amphiphilic spin probe like TEMPO, is sensitive for smallest changes in a system, as for example collapsed, nanoscopic domains. This, in turn, allows for the determination of the early onset of hydrophobic chain collapses.[42] Contrary, large, strongly hydrophobic spin probes (as used in previous EPR studies on Pluronics[57]) and intrinsically macroscopic methods detect only full-grown micelles and are not sensitive towards nanodomains. This is the reason why spin probing EPR with TEMPO detects lower collapse temperatures than other approaches. It is sensitive to nanophase separation that simply precedes meso- and macrophase separation.

The direct detection of even smallest, nanoscopic apolar cavities with the approach presented here is also the reason for the prominent differences between the plots in Figure 4.1.3 a) and b). From these Figures it is evident that χ_A only depends on the ratio of PPO to PEO in a particular Pluronic and not on its molecular weight: The organic mass of PPO groups forming apolar cavities is independent of the overall molecular weight of a polymer strand, if the weight percentage of the polymers is constant. Indeed, the formation of aggregates like micelles, a "real" (meso-)phase transition, would dependent on the molecular weight.[48] It is therefore necessary to interpret the data shown above in terms of apolar cavities, not in terms of micellization values.

In general, data acquired from any probe technique on T_c and CMC values of Pluronics suggest that there are certain transition ranges for phase transition events during which probe signatures change. When the temperature or the polymer concentration is raised above or reduced below this range, a probe's signal changes only slightly or stays constant (sigmoidal development). E.g., fluorescence-probe absorption intensities change drastically between 20 °C and 30 °C for P104 and F108, but remain mainly constant outside this temperature range.[51, 57, 72][73] In all cases presented here the χ_A and χ_B values change even at temperatures close to the boiling point of the solvent.

This translates to growing volume of apolar regions over a wider temperature range than usually observed with other probes. Thus, the formation of apolar cavities is not correlated with the sigmoidal temperature dependence of micelle formation in Pluronics. Still, interpreting data from probing techniques in terms of micellization is reasonable if the employed probes are much bigger and more hydrophobic probes than TEMPO.

4.1.2 Nanophase Transitions of Pluronics

Most important for the following section of this thesis, the behavior of TEMPO inside apolar cavities is dependent on the PEO fraction of the polymers. An increasing temperature and high PEO fractions (≥ 70%) leads to a faster diffusion of amphiphilic TEMPO molecules between the PPO-rich cavities and the surrounding aqueous, PPO-depleted environment. With rising temperature site-exchange frequencies increase steadily (indicating dynamic inhomogeneity). In cases of low PEO fractions (≤ 50%) the hfc values of species B remain constant, which suggests that there is either no exchange at all (indicating static inhomogeneity), or that the rate of a possible exchange is below the EPR timescale. Such, TEMPO allows for the distinction between static and dynamic inhomogeneities. For applications, e.g. in drug transport, knowledge about exchanges of guest molecules in thermoresponsive polymers can become crucial.

4.2 How Structure-Related Collapse Mechanisms Determine Nanoscale Inhomogeneities in Thermoresponsive PPO-co-PG and PEO-co-PDEGA

The present section is dedicated to the expansion of the TEMPO spin probing approach from Pluronics to a selected variety of other, recently developed thermoresponsive alkylene oxide-based polymers. Recent developments in anionic ring-opening polymerization, which allow for specific manipulation of constitutional and topological characteristics of thermoresponsive polymers made the following investigation feasible and poly(alkylene oxide)s the model substrate of choice.[19, 23-25, 57, 74-76] Making this study possible, Dr. Valerie S. Wilms and Dr. Martina Schömer from the group of Prof. Holger Frey from the university of Mainz kindly provided linear polymer systems based on ethylene oxide (EO) / *N,N*-diethyl glycidyl amine (DEGA) copolymers[24] as well as linear and hyperbranched propylene oxide(PO) / glycidol (G) copolymers.[23, 25] The investigated systems have been selected carefully in order to present systematic variations of their constitution and topology: hyperbranched versus linear, block polymers versus random copolymers and varying hydrophobicity of the comonomers.

Experimental results gained from spin probing PEO-*co*-PDEGA[24, 77] and PPO-*co*-PG[23, 25] copolymers are presented first. Subsequently, the collapse mechanisms of the different polymers are discussed.[31-33, 35] Systematic relationships between polymer constitution, collapse mechanism, aggregation properties and the characteristics of interaction with small amphiphiles will be established. These *structure-function correlations* derived from the small amphiphilic TEMPO spin probes may actually help identifying an “appropriate” design for the desired release or hosting properties of polymer-based host-guest systems, e.g., for the delivery of a large variety of molecules, in particular small to intermediate-sized, often amphiphilic drug molecules.[78-80][81]

4.2.1 Results

Spin Probing Poly(propylene oxide)-polyglycidol (PPO-co-PG) Copolymers

In Figure 4.2.1 the high-field EPR lines of TEMPO in 1 wt% aqueous solutions of linear poly(propylene oxide-*co*-glycidol) random copolymers, **PPO-*co*-PG** (Figure 4.2.1 a)), and their hy-

perbranched analogues, ***hb*PPO-*co*-PG** (Figure 4.2.1 b)),[23-25] are depicted as a function of temperature for varying glycidol comonomer contents.

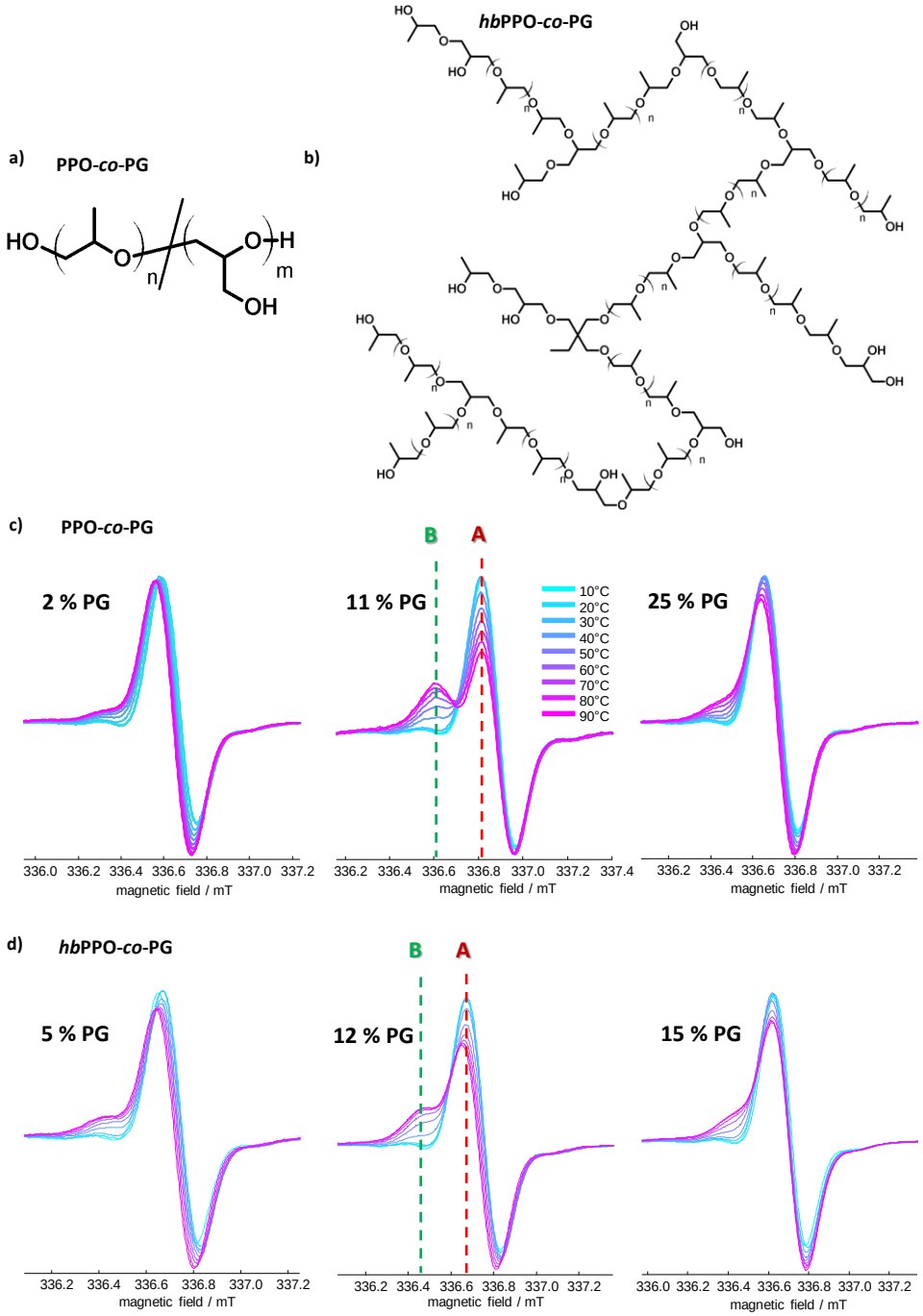

Figure 4.2.1. a) Molecular structure of **PPO-*co*-PG**. b) Molecular structure of ***hb*PPO-*co*-PG**. c) High-field lines from CW EPR spectra of 1 wt% aqueous solutions of the polymers depicted in a) and 0.2 mM TEMPO. d) High-field lines from CW EPR spectra of 1 wt% aqueous solutions of the polymers depicted in b) and 0.2 mM TEMPO. For the complete spectra and for simulations see Appendix A4.2.1 and A4.2.2. The red and green dashed lines indicate the roughly constant field positions of the high-field transitions of the TEMPO species A (polar) and B (apolar).

PPO-*co*-PG as well as ***hb*PPO-*co*-PG** lead to the occurrence of a spectral component B at T > 30 °C for all polymer constitutions (Figure 4.2.1. c) and d)). a_{iso} values of species B of 45.2 ± 0.1 – 45.5 ± 0.1 MHz can be compared with a_{iso} values of TEMPO in chloroform and hence indicate the presence of water-depleted regions constituted primarily of collapsed polymer segments.[82, 83] For both,

PPO-*co*-PG and ***hb*PPO-*co*-PG**, species B exhibits temperature-independent a_{iso} values and thus can be correlated with a *static inhomogeneity*.

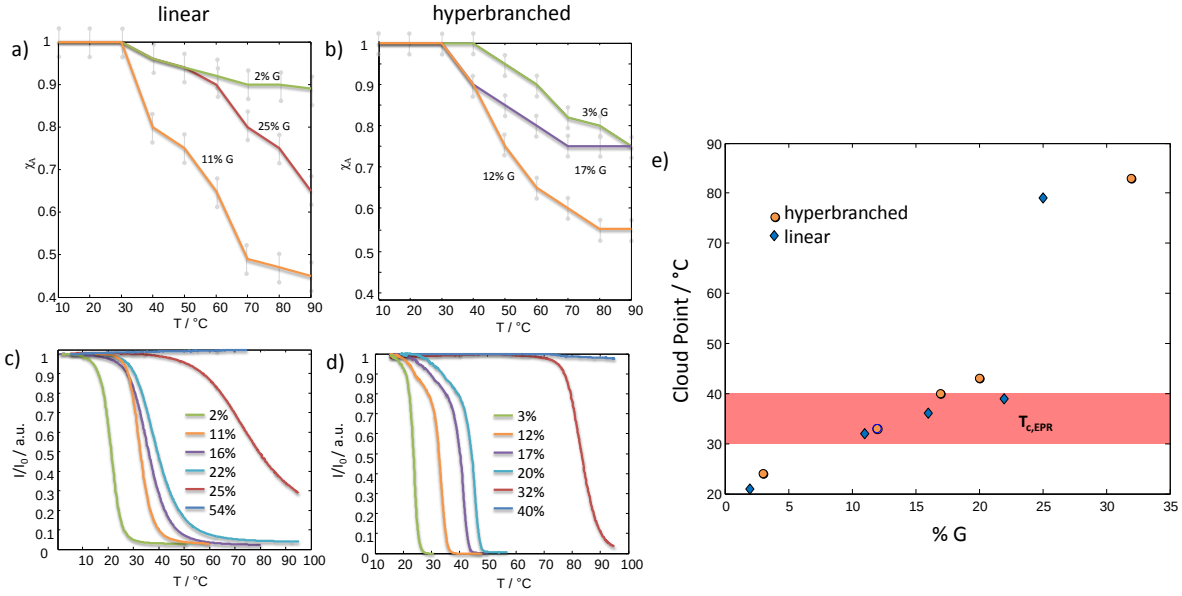

Figure 4.2.2. a) Temperature dependence of χ_A for **PPO-*co*-PG** with 2% (green), 11% (orange) and 25% (red) glycidol. b) Temperature dependence of χ_A for ***hb*PPO-*co*-PG** with 3% (green), 12% (orange) and 17% (violet) glycidol. c) Turbidity profiles for **PPO-*co*-PG** with different amounts of glycidol. d) Turbidity curves for ***hb*P-PO-*co*-PG** with different amounts of glycidol. e) Turbidity-derived cloud points, T_c, of linear (blue diamonds) and hyperbranched (yellow circles) PPO-*co*-PG plotted versus the glycidol content. The red bar indicates the narrow temperature region, in which all $T_{c,EPR}$s are located.

The spectral contribution of species B strongly depends on the glycidol content of the polymers. The maximal χ_B is observed at a glycidol content of 11% for the linear and at 12% for the hyperbranched system. Note that the glycidol content was varied in large steps of 5-15%, such that the optimal percentage for TEMPO uptake might in fact deviate from 11-12%. For both, linear and hyperbranched polymers, no significant contribution of species B could be observed at glycidol contents above 25% and below 2%. χ_A, is plotted comprehensively versus temperature for different glycidol contents in Figure 4.2.2 a) and b).[84][85] From the reduced χ_A for **PPO-*co*-PG** as compared to ***hb*PPO-*co*-PG** at a given temperature, concentration and percentage of glycidol, it follows that the linear polymers incorporate more TEMPO molecules than their hyperbranched analogues. For both types of molecular architectures, the first occurrence of the species B, indicating the onset of the phase transition event, is located between 30 °C and 40 °C. Remarkably, turbidity data[86] of the same polymer reveal cloud points (~20°C – 80°C) that differ drastically from those obtained by CW EPR (30 °C – 40 °C, Figure 4.2.2 c) - e)). Depending on the relative content of glycidol comonomers (i.e. glycerol building units), the "macroscopic" cloud point can shift from 20 °C to 80 °C. To avoid confusion I will refer to the temperature of first occurrence of species B, which is detected by means of spin probing CW EPR, as $T_{c,EPR}$, whereas the cloud point, as detected by turbidity measurements shall like before be denominated as T_c. $T_{c,EPR}$ and T_c should be discerned clearly, since only $T_{c,EPR}$ reports on the early occurrence of polymer-rich, apolar nanoscale cavities in a system, as has been shown in Section 4.1. T_c, in the strict sense of a cloud point, merely reports on the formation of large structures that scatter incident light.

Spin Probing Poly(ethylene oxide)-co-poly(N,N-diethyl glycidyl amine) (PEO-co-PDEGA) Copolymers

Aqueous solutions containing PEO-*co*-PDEGA exhibit a significant dependence of a_{iso} temperature profiles on the polymer constitution. EPR data and the a_{iso} values gained from spin probing linear gradient polymers, **PEO-*co*-PDEGA**, and linear diblock copolymers, **PEO-*block*-PDEGA**, with different DEGA contents are presented in Figure 4.2.3 and 4.2.4. In this particular context 'gradient' means that the probability to find a DEGA monomer at a given site in **PEO-*co*-PDEGA** is not completely random, but changes gradually as one goes from one end of the chain to the other.[24, 77]

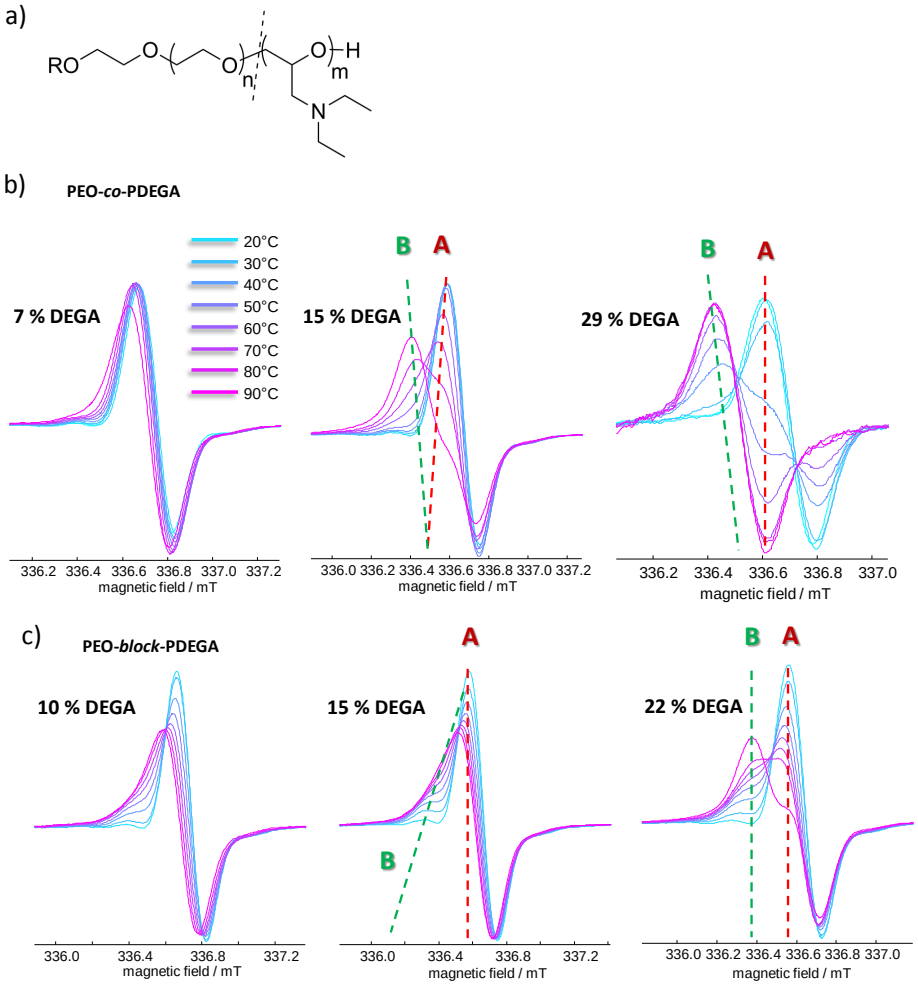

Figure 4.2.3. a) Molecular structure of PEO-*co*-PDEGA. b) High-field transition of TEMPO in 5 wt% aqueous solutions of gradient **PEO-*co*-PDEGA**. In the case of the copolymer with 7% DEGA, no significant temperature-dependent effects can be observed, yet a dynamic inhomogeneity at a DEGA content ≥ 15% occurs. c) High-field transition of TEMPO in a 5 wt% aqueous solution of **PEO-*block*-PDEGA** with different percentages of DEGA. A DEGA content ≤ 15% leads to the occurrence of dynamic inhomogeneities. At a DEGA content of 22% a static inhomogeneity occurs. As guide to the eye the dashed lines qualitatively indicate the temperature-dependent shift of the maxima of the high-field lines of species A (red) and B (green).

For the slightly gradient copolymer with > 15% DEGA (Figure 4.2.3 b)), species B exhibits decreasing a_{iso} values with increasing temperature. Hence, with rising temperature, species B experiences increasing apolarity of its polymer-rich surroundings. At 80 °C, a_{iso} reaches a constant value of 45.5 ± 0.1 MHz. Such, **PEO-*co*-PDEGA**-based systems feature a *dynamic inhomogeneity*. This will be discussed in detail in Section 4.2.2.

At DEGA contents significantly lower than 15%, i.e. ≤ 7% DEGA, no strong temperature-dependence of the TEMPO spectra is detected. This is a consequence of larger fractions of hydrophilic PEO and larger quantities of residual water in aggregated polymers, as can be deduced from literature reports.[44] This leads to weaker hydrophobic interactions between **PEO-*co*-PDEGA** aggregates and TEMPO. Thus, even a considerable formation of apolar regions cannot be observed through TEMPO (Figure 4.2.3 b), left).[62[62] Turbidity data (see Figure 4.2.4 b)),[87] however indicate aggregation of **PEO-*co*-PDEGA** with ≤ 7% DEGA at ~ 80 °C, where the CW EPR data also at least indicate a jumpwise reduction in a_{iso}. The non-observe of significant apolar cavities by means of TEMPO spin probing should not to be confused with the non-existence of such cavities. The above mentioned observation only implies that the interaction between TEMPO and cavities of **PEO-*co*-PDEGA** with ≤ 7% DEGA is not strong enough to influence the CW EPR spectra significantly. In return, one should keep in mind that an increasing turbidity of a solution does not necessarily coincide with a compaction of polymers.

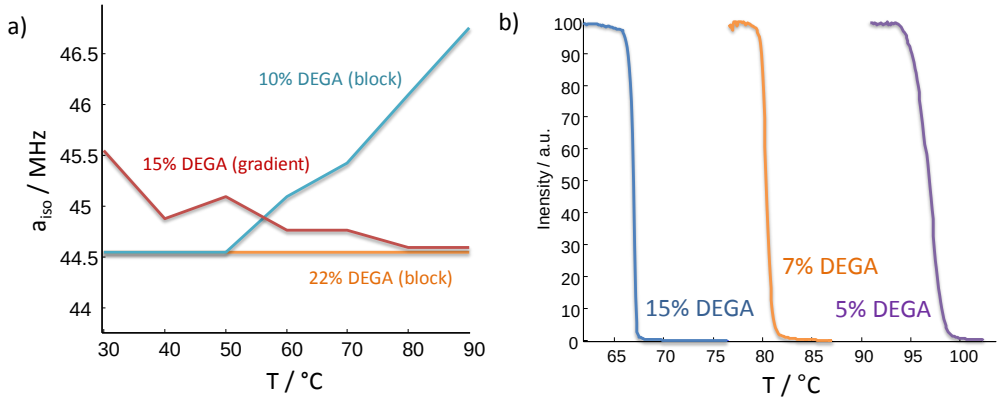

Figure 4.2.4. a) Temperature-dependence of a_{iso} values of species B in different PEO-PDEGA copolymers. b) Turbidity data of **PEO-*co*-PDEGA** solutions with variable amount of DEGA.

For **PEO-*block*-PDEGA** DEGA contents of 10 and 15% lead to increasing a_{iso} for species B with increasing temperature, showing that the probes experience a more polar environment at higher temperatures. Thus, in these cases TEMPO senses dynamic inhomogeneities. In contrast, a DEGA (block) content of 22% leads to the occurrence of static inhomogeneities as they are detected in the cases of **PPO-*co*-PG** and ***hb*PPO-*co*-PG**. Thus, small hydrophobic PDEGA-blocks in **PEO-*block*-PDEGA** can be correlated with *dynamic inhomogeneities* that feature guest exchange at higher temperatures, while large hydrophobic PDEGA-blocks can be correlated with the complete suppression of guest exchange on EPR timescales. Similar observations are made for Pluronics in Section 4.1.

Note that the cloud points derived from turbidity measurements as well as $T_{C,EPR}$ derived from CW EPR, are both independent of the concentrations of the samples in the range from 5 mg/mL to 20 mg/mL and can hence be directly compared.[77] CW EPR measurements are frequently carried out at rather high concentrations, when compared to turbidimetry, to increase the signal intensity.

4.2.2 Discussion

In the following, the correlation between polymer composition and architecture on the one hand and collapse mechanisms on the other hand will be addressed. The three described nanoscopic host-guest interaction schemes that occur during temperature-induced collapses of thermoresponsive polymers will be considered in detail. These three host-guest interaction schemes can be classified into static inhomogeneities and dynamic inhomogeneities, the latter featuring guest exchange either at high temperatures or at temperatures slightly above $T_{c,EPR}$.

General Methodological Reflections

Spin probing with TEMPO yields indirect information about nanoscopic probe surroundings that are polar or apolar. Here, the latter is a consequence of the collapse or aggregation of polymers at $T_{c,EPR}$. It has been demonstrated in Section 4.1 that *macroscopically* detected cloud points can be significantly higher than EPR-derived $T_{c,EPR}$s at a given concentration. This is due to the fact that the macroscopic aggregation of several polymer molecules does not necessarily coincide with the local, nanoscopic, occurrence of apolar, water-depleted cavities, to which EPR measurements with TEMPO as a spin probe are sensitive.[31-33] The cloud point, in contrast, only indicates the temperature at which aggregates become large enough (> 1 µm) to scatter incident light. Nanoscopic inhomogeneities however can just be too small to lead to a detectable increase in the turbidity of a sample. Hence, it is not surprising that the cloud points detected by turbidity measurements are located at higher temperatures than the $T_{c,EPR}$s for **PEO-*co*-PDEGA**, **PPO-*co*-PG** and ***hb*PPO-*co*-PG** (Figure 4.2.2 and Table 4.2.1). In particular all $T_{c,EPR}$s for PPO-*co*-PG are located in the narrow temperature interval between 30 °C and 40 °C, while the turbidity-derived cloud points, T_c, occur in the temperature range between 20 °C and 80 °C, depending on the glycidol content; and for **PEO-*co*-PDEGA** T_c varies from 55 °C to 97 °C, depending on the DEGA content (Table 4.2.1), while $T_{c,EPR}$ is always between 20 °C and 30°C. This observation that $T_{c,EPR}$ is confined to narrow temperature regions, while T_c might vary drastically can be explained by taking into account that spin probe CW EPR is sensitive to *local* apolar cavities. On this local level, the level of oligomeric units and below, the polymers under investigation appear quite similar. I.e. PPO-*co*-PG polymers all feature linear segments of **PPO** of random length, while their overall topology might be linear or hyperbranched and PEO-*co*-PDEGA always features linear DEGA-rich segments. This conclusion is further substantiated by the observation that $T_{c,EPR}$s do, like in the case of Pluronics, not depend on the concentration of the polymers, which indicates that an interpretation based on local apolar cavities formed in unimers or of low aggregation number is appropriate.[32]

In contrast to the local collapse, the macroscopically detected collapse at T_c is dependent on the overall topology of a polymer. Large scale architectures can vary on a broad range for systems with the same or similar monomer and oligomeric units and can cause drastic variants in macroscopically detected cloud points.

Table 4.2.1. Turbidimetry-derived cloud points (T_c) of the copolymers under investigation.[88]

PPO-*co*-PG	**T_c/°C**	***hb*PPO-*co*-PG**	**T_c/°C**	**PEO-*co*-PDEGA**	**T_c/°C**	**PEO-*b*-PDEGA**	**T_c/°C**
2% G	21	3% G	24	29% DEDA	55	22% DEDA	80
11% G	32	12% G	33	15% DEGA	67	15% DEGA	100
16% G	36	17% G	40	7% DEGA	81	10% DEGA	-
22% G	39	20% G	43	5% DEGA	97		
25% G	79	32% G	83				

Also the fractions of hydrophilic and hydrophobic comonomers may affect T_c drastically. The aggregation propensity of macromolecules in aqueous solution is directly related to their hydrophilic-hydrophobic balance.[89] Such, T_c is lower for macromolecules that contain larger fractions of hydrophobic comonomers. As a consequence, more hydrophobic copolymers aggregate and form extended supramolecular assemblies at lower temperatures, compared to their more hydrophilic counterparts.

For both, PPO-*co*-PG and PEO-*co*-PDEGA, turbidimetry detects sharp T_cs (see Figure 4.2.2 and 4.2.4), while EPR detects a slower and steadily increasing χ_B. This can be explained as follows: From literature reports[31] it is known that only a few nanoscopic cross-linking points between different chains are sufficient for the formation of supramolecular assemblies and for meso-/macrophase separation. Such phenomena are detected by means of turbidimetry, although large segments of the chains might still be swollen.[31] The complete dehydration process of all the monomers, as observed through χ_B, may spread over a wider temperature range – similar to the dehydration of Pluronics (Section 4.1). Such, on the one hand, the progressing dehydration of the polymers – subsequent to cross-linking – does not influence the turbidity of a solution. On the other hand, the propensity for incorporation of TEMPO rises with an increasing fraction of dehydrated polymer segments. Therefore, the turbidity transition may appear sharp, although the EPR transition is much broader.

Dynamic Inhomogeneities as a Consequence of a Thermally Induced Two-step Collapse Mechanism of PEO-co-PDEGA

For **PEO-*co*-PDEGA** with ≥ 15% PDEGA a distinct species B can be observed and a_{iso} decreases with temperature. This is a consequence of dynamic inhomogeneities that lead to spin probe exchange at temperatures slightly above $T_{c,EPR}$, but to suppression of exchange at further elevated temperatures.[31, 35, 36] This can be explained in inverse analogy to the two explanations for the shift of a_{iso}in systems of Pluronics with ≥ 70% PEO, as stated in Section 4.1.1.

1) An ongoing dehydration of the apolar cavities, formed above $T_{c,EPR}$, leads to a steady decrease of the polarity of the probes' environment and hence to a decrease in a_{iso} of species B with increasing temperature, ever more separating the two spectral components A and B.

2) With increasing temperature above $T_{c,EPR}$ the volume fraction of collapsed regions and the density of the formed aggregates (due to ongoing dehydration; see point 1) increases and hence dynamic probe exchange between apolar and polar regions becomes less probable. Consequently, averaging between the spectral components A and B diminishes with rising temperature and a_{iso} shifts less and less, until a constant value (of the mere species B) is reached.

Taking into account that DEGA is a rather hydrophobic comonomer (PDEGA as a homopolymer is insoluble in water)[90] and that **PEO-*co*-PDEGA** is consequently an amphiphilic gradient copolymer, one can further identify the process behind the dynamic inhomogeneity discussed here: Amphiphilic random copolymers composed of more hydrophilic (EO) and more hydrophobic (DEGA) monomers feature conformations in aqueous solution, in which i) the hydrophobic monomers cluster due to hydrophobic attraction,[91-93] while ii) PEO-rich polymer segments are swollen and reach out into the medium, like in lyotropic phases. Indeed, several groups reported the observation of small unimer micelles of amphiphilic random copolymers in which hydrophobic comonomers form the micellar core and hydrophilic patches the corona (mesoglobules like in Figure 4.2.5 a) on the left).[94-96] The formation of such micelles, however, is competitive to intermolecular aggregation. Frequently it is observed that an increase in concentration[97] or polymer hydrophobicity[10, 98] lead to large-scale aggregation of the small micelles[99] or to their fusion and the subsequent formation of large aggregates with one large core.[100] Swanson and co-workers furthermore showed that thermoresponsive polymers that randomly incorporate hydrophobic comonomers form intramolecular, flower-like micelles below the transition temperature, while large-scale aggregation takes place above the transition temperature.[10, 101] However, from mere CW EPR and turbidity measurements one cannot deduce the actual morphology of the structures formed during the phase

transition of **PEO-*co*-PDEGA**. Despite this drawback, judging from what is known about amphiphilic random copolymers (as stated above) it is assumed in the following that the phase transition proceeds via the formation of small micelles/aggregates constituted of one or only a small number of polymer strands. The subsequent formation of larger structures takes then place through aggregation of the small micelles/aggregates themselves. Such two-step processes are often observed for amphiphilic copolymers like **PEO-*co*-PDEGA**. In Figure 4.2.5 a) such a mechanism is schematically depicted. Note that it only represents a single one of several different possible two-step mechanisms and should hence only be considered as a clearly arranged schematic visualization of the phase transition of **PEO-*co*-PDEGA**. Nonetheless, Borisov and Halperin have reported and physically described structures like the one depicted in Figure 4.2.5 a) on the left already 15 years ago and showed that bridging effects between these micelles can lead to the formation of larger multimeric structures.[102] Zhang, Winnik and Wu could furthermore show that the transition from a random coil state to such a core-shell structure proceeds via the formation of ordered coils. In this structure the hydrophobic monomers are concentrated in the center of a premicellar conformation, but the polymer is still swollen, such that the hydrophobic monomers do not strongly cluster.[103]

Concluding, micellization may well be facilitated by the nature of copolymerization of gradient **PEO-*co*-PDEGA**, as short patches along the chains with only or mainly DEGA units may exist. Thus, already at low temperatures **PEO-*co*-PDEGA** may adopt a state in which DEGA monomers are clustered or spatially close, surrounded by PEO (Figure 4.2.5 a) left-hand side). With increasing temperature the PEO segments are dehydrated, too, to form dense globules of only a small number of polymer chains. At even higher temperatures these globules subsequently aggregate to form larger objects, since water becomes an increasingly poor solvent for PEO. An ongoing growth of hydrophobic cavities accompanied by the dehydration of PEO residues with rising temperature would arise in this scenario. This would explain the observed CW EPR spectra of **PEO-*co*-PDEGA**. Molecular dynamics (MD) simulations support the assumed collapse mechanism, since simulated aggregates of **PEO-*co*-PDEGA** with 15% PDEGA at 90 °C are constituted of several aggregated globules. The globules themselves are formed formerly (at 45 °C) by individually collapsed unimers (Figure 4.2.5 b)). Note that the data gained from MD simulations are only supporting the assumption of a two-step mechanism since they reproduce the picture one can deduce from the literature, but the simulations should not be regarded as a basis for argumentation: MD simulations of such polymeric systems are likely to become trapped in local energetic minima, depending on the initial constitution of the simulated system and other factors. (Details on the simulations can be found in Appendix A.4.2.)

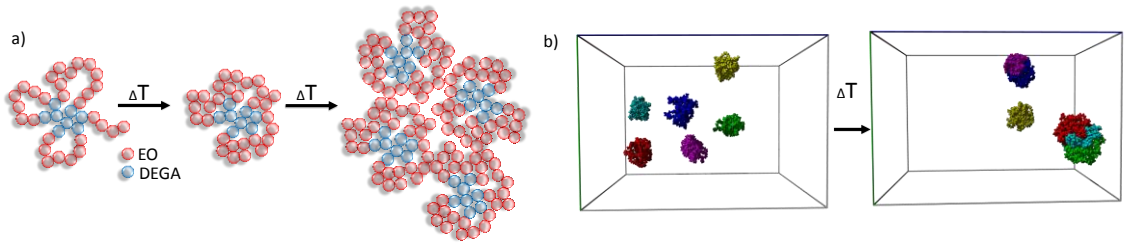

Figure 4.2.5. a) Proposed collapse mechanism for gradient **PEO-*co*-PDEGA** with a PDEGA content of 15% (EO: red, DEGA: blue). b) Aggregates of **PEO-*co*-PDEGA** with 15 % DEGA at 45 °C (left) and 90 °C (right), each after 4 ns of MD simulation. Different colors indicate different polymer strands. Supramolecular aggregates (right) are composed of spherical unimeric objects that occur already at lower temperatures (left).

Despite the exact micelle/aggregate morphology, the sharp macroscopic phase transition that has been observed for **PEO-*co*-PDEGA** (Figure 4.2.4) should be attributed to the formation of large structures through aggregation of a large fraction of **PEO-*co*-PDEGA** (second step of the entire phase transition). $T_{c,EPR}$ should be attributed to the first step of the phase transition, during which small micelles (with apolar interior) are formed that do not influence the turbidity of **PEO-*co*-PDEGA** solutions. The CW EPR data can hence be explained in accordance with the current knowledge about amphiphilic copolymers, which suggests the two-step collapse mechanism. Both explanation for the shifts in a_{iso} that were stated at the beginning of this section are in full agreement with a two-step phase transition: The probes can diffuse in and out of the small micelles/aggregates slightly above $T_{c,EPR}$ (first step), but cannot if the micelles/aggregates dehydrate further and form much larger structures at higher temperatures above T_c (second step).

Static and Dynamic Inhomogeneities in PEO-block-PDEGA Explained by Micellar Configuration

For **PEO-*block*-PDEGA** with high PDEGA (≥ 22%) content TEMPO spin probing reveals static inhomogeneities (i.e. no dynamic exchange at any temperature), while lower PDEGA contents (≤ 15%) lead to dynamic inhomogeneities with static a_{iso} values of species B only at temperatures slightly above $T_{c,EPR}$ and increasing a_{iso} values at higher temperatures. The same explanations as stated in Section 4.1 for the TEMPO spectra for Pluronics with low PPO content can account for the occurrence of the dynamic inhomogeneities in **PEO-*block*-PDEGA** with low PDEGA content (the apparently "reverse" behavior as compared to **PEO-*co*-PDEGA**).[104-106]

In Figure 4.2.6 a) the formation of a micelle is illustrated schematically. Note that this sketch shall only aid to visualize the phase transition of **PEO-*block*-PDEGA,** since by means of CW EPR and turbidimetry one cannot determine which morphology (micellar, lamellar, hexagonal etc.) the **PEO-*block*-PDEGA** aggregates actually have. Figure 4.2.6 demonstrates that in aqueous solutions most of the known conformations of aggregates of amphiphilic diblock polymers consist of an inner segment that is constituted of the more hydrophobic blocks and an outer, solvent-exposed segment that consists of the more hydrophilic blocks (as in common lytropic phases).[27]

The translational displacement of TEMPO is $\sqrt{\langle x_T^2 \rangle} \approx 9$ nm for **PEO-*block*-PDEGA** with 22% DEGA and $\sqrt{\langle x_T^2 \rangle} \approx 17$ nm for 10% DEGA at 80°C (for details on the calculation see Appendix A4.1 and A4.2.5). The fact that one cannot observe any T_c for **PEO-*block*-PDEGA** with 10% DEGA, but a clear $T_{c,EPR}$, as well as a drastic difference between T_c and $T_{c,EPR}$ for 15% and 22% DEGA, furthermore indicates that the formed micelles are in general very small. Molecular dynamics simulations further support the above explanation (Figure 4.2.6 b)). At elevated temperature(s) (90 °C), on average

2845.5 inter-chain contacts per chain are found for **PEO-*block*-PDEGA** with 10% DEGA and 3139.3 for 22% DEGA (at similar overall weight fractions). Assuming inter-chain contacts to be a measure for the density of a micelle, one could state that a micelle composed of only 10% DEGA actually is not as dense as a micelle composed of 22% DEGA. It should be noted that the simulations again merely further support the picture that was deduced above from other experimental sources, but are by no means a stand-alone basis for argumentation.

A similar temperature-dependent behavior has been observed for aqueous Pluronic solutions in the previous section.[32] The block structure of Pluronics and of **PEO-*block*-PDEGA** triggers a comparably promoted ability to form lyotropic phases. This leads to the occurrence of static inhomogeneities at low content of hydrophilic comonomers and to the occurrence of dynamic inhomogeneities at high content of hydrophilic comonomers, as the size of the hydrophobic block is smaller (dynamic inhomogeneity) or larger (static inhomogeneity) than $\sqrt{\langle x_T^2 \rangle}$. Such, the volume fraction of the hydrophobic blocks influences the constitution and properties of micelles at $T_{c,EPR}$[27] and consequently also the interact with small amphiphiles like TEMPO.[62] In contrast, corresponding random copolymers with similar composition are likely to lead to collapse mechanisms as described for **PEO-*co*-PDEGA** and hence would yield dynamic inhomogeneities with probe exchange already slightly above $T_{c,EPR}$.

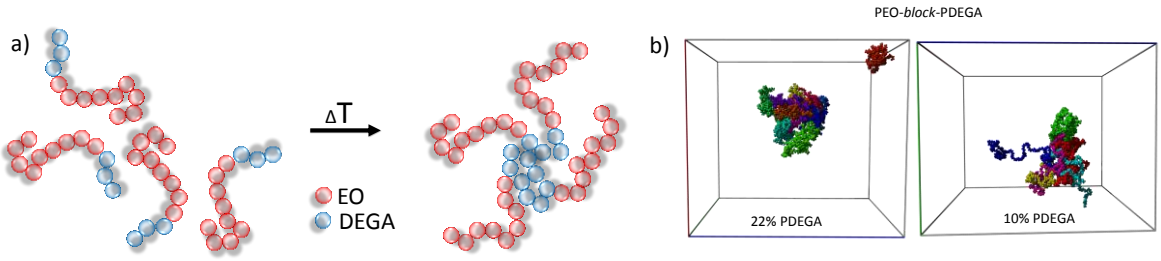

Figure 4.2.6. a) Formation of **PEO-*block*-PDEGA** micelles. The DEGA blocks (blue) are located in the micellar core. The PEO blocks (red) constitute the corona. b) Snapshot from molecular dynamics simulations of micelles formed by **PEO-*block*-PDEGA** at 90°C with different DEGA content. The colors indicate different polymer chains.

Static Inhomogeneities as a Consequence of Aggregation of PPO-co-PG and hbPPO-co-PG

In pronounced contrast to DEGA-containing systems, spin probing with TEMPO in aqueous solutions of **PPO-*co*-PG** and ***hb*PPO-*co*-PG** does not lead to the detection of dynamic inhomogeneities. On the contrary, a_{iso} values remain constant (static inhomogeneities) at any temperature and comonomer ratio, which indicates that no significant conformational reorganizations on length scales of a few nanometers (the direct environment of TEMPO) take place in aggregates of **PPO-*co*-PG** – independent of the PG content. Interestingly, while a_{iso} does not change, the maximum of the mole fraction of the spectral species B, χ_B, varies significantly from 0 to ~0.6, depending on the glycidol-content of **PPO-*co*-PG** and ***hb*PPO-*co*-PG**. From the turbidity data shown in Figure 4.2.2 one can deduce that macroscopic aggregation takes place for all copolymers with a glycidol content ≤ 25%, with a steadily increasing tendency to aggregate earlier, as the glycidol content decreases. Contrariwise, one can observe that χ_B decreases strongly at any given temperature if the glycidol content deviates from 11-12% (in both cases: linear and hyperbranched PPO-*co*-PG copolymers). Judging from the turbidity and the EPR data this is a consequence of the following:

1) At low glycidol contents (below 11%) the aggregates are too dense to be penetrated by the TEMPO spin-probes for two reasons: i) With increasing glycidol content, the a_{iso}-values of the hy-

drophobically enclosed probes increase slightly, yet significantly (from 45.2 ± 0.1 MHz → 45.5 ± 0.1 MHz), accounting for a higher water content of the aggregates (entrapped by glycidol monomers) at higher glycidol contents and for a lower polymer density in the aggregates. ii) CW EPR on **PPO-*co*-PG** with more hydrophobic 16-DSA instead of TEMPO reveals that the spin-labeled fatty acids are taken up by apolar cavities even when TEMPO stays primarily in the water-rich region, because of stronger hydrophobic interactions between DSA and the polymers (see the Appendix Figure A.4.2.4).

2) Above 12% glycidol content, the polymers' tendency to aggregate is low (as can be deduced from the turbidity measurements in Figure 4.2.2), thus the formed aggregates are likely of low density and too loosely packed to act as efficient, strongly interacting hydrophobic hosts.

Concluding, there is an optimal content of glycidol for the incorporation of TEMPO in **PPO-*co*-PG** aggregates, since their molecular composition drastically influences their ability to interact with small guest molecules, as the PG content determines the aggregate density. It is unexpected, though, that changing the polymer constitution from linear to hyperbranched (Figure 4.2.1 a) and b)) does not lead to any fundamental change in the type of inhomogeneity. The a_{iso}-values of incorporated spin probes in aggregates of **PPO-*co*-PG** and ***hb*PPO-*co*-PG** develops similarly with temperature in both cases. Hence, corresponding inhomogeneities can be regarded as static independently of the topology of the polymers. Also the maximum uptake was achieved with approx. 11-12% glycidol in both systems. However, the overall fraction of incorporated TEMPO molecules shrinks when changing the architecture from linear to hyperbranched (Figure 4.2.2). This observation can be explained when assuming that TEMPO is primarily enclosed into aggregates formed by several molecules.

For the sake of simplicity assume that unimers of ***hb*PPO-*co*-PG** are of globular shap (at least closer to globular than their linear analogues).[107] Above $T_{c,EPR}$ water becomes a poor solvent for PPO, but PPO-rich regions are not able to phase separate completely to form the core of an aggregate as there are considerable structural constraints. In contrast, linear **PPO-*co*-PG** molecules can arrange such that PPO-rich segments constitute an aggregated core and glycidol-rich segments build a sparse (the glycidol content is relatively low, ≤ 25%) layer around the hydrophobic PPO clusters, as depicted in Figure 4.2.7. Such, the volume fraction of PPO-rich regions (chain overlap volume in Figure 4.2.7) should be higher for linear copolymers, compared to hyperbranched ones.

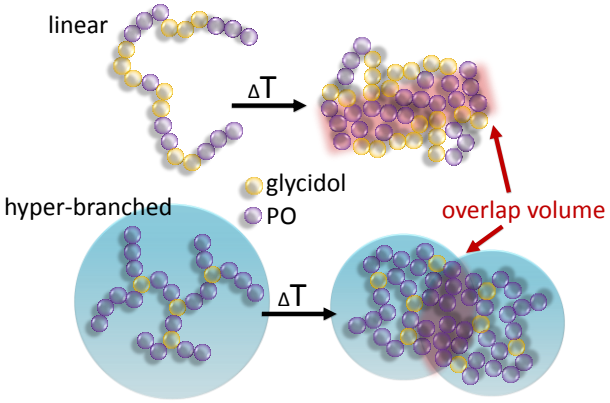

Figure 4.2.7. Proposed way of molecular aggregation of linear and hyperbranched **PPO-co-PG** thermoresponsive polymers (glycidol: yellow, propylene oxide: violet).

Since CW EPR spectra of TEMPO in solutions of **PPO-*co*-PG** and in solutions of ***hb*PPO-*co*-PG** at a given glycidol content are very similar, it is likely that aggregates of several molecules (as indicated in Figure 4.2.7), not mere collapsed PPO strands, primarily constitute hydrophobic cavities in the case of **PPO-*co*-PG**,. If PPO-strand compaction (e.g. by coil-to-globule transition) were the primary mechanism behind the TEMPO incorporation the molecular architecture should lead to more pronounced differences in the CW EPR spectra. This is substantiated by the slope of the turbidity profiles in Figure 4.2.2. The turbidity data strongly suggest that the polymers aggregate already between 30 °C and 40 °C (although the drastic descent of transmitted intensity takes place at higher temperatures), i.e. in the same temperature range in which $T_{c,EPR}$ is located (Figure 4.2.2 c)), since the transmitted light intensity decreases slightly already below T_c (the inflection points of the profiles in Figure 4.2.2). Hence, the onset of the formation of apolar cavities of **PPO-*co*-PG** and ***hb*PPO-*co*-PG** is already accompanied by intermolecular aggregation. This is likely to be a consequence of the small fraction of hydrophilic PG, which might be too small for the development of a dense layer of hydrophilic PG that surrounds the collapsed PPO. Such, PPO above $T_{c,EPR}$ tends to compensate the poor solvent (water) by aggregation with PPO segments of other polymers, which leads to larger aggregates already at $T_{c,EPR}$.

4.2.3 Relating Structure to Temperature-Response

In this section the structural and topological properties of selected poly(alkylene oxide)s are varied and their inverse phase transitions are investigated. One can relate these properties to certain collapse mechanisms and to corresponding inhomogeneities on the nanoscale:

The thermally induced aggregation of amphiphilic block copolymers (**PEO-*block*-PDEGA** and Pluronics) is fostered by the possibility to form lyotropic phases. Such, above $T_{c,EPR}$ initially relatively large and ordered structures are formed that initially do not allow for dynamic exchange of guest molecules like TEMPO, which are incorporated into the micellar cores. However, if the fraction of hydrophobic blocks is low and the micellar cores are consequently small, and of low density (compared to polymers with higher fractions of hydrophobic blocks) guest exchange can take place at high temperatures. Then, the kinetic energy of the guests becomes large, such that the distance from the micellar core to the aqueous medium can be bridged through translational diffusion. Thus, the occurrence of static or of dynamic inhomogeneities that feature guest-exchange at high temperatures can be regulated by adjusting the size of the hydrophobic.

The collapse mechanism of random copolymers as seen on the nanoscale depends crucially on the hydrophobicity/hydrophilicity of the employed comonomers and on the polymer composition. A small amount of strongly hydrophilic comonomers next to a large fraction of relatively hydrophobic comonomers like in **PPO-*co*-PG** and ***hb*PPO-*co*-PG** leads to the exclusive occurrence of static inhomogeneities, because of a strong tendency towards intermolecular aggregation and hence to the formation of large aggregates already at the onset of the nanoscale collapse of the polymers. The tendency towards aggregation is determined by the hydrophilic-hydrophobic balance, though. On the contrary, a small amount of very hydrophobic comonomers in gradient amphiphilic copolymers like in **PEO-*co*-PDEGA** leads to the occurrence of dynamic inhomogeneities, featuring guest-exchange at temperatures slightly above $T_{c,EPR}$, while exchange does not take place at further elevated temperatures. This can be understood taking into account that the strongly hydrophobic DEGA clusters in the center of small micelles/aggregates at $T_{c,EPR}$ to yield only rather small collapsed structures which allow for guest-exchange. With further increasing temperature and decreasing solubility of PEO these small globules form larger aggregates, which do not allow for guest ex-

change anymore. Hence, the occurrence of static or dynamic inhomogeneities in amphiphilic random copolymers can be controlled by the hydrophobicity of the respective comonomers.

Principles as stated above might help to find particular temperature-dependent properties, desired for certain applications of thermoresponsive polymers and, given the general importance of functional PEO and PPO, might facilitate their purposeful, application-oriented synthesis. TEMPO as a small amphiphilic molecule has important features like molecular structure and the ensuing physicochemical properties in common with many drugs and can thus be regarded as a model compound for probing the applicability of thermoresponsive systems in actual drug delivery or in analytical/sensing research.[89]

4.3 Impact of Amino-Functionalization on the Response of Poly(ethylene oxide) to pH-Sensitivity

PEO-*co*-PDEGA is basic through the amino-functionalization with DEGA. In the following section, it will be demonstrated that this leads to remarkable pH-responsiveness. The amino-functionalization will be shown to trigger the emergence of intriguingly complex phase transitions of the otherwise rather simple and widely used PEO. The arising tunable phase transition modes are highly interesting from a materials science point of view, since they allow for targeted transport of guest compounds through body fluid. In particular, the thermoresponsive behavior of PEO-*co*-PDEGA exhibits interesting pH-sensitivity at temperatures between 25 °C and 45 °C. The latter value represents the upper limit of therapeutic hyperthermia, defining the clinically relevant temperature range and underlining the potential importance of PEG-*co*-PDEGA for medical applications.[108]

For investigating the influence of pH on the thermoresponsiveness amino-functionalized PEO **PEO-*co*-PDEGA** with 29% DEGA (molecular weight: 3300 g mol^{-1}) and **PEO-*block*-PDEGA** with 22% DEGA (molecular weight: 6600 g mol^{-1}) were selected. The PDEGA fractions will be omitted in the following. For each measurement the polymer concentration was adjusted to 5 wt%.[32, 33, 35]

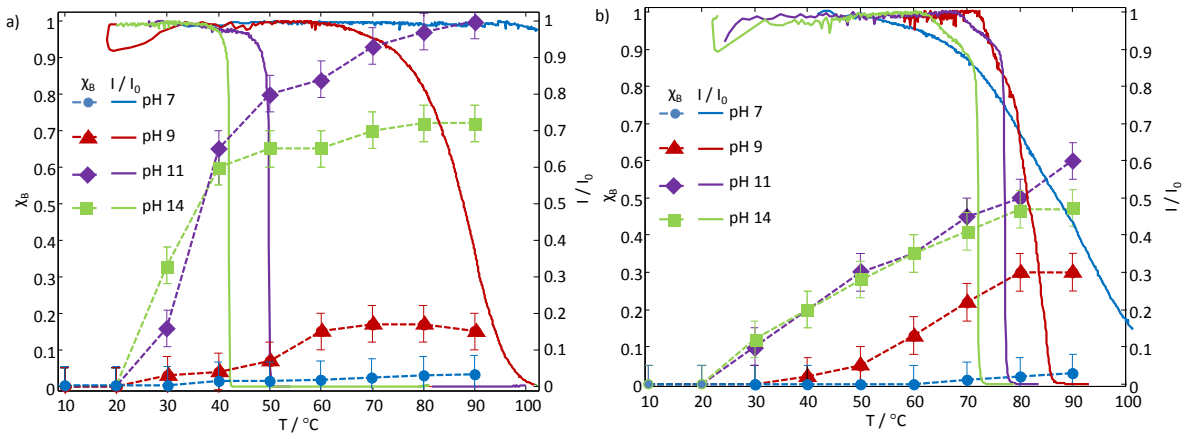

Figure 4.3.1. a) Fraction of TEMPO incorporated into collapsed **PEO-*co*-PDEGA** domains, χ_B, as function of temperature for different pH (symbols connected by dashed lines). The corresponding turbidity measurements of the solutions (transmitted light intensity, I/I_0, respectively) are shown as solid lines (see legend). All measurements were performed at 5 wt% polymer concentration. b) The fraction of TEMPO incorporated into collapsed **PEO-*block*-PDEGA** domains, χ_B, and the transmitted intensity as a function of temperature for different pH. The color code is the same as in a). Error bars denote uncertainties in spectral simulations (see Appendix A4.3.).

In solutions of **PEO-*co*-PDEGA**, the first occurrence of TEMPO species B (χ_B) can be observed in the narrow temperature range between 20°C and 30 °C at pH 9, 11 and 14 (Figure 4.3.1 a)). At pH 7, the fraction of species B is very small, such that it is hard to determine the temperature range in which species B occurs with the same accuracy. Nonetheless, at any pH, the χ_B values > 0 clearly indicate the thermal response and collapse of **PEO-*co*-PDEGA** when exposed to heat. (Note that linear homo-PEO does not give rise to any changes in χ_B or turbidity[24] under the present conditions.) The spectral contribution of species B at a given temperature varies drastically with pH, as a consequence of changing hosting parameters with changing degree of DEGA protonation. Interestingly, for pH 11, χ_B = 1 at 90 °C, which translates to a complete uptake of TEMPO probes into apolar cavities. So far, this has not been observed for any other thermoresponsive system investigated by means of CW EPR at the given concentration (5 wt%).[32, 88]

When inspecting the degree of protonation, the narrowness of the temperature range in which collapsed domains initially occur (between pH 9 and 14: 20 °C to 30 °C) is quite unexpected, since changes in pH alter the chemical structure of the polymer. The pK_a of PEG-*co*-PDEGA is around 10 (see Appendix Figure A4.3.6.). Such, for the percentage of protonated amines one obtains: pH 7: > 99.9 %; pH 9: ~ 90 %; pH 11: ~ 10 %; pH 14: < 0.1 %. Thus, one would expect differences in hydration energy and strong effects on collapse temperatures. This is qualitatively not the case here. Therefore it is reasonable to assume that at any pH (varying) chemically equivalent fractions of non-protonated DEGA units are distributed along the polymer chains, which trigger the local polymer collapse as sensed by TEMPO.[32, 88]

Intriguingly, the turbidity of the **PEO-*co*-PDEGA** solutions remains unchanged, if the temperature does not exceed 42 °C, although structures appear that are large enough to host significant amounts of TEMPO above 20-30 °C. For instance, at pH 11 and 14 more than 50% of the probe molecules experience an apolar environment at 40 °C (Figure 4.3.1 a)). Thus, one can conclude that **PEO-*co*-PDEGA** forms a considerable number of small nanoaggregates at pH 11-14 (likely of globular shape, as shown in the previous section)[88] that are too small to scatter light and that remain dissolved at intermediate temperatures (no increase in turbidity was observed for longer waiting periods). The mean-square diffusional displacement of the TEMPO probes at 40 °C is $\sqrt{\langle x_T^2 \rangle}$ ≈ 3.5 nm at pH 11 and $\sqrt{\langle x_T^2 \rangle}$ ≈ 4.8 nm at pH 14 (see ref. [31] and Appendix 4.1). Taken together, one may estimate the radius of the aggregates to ~5-10 nm from CW EPR. This estimation is independetly substantiated by dynamic light scattering data that yields an average hydrodynamic radius of the nanoaggregates of ~9 nm at 40°C (see Appendix Figure A3.4.5). In contrast at 25°C, where χ_B = 0 and hence all polymers are indiviually dissolved, the unimers exhibit an average hydrodynamic radius of ~2 nm.

In the present context, the sigmoidal and steep development of the χ_B functions with temperature (Figure 4.3.1 a)) is clearly indicative of a high degree of cooperativity of the nanoaggregate formation.[109] Since dehydration of PEO typically is a non-cooperative process[1] it is reasonable to assume as underlying cause for the observed cooperativity that some of the randomly distributed deprotonated, hydrophobic[88] DEGA moieties can always be found on the surface of any collapsed structure of **PEO-*co*-PDEGA**. At increased concentration such surface moieties may well facilitate the attraction of still swollen **PEO-*co*-PDEGA**. As a consequence, a cooperative and for the nanoscale sharp transition can be observed, making it even more interesting that the nanoaggregates remain macroscopically solvated below 40 °C. This explanation is also in agreement with the fact that at pH 9 no cooperative aggregation can be observed: too many DEGA units are charged for an effective hydrophobic attraction of nearby polymers.

The cloud point, T_c, in contrast to the nanoaggregate formation, is dependent on the solution pH to a certain degree and can be shifted from 42 °C at pH 14 to 85 °C at pH 9 (Figure 4.3.1 a)). At 30 °C no changes in turbidity were observed even over hours. At pH 7 changes in turbidity could not be detected, likely as a consequence of the relatively high amount of charged DEGA groups facilitating polymer solvation and elongation in the probed temperature range. Since no abrupt changes in χ_B can be observed at the cloud points at any of the probed pH values, one can deduce that the initially formed nanoscopic aggregates cluster to form large structures at T_c and do not rearrange into other conformations, supporting the previously deduced idea of the two-step collapse mechanism of **PEO-*co*-PDEGA** (see Section 4.2.2). Since T_c decreases with increasing pH, it is at hand to assume that deprotonation of the DEGA units and accompanying loss of coordinating water molecules leads to lower solvation energy of the **PEO-*co*-PDEGA** nanoaggregates (the loss of solvating water with increasing pH is also reflected in the CW EPR spectra, as shown in Appendix A4.3). Note that also this second transition step, the clustering of nanoaggregates, exhibits a high degree of cooperativity at pH 11 and 14, likely again due to deprotonated, surface-exposed DEGA moieties.

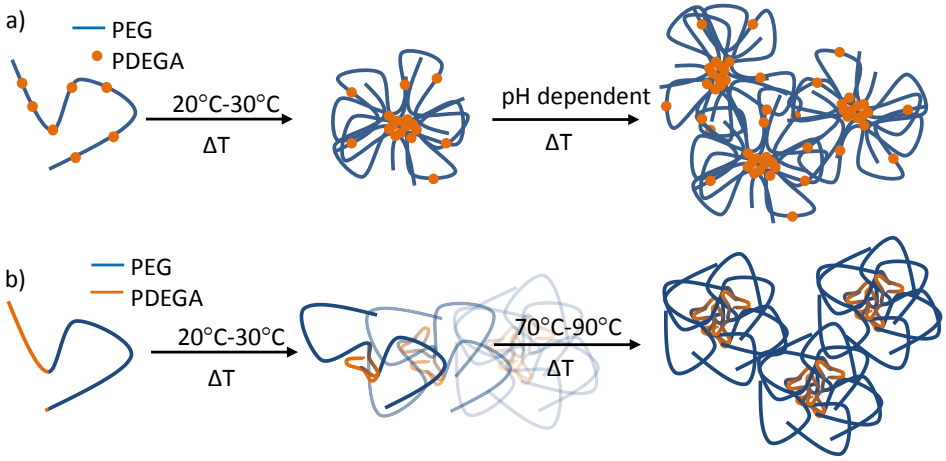

Figure 4.3.2. Schematic illustration of the temperature-triggered phase transitions of PEO-*co*-PDEGA copolymers. a) **PEO-*co*-PDEGA**: Initially small aggregates are formed and remain dissolved. This occurs between 20°C and 30°C. In a second step, the aggregates cluster to form large structures. The aggregation temperature can be shifted from 42 °C to 85 °C by adjusting the pH. b) **PEO-*block*-PDEGA**: above 20 °C-30 °C micelles grow steadily until they aggregate between 70 °C and 90 °C.

The picture of the temperature-induced phase transition of **PEO-*co*-PDEGA** that arises from the data and above interpretation is schematically depicted in Figure 4.3.2 a). The figure should be read as follows: In a first step metastable nanoaggregates occur, which remain dissolved, i.e., the solution remains clear. They are depicted with the hydrophobic DEGA units clustered in the center, which is a likely conformation for amphiphilic random copolymers as explained in the previous section.[10, 88, 102, 103] If the temperature is further increased, the nanoscopic aggregates cluster in a second step to form large structures that precipitate. The first step takes place in a confined temperature range with respect to pH, while the temperature of the second step is stronger dependent on pH. Interestingly, both steps of the phase transition of **PEO-*co*-PDEGA** are very sharp at pH 11 and 14, while conventional PEO normally features a rather broad transition range.[1] This is indicative for a high degree of cooperativity and highlights the impact of amino-functionalization on the physicochemical properties of PEO.

Like for **PEO-*co*-PDEGA** the nanoscale collapse of its block-structured analogue, **PEO-*block*-PDEGA**, sets in between 20 °C and 30 °C at pH 9, 11 and 14. Yet, in contrast to **PEO-*co*-PDEGA**, χ_B grows steadily until a temperature of 80 °C is reached (Figure 4.3.1 b)), indicating a non-cooperative

nanophase separation. Collapsed domains grow steadily, resulting in an increasing volume fraction of water-depleted regions that entrap TEMPO molecules. Notably, again no changes in turbidity can be observed until temperatures above 70°C are reached, suggesting that the formed nanoaggregates remain solvated at intermediate temperatures ($\sqrt{\langle x_T^2 \rangle} \approx 3.0$ nm for species B in both cases, for pH 11 and 14, at 80 °C). Only between 70 °C and 90 °C the nanoaggregates of the block copolymer cluster to form larger structures, as can be deduced from the turbidimetry curves in Figure 4.3.1 b). The turbidity does not decrease as steeply with temperature as for **PEO-*co*-PDEGA** at pH 11 and 14 (initially small slope of I/I_0), indicating a lower degree of cooperativity not only of the nanoscale collapse (see the slopes of the χ_B functions), but also of the macroscopically detectable aggregation step in the case of block architecture. This lack in cooperativity of the phase transition and the more "PEO-like" behavior of **PEO-*block*-PDEGA** is likely a consequence of the block architecture: DEGA blocks form the core of **PEO-*block*-PDEGA** aggregates, while the PEO blocks build the corona as explained in the previous sections (depicted in Figure 4.3.2 b)).[104] Such, the DEGA units are screened by the PEO coronas not allowing for effective attraction of swollen **PEO-*block*-PDEGA** molecules (for the local collapse) or nanoaggregates (for macroscopic aggregation), hampering DEGA-mediated cooperativity. This is also in good agreement with the observation that the average fraction of incorporated TEMPO is much smaller for **PEO-*block*-PDEGA** than for **PEO-*co*-PDEGA**, since different aggregate conformations are very likely to yield differently favorable environments for TEMPO probes. Note that this is also coherent with the observation stated in the previous section that more densely packed structures may incorporate less amphiphiles than looser aggregates of randomly arranged copolymers.[88] At pH 7, no significant interaction between TEMPO and **PEO-*block*-PDEGA** can be observed by means of CW EPR, but a very broad turbidity transition that crosses the other three turbidity functions (Figure 4.3.1 b)). This phenomenon is a consequence of the formation of inverse micelles: Since at pH 7 most of the DEGA units are charged, they constitute the corona of **PEO-*block*-PDEGA** aggregates, while PEO forms the core and now triggers the thermal response. Thus, a broad transition-temperature range is observed, as it is characteristic for PEO.[1]

It is noteworthy that the onset of the nanophase separation (EPR) and the macroscopically visible aggregation event of **PEO-*block*-PDEGA** (turbidity) are separated by more than 50 °C. In a very wide temperature range the block-copolymer forms nanoaggregates that remain dissolved while for **PEO-*co*-PDEGA** the nanoscopic and macroscopic collapse temperatures are significantly closer (see Figure 4.3.1). To the best of my knowledge, such drastic differences between the nanoscale collapse of a polymer and the macroscopic aggregation have not been reported to date. The general phase transition mode of **PEO-*block*-PDEGA** is schematically shown in Figure 4.3.2 b). As for its gradient analogue, the phase transition begins in the narrow temperature range between 20 °C and 30 °C independent of pH. Yet in contrast to **PEO-*co*-PDEGA**, aggregates of **PEO-*block*-PDEGA** grow steadily, until the cloud point is reached.

Hosting amphiphilic structures like TEMPO without precipitating is an unusual and desirable property of polymers for drug transport through body fluid. Drugs could be transported in solution, while not being subject to proteolytic degradation. Obviously **PEO-*co*-PDEGA** and **PEO-*block*-PDEGA** are good examples of the versatility of functional PEO for future drug-delivery applications. Furthermore, the second step of the temperature-induced phase transition of these versatile structures could be exploited to accumulate polymer-drug conjugates in tissue that is subject to hyperthermia and/or pH irregularities,[110] although in the present state precipitation within the temperature range achievable through hyperthermia is only observed at pH 14. This discrepancy, however,

may well be overcome by adjusting the molecular weight of the polymer or by incorporating a higher fraction of DEGA units.

In summary this section shows that amino-functionalization of PEO in combination with a specific copolymer topology can lead to the emergence of previously unexpected physicochemical properties that allow for precise manipulation of complex phase transition modes by adjusting environmental conditions. At high pH **PEO-*co*-PDEGA** surprisingly exhibits a high degree of cooperativity during its nanophase transition, reminiscent of a first-order process.[1, 109] Contrariwise, **PEO-*block*-PDEGA** nanoscopically features a more continuous phase transition (non-first order, like it is known for homo-PEO[111]). For both architectures $T_{c,EPR}$ and T_c can differ up to 50°C and the latter is adjustable through the environmental pH, largely independent of the former (indicating nanoaggregate formation).

4.4 Conclusion

CW EPR spectroscopy and spin probing with amphiphilic[62] TEMPO is a well-suited technique for the observation of the temperature-dependent behavior of thermoresponsive polymers on the molecular- and on the nanoscale. The TEMPO spin probing technique allows for the observation of a system from a guest molecule's point of view. Such, insights into the supramolecular interactions between spin probe guests and host polymers can be gained. Although other probes might also be used to investigate the phase-transition of thermoresponsive polymers,[57, 112] it is the handy and favorable partitioning coefficient of TEMPO between water-rich (polar) and water-depleted (apolar) regions and the rather large hyperfine coupling shifts up to 3 MHz, depending on the immediate environment, that renders spin probing with TEMPO a convenient approach. It aids elucidation not only of the fraction of guest molecules incorporated into collapsed polymer molecules, but also of the aggregates' configurations. Since spin-probing CW EPR is an intrinsically local technique it is also sensitive to smallest changes in the molecular environment of the probes.

In principle, fluorescence spectroscopy can yield information about the constitution of the environment of a probe molecule and about its nanoscale confinement similar to the information derivable from EPR spectroscopy. However, fluorescent probes are typically rather large and rigid organic structures that render the detection of inhomogeneities on length-scales of only a few nanometers difficult.[113] Many available EPR spin probes like TEMPO are small and highly mobile and thus do not suffer from this drawback. Small spin probes can enter also smallest, nanoscopic inhomogeneities. Furthermore, CW EPR spans a well suitable timescale. For an experimental method to be sensitive to a certain process, the observation timescale must underrun the timescale of the observed process.[114] This means that by means of X-band CW EPR with a time scale of ~10^{-5} - 10^{-9} s, rotational motions of a probe molecule on a sub-nanosecond timescale can easily be quantified. Effects of only minor sterical confinement due to small apolar cavities can be observed, even if they do not influence a probe's rotational mobility strongly. Fluorescence probing techniques are in the majority of cases sensitive for the nanosecond timescale only.[115] However, note that for the exact elucidation of configurations of large structures fluorescence spectroscopy is likely to be superior to CW EPR.[116]

EPR here could be used – among other things – to elucidate fundamental kinds of dynamic and static nanoscale inhomogeneities already below T_c (up to 50°C lower) and to show that $T_{c,EPR}$ of a thermoresponsive copolymer is independent of the ratio of hydrophilic to hydrophobic comonomers. Both of these aspects appear to be general properties of alkylene oxide-based materials and

highlight the need for complementary usage of intrinsically local and macroscopic, experimental techniques. The EPR-based evidence on the collapse mechanisms should further be substantiated by referring to MD simulations, well-known structural features of the respective polymers and prior, published, knowledge about amphiphilic polymers.

The insights into the phase behavior of advanced stimuli-responsive polymers derived in this Chapter are only possible through the complementary combination of macroscopic and intrinsically local observation techniques. Yet, they are necessary to estimate the in vivo behavior of a hosting system

References and Notes

[1] V. Aseyev, H. Tenhu, F. M. Winnik, *Adv. Polym. Sci.* **2011**, *242*, 29.
[2] M. Rubinstein, R. Colby, "*Polymer Physics*", Oxford University Press, New York, 2003.
[3] D. Schmaljohann, *Adv. Drug Delivery Rev.* **2006**, *58*, 1655.
[4] E. S. Gil, S. M. Hudson, *Prog. Polym. Sci.* **2004**, *29*, 1173.
[5] C. de las Heras Alarcón, S. Pennadam, C. Alexander, *Chem. Soc. Rev.* **2005**, *34*, 276.
[6] C. Wu, X. Wang, *Phys. Rev. Lett.* **1998**, *80*, 4092.
[7] C. Wu, S. Zhou, *Macromolecules* **1995**, *28*, 5388.
[8] P. Alexandridis, J. F. Holzwarth, T. A. Hatton, *Macromolecules* **1994**, *27*, 2414.
[9] K. Skrabania, J. Kristen, A. Laschewsky, Ö. Akdemir, A. Hoth, J.-F. Lutz, *Langmuir* **2007**, *23*, 84.
[10] C. K. Chee, S. Rimmer, D. A. Shaw, I. Soutar, I. Swanson, *Macromolecules* **2001**, *34*, 7544.
[11] H. Katono, A. Maruyama, K. Sanui, N. Ogata, T. Okano, Y. Sakurai, *J. Control. Release* **1991**, *16*, 215.
[12] J. Zhao, G. Zhang, S. Pispas, *J. Poly. Sci. A: Poly. Chem.* **2009**, *47*, 4099.
[13] F. Tanaka, *Macromolecules* **2000**, *33*, 4249.
[14] B. Obermeier, F. Wurm, C. Mangold, H. Frey, *Angew. Chem. Int. Ed.* **2011**, *50*, 7988.
[15] L. A. Lyon, Z. Meng, N. Singh, C. D. Sorrell, A. S. John, *Chem. Soc. Rev.* **2009**, *38*, 865.
[16] S. Ganta, H. Devalapally, A. Shahiwala, M. Amiji, *Journal of Controlled Release* **2008**, *126*, 187.
[17] Y. Zhou, D. Yan, W. Dong, Y. Tian, *J. Phys. Chem. B* **2007**, *111*, 1262.
[18] R. Liu, M. Fraylich, B. R. Saunders, *Colloid. Polym. Sci.* **2009**, *287*, 627.
[19] C. Weber, R. Hoogenboom, U. S. Schubert, *Prog. Polym. Sci.* **2012**, *37*, 686.
[20] J.-F. Lutz, Ö. Akdemir, A. Hoth, *J. Am. Chem. Soc.* **2008**, *128*, 13046.
[21] J.-F. Lutz, A. Hoth, *Macromolecules* **2006**, *39*, 893.
[22] C. Mangold, B. Obermeier, F. Wurm, H. Frey, *Macromol. Rapid Commun.* **2011**, *2011*, 1930.
[23] M. Schömer, J. Seiwert, H. Frey, *ACS Macro Lett.* **2012**, *1*.
[24] V. S. Reuss, B. Obermeier, C. Dingels, H. Frey, *Macromolecules* **2012**, *45*, 4581.
[25] M. Schömer, H. Frey, *Macromolecules* **2012**, 3039.
[26] M. V. Deshmukh, A. A. Vaidya, M. G. Kulkarni, P. R. Rajamohanan, S. Ganapathy, *Polymer* **2000**, *41*, 7951.
[27] P. Alexandridis, T. A. Hatton, *Colloids and Surfaces A* **1995**, *96*, 1.
[28] J. E. Chung, M. Yokoyama, T. Okana, *J. Control. Release* **2000**, *65*, 93.
[29] B. Wunderlich, *Thermochimica Acta* **2003**, *403*, 1.
[30] L. Leibler, *Macromolecules* **1980**, *13*, 1602.
[31] M. J. N. Junk, W. Li, A. D. Schlüter, G. Wegner, H. W. Spiess, A. Zhang, D. Hinderberger, *Angew. Chem. Int. Ed.* **2010**, *122*, 5818.
[32] D. Kurzbach, M. N. Reh, D. Hinderberger, *ChemPhysChem* **2011**, *12*, 3566.
[33] M. J. N. Junk, U. Jonas, D. Hinderberger, *Small* **2008**, *4*, 1485.
[34] Importantly, a dynamic exchange of spin-probes, the diffusion of probes in and out of hydrophobic cavities, must not be mistaken for dynamic inhomogeneities.

[35] M. J. N. Junk, W. Li, A. D. Schlüter, G. Wegner, H. W. Spiess, A. Zhang, D. Hinderberger, *Macromol. Chem. Phys.* **2011**, *212*, 1229.
[36] M. J. N. Junk, W. Li, A. D. Schlüter, G. Wegner, H. W. Spiess, A. Zhang, D. Hinderberger, *J. Am. Chem. Soc.* **2011**, *133*, 10832.
[37] W. Li, A. Zhang, K. Feldmann, P. Walde, A. D. Schlüter, *Macromolecules* **2008**, *41*, 3659.
[38] D. Hinderberger, *Top. Curr. Chem.* **2012**, *321*, 67.
[39] D. Baute, D. Goldfarb, *J. Phys. Chem. C* **2007**, *111*, 10931.
[40] S. Ruthstein, A. M. Raitsimring, R. Bitton, V. Frydman, A. Godt, D. Goldfarb, *Phys. Chem. Chem. Phys.* **2009**, *11*, 148.
[41] G. Martini, L. Ciani, *Phys. Chem. Chem. Phys.* **2009**, *11*, 211.
[42] D. Kurzbach, M. J. N. Junk, D. Hinderberger, *Macromol. Rapid. Commun.* **2013**, *34*, 119.
[43] P. Alexandridis, T. A. Hatton, *Collois Surfaces A: Physiochem. Eng. Aspects* **1995**, *96*, 1.
[44] A. V. Kabanov, E. V. Batrakova, V. Y. Alakhov, *J. Control. Release* **2002**, *82*, 189.
[45] P. Linse, M. Malmsten, *Macromolecules* **1992**, *25*, 5434.
[46] I. Goldmints, F. K. v. Gottberg, K. A. Smith, T. A. Hatton, *Langmuir* **1997**, *13*, 3659.
[47] A. Sturcová, P. Schmidt, J. Dybal, *J. Coll. Interf. Sci.* **2010**, *352*, 415.
[48] G. Wanka, H. Hoffmann, W. Ulbricht, *Macromolecules* **1994**, *27*, 4145.
[49] P. Alexandridis, V. Athanassiou, S. Fukuda, T. A. Hatton, *Langmuir* **1994**, *10*, 2604.
[50] M. Malmsten, B. Lindman, *Macromolecules* **1992**, *25*, 5440.
[51] A. V. Kabanov, I. R. Nazarova, I. V. Astafieva, E. V. Batrakova, V. Y. Alakhov, A. A. Yaroslavov, V. A. Kabanov, *Macromolecules* **1995**, *28*, 2303.
[52] S. Ruthstein, A. Potapov, A. M. Raitsimring, D. Goldfarb, *J. Phys. Chem. B* **2005**, *109*, 22843.
[53] S. Ruthstein, A. M. Raitsimring, R. Bitton, V. Frydman, A. Godt, D. Goldfarb, *PCCP* **2009**, *11*, 148.
[54] G. Martini, L. Ciani, *PCCP* **2009**, *11*, 211.
[55] M. Florent, R. Shvartzman-Cohen, D. Goldfarb, R. Yerushalmi-Rozen, *Langmuir* **2008**, *24*, 3773.
[56] M. J. N. Junk, W. Li, A. D. Schlüter, G. Wegner, H. W. Spiess, A. Zhang, D. Hinderberger, *Angew. Chem. Int. Ed.* **2010**, *49*, 5683.
[57] A. Caragheorgheopol, H. Caldararu, I. Dragutan, H. Joela, W. Brown, *Langmuir* **1997**, *13*, 6912.
[58] A. Caragheorgheopol, S. Schlick, *Macromolecules* **1998**, *31*, 7736.
[59] R. Shvartzman-Cohen, I. Monje, M. Florent, V. Frydman, D. Goldfarb, R. Yerushalmi-Rozen, *Macromolecules* **2010**, *43*, 606.
[60] M. Vasilescu, A. Caragheorgheopol, H. Caldararu, R. Bandula, H. Lemmetyinen, H. Joela, *J. Phys. Chem. B* **1998**, *102*, 7740.
[61] L. Zhou, S. Schlick, *Polymer* **2000**, *41*, 4679.
[62] J. W. Ma, M. F. Cunningham, K. B. McAuley, B. Keoshkerian, M. K. Georges, *J. Poly. Sci. A: Poly. Chem.* **2001**, *39*, 1081.
[63] The isotropic g-values of the TEMPO probes here correspond to this difference in polarity of their local environments, too: from 10 °C to 90 °C g_{iso} of species A is found to be between 2.0058 – 2.0060, and for species B 4.0061-4.0062 (for more selected g- and A-values see Appendix A4.1.2). The characteristic rotational correlation time, τ_c, which also contributes to line broadening, was around 0.01 ns for species A and 2.0 ns for species B.
[64] M. J. N. Junk, W. Li, A. D. Schlüter, G. Wegner, H. W. Spiess, A. Zhang, D. Hinderberger, *Macromol. Chem. Phys.* **2011**, *212*, 1229.
[65] M. J. N. Junk, W. Li, A. D. Schlüter, G. Wegner, H. W. Spiess, A. Zhang, D. Hinderberger, *J. Am. Chem. Soc.* **2011**, *133*, 10832.
[66] g of species B changes from 2.0061 to 2.0058.
[67] J. A. Weil, J. R. Bolton, J. E. Wertz, "*Electron Paramagnetic Resonance - Elementary Theory and Practical Applications*", John Wiley & Sons Inc., New York, 1994.
[68] Note that the highfield line of TEMPO in aqueous solutions also shifts to the low field, approx. 0.7 MHz between 10°C and 90°C. Hence, the overall shift of 1.0 MHz of the highfield line of species A has to be corrected to ~0.3 MHz.
[69] D. Kurzbach, M. N. Reh, D. Hinderberger, *Chemphyschem* **2011**, *12*, 3566.
[70] P. Linse, *Macromolecules* **1993**, *26*, 4437.
[71] K. Mortensen, J. S. Petersen, *Macromolecules* **1993**, *26*, 805.

[72] P. Alexandridis, T. Nivaggioli, T. A. Hatton, *Langmuir* **1995**, *11*, 1468.
[73] EPR studies using considerably bigger and more lipophilic spin probes (while the experimental design of the study does not differ significantly from that presented here) exhibit a temperature range above T_c (> 40 °C for P85 and TEMPO-hexanoate) where probe distributions and signals remain constant.
[74] G. Ionita, V. Chechik, *Chem. Commun.* **2010**, *46*, 8255.
[75] H. Caldararu, G. S. Timmins, B. C. Gilbert, *PCCP* **1999**, *1*, 5689.
[76] F. M. Winnik, M. F. Ottaviani, S. H. Bossmann, M. Garcia-Garibay, N. J. Turro, *Macromolecules* **1992**, *25*, 6007.
[77] V. S. Reuss, M. Werre, H. Frey, *Macromolecules* **2012**, *DOI: 10.1021/ma300292m*.
[78] G. W. Bemis, M. A. Murcko, *J. Med. Chem.* **1999**, *42*, 5095.
[79] G. W. Bemis, M. A. Murcko, *J. Med. Chem.* **1996**, *39*, 2887.
[80] D. S. Wishart, C. Knox, A. C. Guo, S. Shrivastava, M. Hassanali, P. Stothard, Z. Chang, J. Woosley, *Nucleic Acid Research* **2006**, *34*, D668.
[81] J. T. Koberstein, *J. Poly. Sci. B: Poly. Phys.* **2004**, *42*, 2942.
[82] C. Booth, D. Attwood, *Macromol. Rapid. Commun.* **2000**, *21*, 501.
[83] R. Kjellander, E. Florin, *J. Chem. Faraday Trans. 1* **1981**, *77*, 2053.
[84] Note that in order to yield feasible partitioning coefficients one actually should compare the fraction of TEMPO in solutions of the homo polymers PPO and PG and not the fraction of TEMPO in water with the fraction of TEMPO species B, since the hosting parameters between polymers and guest compounds in water are influenced by the hydrophobicity of the guests. However, for homo PG one only observes a TEMPO species that equals TEMPO in neat water and homo PPO is generally not soluble in water, only polymers of very low molecular weight are.
[85] S. Halacheva, S. Rangelov, C. Tsvetanov, V. M. Garamus, *Macromolecules* **2010**, *43*, 772.
[86] kindly provided by Dr. Martina Schömer
[87] kindly provided by Dr. Valerie S. Wilms
[88] D. Kurzbach, V. S. Wilms, M. Schömer, H. Frey, D. Hinderberger, *Macromol*ecules **2012**, *45*, 7535.
[89] E. Fleige, M. A. Quadir, R. Haag, *Adv Drug Deliver Rev* **2012**, *64*, 866.
[90] Information provided by Dr. Valerie S. Wilms.
[91] P. O. Wahlund, I. Y. Galaev, S. A. Kazakov, V. I. Lozinsky, B. Mattiasson, *Macromol. Biosci.* **2002**, *2*, 33.
[92] A. V. Berezkin, P. G. Khalatur, A. R. Khokhlov, *J. Chem. Phys.* **2003**, *118*, 8049.
[93] K. A. Dill, *Protein Science* **1999**, *8*, 1166.
[94] M. Siu, H. Y. Liu, X. X. Zhu, C. Wu, *Macromolecules* **2003**, *36*, 2103.
[95] X. Zhu, M. Liu, *Langmuir* **2011**, *27*, 12844.
[96] Y. Morishima, S. Nomura, T. Ikeda, M. Seki, M. Kamachi, *Macromolecules* **1995**, *28*, 2874.
[97] P. Dutta, J. Dey, G. Ghosh, R. R. Nayak, *Polymer* **2009**, *50*, 1516.
[98] R. V. Pereira, M. H. Gehlen, *Macromolecules* **2007**, *40*, 2219.
[99] P. Dutta, J. Dey, A. Shome, P. K. Das, *Int. J. Pharm.* **2011**, *414*, 298.
[100] Y. Ogata, M. Iwano, T. Mogi, Y. Makita, *J. Poly. Sci. B: Poly. Phys.* **2011**, *49*, 1651.
[101] S. Rimmer, I. Soutar, L. Swanson, *Poly. Int.* **2009**, *58*, 273.
[102] O. V. Borisov, A. Halperin, *Macromolecules* **1996**, *29*, 2612.
[103] G. Zhang, F. M. Winnik, C. Wu, *Phys. Rev. Lett.* **2003**, *90*, 35506.
[104] Y. Mai, A. Eisenberg, *Chem. Soc. Rev.* **2012**, *DOI: 10.1039/c2cs35115c*.
[105] I. W. Hamley, "*The Physics of Block Copolymers*", Oxford University Press, New York, 1998.
[106] J. Weiss, A. Laschewsky, *Macromolecules* **2012**, *45*, 4158.
[107] J. J. Freire, *Advances in Polymer Science* **1999**, *143*, 35.
[108] G. M. Hahn, *Cancer Research* **1979**, *39*, 2264.
[109] K. E. v. Holde, W. C. Johnson, P. S. Ho, "*Principles of Physical Biochemistry*", Prentice Hall, New Jersey, 1998.
[110] J. R. McDaniel, S. R. MacEwan, M. Dewhirst, A. Chilkoti, *J. Control. Release* **2012**, *159*, 362.
[111] A. Matsuyama, F. Tanaka, *Phys. Rev. Lett.* **1990**, *65*, 341.
[112] M. Lucarini, L. Pasquato, *Nanoscale* **2010**, *2*, 668.

[113] K. Procházka, Z. Limpouchová, F. Uhlík, P. Košovan, P. Matejícek, M. Štepánek, Mariusz Uchman, Jitka Kuldová, R. Šachl, J. Humpolícková, M. Hof, *Adv. Polym. Sci.* **2010**, *241*, 187.
[114] A. Ottochian, D. Leporini, *J. Non-Cryst. Solids* **2011**, *357*, 298.
[115] D. D. Thomas, *Biophys. J.* **1978**, *24*, 439.
[116] F. M. Winnik, A. R. Davidson, G. K. Hamer, H. Kitano, *Macromolecules* **1992**, *25*, 1876.

5. The Phase Transition of Genetically Encoded Elastin-Like Polypeptides

To elucidate the functional complexity of biomimetic matter I will in this chapter focus on so-called elastin-like polypeptides (ELPs) that can undergo an inverse temperature transition (at T_c) and contrast it to the phase transitions of the alkylene oxide-based thermoresponsive polymers described in Chapter 4. With ELPs a further degree of complexity is added to the concept of non-covalent interaction profiles in thermoresponsive soft matter: In particular, the complicated and heterogeneous H-bonding and hydration patterns that arise from their amino acid backbone. As will be shown in this chapter, such a primary structure also leads to strong effects of entropic contributions on the phase transition as a consequence of unfavorable, hydrophobic side chain hydration.

ELPs are recombinant, genetically encoded polypeptides that feature a biomimetic primary structure of repeating Val-Pro-Gly-Xaa-Gly pentapeptide units (where Xaa is a guest residue of any amino acid except Pro). Thus, their physico-chemical properties differ significantly from those of PEO-derivatives and other common synthetic polymers.[1] The properties of ELPs are of interest because these polymers are highly promising candidates for future applications in protein purification,[2, 3] tissue engineering,[4] immunoassays,[5] molecular actuation[6] and drug delivery especially of cancer drugs to tumor tissue.[7-11] In this context, their tunable inverse phase transition is exploited to accumulate ELPs in cancer cells that are subject to clinical hyperthermia.[10-14] Understanding the inverse phase transition process of ELPs is therefore of central importance for their controlled use in medical applications and is thus currently under intense research.[15-19] Changes in the molecular conformation and hydration state of ELPs upon changes in solution conditions, such as temperature, are critical to their ensemble LCST phase transition behavior. (Note that in the context of ELPs the "LCST" is typically used to denote the cloud point. Therefore I will stick to the notion of LCST here, although it may not be thermodynamically precise. EPR-derived collapse temperatures will like before be denoted $T_{c,EPR}$.)[20, 21]

Due to the limited number of available techniques to study these highly disordered macromolecules, linking the molecular properties of ELPs with their ensemble behavior remains a great challenge. For example, studying the solution conformation of ELPs using NMR is difficult because of the broad resonances that arise from their highly repetitive sequence and hindered dynamics above the LCST.[22-25] Circular dichroism (CD) spectroscopy remains the method of choice,[19, 21] but it provides

limited structural information on the ELP and none about the role of solvation. Furthermore, understanding the phase transition behavior of ELPs is also of interest as they provide a simple model system recapitulating aspects of the biophysical behavior of intrinsically disordered proteins, which will be subject in Chapter 6.[26-29]

5.1 A Highly Cooperative Phase Transition in Genetically Encoded Polymers Revealed by EPR Spectroscopy

Although CW EPR offers a powerful and simple methodology to examine the solvation of polymers, as shown in Chapter 4, it has only been used to study ELPs in one previous study by covalent conjugation of an EPR-active nitroxide spin label to an ELP, with the goal of using this conjugate as "molecular thermometer" to monitor mild clinical hyperthermia in vivo.[30] In contrast, the present section investigates the mechanism of the LCST phase transition – in particular temperature-dependent changes in the hydration of ELPs – by utilizing a spin probing approach[31-36] similar to the one described in Chapter 4: The temperature-dependent physical interaction between 16-DSA (instead of TEMPO; Figure 5.1.1) and ELPs of different compositions is monitored in solution. 16-DSA is used because of its strong tendency to accumulate in apolar environments ($\log(P)_{octanol/water}$ = 4.49).[37] Thus, the rationale behind this approach is that 16-DSA is likely to interact strongly with desolvated aggregates of ELPs above the LCST. Incorporation of probe molecules into ELP-based host structures (here: aggregates of ELPs above their LCST) can be detected by its effects on the a_{iso} and rotational correlation time, τ_c. These effects are similar to the effect of TEMPO partitioning between two environments of different polarity (Figure 5.1.1).[36] The values a_{iso} and τ_c are both extracted from rigorous spectral simulations. For the present case TEMPO is not hydrophobic enough to significantly interact with ELP aggregates due to their polar amino acid backbone (see Appendix 5.1).

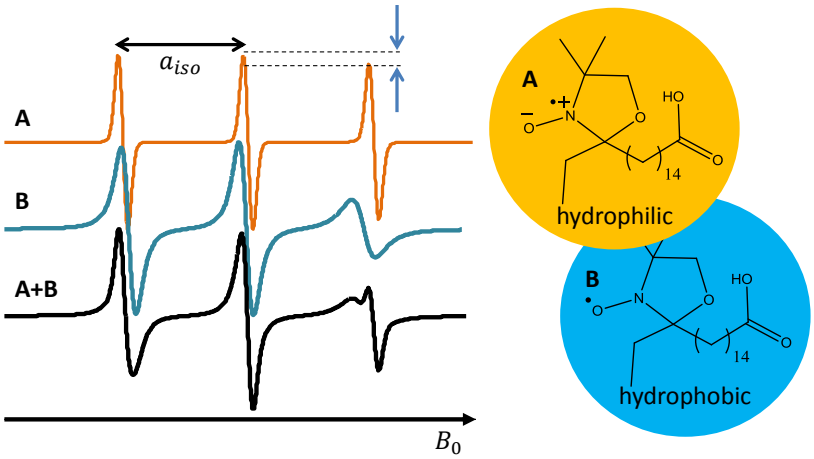

Figure 5.1.1. Environmental sensitivity of a 16-DSA CW EPR spectrum: 16-DSA in a polar environment (A; yellow); 16-DSA in an apolar environment (B; blue); combined, bimodal spectrum (A+B; black). The dashed lines mark the difference in intensity between the central line of 16-DSA and the high-field transitions, which is dependent on τ_c.

5.1.1 Results and Discussion

Here the effect of two orthogonal molecular parameters on the ELPs' LCST phase behavior is systematically studied: (1) the guest residue composition (X in VPGXG), which was varied from 100% alanine (most hydrophilic) to 100% valine (most hydrophobic); and (2) the chain length, which was varied between 40 and 80 pentapeptides. Our nomenclature denotes the alanine content (x) and the repeat unit length (y) as x-y (i.e., 100-40 is a 40 pentamers long ELP in which 100% of the guest

residues are alanine). All ELPs (Table 5.1.1) were recombinantly synthesized by expression of an ELP encoding synthetic gene from a plasmid in E. coli in the group of Prof. Ashutosh Chilkoti by Jonathan McDaniel.

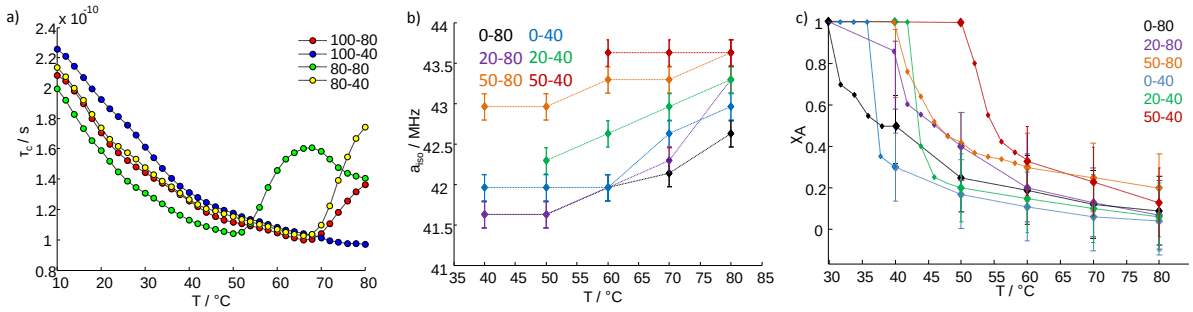

Figure 5.1.2. a) Temperature-dependence of τ_c for ELPs 100-y and 80-y. b) The temperature-dependence of a_{iso} of DSA species B for selected two-component spectra. Note that the data of 0-80 perfectly overlaps with the data of 20-80 below 60°C. The concentration of the ELPs was 1 wt% in all cases and the DSA concentration was 1 mM. c) Fraction of the DSA species A, χ_A, as a function of temperature for selected two-component spectra. Error bars stem from uncertainties in the simulations. Some error bars have been omitted for clarity.

Table 5.1.1. Summary of properties of ELPs: composition and corresponding LCST, as determined by spin-probe EPR and turbidimetry. Note that $T_{c,EPR}$ denotes the onset of observable interaction between the ELP and 16-DSA, while T_c denotes the cloud point of the solution (i.e., the temperature of the inflection point in a turbidity profile).

	100-40[b]	**80-40**[b]	**50-40**	**20-40**	**0-40**
Composition[a]	100% A	80% A / 20% V	50% A / 50% V	20% A / 80% V	100% V
$T_{c,EPR}$ /°C	-	70 ± 1	48 ± 1	38 ± 1	36 ± 1
$T_{c,Turbidimetry}$ /°C	69.2	60.4	49.7	40.8	34.4
	100-80	**80-80**	**50-80**	**20-80**	**0-80**
Composition[a]	100% A	80% A / 20% V	50% A / 50% V	20% A / 80% V	100% V
$T_{c,EPR}$ /°C	70 ± 1	54 ± 1	38 ± 1	36 ± 1	32 ± 1
$T_{c,Turbidimetry}$ /°C	66.4	52.8	41.1	32.9	28.1

[a] "Composition" denotes the composition of the guest residues Xaa, in the otherwise always identical Val-Pro-Gly-Xaa-Gly sequence. [b] The discrepancy between $T_{c,EPR}$ and $T_{c,\ Turbidimetry}$ for ELP 100/80-40 is a consequence of large amounts of residual water in the ELP aggregates above the LCST, which screen the hydrophobic interaction between 16-DSA and the ELP aggregates.

Figure 5.1.1 shows that 16-DSA in a polar, solvent-rich environment (species A; yellow) and 16-DSA in a non-polar, ELP-rich environment (species B; blue) are – like shown for TEMPO in Chapter 4 – discernible, even in the combined, bimodal spectrum (A+B; black). 16-DSA in the presence of ELPs can either exhibit a single-component spectrum (averaged between A and B) or a two-component spectrum (superposition of A+B). For a single-component spectrum, τ_c is the major parameter for the subsequent characterization of the LCST phase transition, since it reports on the rotational freedom of a 16-DSA probe. Increasing τ_c is hence indicative of steric confinement and ELP aggregation. For two-component spectra χ_A is more suitable for the characterization of the LCST phase transition, because τ_c of the pure species A is not effected significantly by the LCST transition. Figure 5.1.2 shows the three parameters, τ_c, a_{iso}, and χ_A for the entire set of ELPs as a function of temperature; the experimental data and respective analysis that yields these plots are contained in Appendix A5.1. Note that this approach only quantifes spectral contribution of strongly interacting probes through χ_B. The fraction of 16-DSA probes incorporated in ELP aggregates might however be larger than χ_B, if the probes reside e.g. in patches of intercalated water inside an aggregate. However,

typically ELP aggregates are assumed to be quite well-ordered,[16] so that χ_B is likely to at least approximately reflect the actual fraction of incorporated probes. Note also that due to the strict ergodicity of time and conformational ensemble for the data under investigation, the spectral contribution of species B exactly corresponds to the fraction of strongly interacting probes. This holds independently of site exchange frequencies of probes as long as the two spectral components are clearly discernible.[34]

For the most hydrophilic ELPs 100/80-y (high alanine content; see Table 5.1.1) one observes a single high-field line above the LCST in the CW EPR spectra (see Appendix Figure A5.1.1). Interaction between 16-DSA and aggregates of these ELPs can be deduced from decreased rotational mobility of the 16-DSA probes (increasing τ_c in Figure 5.1.2 a)) indicating transient guest-incorporation on submicrosecond timescales. In contrast, for ELPs with a valine content ≥ 50%, one observes two clearly separated high-field lines above the LCST (see Appendix Figure A5.1.1), stemming from 16-DSA species A and from 16-DSA species B. For such a two-site situation, one can only observe two well-separated lines if the relation $\tau_B^{-1} \ll \Delta\omega$ holds for the spectral line separation, Δω (where τ_B denotes the residence time of 16-DSA in aggregates of ELPs).[34] When $\tau_B^{-1} \gg \Delta\omega$, one observes a single line averaged between species A and B. Hence, one can unequivocally state that with increasing hydrophobicity of the host structures, the residence time of the guest-molecules in the ELP aggregates becomes longer. On the EPR timescale of 10^{-5} s – 10^{-9} s, 16-DSA appears to be statically bound for ELPs 50/20/0-y (e.g. for ELPs 0/20-80 Δω > 3.5 MHz → τ_B > 0.3 µs).

The different lifetimes of 16-DSA in ELP aggregates of varying hydrophobicity can be rationalized as follows: With increasing ELP hydrophilicity and length, the polarity the probes "feel" through the number of aggregate-bound residual water molecules increases. This water in the vicinity of the probes screens the attractive, hydrophobic interactions between probes and ELPs, which consequently leads to shorter lifetimes of species B. The varying amounts of water sensed by 16-DSA in aggregates of different ELPs can be deduced from Figure 5.1.2 b). There, a_{iso} of species B for ELPs 50/20/0-y is plotted versus temperature. With increasing ELP length and hydrophobicity, a_{iso} is smaller at a given temperature, meaning that the probes feel a lower environmental polarity. This is well observable between 40°C and 50°C, where a_{iso} remains constant for a given ELP. Hence, in longer and more hydrophobic ELP aggregates the probes sense less interaction-screening water in their immediate vicinity (probably through residual backbone or side-chain hydration) than in shorter and more hydrophilic ones. This deduction is further corroborated by the T_cs and $T_{c,EPR}$s, which indicate ever stronger bound hydration shells with increasing chain length and hydrophobicity. Therefore, the non-covalent (likely hydrophobic) interaction of 16-DSA with ELPs becomes stronger with increasing hydrophobicity of the host structures, which results in a longer τ_B. The collapse temperatures are listed in Table 5.1.1. The varying τ_B values remarkably indicate that the molecular/nanoscale properties of different ELPs are dissimilar above their LCST despite the fact that they nominally appear to undergo a similar phase transition at the macroscopic level observed by the change in their turbidity above their LCST. In contrast, depending on the primary sequence, ELP aggregates above the LCST feature significantly differing densities and amounts of residual water, giving rise to different modes of host-guest interactions, as depicted in Figure 5.1.3.

Compared to other synthetic thermoresponsive polymers, ELPs retain more residual hydration above the LCST.[32, 33, 35] The observed hyperfine couplings (see Figure 5.1.2 b); 41.5 MHz < a_{iso} < 44 MHz) are consistent with this observation, as the representative polarity in mixtures of iso-propanol and chloroform range from $a_{iso,i-propanol}$ = 44.2 MHz to $a_{iso,chloroform}$ = 41.4 MHz. In contrast, the polarity of apolar cavities of common thermoresponsive polymers is $\leq$ 41.5 MHz.[32, 33, 35] Be-

tween 40°C and 50°C a_{iso} remains constant for ELPs. This indicates that the exchange frequency does not significantly change in this temperature regime. Above 50°C a_{iso} of species B increases for all ELPs that show a CW EPR spectral component B leading to a merging of the lines of species A and B similar to the observations made for Pluronics and **PEO-*co*-PDEGA** (see Chapter 4). This phenomenon can also here be explained by the onset of diffusional probe site exchange above 50°C (see Figure 5.1.3).[33, 35] The ELP-rich regions – very likely – may nonetheless be dehydrated further with increasing temperature. This is suggested by the observation that the volume that ELP aggregates provide for 16-DSA increases continuously above the LCST, as can be deduced from χ_B that keeps on growing as the temperature rises (see Figure 5.1.2).

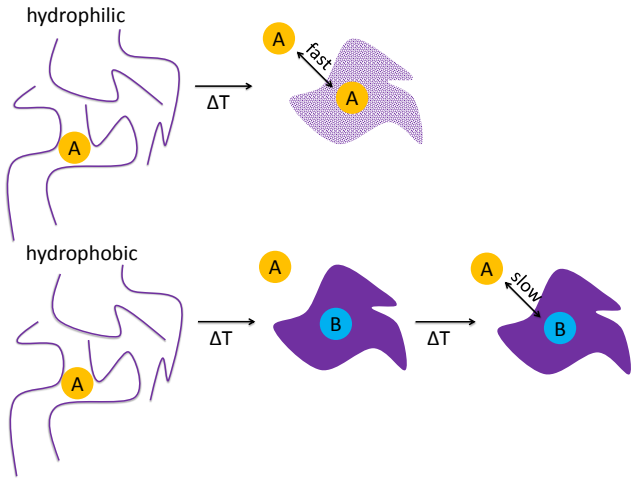

Figure 5.1.3. Sketch of the ELP-DSA interaction. For more hydrophilic ELPs above the LCST the DSA probes can exchange fast between ELP-rich and ELP-depleted regions. For more hydrophobic ELPs, DSA probes do not exchange at temperatures slightly above the LCST, such that two well-separated species appear in the CW EPR spectra. At even further elevated temperature the probes start to exchange slowly.

From a physicochemical point of view, ELPs show significantly different behavior than LCST-exhibiting synthetic polymers. Like shown in Chapter 4, for the latter the onset of the phase transition (proceeding via local collapse and nanoscale inhomogeneities)[36] is frequently located at lower temperatures than the macroscopic LCST ($T_c > T_{c,EPR}$).[33] For ELPs one observes that the macroscopic LCST[17, 38] (from turbidimetry) and the onset of nanoscopic collapse (from EPR) are similar (Table 5.1.1). Taking into account that the incorporation of 16-DSA directly above the LCST is quite prominent for ELPs (0/20/50-y), one can rule out that the cloud point is just a consequence of minor physical interactions leading to, e.g., crosslinking between ELP molecules. Thus, the ELP phase transition does not proceed via local collapse and subsequent percolation or related mechanisms[36] but instead proceeds by initial cooperative aggregation of ELP chains. The temperature-dependence of the χ_A functions in Figure 5.1.2 c) illustrates that the phase transition is extremely sharp for the 40 pentamer ELPs. The respective transitions for the 80 pentamer ELPs are broader and resemble the nanoscale transitions of the synthetic alkylene oxide-based polymers (see Sections 4.1 and 4.2): The volume fraction of apolar domains increases steadily over a wide temperature range.[31-33, 35] Here, in contrast, the χ_A temperature profiles show a clear sigmoidal development and most of the aggregation of the x-40 ELPs occurs in a very narrow temperature range. The ELP inverse phase transition is hence sharp even on the nanoscale. This shows that the dehydration-induced aggregation of the ELPs at the LCST is a highly cooperative process, as proposed by Cremer and co-workers.[39] They deduced that the hydration shell of the backbone of the ELPs and the hydrophobic hydration shell of the side-groups can exist in a coupled state, leading to a cooperative dehydration event. Yet, also

for PNiPAAm it is known that the temperature-induced dehydration is a cooperative process, but still the nanoscopic phase transition is rather broad compared to the transition of the x-40 ELPs.[32, 40, 41]

It is interesting that the phase transition is sharper for the ELPs with only 40 pentamers than the transition of the ELPs with 80 pentamers, although the phase transition of the longer ELPs starts at lower temperatures at a given composition (concentration effects were ruled out; see Appendix Figure A5.1.5). Taking χ_A at 80°C as a reference for the aggregation of ELPs (this is reasonable since χ_A is equal within the error bounds at this temperature for all different ELPs), one can state that over 50% of the mass that the ELPs provide for interaction with 16-DSA aggregates in a range of less than 5°C for the ELPs 0/20-40. This is likely the most rapid inverse phase transition so far observed on nanoscopic length scales (even more rapid than the transition of **PEO-*co*-PDEGA** at pH 14) and may possibly be regarded as a nanoscale first-order phase transition even though more abrupt macroscopic transitions have been reported previously.[31] Note that the samples were allowed to equilibrate for 10 min after each temperature step of 2 K, and that during this interval no changes in the spectra were observed.

The fact that shorter ELPs display a much sharper precipitation event than the longer ELPs may be attributed to a stronger coupling between hydrophilic and hydrophobic hydration shells in shorter ELPs as they bind more water per strand (see Figure 5.1.2 b) and T_cs and $T_{c,EPR}$s in Table 5.1.1) than longer ELPs. This, in turn, may mediate the coupling between the different hydration types.[20, 39] To uncover this unique feature of the temperature-dependent solvation of ELPs their recombinant synthesis was critical, as it provides the necessary, precise control over macromolecular sequence and chain length. This is simply not possible with synthetic polymers that exhibit LCST behavior like the poly(alkylene oxide)s of Chapter 4.[12]

Although the above coupling hypothesis is to some degree speculative at this point, it can account for the fact that the dehydration process starts at lower temperatures for the longer ELPs, while the dehydration process, once started, is much sharper for the shorter ones. If hydrophobic and hydrophilic hydration shells are less strongly coupled in longer ELPs, less energy is needed to initiate the dehydration, since weak coupling may allow for independent dissolution of the two types of hydration shells. Note that one does not typically observe any dependencies of critical temperatures on chain length or concentration by means of CW EPR, since one exclusively monitors the local conformation of the chains.[33, 35] This furthermore corroborates the idea that ELPs initially aggregate without the formation of nanoscopic transition structures.[17]

5.1.2 Conclusion

The LCST phase transition of ELPs does not proceed via nanoscale inhomogeneities and subsequent percolation of dehydrated polymer segments as it does in the case of most synthetic LCST polymer systems. In contrast, the dehydration of ELPs with increasing solution temperature is accompanied by the abrupt aggregation of ELPs, reminiscent of a highly cooperative, first-order phase transition. Although the onset of the transition for longer ELPs is located at lower temperatures for some sequences, they exhibit a broader phase transition that resembles the transitions of the poly(alkylene oxide)s of Chapter 4, for which almost always quite wide transition ranges are observed. The apparent stronger cooperativity in the LCST phase behavior of short ELPs is explained by proposing that hydrophilic and hydrophobic hydration shells are more strongly coupled in shorter ELPs (mediated through larger amounts of bound water) than in longer ELPs. Finally, the above results suggest that hydrophobic ELPs may be useful to physically encapsulate guest molecules of interest such as

chemotherapeutics and imaging agents, though the degree of encapsulation and their stability likely depends on matching the hydrophobicity of the ELP with that of the guest molecules.

References and Notes

[1] D. Kurzbach, J. R. McDaniel, A. Chilkoti, D. Hinderberger, *in preparation* **2012**.
[2] W. Hassouneh, T. Christensen, A. Chilkoti, *Curr. Prot. Protein Sci.* **2010**, 6.11.1.
[3] K. Trabbic-Carlson, L. Liu, B. Kim, A. Chilkoti, *Protein Sci.* **2004**, *13*, 3274.
[4] D. L. Nettles, A. Chilkoti, L. A. Setton, *Adv. Drug. Delivery Rev.* **2010**, *62*, 1479.
[5] J.-Y. Kim, S. O'Malley, A. Mulchandani, W. Chen, *Anal. Chem.* **2005**, *77*, 2318.
[6] B. Kim, A. Chilkoti, *J. Am. Chem. Soc.* **2008**, *130*, 17867.
[7] R. J. Marx, R. D. Osborne, M. S. Stevens, R. V. Ulijn, *Soft Matter* **2006**, *2*, 822.
[8] J. R. McDaniel, D. J. Callahan, A. Chilkoti, *Adv. Drug Delivery Rev.* **2010**, *62*, 1456.
[9] A. Chilkoti, T. Christensen, J. A. MacKay, *Curr. Opinion Chem. Biol.* **2006**, *10*, 652.
[10] S. R. MacEwan, D. J. Callahan, A. Chilkoti, *Nanomedicine* **2010**, *5*, 793.
[11] A. Chilkoti, M. R. Dreher, D. E. Meyer, D. Raucher, *Adv. Drug Delivery Rev.* **2002**, *54*, 613.
[12] R. Rousseau, E. Schreiner, A. Kohlmeyer, D. Marx, *Biophys. J.* **2004**, *86*, 1393.
[13] B. Li, D. O. V. Alonso, V. Dagett, *J. Mol. Biol.* **2001**, *205*, 581.
[14] D. E. Meyer, B. C. Shin, G. A. Kong, M. W. Dewhirst, A. Chilkoti, *J. Control. Release* **2001**, *74*, 213.
[15] R. Glaves, M. Baer, E. Schreiner, R. Stoll, D. Marx, *ChemPhysChem* **2008**, *9*, 2759.
[16] T. Yamaoka, T. Tamura, Y. Seto, T. Tada, S. Kunugi, D. A. Tirrell, *Biomacromolecules* **2003**, *4*, 1680.
[17] D. E. Meyer, A. Chilkoti, *Biomacromolecules* **2004**, *5*, 846.
[18] H. J. Moon, D. Y. Ko, M. H. Park, M. K. Joo, B. Jeong, *Chem. Soc. Rev.* **2012**, *41*, 4860.
[19] M. Miao, J. T. Cirulis, S. Lee, F. W. Keeley, *Biochemistry* **2005**, *44*, 14367.
[20] A. Castiglione-Morelli, A. Scopa, A. M. Tamburro, V. Guantieri, *Int. J. Biol. Macromol.* **1990**, *12*, 363.
[21] D. W. Urry, *J. Protein Chem.* **1988**, *7*, 1.
[22] D. E. Meyer, A. Chilkoti, *Biomacromolecules* **2002**, *2*, 357.
[23] J. L. Frandsen, H. Ghandehari, *Chem. Soc. Rev.* **2012**, *41*, 2696.
[24] D. Kurková, J. Kríz, P. Schmidt, J. Dybal, J. C. Rodríguez-Cabello, M. Alonso, *Biomacromolecules* **2003**, *4*, 589.
[25] D. W. Urry, M. M. Long, E. Gross, *Crit. Rev. Biochem. Mol. Biol.* **1976**, *4*, 1.
[26] G. Platzer, A. Schedbauer, A. Chemeli, P. Ozdowy, N. Coudevylle, R. Auer, G. Kontaxis, M. Hartl, A. J. Miles, B. A. Wallace, O. Glaser, K. Bister, R. Konrat, *Biochemistry* **2011**, *50*, 6113.
[27] V. N. Uversky, *Prot. Sci.* **2002**, *11*, 739.
[28] P. Tompa, *Trends Biochem. Sci.* **2002**, *27*, 527.
[29] H. J. Dyson, P. E. Wright, *Curr. Opinion Struct. Biol.* **2002**, *12*, 54.
[30] M. R. Dreher, M. Elas, K. Ichikawa, E. D. Barth, A. Chilkoti, G. M. Rosen, H. J. Halpern, M. Dewhirst, *Med. Phys.* **2004**, *31*, 2755.
[31] M. J. N. Junk, W. Li, A. D. Schlüter, G. Wegner, H. W. Spiess, A. Zhang, D. Hinderberger, *Angew. Chem. Int. Ed.* **2010**, *49*, 5683.
[32] M. J. N. Junk, U. Jonas, D. Hinderberger, *Small* **2008**, *4*, 1485.
[33] D. Kurzbach, M. Schömer, V. S. Wilms, H. Frey, D. Hinderberger, *Macromolecules* **2012**, *45*, 7535.
[34] N. M. Atherton, "*Principles of Electron Spin Resonance*", Ellis Horwood, New York, 1993.
[35] D. Kurzbach, M. N. Reh, D. Hinderberger, *ChemPhysChem* **2011**, *12*, 3566.
[36] D. Kurzbach, M. J. N. Junk, D. Hinderberger, *Macromol. Rapid. Commun.* **2012**, *34,* 119.
[37] A. N. Cimato, L. L. Piehl, G. B. Facorro, H. B. Torti, A. A. Hager, *Free Radical Bio. Med.* **2004**, *37*, 2042.
[38] J. A. MacKay, D. J. Callahan, K. N. Fitzgerald, A. Chilkoti, *Biomacromolecules* **2010**, *11*, 2873.

[39] Y. Cho, Y. Zhang, T. Christensen, L. B. Sagle, A. Chilkoti, P. S. Cremer, *J. Phys. Chem. B* **2008**, *112*, 13765.
[40] V. Aseyev, H. Tenhu, F. M. Winnik, *Adv. Polym. Sci.* **2011**, *242*, 29.
[41] Y. Okada, F. Tanaka, *Macromolecules* **2005**, *38*, 4465.

6. The Conformational Space of Intrinsically Disordered Proteins

Intrinsically disordered proteins (IDPs) are proteins that do not feature any significant amounts of secondary or tertiary structure elements in their monomeric state.[1-3] Such, they cannot be crystallized and structure determination becomes challenging. From the point of view of non-covalent interaction profiles IDPs constitute the most complex substrates encountered in this thesis. Like in ELPs the interplay between hydrogen bonds and hydrophobic interactions is central to the ensemble characteristics of IDPs. Additionally attractive and repulsive electrostatic forces due to acidic and basic residues come into play, determining conformational ensembles of IDPs. Also entropic contributions due to hydration forces and system configuration are an important factor. Thus, in IDPs a multitude of structuring forces is finally combined in quite complex interaction profiles that serve as structuring principles for IDPs' polypeptide backbones and amino acid side chains.

Yet, IDPs are not only interesting from a physico-chemical point of view, but have also attracted substantial biomedical attention in recent years. In particular, the discovery of the importance of IDPs for eukaryotic life and of their central role in protein interaction networks raised interest. In contrast to reasonably stable and well-folded globular proteins – often characterized by the classical lock and key interaction scheme – IDPs feature a rather flexible nature. The efficient sampling of a vast and heterogeneous conformational space endows them with enormous potential to simultaneously interact with and control multiple binding partners.[2, 4] This structural heterogeneity (ambiguity) of IDPs also enables substantial evolutionary adaptability[5] that is likely to be a necessary prerequisite for their involvement in increased phenotypic variation observed in higher organisms. Thus, it was proposed that the structural plasticity and adaptability of IDPs allow them to efficiently engage in weak regulatory linkages and to act as efficient substrates for biological evolution.[6] Although, from a traditional point of view, IDPs lack a well-folded structure they nonetheless fulfill many vital functions and seem therefore to contradict or at least amend the classic *structure = function* paradigm of molecular biology. This makes IDPs intriguing substrates for studies in modern proteomics. However, from a biophysical and structural biology point of view, IDPs remain puzzling in many aspects. Structural polymorphism (or rheomorphism, according to Holt and Sawyer[7]) calls

for new approaches, combining appropriate theoretical concepts and experimental technologies. Yet, for the structural and functional characterization of IDPs only a few experimental techniques are suitable and structural concepts are rare. Their solution states, conformational space and modes of conformational sampling are still to a large degree undiscovered.[6]

6.1 Cooperatively Folded Conformational Substates in Osteopontin

It is known that proteins commonly classified as disordered or unstructured can be described best as an "ensemble of a continuum of rapidly interconverting structures",[8] that can contain a very heterogeneous assembly of conformations; ranging from random coils to quite compact structures.[9-11] Transitions between random coil and compact conformations are typically described as first order processes, hence these states are energetically (thermodynamically) well separated.[12] Here it is shown that the IDP Osteopontin (OPN), a cytokine involved in metastasis of several kinds of cancer,[4, 13] does not only sample a broad distribution of conformations, as expected for an IDP, but also cooperatively folded structures, reminiscent of globular proteins. The classification of IDPs in terms of rapidly interconverting structures therefore has to be augmented with properties that have so far only been associated with natively folded proteins: I.e., the conformational ensemble of OPN comprises a fraction of significantly populated states that are cooperatively folded.

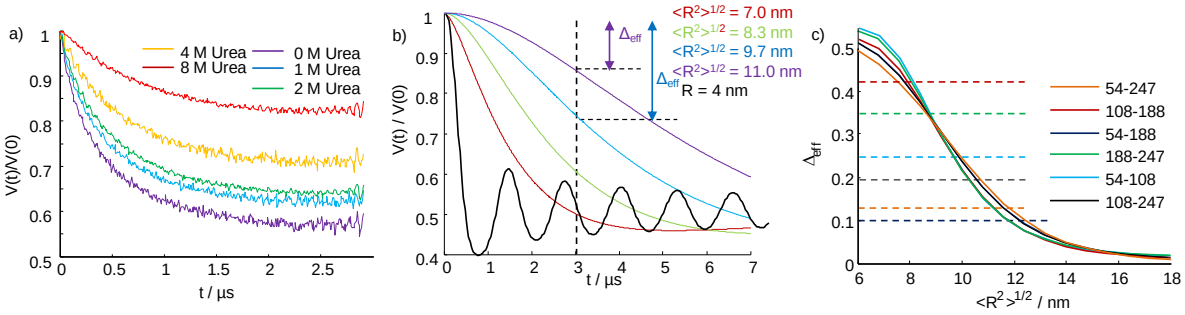

Figure 6.1.1. a) DEER time traces of C108-C188 at different urea concentrations. b) Calculated DEER time traces for different interspin distance distributions based on random coils with different $\langle R^2 \rangle^{1/2}$. Δ_{eff} is defined as the signal decay at t = 3 µs, as indicated by the double-headed arrows. The black time trace corresponds to a single interspin distance of 4 nm. c) Δ_{eff} as a function of $\langle R^2 \rangle^{1/2}$ of hypothetical random coil polypeptides (distance distribution) with segment numbers corresponding to the residues between the labeling sites of the different double mutants. The dashed lines indicate the maximum, experimentally observed Δ_{eff} for a given double mutant. Note that the shift of $\langle R^2 \rangle^{1/2}$ at a given segment number was calculated as changes in c_∞ (see Appendix A6.1.2).

6.1.1 Results and Discussion

Here DEER is applied to gain coarse-grained information about the conformational states of OPN. The original study and results have been complemented with NMR data from Gerald Platzer working in Robert Konrat's group at the Max F. Perutz Laboratories in Vienna to yield residue-resolved information about OPN's compact conformations.[14-18] Yet here, I will primarily focus on the EPR part of this methodologically integrated research project, but will nonetheless take critical NMR data into account.

Conformational States of OPN

Structural preferences of OPN were probed by applying DEER spectroscopy to six spin-labeled Cys-double mutants of 220 residues long truncated OPN (residues 50-270 of the native protein spin-labeled with MTSL; S-(2,2,5,5-tetramethyl-2,5-dihydro-^{1}H-pyrrol-3-yl)methyl methanesulfonothio-

ate). The mutants C54-C108, C108-C188 and C188-C247 each comprise approx. 1/3 of the whole protein, the mutants C54-C188 and C108-C247 about 2/3 and the mutant C54-C247 nearly the whole truncation mutant. Conformational stabilities of individual structural segments in OPN were investigated by recording DEER time traces for different double mutants in dependence of urea concentration.[16] Typical DEER data for an OPN double mutant at different urea concentrations are shown in Figure 6.1.1 a). Since no clear-cut modulations are observable after experimental background correction, one can assume that the pair-distribution functions, $P(R)$, between the two spin labels of a given mutant are quite broad, as expected for an IDP in its monomeric state. For a single, stably folded conformation one would however observe such modulations (Figure 6.1.1 b)). The complete data set for all double mutants is shown in the Appendix A6.1.1. All time traces are devoid of modulations.[15][19] DEER time traces are analyzed through an effective modulation depth, Δ_{eff}, as sketched in Figure 6.1.1 b), which denotes the total signal decay at t_{max} = 3 µs (see Section 1.6 on DEER for details on the pulse sequence). Δ_{eff} is an approximate measure of average interspin distances for broad $P(R)$s in protein double mutants. For broad distance distributions, Δ_{eff} decreases with increasing interspin distance, R, as depicted in Figure 6.1.1 b) and c) for simulated data. In Figure 6.1.1 c) Δ_{eff} is plotted for time traces calculated from $P(R)$s of random coils of different length as a function of the root-mean-square end-to-end distance, $\langle R^2 \rangle^{1/2}$.[20] This essentially quantifies how an elongation of an interspin distance distribution translates into Δ_{eff}. The functions of Δ_{eff} were calculated for our specific experimental setup with $\lambda = 0.516$. λ determines the modulation depth at $t \rightarrow \infty$ for doubly spin-labeled proteins (see eq. 1.1.80).[21] From Figure 6.1.1 c) one can deduce that Δ_{eff} decays exponentially with $\langle R^2 \rangle^{1/2}$ of random coils if Δ_{eff} is always sufficiently smaller than λ. This is true in our experiments, since $\Delta_{eff} < 0.45$ in all cases. Note that although for all calculations random coil distributions were assumed, the above assumptions are valid for all distributions that are symmetric around $\langle R^2 \rangle^{1/2}$.

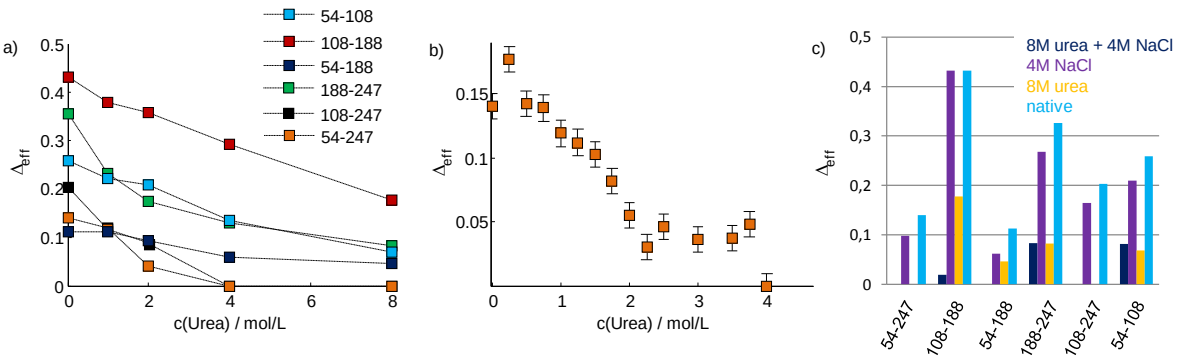

Figure 6.1.2. a) Δ_{eff} for selected double mutants as a function of urea concentration. The entire data for all double mutants under investigation can be found in Appendix A6.1.1. b) Detailed representation of Δ_{eff} for C54-C247 as a function of urea concentration. Error bars stem from signal noise. c) Δ_{eff} for the different double mutants under different denaturing conditions (4 M Nacl (violet)/8 M urea (yellow)/4M Nacl + 8M urea (dark blue)/native (light blue)).

In Figure 6.1.2 a) experimental Δ_{eff} values are shown as a function of urea concentration for all investigated double mutants. For C188-C247 one can observe an exponential decay as expected for a linear expansion of this OPN segment. However, since the relation between $\langle R^2 \rangle^{1/2}$ and the urea concentration remains unknown this does not necessarily imply an actual linear expansion of C188-C247 with the urea concentration. This mutant gives nonetheless rise to the steepest observed slope of a Δ_{eff} function. Hence, it can be regarded as a relative reference for the effect of conformational destabilization on unstably folded protein segments of potentially random coil-like character. For the mutant C108-C247 (as well as for mutants C54-C108 and C108-C188) one observes an ap-

proximately linear decrease of Δ_{eff} with urea concentration, indicating that the OPN segment framed by this mutant is on average conformationally more stable than the segment between C188 and C247. Nonetheless, mutants C54-C108, C108-C188 and C188-C274 show the urea-dependence one would expect for a largely unstructured, random coil- or (pre)molten globule-like protein. Strikingly for the mutant C54-C247 (and less pronounced C54-C188) a sigmoidal development of the Δ_{eff} function can be observed. Sigmoidality is a hallmark for cooperative folding of protein conformations and unexpected for an IDP. This sigmoidal development of Δ_{eff} is depicted in more detail for C54-C247 in Figure 6.1.2 b). It is indicative for stably and cooperatively folded structures of OPN, since for low urea concentrations up to 0.75 M the whole protein does not expand significantly (as seen in a nearly constant Δ_{eff}). This observation of stable, compact conformations is surprising as $P(R)$s for OPN are generally quite broad, which is reflected in the non-modulated time traces (see Appendix Figure A6.1.1 and Figure 6.1.1 a)). One would expect such time traces for extended conformations like random coils but not for cooperatively folded structures. This seemingly contradicting finding can be reconciled by ascribing both, cooperatively folded and extended conformations to the structural ensemble of OPN, such that both contribute to the DEER signals. This interpretation is substantiated by the fact that sigmoidal Δ_{eff} profiles can only be observed for double mutants with labeling sites that are separated by more than 130 residues but not for the three mutants that comprise only 1/3 of OPN: With increasing mean distance between the labels and consequently broader $P(R)$[20] the contribution of extended structures to the overall Δ_{eff} decreases. This means that with increasing separations between two labeling sites in an OPN double mutant the relative contribution of compact conformations to Δ_{eff} of corresponding time traces increases. This is shown in detail in Appendix A6.1.2. Compact conformations consequently dominate the urea dependence of Δ_{eff} for C54-C247 (and C54-C188), while extended conformations contribute more significantly to Δ_{eff} for C188-C247, C108-C188 and C54-C108. One may be tempted to think of OPN as partially structured to explain the data. However, the superposition of DEER data from compact and extended states existing simultaneously in OPN is the only feasible explanation: The sigmoidal Δ_{eff} profile of the entire analyzed protein fraction (C54-C247), together with the fact that the smaller segments do not exhibit sigmoidal profiles, allows no other reasonable explanation.

Stabilization of cooperatively folded structures of OPN is likely triggered by electrostatic interactions. In Figure 6.1.2 c) the effect of 4 M NaCl on Δ_{eff} is shown for the presence and the absence of 8 M urea. NaCl screens electrostatic interactions, while urea does not.[22-24] Since Δ_{eff} for C108-C188 and C54-C188 depends on the NaCl concentration even at 8 M urea, one can state that urea does not completely unfold OPN, although it is classified as IDP. This indicates that electrostatics significantly stabilize the conformations of OPN. This will be discussed in more detail below, taking into account paramagnetic relaxation enhancement (PRE) data, too. Note that the observation of incomplete unfolding at 8 M urea could be mistaken for an artifact from dimerization. Yet, a completely homogeneous distribution of OPN is observed through DEER on the corresponding four single mutants (C54, C108, C188 and C247), displaying that OPN does not show any form of aggregation at the concentrations (0.8 mM) used for the DEER measurements.

The stably folded structure of OPN is furthermore mirrored in the NMR data gained by the group of Robert Konrat. They observed the urea-dependence of OPN conformations by means of NMR chemical shift and ^{13}C-^{1}H HSQC (heteronuclear single quantum coherence) on $^{13}CH_3$-Lys-labeled OPN. NMR ^{15}N-^{1}H chemical-shift changes and ^{13}C-^{1}H HSQC data (that is, backbone- as well as side-chain-based data) both additionally demonstrate the existence of compact, cooperatively folded substates in the conformational ensemble of OPN.[25]

Properties of compact conformations

Here I will give a short outlook on how EPR and NMR data can go hand in hand for the description of IDPs through the combination of DEER and PREs from HSQC signal intensities. Since OPN samples cooperatively folded conformations, it is reasonable to assume that these should give rise to significant PRE effects for the four single mutants C54, C108, C188 and C247, owing to the very steep distance dependence of PREs. The different PRE-residue plots in Figure 6.1.3 a) show that the conformational ensemble of OPN features distinct long-range interactions. Specifically, the PRE results obtained for the mutants C108 and C188 provide clear evidence for the prevalence of a structurally compact region in OPN encompassing residues 100-200 (intermolecular contributions could be ruled out by DEER on the single mutants). The structural stability of this compact region as a function of urea and NaCl concentration was monitored further by condition-dependent PRE changes. Figure 6.1.3 b) shows experimental PRE differences (ΔPRE) measured under NaCl as well as high urea conditions.

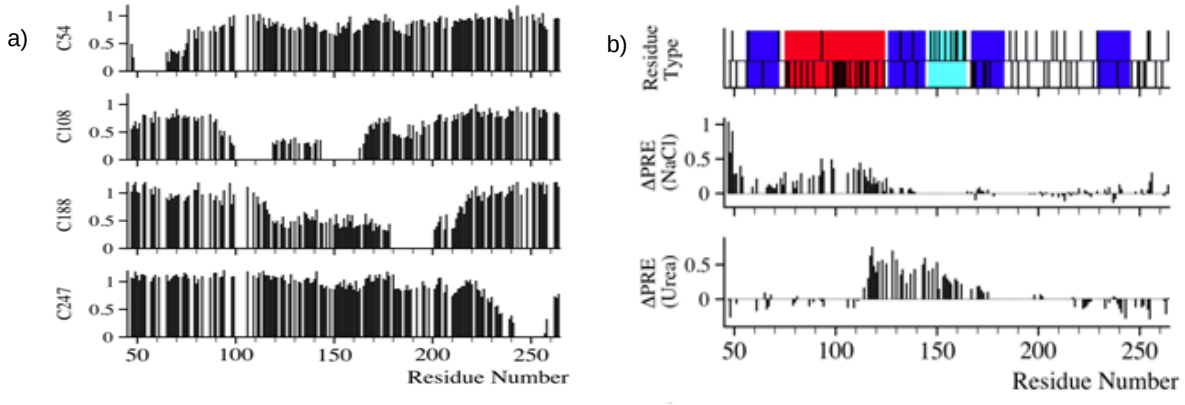

Figure 6.1.3. a) PRE data for the four single mutants C54, C108, C188 and C247. b) A charge map of OPN (top) and PRE changes ΔPRE for high salt (center) and urea (bottom) conditions obtained for the C188 mutant. Stretches of basic and acidic residues are indicated in cyan and red, while the hydrophobic regions in OPN are depicted in dark blue in the charge map. Note that the unreasonable, N-terminal ΔPRE for C188 at high salt conditions of approx. unity is a consequence of significant ^{15}N-^{1}H HSQC signal overlap.

The highly charged region encompassing residues 75-125 is nearly unaffected by urea but displays sizeable PRE changes under high NaCl conditions, while residues 125-150 are affected strongly by urea. Hence, not only hydrophobic interactions contribute to the structural stability of OPN, but electrostatics play a pivotal role in stabilizing the compact sub-states of OPN in solution (also compare with Figure 6.1.2 c)). These findings can be rationalized by a closer look at the charge map of OPN (Figure 6.1.3 b), top). In OPN negative charges are concentrated in the region between residues 75 and 125, while there is a high density of positive charges in the region between residues 145 and 165. The attraction between these positively and negatively charged regions and between the hydrophobic patches around residues 60, 130 and 180 suggests stabilizing interactions and consequently higher tertiary structure propensity between residues 60 and 180, compared to other regions of OPN. This is further corroborated by previous NMR solution data suggesting a more rigid structural core in OPN.[13] The NMR data indicate significantly populated compact structures in OPN that are cooperatively stabilized by both hydrophobic as well as electrostatic interactions. It is reasonable to conclude that the subtle interplay between conformation-stabilizing enthalpic contributions and destabilizing entropic contributions ultimately account for OPN's conformational flexibility and its ability to adopt both extended as well as cooperatively folded structures.[11]

6.1.2 Conclusion

In this section it is shown that the IDP OPN cannot be described by polymer physical models such as random coil or molten globule polymers that are typically used in the description of IDPs.[12] Instead, OPN simultaneously populates extended as well as cooperatively folded structures. This observation for OPN is, to the best of my knowledge, the first convincing experimental demonstration of cooperative behavior in an intrinsically disordered protein, proving recently found first hints on cooperativity.[26] The fact that OPN samples cooperatively stabilized as well as extended conformations further gives rise to novel reflection potentials in the context of IDP binding mechanisms: This property may provide an efficient mechanism to control interaction interfaces across cellular surfaces and thus endows OPN with unique possibilities to modulate interaction patterns with its several natural ligands.[4] Most importantly, the existence of structural cooperativity in IDPs calls for a novel conceptual view of IDPs that goes beyond the traditional binary scheme of order vs. disorder. Undoubtedly, a paradigm shift is needed in order to adequately address the subtleties of heterogeneous conformational sampling in IDPs and their putative relevance for biological functions.

6.2 Conformational Adaptions of Osteopontin upon Heparin Binding

Knowing about condition-dependent peculiarities of the conformational space of OPN it is of interest how it will change when OPN interacts with one of its natural ligands. To this end, this section addresses the interplay between OPN and heparin.[13] It will be shown which structural adaptions follow from the complex formation and how entropic penalties due to heparin binding are compensated through partial unfolding of OPN. Again, the integrated NMR and EPR experimental technique could give rise to highly detailed data, which is simply not producible with classic experimental approaches. I will focus here on the EPR data again. But by using certain input from NMR, this section will nonetheless elucidate a novel kind of fuzzy complex in the realm of functional IDPs by an integrated magnetic resonance approach.

6.2.1 Results and Discussion

In the following all data will be concerning signal differences between the apo- and the heparin-bound state. This is of special importance for PRE data as ΔPRE = PRE(heparin-bound)-PRE(apo).

The Central Segment of OPN Expands upon Heparin Binding

When interpreting PREs of IDPs one should be aware that due to their rapid conformational sampling one always observes ensemble averages through PRE data.[17] Hence, all conclusions drawn from these refer to “average” conformations. ΔPRE is calculated as the change in ^{15}N-^{1}H HSQC signal intensities upon heparin binding to OPN. Hence, ΔPRE > 0 indicates “on average” increasing distance between labeling site and a residue, ΔPRE < 0 denotes the opposite. A residue plot, kindly provided by Gerald Platzer and Robert Konrat, is shown in Figure 6.2.1. It shows residue specific, differential PREs for heparin binding to the four available OPN single mutants. The red bar indicates the heparin binding site, as known from an earlier study.[13] Residues located in this region were excluded from the analysis because of significant overlap and reduced intensities in the heparin bound state. As can be observed, OPN loses significant long-range backbone contacts around this site, as heparin binds (ΔPRE > 0). Especially spin labels attached to residues C108 and C188 gain distance from the central region of OPN, that is, from residues 120-150. Additionally, C108 gains distance from residues 150-200. Similar but less pronounced PRE changes were observed for the region 90-100 for both, C108 and C188.

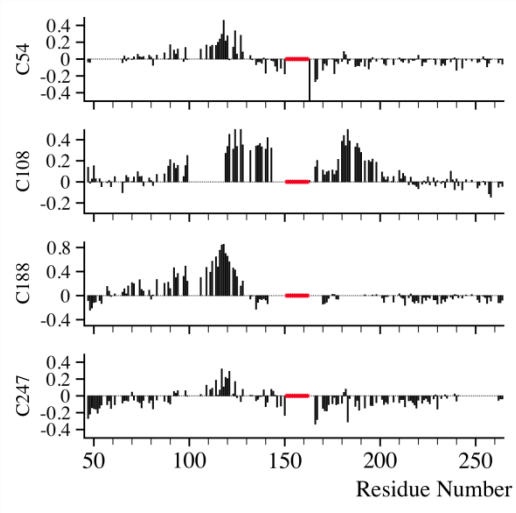

Figure 6.2.1. a) ΔPRE for the four different labeling sites upon heparin binding from ^{15}N-^{1}H HSQC signal intensity changes. ΔPRE > 0 indicates increasing distance between labeling site and a residue, ΔPRE < 0 the opposite. (ΔPRE = ^{15}N-^{1}H HSQC-Intensity (heparin-bound) – ^{15}N-^{1}H HSQC-Intensity (apo)). Residues located in the region depicted in red were excluded from the analysis because of significant overlap and reduced intensities in the heparin-bound state.

The decreasing compactness of the central region of OPN is further mirrored in its motional dynamics, as shown in reference [25]. There ^{15}N relaxation measurements (^{15}N T_1, T_2 and ^{15}N-^{1}H heteronuclear Overhauser enhancement, NOE) are presented both, in the apo- (ligand free) and heparin-bound state. It is shown that the region containing most of the heparin binding site (140-170 & 180-200) displays a decrease in ^{15}N T_2 due to local rigidification of the backbone upon binding (nanosecond time scale motions). Simultaneously, larger ^{15}N-^{1}H NOE values indicate reduced fast,picosecond timescale backbone motions. The region encompassing residues 90-120 exhibits a contrary behavior: Increased backbone flexibility in the bound state as seen by both, increased T_2 values and decreased heteronuclear NOEs. The finding that residues 90-120 are more flexible in the heparin bound state is in good agreement with decreased PRE values and strongly supports the assumption that the central region becomes loosened and more displaced from the heparin binding site and thus less restrained upon complex formation. Probing nano- to microsecond motions complementary to NMR, CW EPR on the four available OPN single mutants reveals that the label attached to residue C108 gains mobility through heparin binding, while the mutant C188 exhibits a more restricted rotational motion than in the apo state ($\tau_{c,108}$(apo) = 0.52 ns, $\tau_{c,108}$(bound) = 0.43 ns, $\tau_{c,188}$(apo) = 0.69 ns and $\tau_{c,188}$(bound) = 0.87 ns; see Appendix Figure A6.2.2). τ_cs of spin labels attached to residues C54 and C247 appear not to be affected significantly by heparin binding. The increasing rotational mobility of MTSL at C108 is indicative for pronounced solvent exposure of this labeling site and expansion of the core segment of OPN.[27, 28] The decrease in rotational mobility at C188 can be attributed to sterical confinement of the spin label due to ligand binding.[25][29] The observed “on average” conformational expansion of the central region of OPN upon heparin binding can be rationalized when taking into account that heparin is a highly negatively charged polyelectrolyte that predominantly interacts electrostatically with its environment (see charge map in Figure 6.1.3)

In an earlier study[13] heparin has been shown to bind to the region around the positively charged patch of OPN (Figure 6.1.3 b)), in order to exploit favorable electrostatic interactions.[13, 25] However, the large negatively charged patch around residues 80-120 interacts repulsively with heparin due to like charges and therefore becomes displaced from the central region of OPN around residue 155 as

soon as heparin binds. Recall from Section 6.1 that negatively and positively charged patches of OPN feature high propensities for close contacts in the cooperatively folded state of OPN. In the apo-state the negatively charged region around C108 is attracted by the positive patch around residue 155.[25] This structural peculiarity is likely to accentuate the difference in compactness of the core segment between the expanded heparin-bound and the compacted apo state of OPN, leading to a clearly observable expansion of the central region of the protein and to positive ΔPRE as shown in Figure 6.2.1. Concluding, the OPN/heparin complex reveals an electrostatic binding mode largely governed by complementary charge patterns as often found in molecular recognition processes.[23, 30]

The expansion of the heparin core segment can thermodynamically be rationalized when taking into account that it compensates losses in conformational entropy of the OPN/heparin system due to ligand binding and restrained rotational and torsional freedom close to the heparin binding site.[31, 32] Through this compensation, the overall thermodynamic equilibrium between counteracting contributions like solvation enthalpy and configurational entropy may cancel, allowing for large binding and dissociation constants, as typical for IDPs.[2, 33] Interestingly, increased PRE values upon heparin binding can be found for the mutants C54 and C247 within a residue stretch located close to the heparin binding site. In particular, for the mutant C247 significantly larger ^{15}N-^{1}H HSQC signal intensities were observed for residues 160-170. This indicates that the two termini "on average" fold back stronger to the core region of OPN in the heparin-bound state than in the apo state, likely gaining enthalpy through favorable backbone contacts.

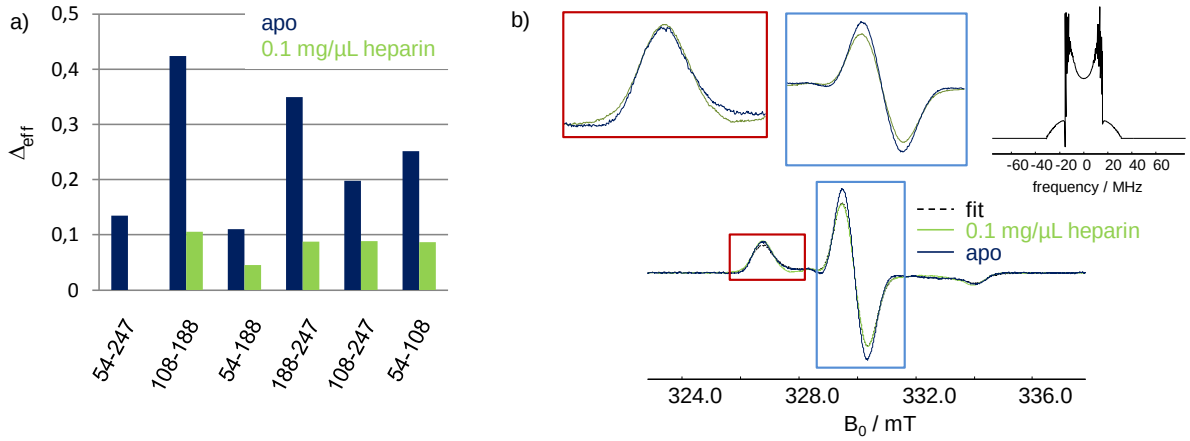

Figure 6.2.2. a) Δeff for the six double mutants under investigation in the apo and in the heparin-bound state. b) Pseudo-modulated low-temperature electron spin echo for C54-C247 in the denatured and in the heparin-bound state. The latter could be fitted by convolution of the spectrum corresponding to the denatured form with a Pake spectrum (see inset).

The Termini of OPN Approach each other upon Heparin Binding

To complement the NMR-derived data on OPN, DEER was again applied to the six available OPN double mutants. The raw data are shown in Appendix Figure A6.2.1. No clear-cut modulations are observable in any case. Again, DEER time traces are analyzed through an effective modulation depth, Δ_{eff}, as defined in the previous section. Yet, here t_{max} = 2 µs. In Figure 6.2.2 a) Δ_{eff} values for the six double-mutants in the apo and heparin-bound state are shown. In all cases heparin binding leads to a clear decrease in Δ_{eff}. This is in excellent agreement with the expansion of the central segment of OPN upon heparin binding, observed by means of NMR.

Yet, for C54-C247 one observes a strong dipolar broadening of the low-temperature ESE (see the General Introduction on electron spin echoes), when heparin binds to OPN. Such an observation typically indicates very short distances < 1.5 nm between the two spins of a double mutant, but not an expansion.[34] Fitting the broadened ESE by convolution of the echo of completely denatured C54-C247 (in the presence of 8 M urea and 4 M NaCl)[25] with a Pake pattern, based on a Gaussian distance distribution, (see Figure 6.2.2 b)) yields a mean distance between the two labels of ~0.8 nm with a FWHM (full width at half maximum) of ~0.4 nm in the heparin bound state. Approximately 80% of the CW EPR spectrum is subject to dipolar broadening. Note that even by a convolution approach distances < 1.5 nm can often not be determined free of errors, due to overrepresentation of short distances and other factors. [34] Therefore, the above values should only be regarded as qualitative indication for short distances in the conformational ensemble of OPN. Nonetheless, these short distances give rise to significant PRE effects for C247. The mutant exhibits negative ΔPREs at the N-terminal region. The reduced ^{15}N-^{1}H HSQC signal intensities in the complex indicate shorter distances between positions C54 and C247 site upon complex formation. The PRE data (Figure 6.2.1) are therefore in full agreement with the EPR-derived assumption of shortened distances between the termini of OPN in the heparin-bound state. Thus, although on average OPN loses "compactness" in its central region upon heparin binding, the termini come closer together in space. With most of the distances between C54 and C247 being quite short one can further explain the decrease in Δ_{eff}, by non-excited lines of the Pake doublet, but not by increasing interspin distances. At the given pump-pulse length, τ_P, of 12 ns the shortest interspin distance for an excitable dipolar coupling between observer- and pump-spins amounts to: $r_{min} = (2\hbar\gamma^2\pi^{-1}\tau_p)^{1/3} \approx 1.6$ nm.[35] Hence, the decrease in Δ_{eff} indeed corresponds to an increase in mean interspin distance for all double mutants except C54-C247, where it corresponds to a significant decrease in interspin distance.

6.2.2 Conclusion

By combining NMR and EPR measurements it could be shown that heparin-binding to OPN leads to complex structural adaptions of this IDP predominantly mediated through electrostatic interactions. Central unfolding of OPN very likely compensates losses in configurational entropy due to ligand binding. Although there is local rigidification in the heparin binding cleft (region 160-180) the resulting entropic penalty is partly relieved by a compensatory increase in conformational flexibility of the negatively charged region around residues 80-120. This thermodynamic property might be crucial for the versatility of host-guest interactions of IDPs, since compensation of losses in configurational entropy is crucial for rapid binding and dissociation kinetics. Next to the central unfolding a decreasing distance between the two IDP termini could be detected, potentially mediated through hydrophobic patches at each end of the protein. Also, the mutants C54 and C247 interact stronger with the core region upon heparin binding as shown by means of PRE. While the central segment of OPN expands the terminal parts of OPN fold back stronger in the heparin bound-state. In general one can state that the binding mode between OPN and heparin features central "unfolding-upon-binding" as well as terminal "folding-upon-binding". This might also be described in terms of a novel kind of fuzzy complex.[36]

6.3 Structural Response of Intrinsically Disordered BASP1 to pH Variation

On the one hand, the polymorphism of IDPs and the subsequent structural adaptability allows for multiple interactions with different binding partners and for functional ambiguity, but on the other hand it also gives rise to drastic structural responses to even minor changes in primary sequence or

solution conditions.[37] This has partly been shown in the previous section with OPN as an example of sensitivity to co-solutes. The pronounced response of IDPs to environmental irregularities is of special scientific interest, because structural distortions and the following protein dysfunctions frequently constitute the molecular basis for tumor genesis or other diseases.[4] Thus, a deeper understanding of IDPs' structural responsiveness to stimuli is worthwhile when having an eye on future medicinal developments. In this context, I aim at showing how the brain acid soluble protein 1 (BASP1) responds to variations in solution pH. Since BASP1, among other things, is a co-suppressor for WT1 function (Wilms' Tumor suppressor protein1) insights into BASP1's environment-dependent conformational adaptions might possibly contribute to a better understanding of certain tumor suppression pathways.[38] On these grounds it will be demonstrated here how conformational adaptions of BASP1 are governed by complementary electrostatic and hydrophobic interactions as well as hydrogen bonds. A decrease in pH and subsequent neutralization of acidic residues leads to complete restructuring of the IDP demonstrating a subtle interplay between these non-covalent forces.[37, 39] The subsequent restructuring includes global cooperative compaction, local increase in helicity, a C-terminal compaction on intermediate length scales and at the same time a N-terminal expansion.

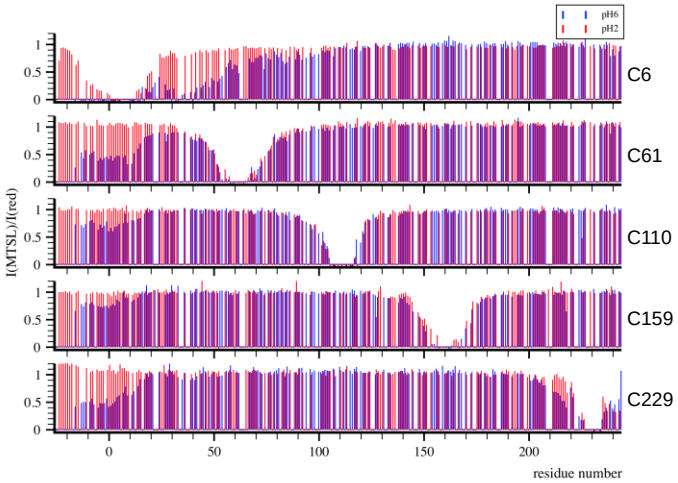

Figure 6.3.1. PRE vs. residue plots of five MTSL labeled single-mutants of BASP1 (from top to bottom: residues C6, C61, C110, C159 and C229). PREs at high pH are shown in blue. PREs at low pH are shown in red.

6.3.1 Results

To get a hint of the pH-dependent conformational characteristics of the recombinant 244 residues long BASP1, comprising an additional N-terminal His-tag, NMR and EPR experiments were performed at pH 6 (denoted 'high' in the following) and at pH 1-2 (denoted 'low' in the following).[17] Concerning NMR, I will again restrict myself to crucial PRE data only that yields residue-resolved information about encounters between single amino acids and site specific spin labels on length scales below ~3 nm (as calculated for the present case according to Solomon-Bloembergen).[40] The PRE data is kindly provided by Leonhard Geist from Robert Konrat's group.

PRE Data

In Figure 6.3.1 PRE-residue plots are shown for five MTSL-labeled mutants of BASP1 (C6, C61, C110, C159 and C229) at high (blue) and at low pH (red). Intermolecular PREs could be ruled out by DEER on BASP1 single mutants, which show perfectly homogeneous distributions of the spin labels. Despite the short-range PREs expected in a radius of 3 nm (approx. 10 residues) around the labeling

sites, the data for high pH show noteworthy effects at the N-terminus of BASP1 for mutants C61 and C229. This indicates significant encounters of these two labeled residues with the N-terminus of BASP1. For mutants C110 and C159 this effect of N-terminal encounters to the labeled region is less pronounced, yet still detectable. Furthermore, an approx. 120 residues broad N-terminal region shows significant PREs if MTSL is attached to C6. As noted above, PREs only give rise to ensemble-averaged data due to the rapid conformational sampling of IDPs. For the present case all PRE data at high pH together indicate an "average" conformation in which a ~120 residues broad N-terminal region (comprising C6 as well as C61) is more compact than the rest of the polypeptide chain. Further, the C-terminus samples the residual polypeptide chain with a propensity for encounters with the N-terminus. The weak interactions between C110 and C159 and the N-terminus can in this scenario be regarded as a consequence of dynamic back folding.

When lowering the solution pH, the conformational space of BASP1 undergoes drastic changes: Firstly, back folding is not observable anymore by means of NMR since all N-terminal PREs vanish that are observable at high pH. Secondly, the N-terminal, 120 residues comprising region that exhibits significant PREs for C6 at high pH is devoid of PREs at low pH. Only the closest ~10 amino acids around the labeling site are still subject to PRE, like one would observe it in an entirely unstructured polypeptide.[41] In general only short-range PREs in immediate vicinity of the labeling sites remain detectable for BASP1 at low pH. Thus, one can already unequivocally state that BASP1 loses compactness on length scales below 3 nm (the PRE sensitivity range) upon a decrease in pH. The PRE data demonstrate that the N-terminal region around C6 is not as compact anymore as at high pH and that BASP1 features lower back folding propensity since long-range intra-chain contacts disappear at low pH that point to more compact structures.

DEER Data

While PREs detect spin-residue encounters below 3 nm, DEER allows for complementary probing of distances up to 8 nm under aqueous conditions. In Figure 6.3.2 a) time traces on four doubly spin-labeled BASP1 mutants (C6-C110, C61-C159, C110-C229 and C6-C229) are shown at physiological and at low pH. Data on C61-C159 and C6-C229 at low pH appear experimentally as homogeneous spin distributions (here t_{max} = 4 µs). Such an observation indicates very long distances between the respective MTSL labels of C6-C229 and C61-C159 at low pH, since no dipolar broadening of the ESEs is observed..[25] Like OPN, BASP1 features quite broad distributions of interspin distances between two spin-labeled residues. This is reflected in the fact that all time traces are void of modulations. Such, an analysis based on Δ_{eff} is again possible. Background correction was done experimentally through DEER on single mutants.

At high pH one observes that for C6-C229 Δ_{eff} is close to the Δ_{eff} values of mutants C6-C110 and C110-C229 (see Table 6.3.1). Yet, the number of residues between the spin labels, *N*, for the latter two mutants is much smaller for C6-C229. This is in a very good agreement with the PRE-derived picture of N- and C-terminal encounters through back folding, since $\langle R^2 \rangle^{1/2}$ does not scale positively with *N*,[20] but is smaller for larger *N*.

To gain a more detailed picture of interspin distances in BASP,1 the DEER time traces were not only analyzed through Δ_{eff}, but also fitted to Gaussian distance distributions. These are depicted in Figure 6.3.2 2b). For all mutants except for C110-C229 the mean distance between two spin labels is between 4.5 and 5 nm (see Table 6.3.1). For C110-229 the mean distance is approx. 6 nm. Yet, note that for C61-C159 $\Delta_{eff} \approx 0.16$. Taking into account that $\lambda = 0.516$, distance distributions derived for C61-C159 feature significant uncertainties, as the DEER signal does not decay to λ within t_{max} = 4 µs.

Nevertheless, observing comparable mean distances between C6-C229 and the other double mutants, despite drastic differences in the number of separating residues between the respective labeling sites at high pH, again substantiates the picture of an on average back folded mean conformation. Since the extraction of distance information from DEER-time traces is a moderately ill-posed problem,[21] mean values of simple Gaussian distribution functions are only compared qualitatively here, such that also possible deviations of ~0.5 nm from the real 'physical' distributions do not influence the results of the data analysis.[42]

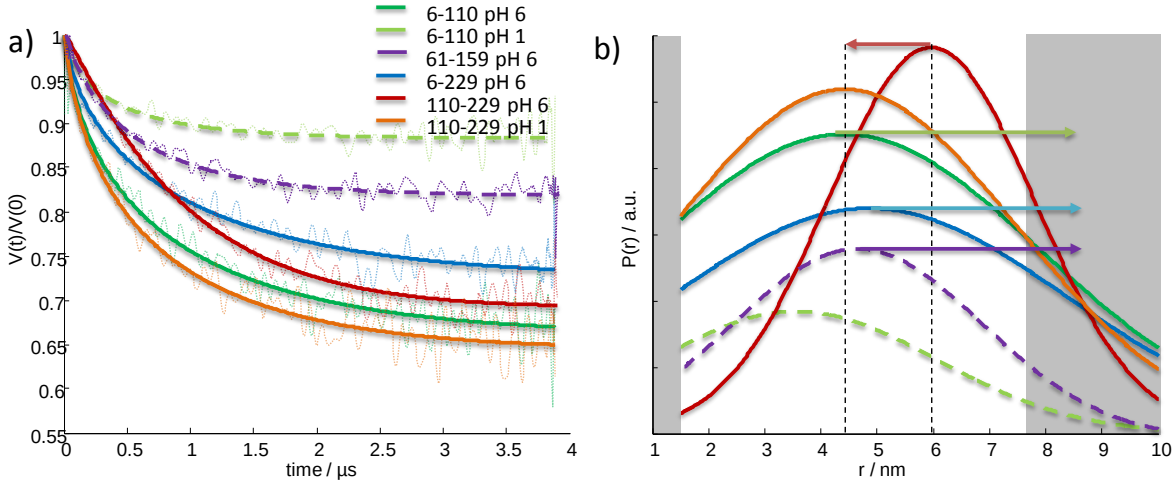

Figure 6.3.2. a) DEER time traces for BASP1 double mutants C6-C110, C61-C159, C110-C229 and C6-C229 (dotted lines) and fits to Gaussian distance distributions (solid and dashed lines). b) Distance distributions corresponding to the fits in a). The gray shaded regions indicate distances outside the DEER sensitivity range. [35] The dashed lines indicate that the distance distribution is based on time traces with low Δ_{eff} and has to be interpreted carefully. In the case of C6-C110 the apparent shift to lower distances is actually overcompensated by a larger fraction of conformations featuring significantly elongated C6-C110 distances. Similar caution should be taken when interpreting the distance distribution for C61-C159. Arrows indicate shifts of the distributions upon decreasing pH.

As the pH decreases Δ_{eff} for C110-C229 increases and the DEER signal decay becomes steeper. In contrast, for C6-C110 one observes a significant loss in Δ_{eff} and even a complete reduction to zero for C61-C159 and C6-C229. Since with decreasing Δ_{eff} the mean interspin distance increases[25] BASP1 clearly expands upon lowering pH on DEER length scales. In particular, the interspin distance for C61-C159 and C6-C229 on average increase significantly when decreasing the pH. This is in good agreement with the loss of compact structures upon decreasing pH as observed by means of PRE.

Table 6.3.1. List of the effective modulation depths, Δ_{eff}, and of the mean distance, $\langle R^{1/2} \rangle^2$, as gained from fits of the DEER time traces to Gaussian distance distributions for all double mutants under investigation.

high pH				
	6-110	61-159	110-229	6-229
Δ_{eff}	0.31	0.18	0.30	0.26
$\langle R^{1/2} \rangle^2$	4.4 nm	4.6 nm[a]	5.9 nm	4.8 nm
low pH				
	6-110	61-159	110-229	6-229
Δ_{eff}	0.12	0	0.34	0
$\langle R^{1/2} \rangle^2$	3.6 nm[a]	-	4.3 nm	-

[a] Note that these values might be subject to significant error margins.

An equal assumption is valid for C6-C110, where Δ_{eff} is 0.12 only at low pH. Furthermore, the N-terminal expansion observed by PRE is mirrored in the fact that MTSL at C6 gains rotational freedom as the pH decreases. The rotational correlation times for C6 as determined from room temperature CW EPR amount to: $\tau_{c,\ high\ pH}$ = 0.63 ns; $\tau_{c,\ low\ pH}$ = 0.39 ns, which indicates less sterical confinement as a consequence of the pH-triggered expansion (Appendix Figure A6.3.1).

Although the N-terminal region of BASP1 clearly expands upon a decrease in pH and the two termini gain distance from each other, there is also evidence for a contrary phenomenon extractable from the DEER data. The mutant C110-C229 indicates an unexpected compaction of the IDP, as reflected in higher Δ_{eff}, steeper descent of the time trace and a by ~1.5 nm reduced mean interspin distance as indicated by the Gaussian fits in Figure 6.3.2 b) (see also Table 6.3.1). Thus, despite all the evidence for an expansion of BASP1 the DEER data indicates compaction of the central to the C-terminal part of the protein upon decreasing pH. This discrepancy can be satisfactorily explained with assuming that the N-terminus expands upon decreasing pH and the C-terminus compacts. In such a scenario the two termini would gain distance and all other observations (PRE and DEER) could be consistently explained, since C-terminal compaction is in no conflict with increasing distance between C6 and C110/C229. Yet, it should be noted that the "average" compaction of the C-terminal region, although evident from DEER, is not reflected in the PRE data. This indicates that the compaction only takes place on intermediate length scales, such that the interspin distance between C110 and C229 does not become significantly shorter than 3 nm in most of BASP1's conformations. This displays the necessity to probe different length scales in order to entirely characterize an IDP. Based on the rotational mobility of MTSL attached to C110 and C229 one can assume that compaction takes place on length scales of a few nanometers, but not on single residue level (C110: $\tau_{c,\ phys.\ pH}$ = 0.35 ns, $\tau_{c,\ low\ pH}$ = 0.32 ns; C229: $\tau_{c,\ phys.\ pH}$ = 0.38 ns, $\tau_{c,\ low\ pH}$ = 0.36 ns). I.e., the spin labels in the compacted region retain inherent fast rotational motion that gives rise to a high local mobility.

6.3.2 Discussion

The N-terminal expansion in combination with C-terminal compaction of BASP1 upon decreasing pH can be rationalized when taking into account the residue charges. In Figure 6.3.3 a charge map of the IDP is shown at high (top) and at low pH (bottom).

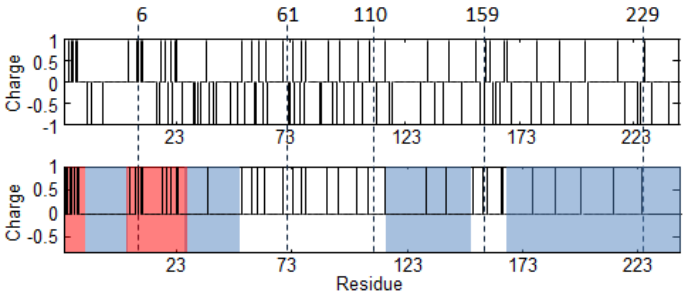

Figure 6.3.3. Charge map of BASP1 at high (top) and low (bottom) pH. Regions marked red indicate high populations of positive charges, while blue marked ones indicate charge neutralized patches.

As can be observed at high pH, charged residues are quite homogeneously distributed along the BASP1 chain, except for the N-terminal region with a more inhomogeneous distribution of positive and negative charges. This might be the reason for the compact N-terminus at high pH, as observed through PREs (Figure 6.3.1; top). In contrast, at low pH with all the negative charges neutralized, the N-terminal region features two patches with dense populations of positive charges. Consequent like-charge repulsion may be the cause for the observed expansion of the N-terminal region. Similar

considerations can account for the compaction of the C-terminal region. Since at low pH this part of the IDP is to a very large degree charge depleted it is at hand to assume that hydrophobic interaction and intramolecular hydrogen bonds between discharged patches along the chain provide the driving force for the C-terminal compaction. The resulting "average" structure of BASP1 at physiological and at low pH that can be deduced from the combined PRE and DEER measurements is schematically depicted in Figure 6.3.4. At high pH, BASP1 exists in a back-folded mean conformation. Yet, judging from residue mobility (as reflected in the quite short τ_cs) this IDP is locally, on the level of single amino acids, very flexible like one would expect it for a random coil. The relatively short distance between the two termini clearly shows that random-coil or other polymer physical models are not sufficient to describe the conformations of BASP1. As the pH decreases, the discharging of basic side chains along the protein leads to an expansion of the N-terminal region and a compaction of the C-terminal region and consequently to a "mean" structure as depicted in Figure 6.3.4 on the right.

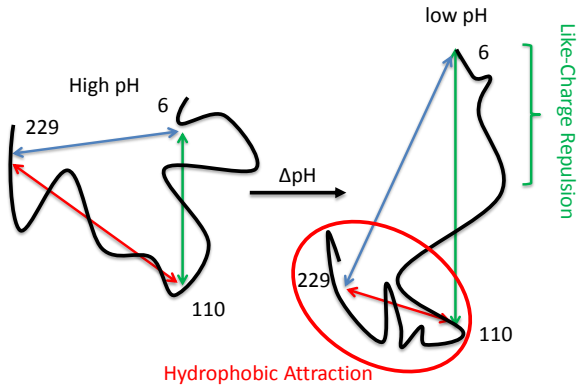

Figure 6.3.4. Schematic depiction of the "average" conformation of BASP1 at high (left) and low pH (right). At low pH like-charge repulsion leads to an expansion of the N-terminus of BASP1, while hydrophobic attraction leads to a compaction of C-terminal region.

The pH-dependent interplay between compaction and expansion in BASP1 is furthermore reflected in previously published data on IDP pH-dependence.[43] It has been reported that BASP1 undergoes a significant compaction upon lowering solution pH. The hydrodynamic radius shrinks from approx. 3.8 nm to approx. 2.8 nm. Thus, the observed compaction of the C-terminal region of BASP1 is in agreement with the pH-dependence of the hydrodynamic radius. Since here an expansion of the N-terminal region upon decreases in pH and loss of long-range intrachain contacts is also reported, it is reasonable to assume that the C-terminal compaction leads to stronger impact on the overall hydrodynamic radius of BASP1 than the N-terminal expansion. Furthermore, contrary to the N-terminal expansion shown by DEER and PREs it has been reported that BASP1 features increased propensities for alpha-helicity especially in the N-terminal region at low pH. [43] Increased alpha-helicity is, however, typically associated with chain compaction, not expansion. [13]

The conflicting findings of overall compaction and expansion of the N-terminus of BASP1 can be reconciled when taking into account the length scales of all the different observations. Increased alpha-helicity leads to local compaction, i.e. on length scales of only a few amino acids. Yet, decreasing PRE effects and modulation depth report an expansion on length scales of a few nanometers. Thus, all the different observations concerning the N-terminal region of BASP1 can be combined in the following picture: Upon decreasing pH, the N-terminal region gains alpha-helix propensities, local compactness and consequently also chain stiffness. The latter results in longer interresidue distances and hence in elongation on length scales longer than a few residues. Yet, on the global

scale BASP1 compacts upon lowering pH, as mirrored in the reduced hydrodynamic radius and DEER on C110-C229 that shows C-terminal compaction of BASP1. Interestingly, the hydrodynamic radii reported for BASP1 are even at high pH smaller than one would expect it for an unfolded protein: I.e. approx. 5.1 nm as calculated from empirical relations.[44] Thus, BASP1 features a globally more compact structure than an unfolded protein (even more compact at low pH) in its monomeric state, but also a quite mobile (as deducible from pH-independent τ_cs at C110 and C229) and expanded conformation on the level of single residues. Hence, from a detailed analysis of BASP1's conformational space it is evident that for a description of IDPs one has to discern local and global length scales in order to take into account complicated structuring principles.

6.3.3 Conclusion

To gain deeper understanding of the pH-dependence of the conformational space of BASP1 here state-of-the-art NMR and EPR methodologies are combined addressing average conformations and structural peculiarities on several length scales. While BASP1 features significantly back folded conformations at high pH, leading to encounters between N- and C-terminus, it features a rather complex structure at low pH. Firstly, the C- and the N-terminus gain distance. Secondly, on length scales of a few nanometers the C-terminal region compacts and the N-terminal region expands. Simultaneously, the whole protein gains helix propensities and hence local compactness. On the global scale the whole IDP compacts, although it retains a local, apparently inherent fast single-residue-motion; an issue, which gives rise to a compact, yet simultaneously highly mobile conformational state. The rather complicated picture of BASP1's conformational space at low pH could only be elucidated by probing several length scales. Thus, the investigation of the solution structure of BASP1 prominently displays the necessity of combined experimental approaches that probe different distance regimes. Furthermore, this section shows that structural adaptions of BASP1 upon pH decrease can to a large degree be estimated by taking into account both charged and charge-depleted patches along the protein backbone and resulting non-covalent forces that govern the IDP's conformational space. Since a similar observation has already been made for OPN above,[25] it is at hand to speculate that coarse-grained information about tertiary structural properties of IDPs can to a significant degree be anticipated through considerations about simple non-covalent interaction patterns.

References and Notes

[1] P. Tompa, *Trends. Biochem. Sci.* **2002**, *27*, 527.
[2] V. N. Uversky, *Int. J. Biochem. Cell Biol.* **2011**, *43*, 1090.
[3] A. K. Dunker, Z. Obradovic, *Nature Biotech.* **2001**, *19*, 805.
[4] A. Bellahcène, V. Castronovo, K. U. E. Ogbureke, L. W. Fisher, N. S. Fedarko, *Nat. Rev.* **2008**, *8*, 212.
[5] D. D. Boehr, R. Nussinov, P. E. Wright, *Nat. Chem. Biol.* **2009**, *5*, 789.
[6] R. Konrat, *Structure* **2010**, *18*, 416.
[7] C. Holt, L. Sawyer, *J. Chem. Soc. Farad. Trans.* **1993**, *89*, 2683.
[8] V. Ozenne, R. Schneider, M. Yao, J.-r. Huang, L. Salmon, M. Zweckstetter, M. R. Jensen, M. Blackledge, *J. Am. Chem. Soc.* **2012**, *134*, 15138.
[9] J.-r. Huang, S. Grzesiek, *J. Am. Chem. Soc.* **2010**, *132*, 694.
[10] T. Mittag, J. Marsh, A. Grishaev, S. Orlicky, H. Lin, F. Sicheri, M. Tyers, J. D. Forman-kay, *Structure* **2010**, *18*, 494.
[11] J. A. Marsh, J. D. Forman-Kay, *J. Mol. Biol.* **2009**, *391*, 359.
[12] V. N. Uversky, *Prot. Sci.* **2002**, *11*, 739.

[13] G. Platzer, A. Schedbauer, A. Chemeli, P. Ozdowy, N. Coudevylle, R. Auer, G. Kontaxis, M. Hartl, A. J. Miles, B. A. Wallace, O. Glaser, K. Bister, R. Konrat, *Biochemistry* **2011**, *50*, 6113.
[14] R. Schneider, J.-r. Huang, M. Yao, G. Communie, V. Ozenne, L. Mollica, L. Salmon, M. R. Jensen, M. Blackledge, *Mol. BioSyst.* **2011**, *DOI: 10.1039/c1mb05291h*.
[15] M. Drescher, *Top. Curr. Chem.* **2012**, *321*, 91.
[16] G. Jeschke, Y. Polyhach, *PCCP* **2007**, *9*, 1895.
[17] G. M. Clore, C. Tang, J. Iwahara, *Current Opinion in Structural Biology* **2007**, *17*, 603.
[18] B. Morin, J. M. Bourhis, V. Belle, M. Woudstra, F. Carriere, B. Guigliarelli, A. Fournel, S. Longhi, *J Phys Chem B* **2006**, *110*, 20596.
[19] Note that background reference measurements on single mutants were performed at similar protein concentrations to assure constant excluded volume effects. Thus, the spin concentration is only half the concentration as in the case of double-mutants. This adds a factor of 2 to the background function (eq. 1.1.82). For the relative comparison done here this factor is negligible.
[20] M. Rubinstein, R. Colby, "*Polymer Physics*", Oxford University Press, New York, 2004.
[21] G. Jeschke, A. Koch, U. Jonas, A. Godt, *J Magn Reson* **2002**, *155*, 72.
[22] C. Tanford, *J. Am. Chem. Soc.* **1964**, *86*, 2050.
[23] N. Sinha, S. J. Smith-Gill, *Current Protein and Peptide Science* **2002**, *3*, 601.
[24] F. Avbelj, L. Fele, *J. Mol. Biol.* **1998**, *279*, 665.
[25] D. Kurzbach, G. Platzer, M. Henen, T. Schwarz, R. Konrat, D. Hinderberger, *submitted* **2012**.
[26] V. N. Uversky, C. Santambrogio, S. Brocca, R. Grandori, *Febs Lett* **2012**, *586*, 70.
[27] W. Hubbell, D. Cafiso, C. Altenbach, *Nature Struct. Biol.* **2000**, *7*, 735.
[28] W. Hubbell, H. Mchaourab, C. Altenbach, M. Lietzow, *Structure* **1996**, *4*, 779.
[29] Note that intermolecular contributions to PRE data can be ruled out through DEER on the four single mutants, which showed perfectly homogenous spin distributions in the solutions.
[30] B. Honig, A. Nicholls, *Science* **1995**, *268*, 1144.
[31] C. E. A. Chang, W. Chen, M. K. Gilson, *P Natl Acad Sci USA* **2007**, *104*, 1534.
[32] K. K. Frederick, M. S. Marlow, K. G. Valentine, A. J. Wand, *Nature* **2007**, *448*, 325.
[33] S. Chiba, Y. Harano, R. Roth, M. Kinoshita, M. Sakurai, *J Comput Chem* **2012**, *33*, 550.
[34] J. E. Banham, C. M. Baker, S. Ceola, I. J. Day, G. H. Grant, E. J. J. Groenen, C. T. Rodgers, G. Jeschke, C. R. Timmel, *J Magn Reson* **2008**, *191*, 202.
[35] Y. D. Tsvetkov, A. D. Milov, A. G. Maryasov, *Russ. Chem. Rev.* **2008**, *77*, 487.
[36] P. Tompa, M. Fuxreiter, *Trends Biochem Sci* **2008**, *33*, 2.
[37] V. N. Uversky, *Protein J* **2009**, *28*, 305.
[38] B. Carpenter, K. J. Hill, M. Charalambous, K. J. Wagner, D. Lahiri, D. I. James, J. S. Andersen, V. Schumacher, B. Royer-Pokora, M. Mann, A. Ward, S. G. E. Roberts, *Mol Cell Biol* **2004**, *24*, 537.
[39] J. A. Marsh, J. D. Forman-Kay, *Biophysical Journal* **2010**, *98*, 2383.
[40] J. Iwahara, C. D. Schwieters, G. M. Clore, *J. Am. Chem. Soc.* **2004**, *126*, 5879.
[41] K. Teilum, B. B. Kragelund, F. M. Poulsen, *J Mol Biol* **2002**, *324*, 349.
[42] S. D. Köhler, M. Sptzbarth, K. Diedrichs, T. E. Exner, M. Drescher, 2011, 167., *J. Magn. Reson.* **2011**, *208*, 167.
[43] L. Geist, M. A. Henen, S. Haiderer, D. Kurzbach, A. Zawadzka-Kazimierczuk, S. Saxena, S. Żerko, W. Koźmiński, D. Hinderberger, R. Konrat, *Submitted* **2012**.
[44] D. K. Wilkins, S. B. Grimshaw, V. Receveur, C. M. Dobson, J. A. Jones, L. J. Smith, *Biochemistry* **1999**, *38*, 16424.

7. Summary and Outlook

This thesis is concerned with the study of non-covalent forces as structuring principles of soft matter of varying complexity. By means of EPR spectroscopy, frequently augmented with other experimental and computational techniques, it is investigated how electrostatic and hydrophobic interactions as well as hydrogen bonds and combinations among these together with entropic effects lead to structuring of soft matter, especially of polymers on length scales spanning 0.1 to 100 nm. By carefully tuning equilibria between repulsive and attractive potentials among the polymers it is possible to utilize interaction patterns (or profiles) between different kinds of non-covalent forces for the generation of a variety of supramolecular structures. This is not just a finger exercise. Contrary, targeted generation of purposeful structures is likely to be the basis for many future applications derived from 'nano technology'. This assumption is mirrored, e.g., in the fact that thermoresponsive polymers are assumed to have great potential for future drug delivery applications, because of their ability to undergo an inverse phase transition at tunable temperatures. Further, macromolecular structuring – due to elaborated non-covalent interaction patterns – is also crucial for many biological functions, like for protein interaction networks: Disordered proteins are able to simultaneously interact with several ligands only because they can adopt specific structures upon directional, non-covalent substrate interaction. To explore the apparently interesting and important molecular structuring effects that arise from different non-covalent interaction profiles, selected examples have been investigated throughout this thesis. Each of the studied systems is governed by specific non-covalent force equilibria:

In **Chapter 2** it is shown that correlations among electrostatic interaction can lead not only to structuring of densely charged polyelectrolytes, like in DNA condensation, but also of small ionic building blocks that as a result form 'supramolecular polyelectrolytes' that were coined colloid-like ionic clusters or Ionoids. In the case of DNA condensation, counterions adopt a correlated structure on the surface of the polyelectrolytes leading to highly defined rod-like condensates. In the case of Ionoids, electrostatic correlations between cationic macrocycles and anionic Fremy's salt combined with influences of solvent entropy lead to the formation of transient, yet defined colloid-like ionic clusters in solution. Both systems demonstrate the impact that correlations between non-covalent forces can have on molecular level structures of soft matter.

In **Chapter 3** electrostatics are supplemented with hydrophobic interactions. It is demonstrated by means of novel applications of DEER spectroscopy that with peripherally charged dendronized polymers it is possible to achieve spatial separation of external electrostatic and internal hydrophobic interactions. This is possible because denpols constitute molecular objects with a defined and persistent envelope. Such, self-assembly of guest compounds on their surface and in their interior is individually possible. Even condensation of internally guest-loaded denpols can be achieved by increasing the charge of the ionic surface guests above 2e. Such, the transfer of the concept of DNA condensation to denpols is achieved. Since all structuring processes in denpols are reversible through adjustment of the solution pH or concentration of co-solutes, a load-collapse-release cascade could actually be realized and characterized by EPR in combination with TEM.

In **Chapter 4** the focus is shifted from electrostatics to equilibria between solution state-stabilizing hydrogen bonds and counteracting hydrophobic attraction in thermoresponsive alkylene oxide-based polymers. By combining intrinsically local spin probing CW EPR with macroscopic turbidity

measurements different mechanisms of the thermally induced inverse phase transition of a selected ensemble of polymers could be elucidated in great detail. It is shown that the inverse phase transition of poly(alkylene oxide)s always proceeds via nanoscopic inhomogeneities that precede large scale (macroscopic) aggregation / precipitation and that different types of nanoscale inhomogeneities are correlated with certain types of phase transition mechanisms. In this context nanoscale collapses turn out to be largely independent of exact topologies, but only dependent on the local, molecular structure of a polymer. In contrast, macroscopic aggregation is critically dependent on topology and molecular constitution.

In **Chapter 5** the phenomenon of thermoresponsiveness is studied in biomimetic matter, namely in genetically engineered elastin-like polypeptides, and contrasted against the synthetic poly(alkylene oxide)s. In the case of ELPs hydrogen bonds and hydrophobic interactions mediate temperature-dependent interaction strength between the polymers and the solvent, too. Yet, due to the complicated amino acid backbone non-covalent interaction patterns in ELPs are more complex than in the alkylene oxide polymers. It is shown that the amino acid-based backbone leads to thermoresponsive behavior of ELPs that is conceptually drastically different from the behavior of the synthetic structures. This is a consequence of two different types of hydration layers in ELPs: Hydrophobic side chain and hydrophilic backbone hydration shells. The phase transition of ELPs is dependent on coupling between the two different types of hydration. Coupling between hydration shells can lead (in dependence of primary structure) to highly cooperative dehydration events and massively rapid phase transitions, reminiscent of first-order processes.

In **Chapter 6** intrinsically disordered proteins (Osteopontin and BASP1) are investigated by means of CW EPR, DEER and complementary by NMR. Here not only H-bonds and hydrophobic side chain interactions constitute the structuring principle, but additionally electrostatics come into play. The functional and conformational versatility of IDPs is only possible because of the combination of these three non-covalent forces in one interaction profile that governs conformational space as structuring principle in combination with entropy. This leads to complicated sampling of heterogonous conformational spaces (comprising even cooperatively folded structure), to complex, “fuzzy” host-guest interactions and to delicate pH-response. Finally, the structural peculiarities of IDPs appear to be predictable to some degree through analysis of charge-rich (electrostatics) and charge-depleted regions (hydrophobic interactions and H-bonds) along the polymer backbone.

Many phenomena arising from non-covalent interaction profiles in soft matter are often counterintuitive and surprising. This is the case not at least because different investigated length scales give rise to sometimes very different experimental observations. Also stimuli responsiveness to temperature, pH, ionic strength, co-solutes and concentration as a consequence of the, compared to a classic chemical bond, weak nature of non-covalent interactions is frequently complicated to understand. Yet, the stimuliresponsive nature of structuring principles makes soft matter especially interesting for many applications, e.g., in targeted molecular delivery. In this context, EPR spectroscopy has turned out to be excellently suited for the elucidation of structuring events on nanoscopic length scales, as well as of underlying mechanisms of stimulus triggered phase transitions. Since EPR is predestined for investigations on nanoscopic length scales, the combination with other experimental techniques that probe larger length scales has turned out to be very fruitful. In future investigations of functional or smart materials this combination of different techniques should (in my eyes) be considered necessary in order to derive comprehensive pictures of molecular processes and non-covalent interaction profiles. These have to be well-understood if a targeted application of functional materials, novel drugs and molecular transporters is envisaged.

Abbreviations and Acronyms

AFM	atomic force microscopy
BASP1	brain acid soluble protein 1
CMC	critical micellization concentration
CMT	critical micellization temperature
CW	continuous wave
DEER	double electron-electron resonance
DLS	dynamic light scattering
de-PG	deprotected polyacrylic acid denpol generation
denpol	dendronized polymer
DMSO	dimethyl sulfoxide
DNA	deoxyribonucleic acid
DSA	4,4-dimethyl-oxazolidine-N-oxyl stearic acid
ELP	elastin-like polypeptides
EPR	electron paramagnetic resonance
ESE	electron spin echo
ESEEM	electron spin echo envelope modulation
FS	Fremy's salt
FT	Fourier transformation
hb	hyperbranched
HSQC	heteronuclear single quantum coherence
HYSCORE	hyperfine sublevel correlated spectroscopy
IDP	intrinsically disordered protein
LCST	lower critical solution temperature
MC	Monte Carlo
MD	molecular dynamics
MISS-DEER	mixed isotopologues for spectral selections-DEER
MTSL	S-(2,2,5,5-tetramethyl-2,5-dihydro-^{1}H-pyrrol-3-yl)methyl methanesulfonothioate
NMR	nuclear magnetic resonance
NOE	nuclear Overhauser enhancement
OSF	Odijk-Skolnick-Fixman
PAMAM	poly(amidoamine)
PB	Possion-Boltzmann
PDEGA	poly(N,N-diethyl glycidyl amine)
PEO	poly(ethylene oxide)
PG	poly(glycidol)
PNiPAAm	poly(N-isopropyl acryl amide)
PPI	poly(propylenimine)
PPO	poly(propylene oxide),
PRE	paramagnetic relaxation enhancement
OPN	Osteopontin
SNR	signal-to-noise ratio

TEM	transmission electron microscopy
TEMPO	(2,2,6,6-Tetramethylpiperidin-1-yl)oxyl
TFA	trifluoroacetic acetate
VdW	Van-der-Waals
WLC	worm-like chain

Appendix

A2. Electrostatics as a Structuring Principle for Molecular Assemblies

A2.1 Highly Defined Colloid-Like Ionic Clusters Through Self-Assembly in Solution.

A2.1.1 Experimental

CW EPR Measurements

A Miniscope MS200 (Magnettech, Berlin, Germany) benchtop spectrometer was used for X-band CW EPR measurements at a microwave frequency of ~9.4 GHz. Measurements were performed at room temperature (293 K) using a modulation amplitude of 0.05 mT. The microwave frequency was recorded with a frequency counter (Racal-Dana, model 2101).The temperature was set with a HO2-temperature control unit.
All spectral simulations were performed with home-written programs in MATLAB (The MathWorks, Inc.) employing the EasySpin toolbox for EPR spectroscopy.[1] Simulations of CW EPR spectra in fluid solution were performed by using the model, which is based on the slow-motion theory developed by Schneider and Freed as implemented in EasySpin.[2]

DEER Measurements

DEER is applied to glassy solids obtained by freeze-quenching the denpol solutions in supercooled iso-pentane. In this way a snapshot representative for the solution at the glass-transition point is detected. The sample volume was always large enough to fill the complete resonator. The four pulse DEER sequence $\pi/2(\nu_{obs})$ - τ_1 - $\pi(\nu_{obs})$ - (τ_1 + t) - (ν_{pump}) - (τ_2 - t) - $\pi(\nu_{obs})$ - τ_2 - echo was used to obtain dipolar time evolution data at X-band frequencies (9.2 to 9.4 GHz) with a Bruker Elexsys 580 spectrometer equipped with a Bruker Flexline split-ring resonator ER4118X_MS3. The dipolar evolution time t was varied, whereas τ_2 = 3 µs and τ_1 were kept constant. Proton modulation was averaged by the addition of eight time traces of variable τ_1, starting with $\tau_{1,0}$ = 200 ns and incrementing by $\Delta\tau_1$ = 8 ns. The resonator was overcoupled to Q ≈ 100. The pump frequency, ν_{pump}, was set to the maximum of the EPR spectrum (Figure S1b)). The observer frequency, ν_{obs}, was set to ν_{pump}+ 57.4 MHz, coinciding with the low field local maximum of the nitroxide spectrum (Figure S1b)). The observer pulse lengths were 32 ns for both π/2 and π pulses, and the pump pulse length was 12 ns. The temperature was set to 50 K by cooling with a closed cycle cryostat (ARS AF204, customized for pulse EPR, ARS, Macungie, PA). The total measurement time for each sample was around 12 h. The raw time domain DEER data were processed with the program package DeerAnalysis2010.[3] Background-contributions were removed dividing the time traces by an experimental background function (dimensionality = 3), derived from DEER on 6 mM $\mathbf{3}^{2-}$ solutions. The resulting time traces were normalized at t = 0.

Sample Preparation

Sample preparation and compounds: All compounds were synthesized as reported earlier.[4] Samples for EPR were prepared as follows: 6 mM $\mathbf{3}^{2-}$ were dissolved in a 1:1 mixture of DMSO and 88% aqueous glycerol solution. Afterwards, 2 mM of $\mathbf{1}^{4+}$ were dissolved in the $\mathbf{3}^{2-}$ solution. The final mixture was subsequently transferred to 3 mm outer diameter quartz tubes. For DEER the samples were additionally freeze-quenched in super-cooled iso-pentane. For DLS 3 mM of $\mathbf{2}^{2-}$ was dissolved in the solvent mixture and 1 mM of $\mathbf{1}^{4+}$ were added subsequently.

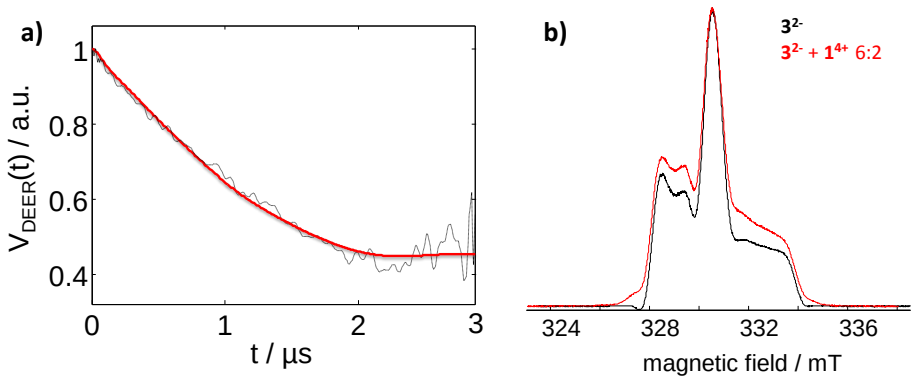

Figure A2.1.1. a) background corrected DEER signal of a solution of 6 mM 32- and 2 mM 14+. The red line corresponds to a fit gained from Tikhonov regularization with a regularization parameter of 100. b) The field-swept EPR spectrum of 32- (black) and 32-/14+ 6:2 (red) in DMSO / 88% glycerol at 50K is depicted. The 32-/14+ 6:2 spectrum appears slightly broadened, accounting for a close-contact confinement of 32- due to the presence of 14+.

A2.1.2 Supplementary CW-EPR Data

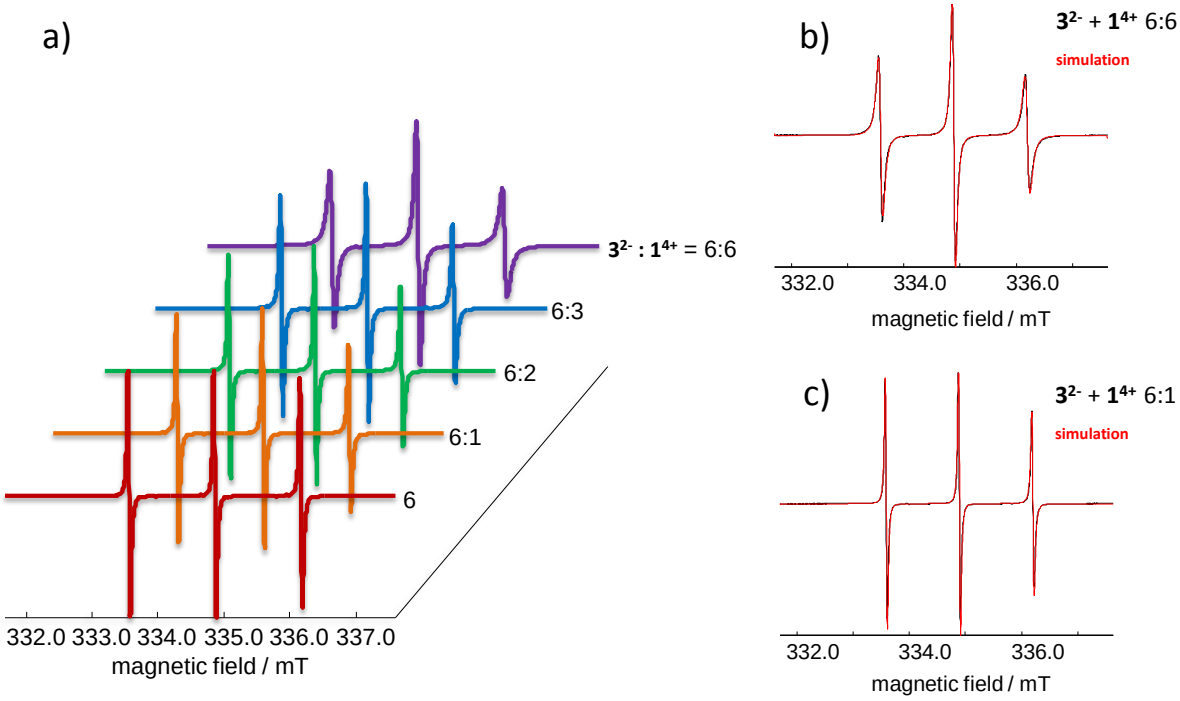

Figure A2.1.2. a) CW EPR spectra at room temperature of 6 mM $\mathbf{3}^{2-}$ and different concentrations of $\mathbf{1}^{4+}$ in 1:1 DMSO / 88% glycerol. With increasing $\mathbf{1}^{4+}$ concentration the $\mathbf{3}^{2-}$ molecules rotate slower. b) 6 mM $\mathbf{3}^{2-}$ and 6 mM $\mathbf{1}^{4+}$ is shown: A spectral simulation (red) is superimposed on the experimental spectrum (black).

Applied spectral parameters for the simulation were: g_{iso} = 2.0065; A_{iso} = 36.3 MHz; D = [$1.5\cdot10^{8}$, $6.9\cdot10^{9}$] s^{-1}. c) The spectrum of 6 mM $\mathbf{3}^{2-}$ and 1 mM $\mathbf{1}^{4+}$ is shown in black. A spectral simulation is superimposed in red. Applied spectral parameters for the simulation were: g_{iso} = 2.0065 A_{iso} = 36.3 MHz D = [$6.7\cdot10^{8}$, $1.2\cdot10^{10}$] s^{-1}. Note that the tumbling rotation motion is not isotropic. Yet, it can be well characterized in terms of the effective rotational correlation time, which is defined as $\tau_c = 6^{-1}(D_{\perp} D_{\parallel})^{-1/2}$, with $D_{\perp}$, denoting the principal components of the rotational diffusion tensor, perpendicular

to the magnetic field axes and $D_{\parallel}$, denoting the principle components of the rotational diffusion tensor, parallel to the magnetic field axes.

The simulated rotational diffusion tensor, extractable from Figure A2.1.1 2b), indicates a slowed-down rotation around the molecular x- and z-axes. This implies a coordination of the two sulfonate groups to $\mathbf{1}^{4+}$. Since the molar ratio of $\mathbf{3}^{2-}$ to $\mathbf{1}^{4+}$ is 1:1, it is likely that one $\mathbf{3}^{2-}$ molecule is coordinated by only 1 $\mathbf{1}^{4+}$ pocket. With decreasing $\mathbf{1}^{4+}$ content in the solution, D becomes more isotropic, until, at a molecular ratio of 6:1, only the rotation around the molecular z-axes is slowed down a little, compared to mere $\mathbf{3}^{2-}$ in solution. This fast rotation indicates that $\mathbf{3}^{2-}$ is only weakly bound to $\mathbf{1}^{4+}$. Combining this knowledge with the DEER and DLS data leads to the conclusion that $\mathbf{3}^{2-}$ at a ratio of 6:1 to $\mathbf{1}^{4+}$ rotates quite freely, while it still populates certain points in space in the defined nano-objects, as described in the main text.

A2.2 DNA-Condensation with Spermine-Dendrimers: Interactions in Solution, Charge Inversion, and Morphology Control

A2.2.1 TEM - Experimental.

Carbon-coated 200 mesh copper grids were pretreated by glow discharge for 75 s at 25 mA in vacuo. The particular dendriplex dispersions were left 10s on a mesh to absorb, which were subsequently washed with water, three times. To increase contrast 1% uranyl acetate negative staining was applied to all samples for 10 sec prior to air drying. All samples were examined on a Tecnai T12 microscope at 120 kV.

A2.2.2 Polymerase Chain Reaction (PCR).

The aim was to amplify a double-stranded DNA fragment with a length of 884 bp. A total of 1000 µl PCR mixture containing 0.08 mM dNTP mix (Fermentas), 1 U Taq DNA Polymerase (Fermentas), 50 pg plasmid DNA pBR322 DNA (Fermentas), 1 µM forward and backward primers (Sigma Genosys), PCR buffer (100 mM Tris-HCl, 500 mM KCl and 0.8 % Nonidet P40, pH 8.8 at 25 °C) and 2.5 mM $MgCl_2$ were subjected to thermal cycling. The thermal cycle included the sequent steps: 4 min at 95 °C and thereupon 30 cycles of 30 s at 95 °C for denaturation, 2 min at 58 °C for annealing and 1 min at 72 °C for extension in a Thermocycler (MyCycler, BIO-RAD). The amplified PCR product was purified by QIAquick PCR Purification Kit from Quiagen GmbH (Germany) using sterilized H_2O for elution. After the purification the PCR product was concentrated with a vacuum concentrator (Eppendorf Concentrator 5301). The amplified ds DNA had 884 bp. After purification the concentration of DNA was determined by photometry (NanoDrop 8000, Peqlab).

A2.2.3 EPR Spectroscopy – Experimental.

In all cases the required amount of SL-G2 was solved in freshly prepared 10x trizma (0.5 M) base buffer at pH = 7.2 and subsequently transferred to the DNA solutions (1 eq. v/v) to yield the intended charge ratio. Afterwards the solution was transferred to 3 mm outer diameter quartz tubes, which were previously treated with PlusONE repell silane to avoid adsorption of the DNA onto the quartz glass.

A2.2.4 TEM Figures

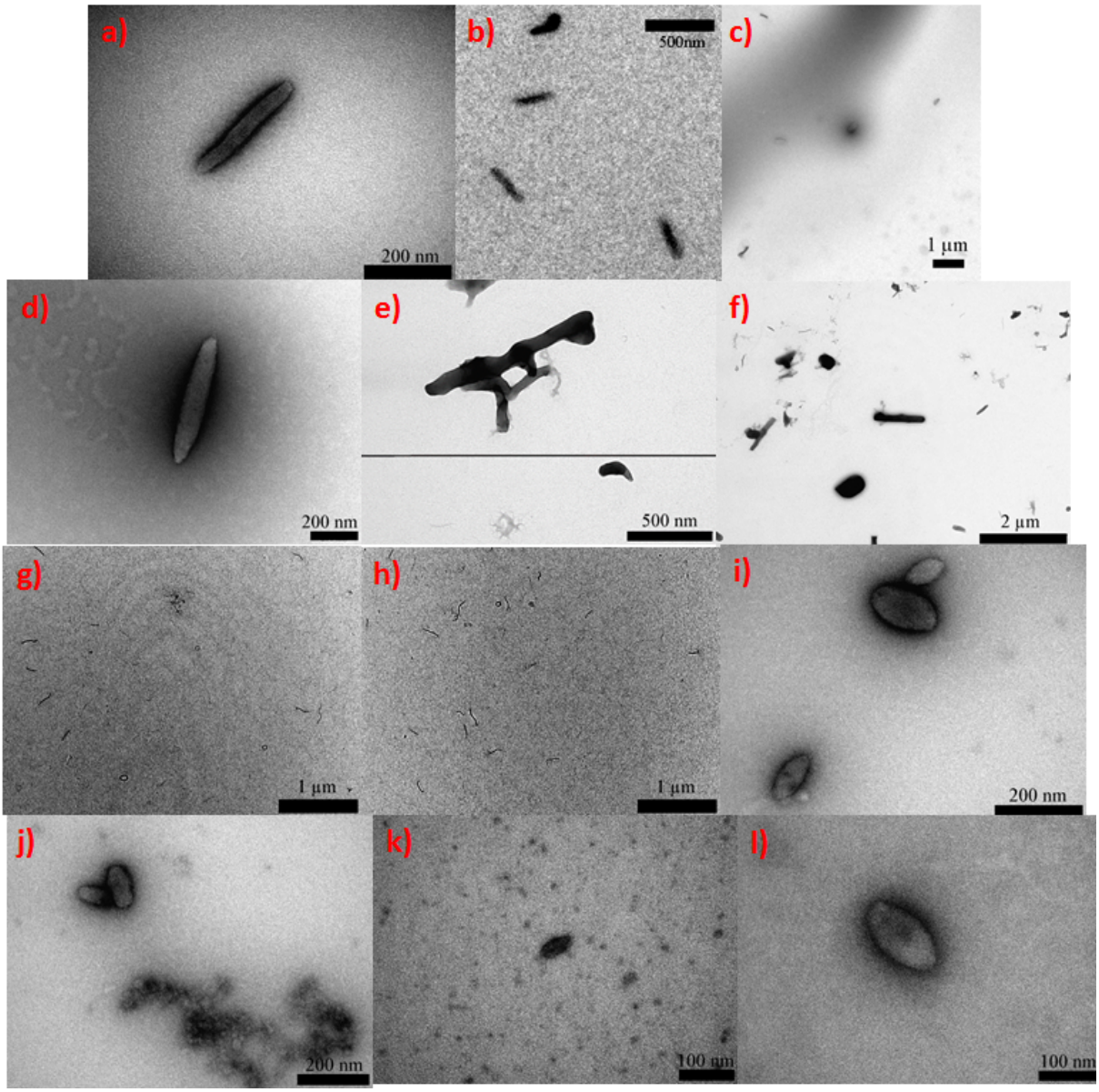

Figure A2.2.1: a) and b) Some more TEM of SL-G2 rod-like condensates at cr = 2.3 and 2.3 mM nucleotides in the solution. c) and d) TEM of SL-G2 rod-like condensates at cr = 2.3 and 0.23 mM nucleotides in the solution. e) and f) Some more TEM of SL-G2 aggregates at cr = 2.3 and 35 mM NaCl. g) and h) Some more TEM of SL-G2 fibers at cr = 2.3 and 35 mM NaCl after 10/1 dillution. i) and j) TEM of SL-G1 condensates (left) and condensates together with free DNA strands (right) at cr = 0.7. k) and l) TEM of SL-G1 at cr = 1.0.

A2.2.5 Supplementary CW-EPR Spectra

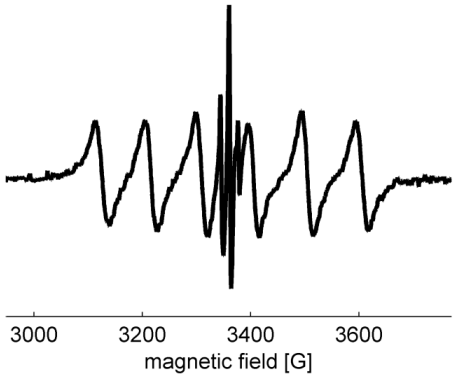

Figure A2.2**.2:** CW-EPR spectra of SL-G2 at cr =2.3 and 10 / 1 dilution (nucleotide concentration: 0.23 mM). Please note that the spectrum looks exactly as the one at a nucleotide concentration of 2.3. Therefore, one can infer that no structural variation takes place upon dilution, as confirmed by TEM. (Figure A4.1.1.)

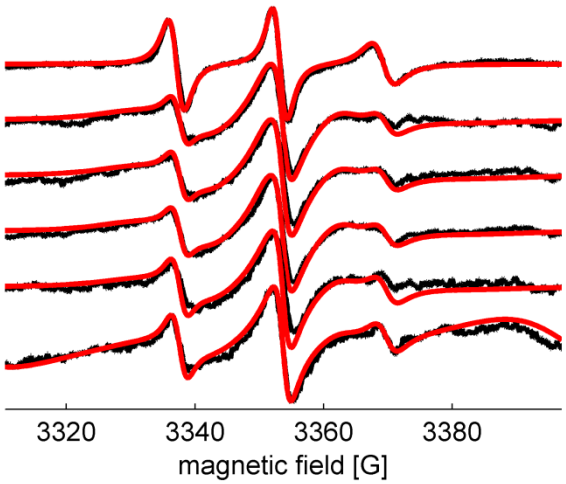

Figure A2.2.3: CW-EPR spectra of SL-G2 at different cr (top to bottom: 0.00, 0.35, 0.68, 1.20, 1.76, 2.30) and a nucleotide concentration of 2.3 mM. The spectra are shown in black, the simulations in red.

A2.2.6 Simulations of SL-G2 at different charge ratios.

In every case, the spectral components of the slow spiecies were approximated by an anisotropic g-tensor of [2.008 2.0043 2.003]. Hyperfine splitting constants were [4.5 4.5 39.5] G. An asymmetric diffusion tensor of [$7\cdot10^8$,$3\cdot10^8$,$1\cdot10^8$] 1/s with orientation of [0 59 60]° of its coordinate system relative to the molecular coordinate system were assumed.

The fast spectral componentes of the fast species were approximated applying a g-Tensor of [2.009 2.0043 2.003] and HF values of [4.5 4.5 39.5] G. The diffusion tensor was [$7\cdot10^8$,$3\cdot10^8$,$1\cdot10^8$] 1/s, with orientations of [0 59 60]° relative to the molecular framework, indicating a faster rotation around the molecular x-axis.

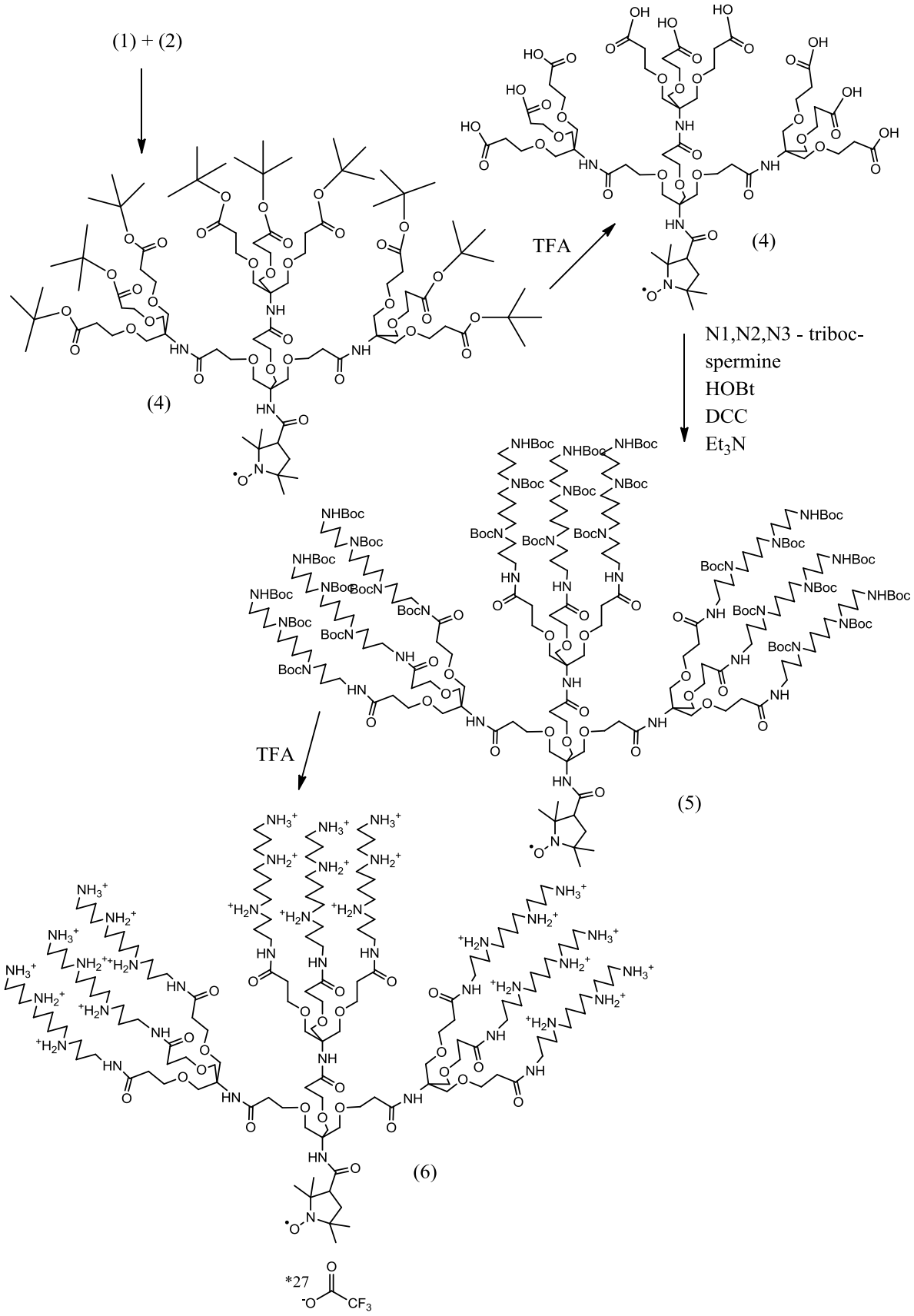

Scheme A2.2.1: Synthetic route towards SL-G2.

A2.2.7 Synthesis of Spin-Labeled Spermine and its Derivatives

Mass spectra were done using FD techniques on a VG-Instruments TRIO-200 and ZAB 2-SE-FPD. NMR spectra were done with a Bruker Spectrospin 250 at room temperature. Chemical shifts are given relative to Tetramethylsilane in the δ-scale (ppm) and were calibrated through the deuterium-locking-signal. Analytical thin-layer-chromatography (TLC) was performed with Macherey-Nagel Alugram SIL G/ UV254 silica-gel plates. Detection of the R_f-values was performed through fluorescence quenching at 254 nm UV or staining with KMnO4 solution.

Synthesis of SL-G2

Tris{[2-(tert-Butoxycarbonyl)ethoxy]methyl}methylamine (1) and Proxyl-N-Tris{[2-(tert-Butoxycarbonyl)ethoxy]methyl}methylamide (2) were synthesized according to literature.[5, 6]

Proxyl-N-Tris[(2-{[(tris{[2-(tert-butoxycarbonyl)ethoxy]methyl}methyl)amino]carbonyl}ethoxy)methyl]methylamide (3)

462.79 mg (0.91 mmol) of acid (2), 566.99 mg (2.75 mmol) DCC, 371.31 mg (2,75 mmol) hydroxybenzotriazole (HOBt) and 278.07 mg (2.75 mmol) triethylamine were solved in 40 ml THF. Afterwards 1.39 g (2.75 mmol) of amine (1) in 10 ml THF were added dropwise while stirring. After 24 h precipitated DCU was extracted from the solution by filtration and after additional 48 h the suspension was filtered again. Afterwards the crude product was purified by column chromatography [SiO_2 (0.2-0.5mm); DCM/MeOH 20:1]. After removing the solvent and drying in vacuum orange oil remained. Yield: 381.46 mg (0.19 mmol)

TLC: R_f(DCM/MeOH 20:1): 0.27, visible through UV; FD-MS: 1970.8 m/z.

Proxyl-N-Tris[(2-{[(tris{[2-carboxyethoxy]methyl}methyl)amino]carbonyl}ethoxy) methyl]methylamide (4)

381.46 mg (0.19 mmol) of ester (3) were solved in 10 ml DCM. While stirring under nitrogen 10 ml TFA were added dropwise. After five minutes the solution started to darken. After 45 min. stirring TFA and DCM were removed in vacuum and brown viscous oil remained. Yield: 273.75 mg (0.19 mmol).

TLC: R_f (SiO_2; DCM/MeOH/NH_4OH 70:10:1): 0.01, visible through UV.

SL-G1-tri-Boc-Spermine (5)

273.75 mg (0.19 mmol) of acid (4), 652.00 mg (3.15 mmol) DCC, 426.98 mg (3.15 mmol) HOBt and 319.16 mg (3.15 mmol) triethylamine were solved in 80 ml ethylacetate. While stirring 1053.97 mg (2.09 mmol) of N1,N2,N3-tri-Boc-Spermine in 30 ml ethylacetate were added dropwise. In 24 h intervals 50 mg (0.10 mmol) N1,N2,N3-tri-boc-Spermine, 50 mg HOBt (0.37 mmol) and 50 mg (0.24 mmol) DCC were added to the solution after three days the precipitated DCU was removed by filtration. The crude product was purified by column chromatography [SiO_2 (0.2-0.5mm); DCM/MeOH/konz. NH_4OHaq 70:10:1]. Orange oil remained. Yield: 912.37 mg (0.16 mmol).

TLC: R_f(DCM/MeOH/konz. NH_4OH 70:10:1): 0.68, visible through UV; MALDI-TOF: 5352; 5855.

[MALDI-TOF showed that next to the product also a dendron with only eight arms remained in the solution.]

SL-G2 (6)

609.8 mg (0.10 mmol) of dendron (5) were solved in 25 ml DCM and washed with 25 ml of a saturated NaCl solution. Afterwards 25 ml TFA were added to the organic layer and the mixture was

stirred for 45 min. After removing DCM and TFA by vaporisation the substance was washed two times with water and DCM. Brown oil remained that crystallized slowly into a yellow solid. Yield: 649.81 mg (0.10 mmol).

TLC: R_f(DCM/MeOH/konz. NH_4OH 70:10:1): 0.01, visible through UV.

References and Notes

[1] S. Stoll, A. Schweiger, *J. Magn. Reson.* **2006**, *178*, 42.
[2] S. J. Schneider, J. H. Freed, "*Biological Magnetic Resonance Vol. 8 - Theory and Applications*", Plenum Press, New York, 1989.
[3] G. Jeschke, V. Chechik, P. Ionita, A. Godt, H. Zimmermann, J. Banham, C. R. Timmel, D. Hilger, H. Jung, *Appl. Magn. Reson.* **2006**, *30*, 473.
[4] H.-Y. Gong, B. M. Rambo, E. Karnas, V. M. Lynch, J. L. Sessler, *Nature Chemistry* **2010**, *2*, 406.
[5] C. M. Cordona, R. E. Gawley, *J. Org. Chem.* **2002**, *67*, 1411.
[6] D. Kurzbach, C. Velte, P. Arnold, G. Kizilsavas, D. Hinderberger, *Soft Matter* **2011**, *7*, 6695.

A3. Dendronized Polymers as Molecular Objects and Transporters

Note that the used denpols were a kind gift of Prof. A. Dieter Schlüter's group from Zürich. All the denpols were synthesized by Dr. Baozhong Zhang as reported earlier.[1-3]

A3.1 Assessing the Solution Shape and Size of Charged Dendronized Polymers Using Double Electron Electron Resonance.

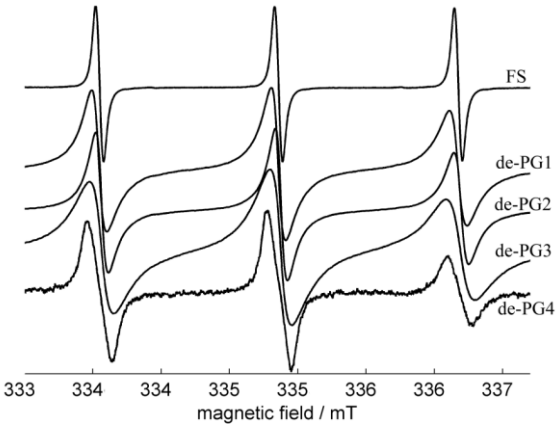

Figure A3.1.1. Continuous wave EPR spectra of 1 mM aqueous solutions of Fremy's Salt together with 1 wt % of the particular denpol generation. The rotational correlation time decreases with increasing generation.

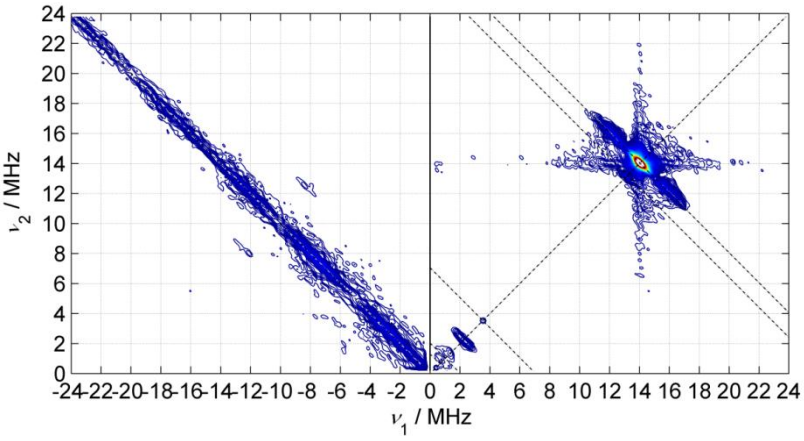

Figure A3.1.2: HYSCORE spectrum of the generation 1 denpol at 10K. The two ridges in the (-/+) region indicate a strong of ^{13}C to the spin probes.

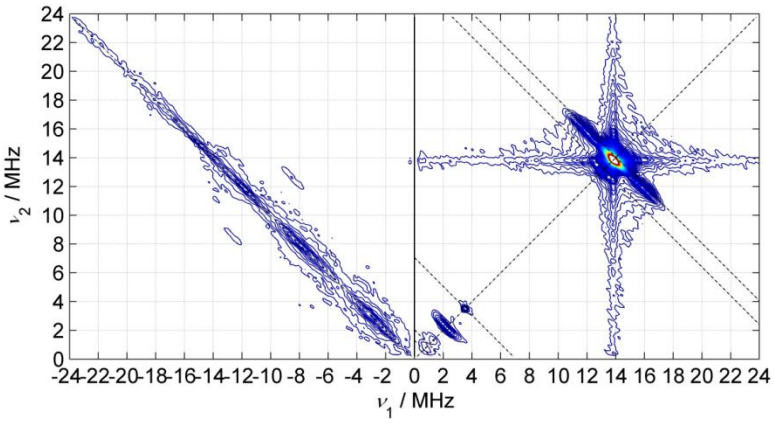

Figure A3.1.3: HYSCORE spectrum of the generation 4 denpol at 10K. The two ridges in the (-/+) region indicate a strong of ^{13}C to the spin probes.

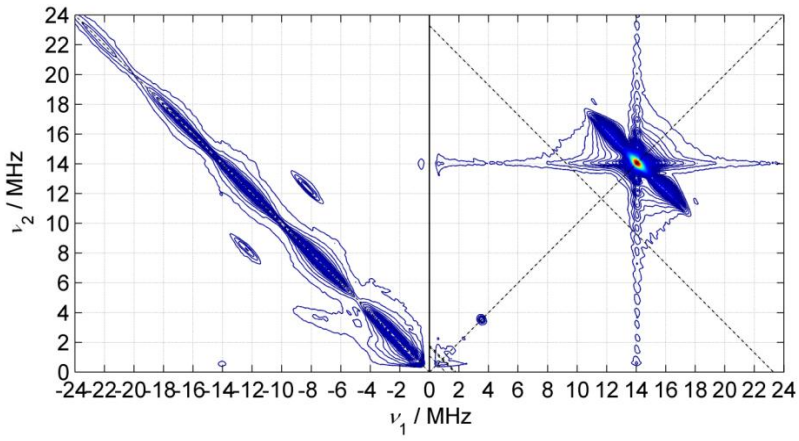

Figure A3.1.4: HYSCORE spectrum of Fremy's Salt in water. In contrast to Figure S3 and S5 no ^{1}H couplings or ^{13}C couplings are visible, but a strong ^{39}K matrix peak appears at 2 MHz.

A3.1.1Sample Preparation and EPR Measurements.

All samples were prepared equally: We added small concentrations (2 mM) of Fremy's Salt, a two times negative charged spin-probe, to 1 wt % aqueous solutions of four different generations of the denpols presented in Figure 1. HYSCORE and DEER is applied to glassy solids obtained by freeze-quenching the denpol solutions in supercooled iso-pentane

A3.2 Loading and Release Capabilities of Charged Dendronized Polymers.

A3.2.1 Synthesis of Compounds

Isotope labeled dipotassium nitrosodisulfonate (Fremy's salt, ^{15}N-FS) was prepared by electrolytic one-electron oxidation of the corresponding ^{15}N-hydroxylaminedisulfonate. With minor modifications, the procedure of Wehrli and Pigott was followed. Unless stated otherwise, the reaction mixture was constantly stirred by a magnetic stirrer. In a jacketed, thermostated (Huber ministat 125-cc-NR) 100 mL flask, 600 mg of sodium nitrite-^{15}N (8.57 mmol, Aldrich, 98 atom % ^{15}N) and 1.62 g of sodium bisulfite (15.6 mmol) are added to 10 g of crushed ice. After addition of 877 µL of acetic acid, the reaction mixture is stirred for 90 minutes at a constant temperature of -2°C (final pH = 5). A solution of 1.94 g of sodium carbonate in 10 mL of water is added. The resulting colorless, buffered solution of disodium hydroxylaminedisulfonate (pH = 11) is subject to electrolytic oxidation: A 3 cm

by 4 cm mesh of stainless-steel is used as working electrode. The cathode is formed from a piece of stainless steel wire wound to a cylindrical coil, which is immersed in an aqueous 10 wt % Na_2CO_3 solution and coupled to the anodic compartment by a salt bridge (equally filled with 10 wt % Na_2CO_3). The salt bridge causes a comparably high resistance and IR-drop, what necessitates a higher potential (up to 35 V) and increasing the reaction time (15 h) compared to the original procedure (using a porous porcelain thimble). At the low temperatures employed, we did no observe adverse effects due to this approach. In total 307 mAh have been converted (1.3 eq.). To the deep purple solution of disodium nitrosodisulfonate so obtained, a solution of 1.45 g of potassium chloride in 4 mL of water is added at – 4°C. On standing over night (at -4 °C), the orange-yellow Fremy's salt precipitates. The crystals are filtered with suction, washed twice with cold 1 N aqueous potassium-hydroxide, once with cold ethanol containing 2.5 mL 25 wt % ammonia solution, and once with acetone. From the filtrate, a second fraction crystallizes in the cold. The damp crystals were dried at room temperature in a desiccator over Silica Gel Orange and in vacuo, eventually yielding a total of 1.39 g (5.17 mmol, 60%). Note that dry Fremy's salt has been reported to sometimes undergo spontaneous decomposition, which occasionally resulted in a violent explosion.[4, 5]

A3.2.2 Sample Preparation

1 wt % (for CW EPR) or 4 wt % (for DEER) of the desired generation of the denpols de-PG1-4 were dissolved in deionized water. Afterwards, 1 v/v % of a 100 mM solution of 5- or 16-DSA in dry ethanol was added. For DEER measurements, then, 1 v/v % of a 100 mM solution of ^{15}N-Fremy's Salt (FS) was added. After stirring the solution for 1 min 30 v/v % glycerol were added to prevent crystallization of the samples upon freeze-quenching the denpol solutions in supercooled iso-pentane. In this way a snapshot representative for the solution at the glass transition temperature is detected.

All used chemicals were synthesized as mentioned above or commercially available and used without further purification.

A3.2.3 Determination of Loading Capacities

Multicomponent spectra were simulated by superimposing weighted, double-integral normalized CW EPR spectra. The maximum loading capacity of the denpols was determined by attempting to fit 1 component (for de-PG1 and 2) or 2 component (for de-PG3 and 4) spectra to the experimental data. If this was not possible and a third, free and/or strongly exchange coupled DSA-species occurred in the spectra, we assume that the maximal loading capacity of a denpol was exceeded. The experimentally obtained maximum amount of DSA molecules incorporated per denpol monomer is given in Table A3.2.1. It should be noted that the DSA concentration was increased in steps of 1 mM. Hence, the maximal loading capacity could be slightly higher than the values listed in Table A3.2.1.

Table A3.2.1. From top to bottom: Molecular weight of the denpol monomers, their concentration at 1 wt % denpols in aqueous solutions, the dissolved amount of DSA and the molar ratio of DSA to denpol monomers that could maximally be added without yielding precipitated or free DSA.

	de-PG1	de-PG2	de-PG3	de-PG4
M_W(Monomer) / g /mol	586	1308	2735	5648
c(Monomer) / mM	17.0	7.6	3.7	1.8
c(x-DSA) / mM	>1	>2	>2	>4
x-DSA / Monomer	0.06	0.26	0.57	2.20

A3.2.4 MISS-DEER

The four pulse DEER sequence $\pi/2(\nu_{obs})$ - τ_1 - $\pi(\nu_{obs})$ - (τ_1 + t) - (ν_{pump}) - (τ_2 - t) - $\pi(\nu_{obs})$ - τ_2 - echo was used to obtain dipolar time evolution data at X-band frequencies (9.2 to 9.4 GHz) with a Bruker Elexsys 580 spectrometer equipped with a Bruker Flexline split-ring resonator ER4118X_MS3. The dipolar evolution time t was varied, whereas τ_2 = 0.5 µs and τ_1 were kept constant. Proton modulation was averaged by the addition of eight time traces of variable τ_1 , starting with $\tau_{1,0}$ = 200 ns and incrementing by $\Delta\tau_1$ = 8 ns. The resonator was overcoupled to Q = 100. The pump frequency, ν_{pump}, was set to the high-field shoulder marked *pump* in Figure 3.2.2a) and A3.2.2 of the electron spin echo EPR spectrum. The observer frequency, ν_{obs}, was set to ν_{pump}+ 131.6 MHz, coinciding with the low field local maximum, marked with the *observer* in Figure 3.2.2a) and A3.2.2 of the nitroxide spectrum. The observer pulse lengths were 32 ns for both π/2 and π pulses, and the pump pulse length was 12 ns. The temperature was set to 50 K by cooling with a closed cycle cryostat (ARS AF204, customized for pulse EPR, ARS, Macungie, PA). The total measurement time for each sample was around 12 h. The raw time domain DEER data were processed with the program package DeerAnalysis2010.[6] Inter-aggregate contributions were removed by division by an exponential decay with a dimension of d = 3. The resulting time traces were normalized to t = 0 (see the SI). From the so-corrected time traces similarly processed traces of DSA-DSA reference measurements were subtracted, to yield the signal of the mere FS-DSA interaction.

A3.2.5 MISS-DEER Analysis

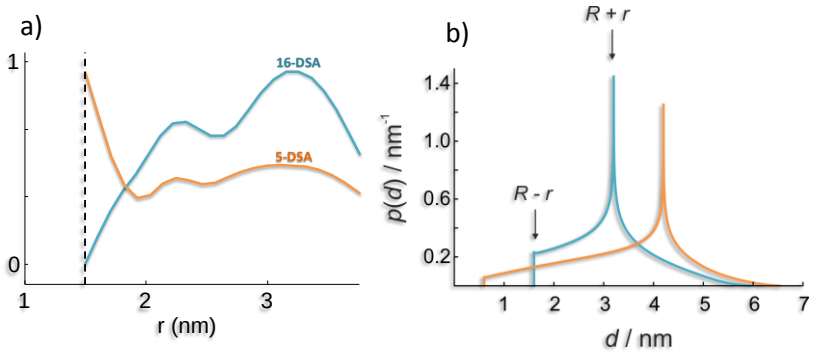

Figure A3.2.1 a) Distance distribution obtained from Tikhonov regularization of the MISS-DEER time-traces. b) Theoretical distance distributions predicted for particles distributed on interleaved cylinders (eq. 4-6, *L* = 5 nm, *R* = 2.4 nm and *r* = 0.8 nm (16-DSA) or 1.8 nm (5-DSA))

Note, that in Figure A3.2.1a) the low population of short distances in the 16-DSA case corresponds well with the slow decay of the 16-DSA time trace. In contrast the 5-DSA distribution indicates the presence of shorter distances. The dashed line indicates the lower sensitivity boundary of DEER. Note that distances above 2 nm should be interpreted carefully, since t_{max} = 500 ns, only. In Figure A3.2.1b) a distance distribution is depicted, corresponding to a model for which FS is distributed on an outer cylinder of radius R and the DOXYL groups of DSA are located on inner, concentrically cylinder of radius r (see Figure 3.2.3c)). L denotes the cylinder height. The distance distribution can be derived using an approach as shown in A3.1.2.[7, 8]

Note that for the investigated samples the dipolar evolution is only accessible for *t* < 0.5 µs due to fast phase relaxation. This limits the discussion to qualitative features, the strong difference in modulation depth and to a lesser degree the observation/absence of short distances. Since it is not necessary for our conclusions of how DSA is incorporated, I refrain from a detailed interpretation of the fits here. Yet, the simple geometrical model reproduces characteristic features of the Tikhonov reconstruction of the pertinent distances. In particular short distances and a flat distribution in the range from 2 to 4 nm are predicted and found for 5-DSA, while 16-DSA is void of small distances and exceeds the 5-DSA curve above 3 nm. Note that distances shorter than 1.6 nm cannot be observed

by DEER. The distributions, depicted in Figure A3.2.1b), are based on L = 5 nm, R = 2.4 nm and r = 0.8 nm (16-DSA) or 1.8 nm (5-DSA).

A3.2.6 Supplementary EPR

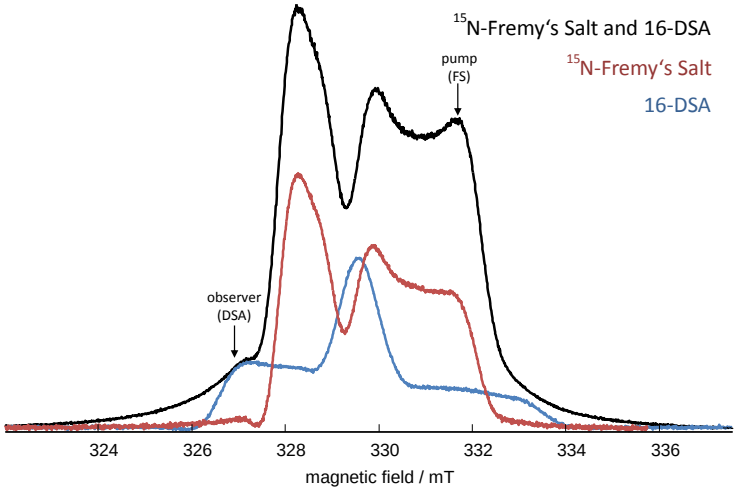

Figure A3.2.2. The electron spin echo (ESE) spectra of a 1mM solution of ^{15}N-Fremy's Salt (FS)), a 4 mM solution of 16-DSA (containing the nitroxide label with naturally abundant mixture of nitrogen isotopes, i.e. predominantly ^{14}N) , and a mixture of a 1 mM solution of ^{15}N-FS and a 4 mM solution of 16-DSA (black), all containing 4 wt % de-PG4 . The field position of the pump-pulse of the MISS-DEER experiment and the position of the observer-pulse are marked with arrows. In contrast to 5-DSA (Figure 3.2.2a)), a strong line broadening of the two-component spectra can be detected, which is most-likely the reason for 16-DSA being less prominent than 5-DSA in the bimodal spectrum.

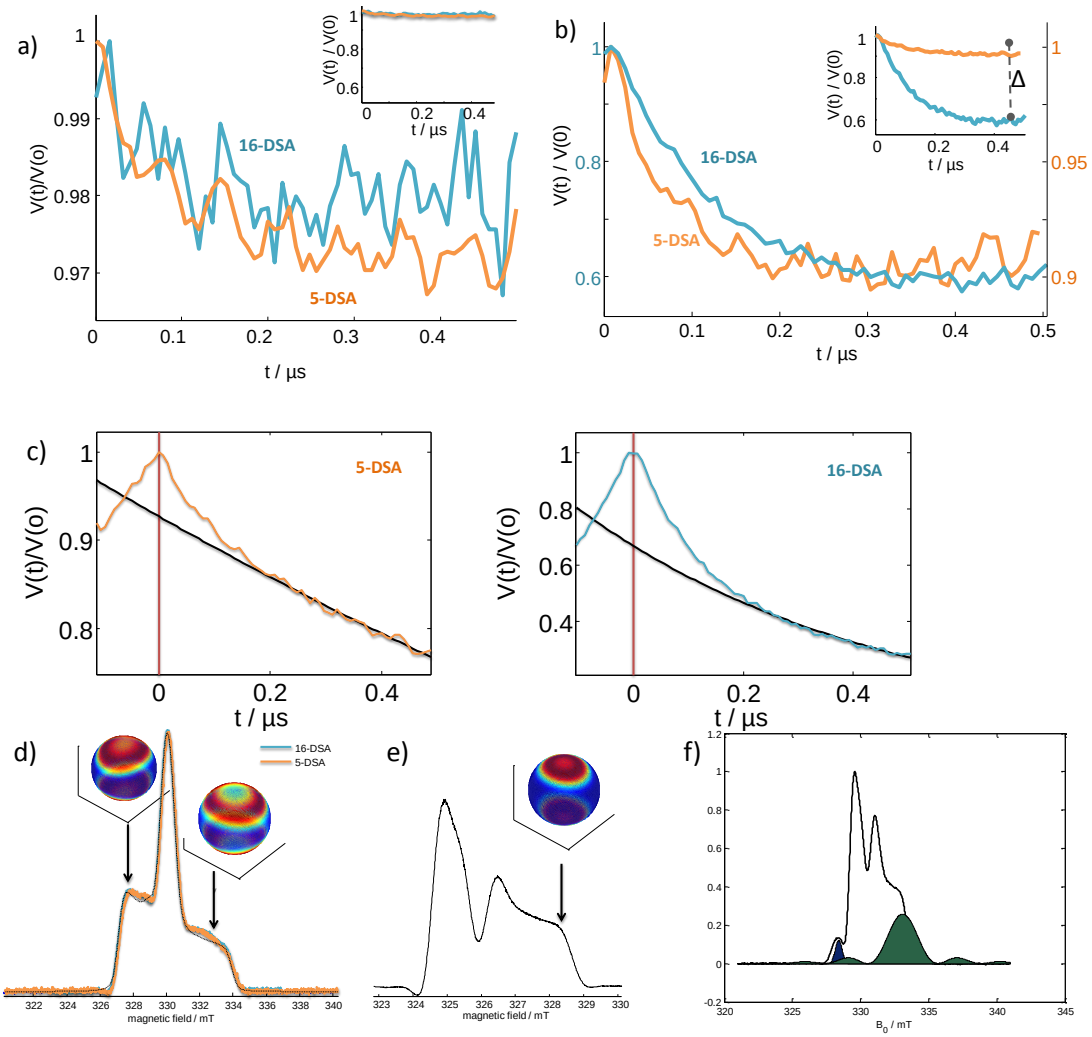

Figure A3.2.3. a) Background-corrected DEER-time traces of 4 mM 16-DSA (blue) and 5-DSA (orange) in 4 wt % de-PG4. Note that the modulation depth is less than 0.03. Therefore, one could neglect contributions of dipolar couplings of the DSA-probes among each other in the discussion of the MISS-DEER experiment, instead of subtracting them from the original time traces, shown in b). The pump- and observer-pulse position were exactly the same as indicated in Figure 3.2.2a) and A3.2.2. b) Background-corrected time-traces of the ^{14}N-^{15}N-DEER experiments (see also Figure 3.2.2b). The inset shows the non-rescaled data. The dashed line indicated the modulation depth. The pure FS-DSA interaction was extracted from this data, subtracting the appropriately weighted time-traces shown in a). With the indicated pump and detection positions (Figure 3.2.2 and A3.2.2) the raw time-traces yield: for 5-DSA/FS V(observed) = 0.76 V(MISS DEER) + 0.23 V(DSA-DSA DEER) + (<0.01) V(FS-FS-DEER). And for 16-DSA/FS: V(observed) = 0.62 V(MISS DEER) + 0.07 V(DSA-DSA DEER) + 0.28 V(FS-FS-DEER). c) Uncorrected, original DEER echoes of the ^{14}N-^{15}N experiments. The zero-time is marked by the red vertical line. The black curves represent the backgrounds, which were subtracted from the echoes, to yield the time-traces shown in b). d) Electron-spin-echo of 5- and 16-DSA in de-PG4. The field-positions of the pump- (highfield) and observer-pulses (lowfield) applied are marked with black arrows. The excited directions, as indicated by the red areas on the spheres above, are similar for both, 5-DSA and 16-DSA, because there is only little difference between the two echoes. The dashed line corresponds to a spectral simulation of the ESE. e) Electron-spin-echo of ^{15}N-FS. Orientations excited by the pump-pulse applied in the DEER experiments are indicated by the red colour on the sphere above. f) Excitation profiles of the applied pump- and observer-pulses. For the ^{14}N-5-DSA/^{15}N-FS the spectrum is shown and the experimental conditions are summarized in the main text (12ns pump pulse, 32 ns observer pulses, observation and pump position and 5-DSA/^{15}N-FS ratio). The contribution of ^{14}N-^{14}N distances is smaller by a factor 2.96 compared to ^{14}N-^{15}N distances. Thus, provided that both types of distances are a priori of similar probability, the DEER spectrum/distance distribution is always dominated by the heteronuclear distances. However, we have separately recorded the ^{14}N-DSA spectra under identical conditions. Subtracting this reference dipolar time trace from the MISS DEER time trace, the ^{14}N-^{15}N distances are obtained in good approximation. Note that in any case the not significant ^{14}N-

^{14}N-distances show up in the reference spectrum in the accessible distance range. For ^{14}N-16-DSA/^{15}N-FS the enhancement factor of the heteronuclear distances is 1.8. Again our background correction did not indicate a significant contribution of ^{14}N-^{14}N distances.

Note that the subtracted background functions (Figure A3.2.3c)) are exponentials, corresponding to a three dimensional background. In the case of the cylindrically shaped denpols one could however expect a one or two dimensional background. Yet, section 3.1 showed that for the mere FS-distribution around a denpol, subtraction of a 3D background is appropriate, due to the spatial distribution of FS around the denpols and the short contact time of FS on the denpol's surface.[7] For DSA we assume that for longer τ_2 the background function could become two or one dimensional. However, with the qualitative interpretation one can safely state that the dimensionality of the subtracted background-function does not affect the relative comparison of the FS-5-DSA and FS-16-DSA time-traces at all. Assuming the background to be exponential in nature, uncertainties about the correct contribution of the background to the raw data have to be considered, too, since the intramolecular contributions also lead to nearly exponential form factors. However, the faster initial decay of the 5-DSA-FS trace compared to 16-DSA-FS, as well as the difference in modulation depth, remain virtually identical for all possible combinations of background contributions. Hence, uncertainties about the background subtraction do not affect qualitative interpretations.

Spectral Simulations

Table A3.2.2. Selected simulation parameters of 5-DSA and 16-DSA. The parameters correspond to a concentration of 1 mM DSA and 1 wt % of the respective denpol. For two-component spectra the notation is: species A/species B

	5-DSA / de-PG1	**5-DSA / de-PG2**	**5-DSA / de-PG3**	**5-DSA / de-PG4**
g_{iso}	2.0059	2.0058	2.0058/2.0055	2.0059/2.0055
A_{iso} / MHz	41.10	41.10	40.63/ 40.63	40.17/40.17
D /s^{-1}	[$1.1\cdot10^8$ $1.0\cdot10^8$]	[$0.7\cdot10^8$ $1.0\cdot10^8$]	[$1.5\cdot10^8$ $1.0\cdot10^7$] / [$1.0\cdot10^7$ $2.0\cdot10^6$ $3.0\cdot10^8$]	[$1.5\cdot10^8$ $1.0\cdot10^7$]/ [$1.0\cdot10^7$ $2.0\cdot10^6$ $3.0\cdot10^8$]
	16-DSA / de-PG1	**16-DSA / de-PG2**	**16-DSA / de-PG3**	**16-DSA / de-PG4**
g_{iso}	2.0056	2.0057	2.0061/2.0055	2.0060/2.0055
A_{iso} / MHz	42.50	42.50	41.57/41.57	40.17/40.17
D /s^{-1}	[$1.0\cdot10^8$ $1.0\cdot10^8$]	[$1.2\cdot10^8$ $1.0\cdot10^8$]	[$2.0\cdot10^8$ $1.0\cdot10^8$]/ [$1.0\cdot10^7$ $2.0\cdot10^6$ $3.0\cdot10^8$]	[$2.2\cdot10^8$ $1.0\cdot10^8$]/ [$1.0\cdot10^7$ $2.0\cdot10^6$ $3.0\cdot10^8$]

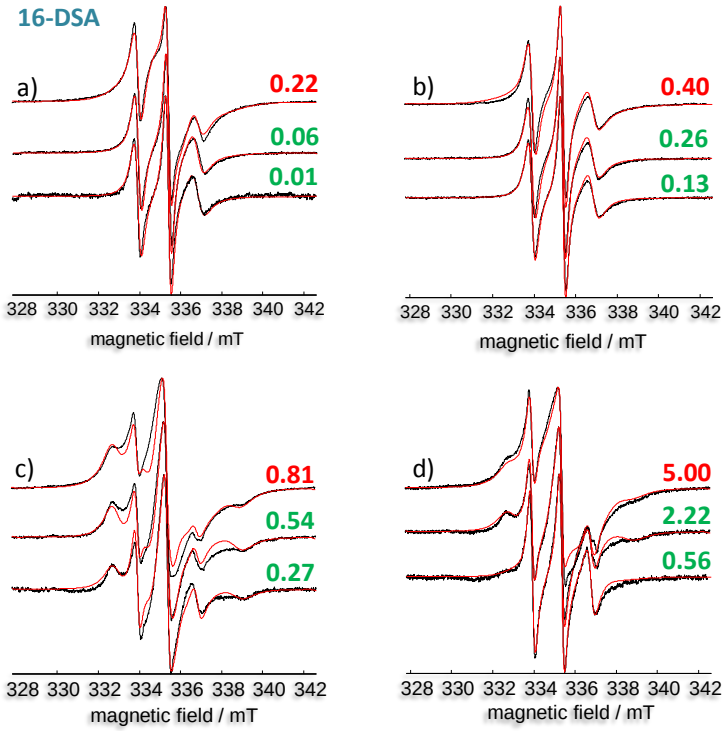

Figure A3.2.4. CW EPR spectra (black) and corresponding spectral simulations (red) for a) 1 wt % de-PG1, b) 1 wt % de-PG2, c) 1 wt % de-PG3 and d) 1 wt % de-PG4, in solution with 16-DSA. The numbers on the right of each spectrum indicate the ratio of n(16-DSA)/n(denpols monomer) in a 1 wt % solution of denpols (see Table A3.2.2 for the details on the calculations). Green indicates that the simulation includes no free or precipitated 16-DSA, red the contrary. Spectra of 16-DSA incorporated in de-PG3 or de-PG4 were simulated with two (or three) components.

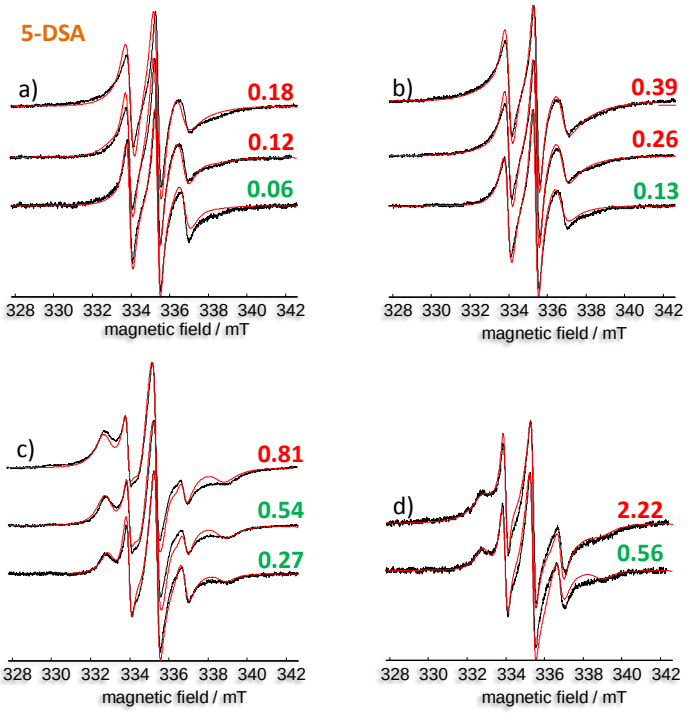

Figure A3.2.5. CW EPR spectra (black) and corresponding spectral simulations (red) of 5-DSA contained in solutions of a) 1 wt % de-PG1, b) 1 wt % de-PG2, c) 1 wt % de-PG3 and d) 1 wt % de-PG4. The numbers on the right of each spectrum indicate the ratio of n(5-DSA)/n(denpol monomers) (see Table A3.2.2 for details on the

calculations). Green indicates that the simulation includes no free or precipitated 5-DSA, red the contrary. Spectra of incorporated 5-DSA and de-PG3 and 4 were simulated with two (or three) components.

Note that 5-DSA and de-PG4 at a ratio of 2.22 was simulated with only a minimal contribution of precipitated 5-DSA. Therefore, 5-DSA shows only a minimally smaller ability to incorporate into de-PG4 then 16-DSA. Therefore, 2.20 DSA molecules per denpol-monomer reported as maximal loading capacity for both probes, 16- and 5-DSA. All the other values, correspond exactly to those obtained from measurements on 16-DSA.

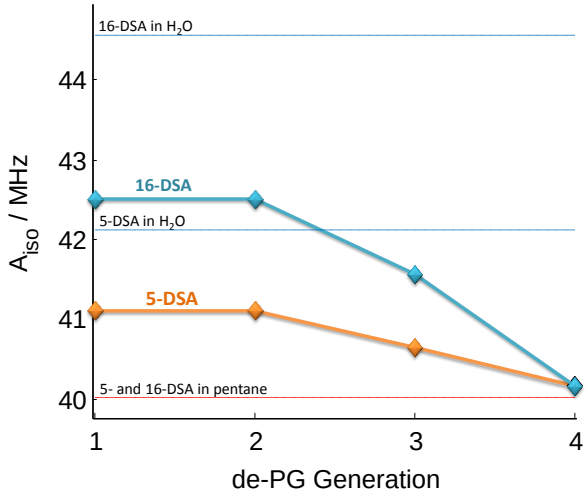

Figure A3.2.6. Isotropic hyperfine coupling constant A_{iso} of the nitroxide group of 5-DSA (orange) and 16-DSA (blue) as obtained from spectral simulations of the CW EPR data (see Figure A3.2.4 and A3.2.5) plotted versus the generation of the dendronized polymer incorporating the probe. The hfc-values of 5- and 16-DSA in pure water and pentane are indicated by the dotted blue and red lines.

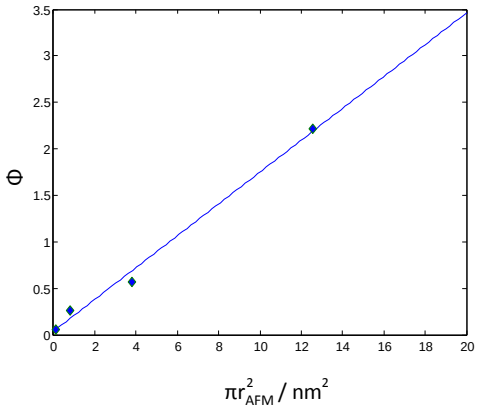

Figure A3.2.7. The loading capacity Φ (i.e. guest-molecules per denpol monomer-unit) plotted versus the area of the cylinder cross-section of the respective denpol generation (estimated based on radii from AFM tapping heights of the denpols PG1-4).[1] Assuming a constant height of the repeat units, the cross-section is directly proportional to the volume of the cylinder. Thus, the AFM radius and the loading capacity depend on the generation in the same manner. The data points for the different generations were fitted linearly: $b*(\pi r^2_{AFM})+a$, where b = 0.17 nm^{-2} ± 0.01 nm^{-2} and a = 0.038 ± 0.07.

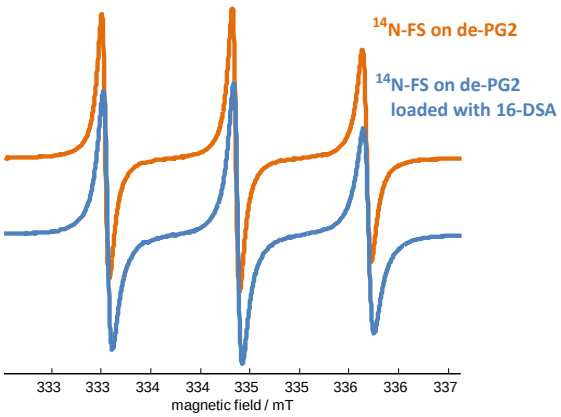

Figure A3.2.8. CW EPR spectra of 1mM ^{14}N-FS in presence of de-PG2 (yellow; for details on the coordination of FS with charged denpols see section 3.1)[7] and ^{14}N-FS in presence of de-PG2 that is loaded with 1 mM 16-DSA (1 wt % aqueous solution). As can be seen, no significant differences in the spectra of FS on the loaded and the unloaded denpol occur. Hence, a coordination of DSA on the surface of the cylinder is unlikely since the hydrophobic tail would drastically affect the coordination behavior of the FS probes. Note that the spectral contribution of 16-DSA cannot be detected clearly, due significantly strong line broadening, compared to FS. Therefore, we chose 4 mM and 4 wt % denpol for the ^{14}N – ^{15}N DEER experiment, to increase the 5- and 16-DSA signal intensity.

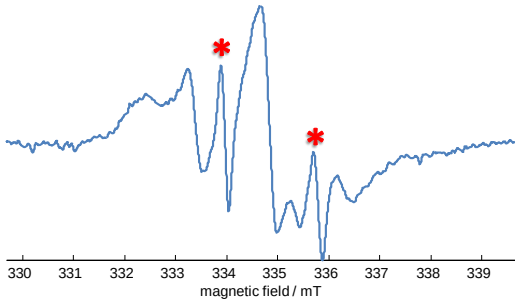

Figure A3.2.9. CW EPR spectrum of 1 mM 16-DSA and 0.1 mM ^{15}N-FS in an aqueous solution 1 wt % de-PG3. Here the superposition of both paramagnetic species is clearly visible. The lines stemming from ^{15}N-FS are marked with the red asterisks.

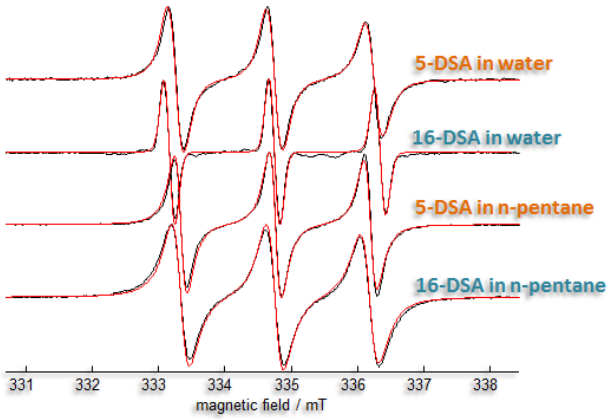

Figure A3.2.10. CW EPR spectra of 5- (orange label) and 16-DSA (blue label) are shown in black and the corresponding spectral simulations are overlaid in red. Thus, the A_{iso} values for DSA in aqueous and organic media were determined. Thereby A_{iso}-values of 42.04 MHz for 5-DSA in water, 44.65 MHz for 16-DSA in water, 40.17 MHz for 5 and 16-DSA in n-pentane were obtained, as depicted in Figure A3.2.6. The differences in A_{iso} and linewidth of 5-DSA and 16-DSA in water may be traced back to micellization of DSA in water.[9]

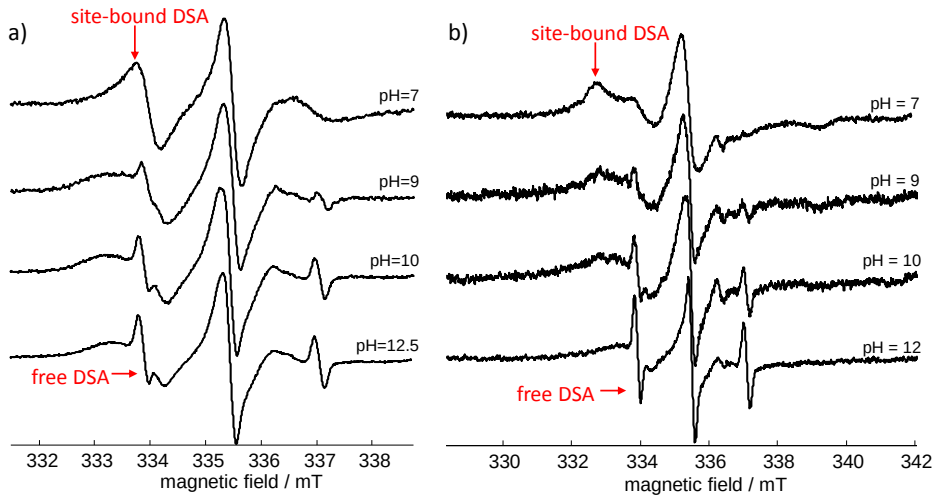

Figure A3.2.11. a) Release of 16-DSA from de-PG3 by $BmimBF_4$. Over 90% of the 16-DSA guest-molecules were released by addition of only 20 v/v % of the release agent. b) The response of 5-DSA incorporated into de-PG3 to an increasing pH. DSA is released significantly from the denpols, as the pH is raised. At pH = 12.5 most of the 16-DSA probes (approx. 60%) are release from de-PG3. No significant further release of 16-DSA is observed, when the pH is raised from 12.5 to 14. Note that the spectrum of 16-DSA in de-PG3 is strongly shifted towards the species **B**, when compared to the spectrum in Figure 1b). This might be traced back to aging of the denpol over time due to intramolecular H-bond formation and a decreasing number of looser binding sites **A** for DSA. Yet, the principle possibility to release DSA from the denpols can still be observed clearly.

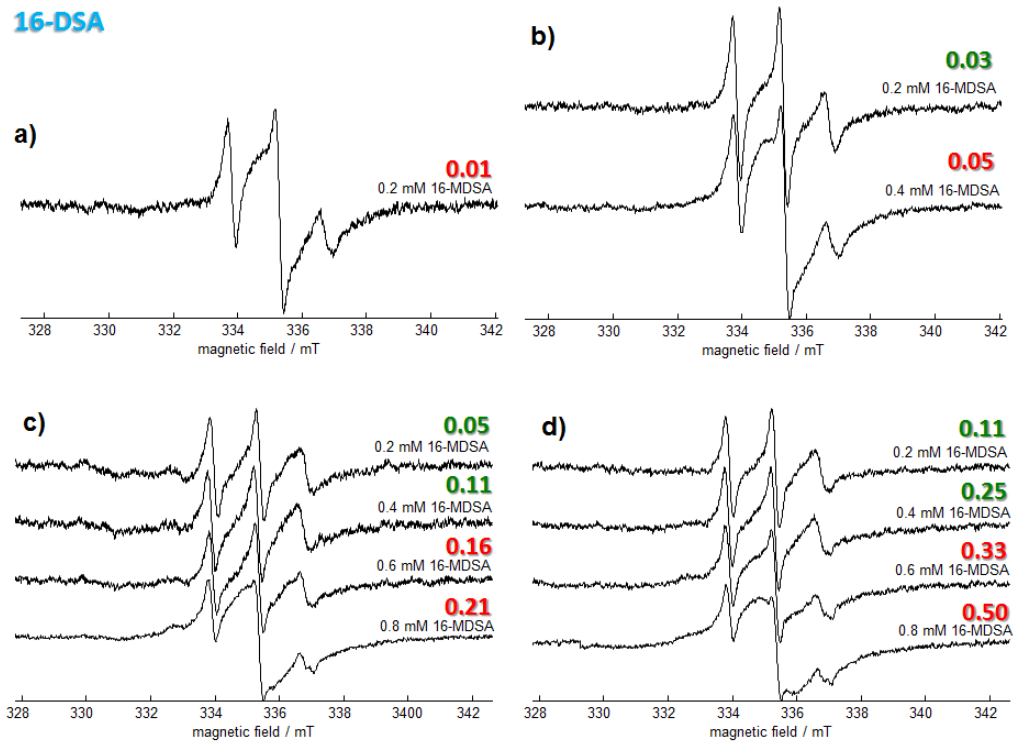

Figure A3.2.12. CW EPR spectra a) 1 wt % de-PG1, b) 1 wt % de-PG2, c) 1 wt % de-PG3 and d) 1 wt % de-PG4, together in solution with 16-methyl(M)-DSA. The numbers above the spin-probe concentration on the right of each spectrum indicate the ratio of n(16-MDSA)/n(denpols monomer) at 1 wt % solution of denpols (see Table 1 for details on the principle calculation). Green indicates that the spectra appear to feature no contribution from free or precipitated 16-MDSA, red the contrary. Simulation of the depicted spectra is hardly possible, due to the bad signal-to-noise ratio and precise, reliable values cannot be extracted from them by means of

spectral simulation. Yet, from the apparent line shapes it can reliably be concluded that the amount of MDSA that can be incorporated by the denpols is much lower than the amount of not esterified DSA.

A3.3 Counterion-Induced Condensation of Charged Dendronized Polymers

All chemicals used were commercially available or synthesized as reported earlier.[10-12] All samples were prepared as follows: 2 mg / mL of the denpol were solved in deionized water and 1 v/v eq. of an aqueous solution of the condensation agent was added. The concentration of the condensation agent was chosen, to yield the required charge ratio (0.5, 1 or 1.5). TEM was performed as described in section A2.2.

A3.3.1 TEM - Experimental.

Carbon-coated 200 mesh copper grids were pretreated by glow discharge for 75 s at 25 mA in vacuo. The particular dendriplex dispersions were left 10s on a mesh to absorb, which were subsequently washed with water, three times. To increase contrast 1% uranyl acteate negative staining was applied to all samples for 10 sec prior to air drying. All samples were examined on a Tecnai T12 microscope at 120 kV.

A3.3.1 Supplementary TEM Micrographs

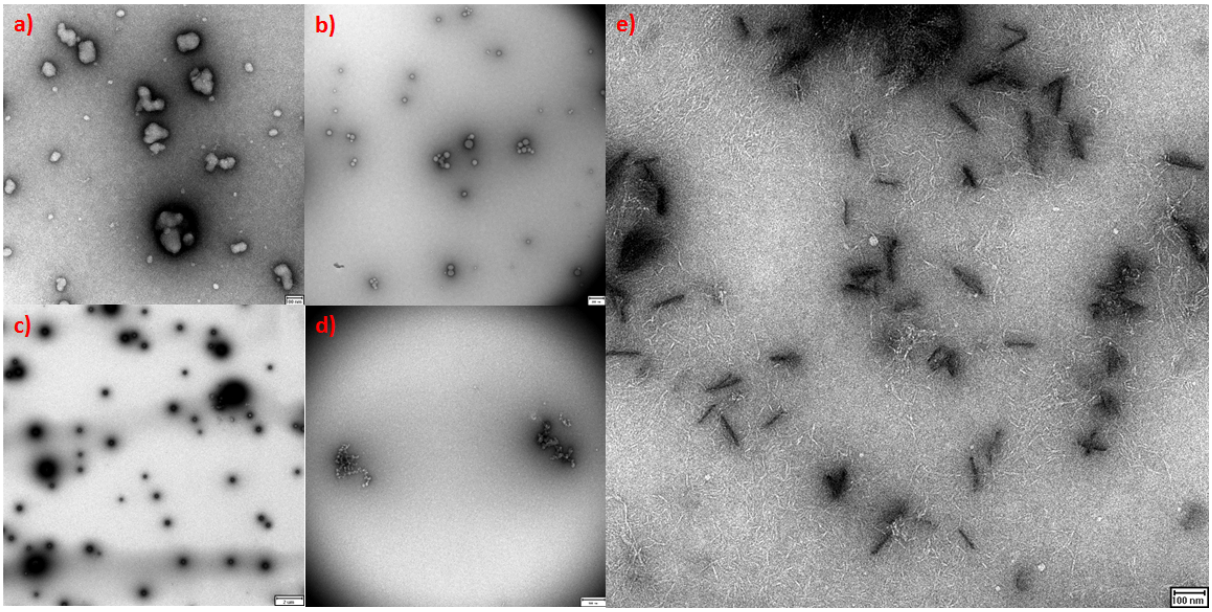

Figure S3.3.1. a) TEM micrograph of COOK-PG-2 and de-PG3 together in solution at cr = 1. The resulting aggregates do not exhibit a defined structure, as do the condensates in Figure 4.2.2. b) TEM overview of KOOC-PG-2 and SL-G2 at cr =1.5. c) TEM overview of KOCC-PG-2 and SL-G2 at cr =0.5. d) TEM overview of de-PG3 and $K_3[Fe(CN)_6]$ at cr =1.5. d) TEM overview of the rods of COOK-PG-2 at cr = 1.

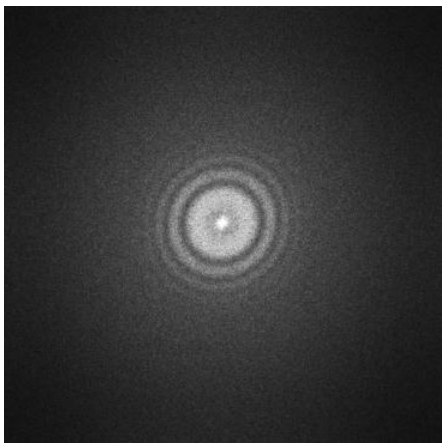

Figure A3.3.2. Power spectrum of the electron beam directed at one of the rods. No Bragg reflexes can be observed.

References and Notes

[1] B. Zhang, R. Wepf, K. Fischer, M. Schmidt, S. Besse, P. Lindner, B. T. King, R. Sigel, P. Schurtenberger, Y. Talmon, Y. Ding, M. Kröger, A. Halperin, A. D. Schlüter, *Angew. Chem. Int. Ed.* **2011**, *50*, 737.
[2] A. Ingerl, I. Neubert, R. Klopsch, A. D. Schlüter, *Eur. J. Org. Chem.* **1998**, *1998*, 2551.
[3] R. Klopsch, S. Koch, A. D. Schlüter, *Eur. J. Org. Chem.* **1998**, 1275.
[4] H. Zimmer, D. C. Lankin, S. W. Horgan, *Chem. Rev.* **1971**, *71*, 229.
[5] P. A. Wehrli, F. Pigott, *Org. Synth.* **1972**, *52*, 1010.
[6] G. Jeschke, V. Chechik, P. Ionita, A. Godt, H. Zimmermann, J. Banham, C. R. Timmel, D. Hilger, H. Jung, *Appl. Magn. Resonance* **2006**, *30*, 473.
[7] D. Kurzbach, D. Kattnig, B. Zhang, A. D. Schlüter, D. Hinderberger, *J. Phys. Chem. Lett.* **2011**, *2*, 1583.
[8] D. Kurzbach, D. R. Kattnig, B. Z. Zhang, A. D. Schluter, D. Hinderberger, *Chem Sci* **2012**, *3*, 2550.
[9] S. Ruthstein, A. Potapov, A. M. Raitsimring, D. Goldfarb, *J. Phys. Chem. B* **2005**, *109*, 22843.
[10] D. Kurzbach, C. Velte, G. Kizilsavas, P. Arnoldt, D. Hinderberger, *Soft Matter* **2011**, *accepted*.
[11] A. D. Schlüter, J. P. Rabe, *Angew. Chem. Int. Ed.* **2000**, *39*, 864.
[12] E. Kasemi, W. Zhuang, J. P. Rabe, K. Fischer, M. Schmidt, M. Colussi, H. Keul, Y. Ding, H. Colfen, A. D. Schlüter, *J. Am. Chem. Soc.* **2006**, *128*, 5091.

A4. The Nanoscale Collapse Behavior of Alkylene Oxide-Based Thermoresponsive Polymers

4.1 The Phase Behavior of Pluronic Triblock Copolymers

The mean-square diffusional displacement, $\langle x^2 \rangle$, of a molecule is generally described by:

$$\langle x^2 \rangle = 6 D_T \tau_t \quad \text{(A4.1.1)}$$

It can be shown that for equal line-width and spectral contribution of the two TEMPO-species A and B the translational displacement of species B can be calculated by:

$$\langle x^2 \rangle \leq z \frac{R_{H,R}^3}{R_{H,T}} \quad \text{(A4.1.2)}$$

$$z = \frac{8}{6} \cdot \frac{t}{\tau_c} \quad \text{(A4.1.3)}$$

$$t = 8 \frac{1}{T_2} \frac{1}{10(\Delta\omega)^2} \quad \text{(A4.1.4)}$$

assuming no extra line-broadening due to dynamic exchange.[1, 2] $R_{H,T}$ is the translational and $R_{H,R}$ the rotational hydrodynamic radius. For TEMPO in aqueous solution the ratio $\frac{R_{H,R}^3}{R_{H,T}} = 0.08$. t denotes the reduced lifetime, τ_c the rotational correlation time, $\frac{1}{T_2}$ the spectral width of the spectral components and $\Delta\omega$ the spectral separation of the two lines.

A4.1.1 Spectra and Simulations

The detected spectra are shown in black and the red, dotted lines represent the spectral simulations. The plot on the left-hand side shows spectra detected, when the temperature was raised from 10°C to 90°C in steps of 10°C (From top to bottom).

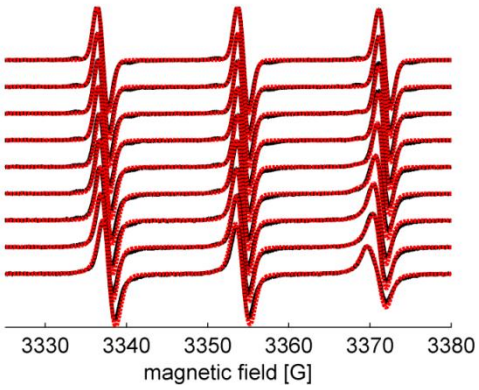

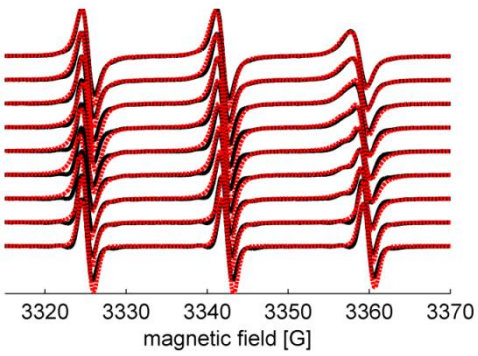

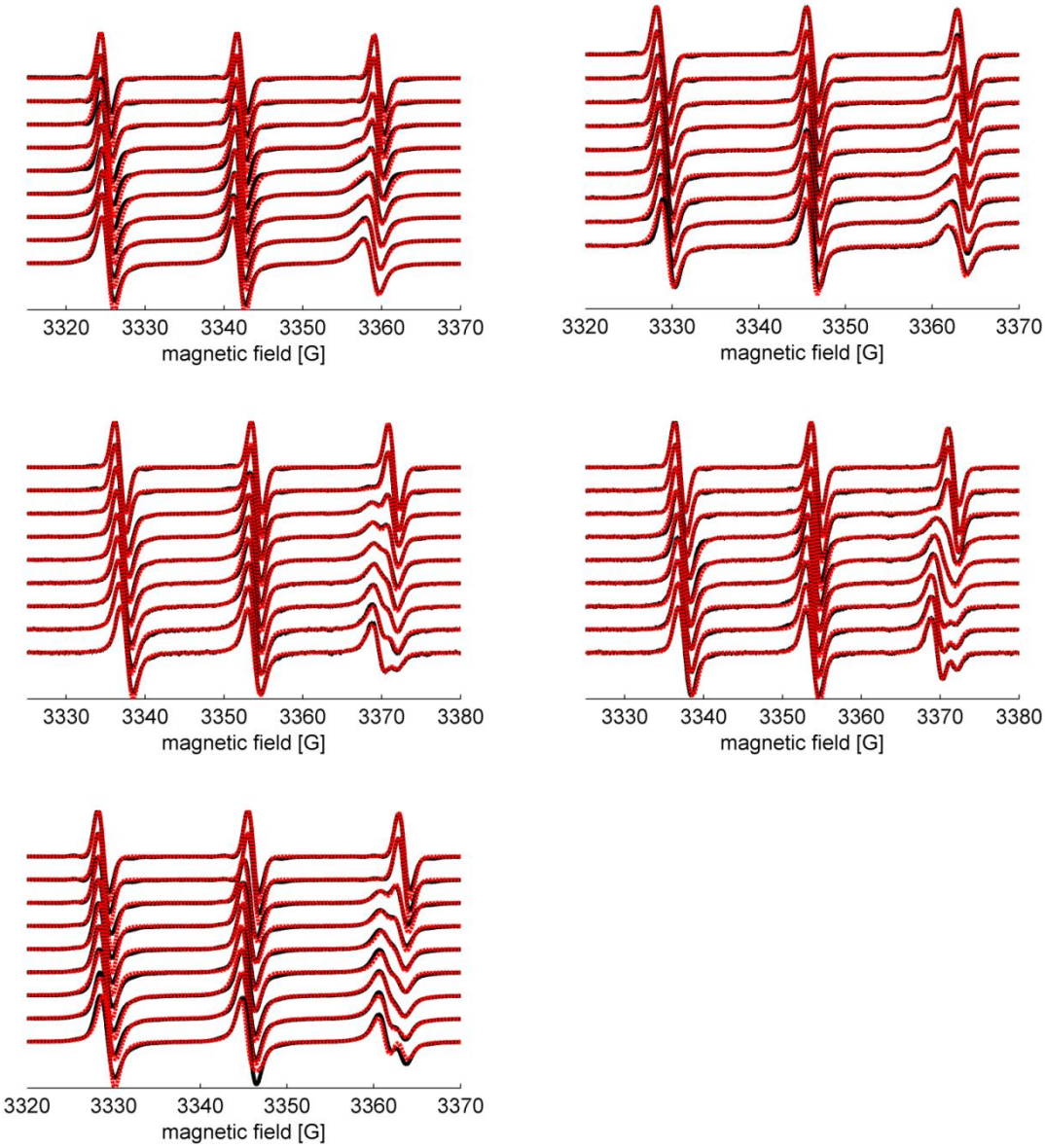

Figure A4.1.1. CW EPR spectra of F68 10 wt% in a 1 mM TEMPO aqueous solution. F127 10 wt% in a 1 mM TEMPO aqueous solution. F10810 wt% in a 1 mM TEMPO aqueous solution. L64 10 wt% in a 1 mM TEMPO aqueous solution. P105 10 wt% in a 1 mM TEMPO aqueous solution. P84 10 wt% in a 1 mM TEMPO aqueous solution.

A4.1.2 Selceted g_{iso}- and A_{iso}-Values

Table A4.1.1. Simulated values for F108 CW EPR spectra for 10°C → 90°C

	283 K	293 K	303 K	313 K	323 K	333 K	343 K	353 K	363 K
g_{iso} (A)	2.0058	2.0058	2.0058	2.0057	2.0057	2.0056	2.0056	2.0056	2.0056
A_{iso} / MHz (A)	48.68	48.68	48.45	48.45	48.45	48.12	48.12	47.78	47.71
g_{iso} (B)			2.0061	2.0060	2.0060	2.0060	2.0060	2.0058	2.0058
A_{iso} / MHz (B)			44.22	44.54	45.22	45.88	45.88	45.88	45.65

Table A4.1.2. Simulated values for P84 CW EPR spectra for 10°C → 90°C									
	283 K	**293 K**	**303 K**	**313 K**	**323 K**	**333 K**	**343 K**	**353 K**	**363 K**
g_{iso} (A)	2.0058	2.0058	2.0057	2.0057	2.0057	2.0058	2.0058	2.0058	2.0056
A_{iso} / MHz (A)	48.65	48.55	48.01	47.76	47.60	47.60	47.71	48.05	47.38
g_{iso} (B)			2.0062	2.0062	2.0061	2.0062	2.0061	2.0061	2.0062
A_{iso} / MHz (B)			45.22	45.54	45.54	45.54	45.21	44.88	44.65

A4.2 How Structure-Related Collapse Mechanisms Determine Nanoscale Inhomogeneities in Thermoresponsive PEO-co-PDEGA and PPO-co-PG

A4.2.1 CW EPR SPECTRA AND CORRESPONDING SIMULATIONS

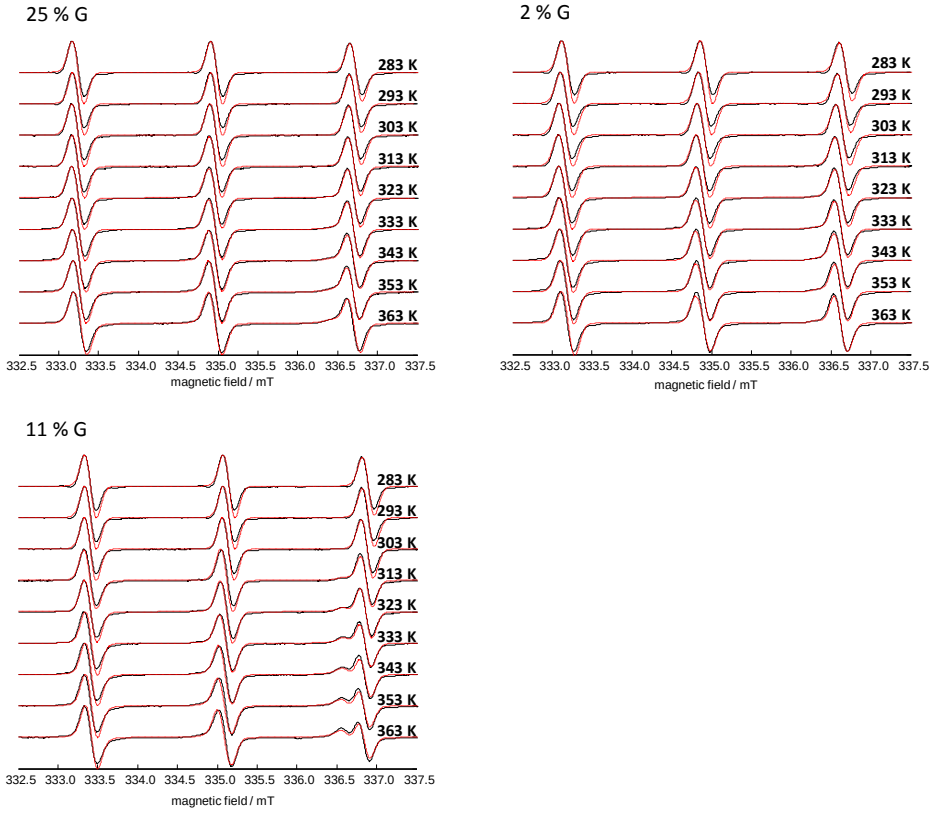

Figure A4.2.1. Full set of spectra (black) and corresponding spectral simulations (red) for 1 mM TEMPO in solution together with 1 wt % **PPO-*co*-*lin*PG**.

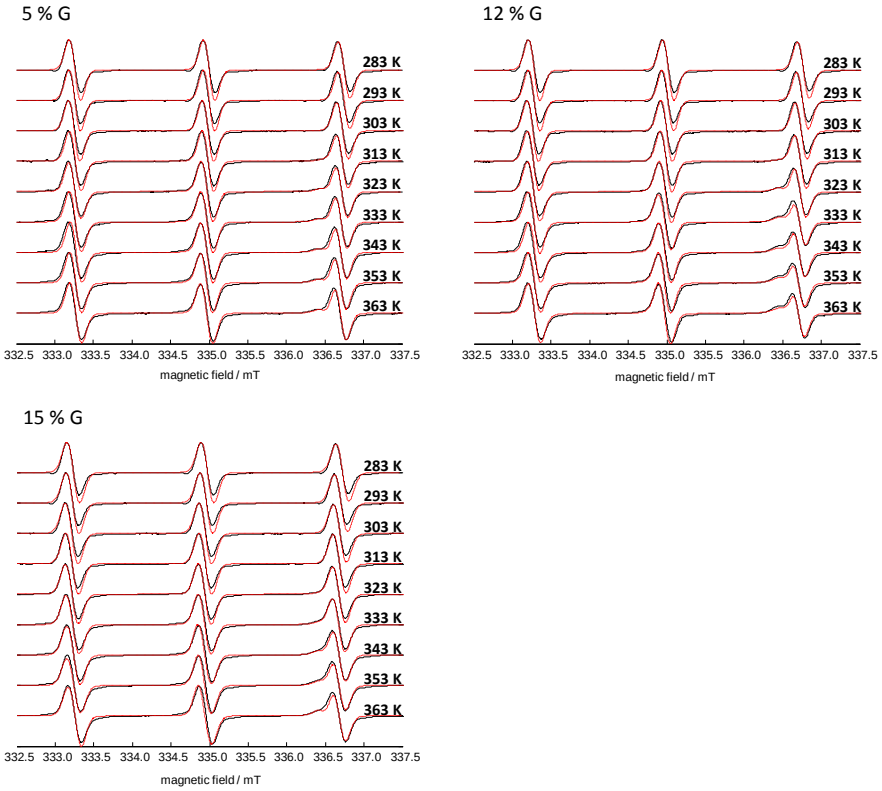

Figure A4.2.2. Full set of spectra (black) and corresponding spectral simulations (red) for 1 mM TEMPO in solution together with 1 wt % ***hb*PPO-*co*-PG**.

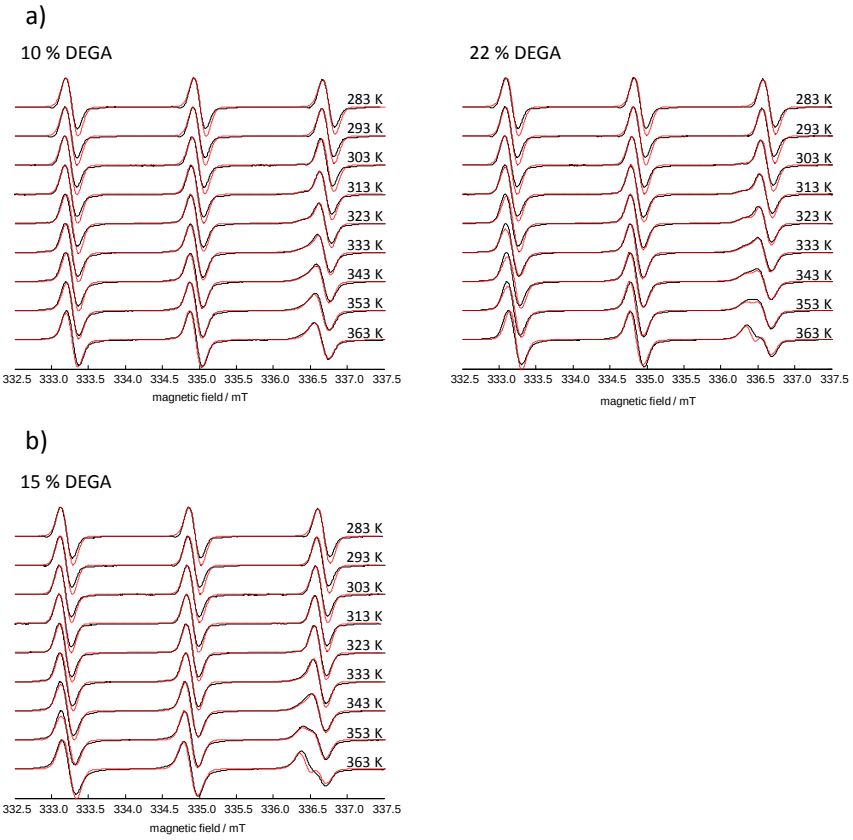

Figure A4.2.3. a) Full set of spectra (black) and corresponding spectral simulations (red) for 1 mM TEMPO in solution together with 5 wt % **PEO-*block*-PDEGA**. b) Full set of spectra (black) and corresponding spectral simulations (red) for 1 mM TEMPO in solution together with 5 wt % **PEO-*co*-PDEGA**.

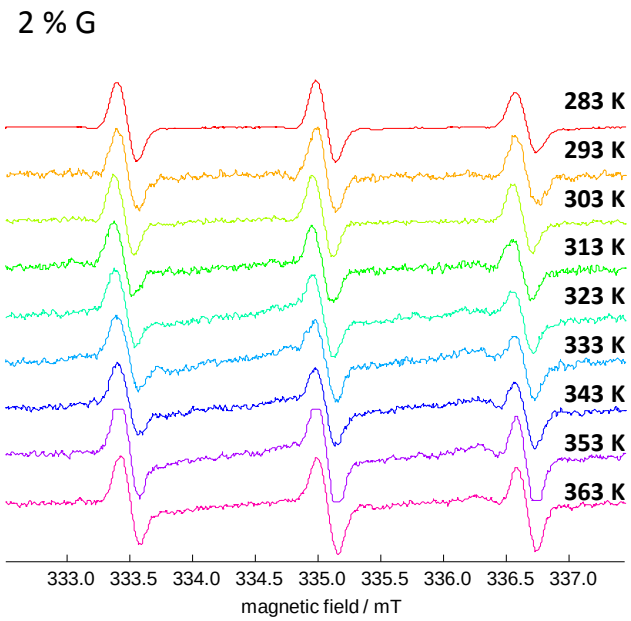

Figure A4.2.4. 1 wt % **PPO-*co*-PG** probed with 0.5 mM 16-DSA (doxyl-stearic acid). Broad lines clearly indicate an incorporation of the spin-probe into collapsed PPO-rich domains, although one cannot detect these with the less hydrophobic spin-probe TEMPO.

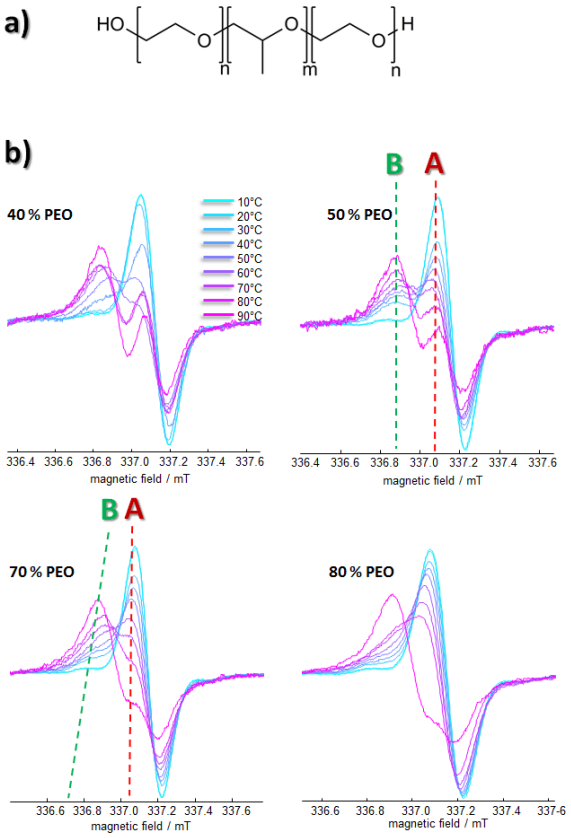

Figure A4.2.5. a) Molecular structure of Pluronic triblock copolymers. b) High-field transitions of TEMPO in 5 wt % aqueous solutions of Pluronics with differing percentage of the PEO blocks. Note that spectra obtained from 10 wt% solutions have already been published and show slightly different temperature-dependent developments.[3] The red and green dashed lines indicate the positions of the TEMPO-species A and B in cases of static (50% PEO) and dynamic (70% PEO) inhomogeneities.

A4.2.2 SELECTED SPECTRAL PARAMETERS

Table A4.2.1. PPO-*co*-*lin*PG 25% G

	283 K	293 K	303 K	313 K	323 K	333 K	343 K	353 K	363 K
g_{iso}(A)	2.0058	2.0058	2.0057	2.0057	2.0057	2.0056	2.0056	2.0056	2.0056
A_{iso}(A) / MHz	48.93	48.76	48.76	48.60	48.60	48.43	48.43	48.26	48.26
g_{iso}(B)			2.0062	2.0062	2.0062	2.0061	2.0060	2.0059	2.0059
A_{iso}(B) / MHz			45.26	45.26	45.26	45.26	45.26	45.26	45.26

Table A4.2.2. *hb*PPO-*co*-PG 12% G

	283 K	293 K	303 K	313 K	323 K	333 K	343 K	353 K	363 K
g_{iso}(A)	2.0058	2.0058	2.0058	2.0057	2.0057	2.0056	2.0056	2.0056	2.0056
A_{iso}(A) / MHz	48.93	48.76	48.76	48.59	48.59	48.43	48.26	48.26	48.26
g_{iso}(B)			2.0062	2.0062	2.0062	2.0061	2.0061	2.0061	2.0061
A_{iso}(B) / MHz			45.54	44.88	44.76	45.43	45.09	45.26	45.26

Table A4.2.3. PEO-*block*-PDEGA 10% DEGA

	283 K	293 K	303 K	313 K	323 K	333 K	343 K	353 K	363 K
g_{iso}(A)	2.0059	2.0059	2.0058	2.0057	2.0057	2.0057	2.0056	2.0056	2.0056
A_{iso}(A) / MHz	48.76	48.76	48.76	48.43	48.10	47.93	47.60	47.60	47.60
g_{iso}(B)				2.0062	2.0062	2.0062	2.0062	2.0061	2.0061
A_{iso}(B) / MHz				44.54	44.54	45.10	45.43	46.10	46.76

A4.2.3 Molecular Dynamic Simulations

MD-simulations were performed using the YASARA software-package. The AMBER 03 force field was employed with periodic boundary conditions.[4] Non-bonded interactions were cut off at 10.5 Å. Long-range Coulombic interactions were treated by a smoothed particle-mesh Ewald method.[5] Models of the simulated block-polymers were built using YASARA and semi-quantum-mechanically parameterized (YAPAC-AM1). The models of the polymers were built according to the polymers used for the experimental studies. For **PEO-*block*-PDEGA** with 10% 13 DEGA units and 113 EO units where attached in a linear manner. For **PEO-*block*-PDEGA** with 22% 22 DEGA units and 113 EO units where used. **PEO-*co*-PDEGA** was modeled as random copolymer with a random distribution of DEGA monomers, although it is known to be slightly gradient-like. 22 DEGA units very randomly distributed between 124 EO units. The obtained linear structures were subsequently randomly distorted. The random model structures were subject to energy minimization in vacuum, subsequently randomly placed in the simulation box and solvated by water at pH = 12 (104532 water molecules (**PEO-*co*-PDEGA** 15% DEGA), 85178 water molecules (**PEO-*block*-PDEGA** 22% DEGA) and 93412 water molecules (**PEO-*block*-PDEGA** 10% DEGA)), and again minimized (steepest descent minimization followed by simulated annealing). The chosen time increment was 1 fs. After energy-minimization and equilibration for 10 ns at 25°C in order to yield a energetically acceptable structures, MD trajectorys of 5.0 ns length were accumulated at 25°C and 90°C for the three systems. Intermolecular forces were recalculated at every second simulation sub-step. Temperature rescaling was employed with a set-temperature of 25°C or 90°C. The box dimensions (cubic of 120 - 150 Å side length) were controlled so as to yield a solvent pressure of 1 bar. Snapshots of the simulations were taken every 2000 fs. The average number of inter-chain contacts was calculated by counting per-chain inter-

atomic distances shorter than 0.5 nm, excluding intramolecular distances, for every snapshot. Note that the described method is likely to yield structures that fluctuate around local energetic minima, as explained in the main text and data should be interpreted with caution.

A4.2.4 Supplementary CW EPR

In Figure A4.2.5 the temperature-dependent development of the high-field transition of TEMPO in a 5 wt% solution of different Pluronic PEO-PPO-PEO triblock copolymers (40 % PEO: F64 / 50 % PEO: P105 / 70 % PEO: F127 / 80 % PEO: F108) is shown. With increasing PEO content, the high-field lines of species B shift to higher fields indicating dynamic spin-probe exchange at high temperatures, as it was observed more clearly for 10 wt % solutions before.[3] Such low PEO content leads to static inhomogeneities, while high PEO content leads to dynamic inhomogeneities featuring dynamic exchange at high temperatures. Hence, Pluronics and **PEO-*block*-PDEGA** have the transition from static to dynamic inhomogeneities with increasing content of hydrophilic comonomers in common.

A4.2.5 Calculation of Diffusional Displacement

According to the equations in section A4.1, for PEO-block-PDEGA with 22% PDEGA $\tau_c = 0.3\,ns$; $\Delta\omega = 5.0\,MHz$; $1/T_2 = 5.9\,MHz$ at 80 °C, as extracted from spectral simulations. For PEO-block-PDEGA with 10% PDEGA at 80 °C $\tau_c = 0.2\,ns$; $\Delta\omega = 2.9\,MHz$; $1/T_2 = 5.3\,MHz$. Thus, for 22% PDEGA $\sqrt{\langle x^2 \rangle} \approx 9\,nm$ and for 10% PDEGA $\sqrt{\langle x^2 \rangle} \approx 17\,nm$.

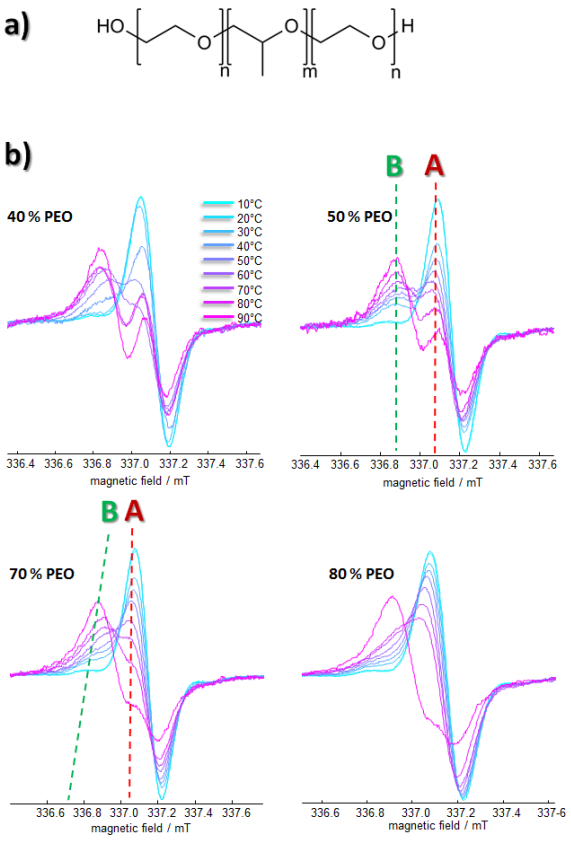

Figure A4.2.5. a) Molecular structure of Pluronic triblock copolymers. b) High-field transitions of TEMPO in 5 wt % aqueous solutions of Pluronics with differing percentage of the PEO blocks. Note that spectra obtained from 10 wt% solutions have already been published and show slightly different temperature-dependent developments.[3] The red and green dashed lines indicate the positions of the TEMPO-species A and B in cases of static (50% PEO) and dynamic (70% PEO) inhomogeneities.

A4.3 Impact of Amino-Functionalization on the Response of Poly(ethylene oxide) to pH-Sensitivity

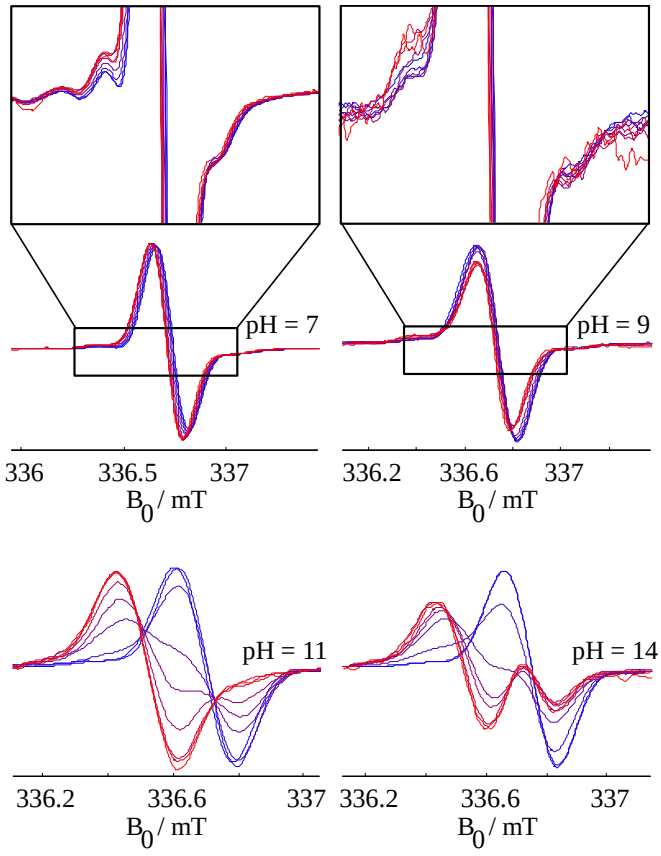

Figure A4.3.1. The development of the high-field transition of 0.2 mM TEMPO in solution with 5 wt% PEG-*co*-PDEGA with temperature at pH 7, 9, 11 and 14. Note that with increasing pH the lines stemming from species A and B separate more and more indicating stronger dehydration of PEG-*co*-PDEGA with increasing pH.

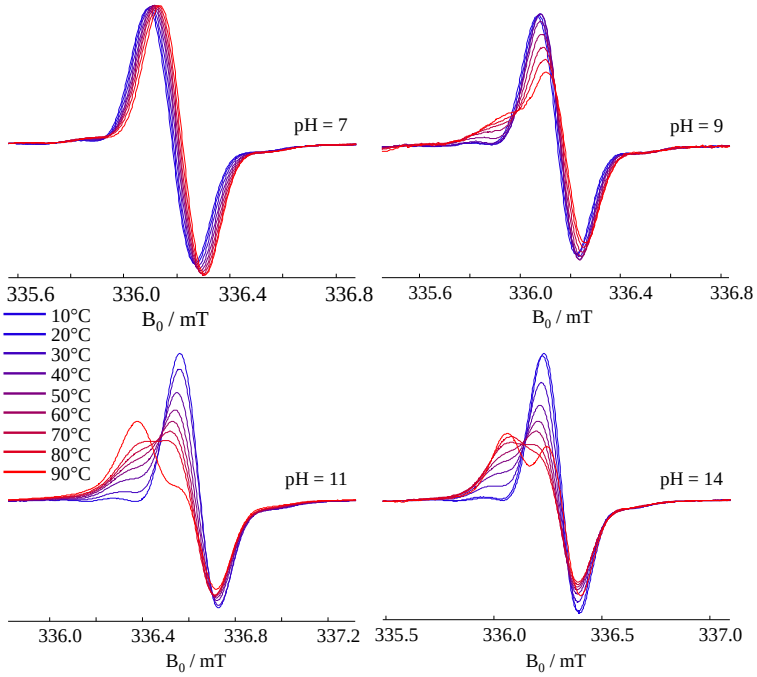

Figure A4.3.2. The development of the high-field transition of 0.2 mM TEMPO in solution with 5 wt% PEG-*b*-PDEGA with temperature at pH 7, 9, 11 and 14.

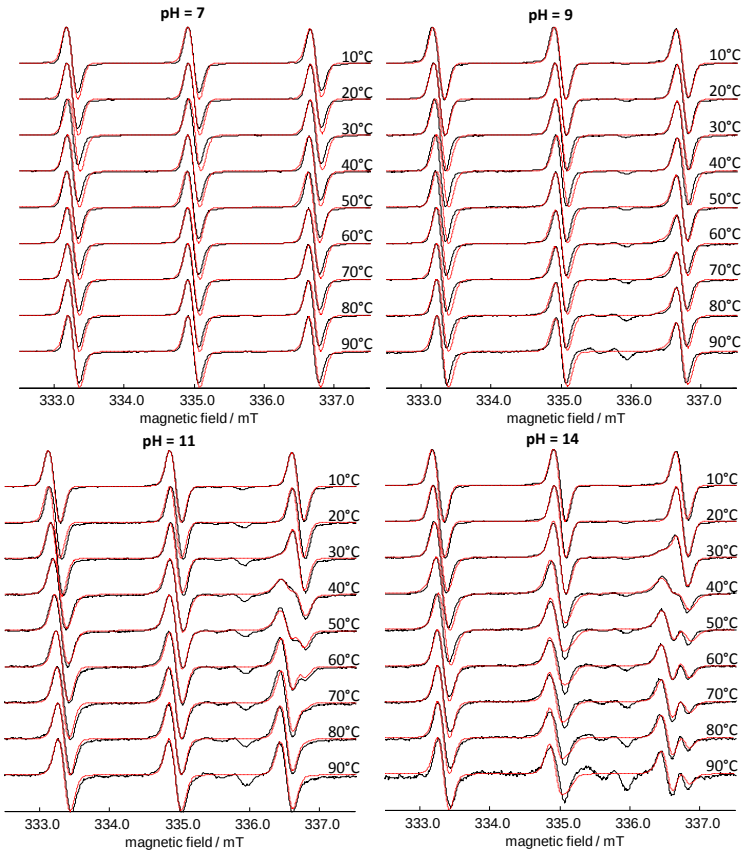

Figure A4.3.3. Experimental CW EPR spectra (black) and corresponding spectral simulations (red) between 10 °C and 90 °C at pH 7, 9, 11 and 14 of PEG-*co*-PDEGA.

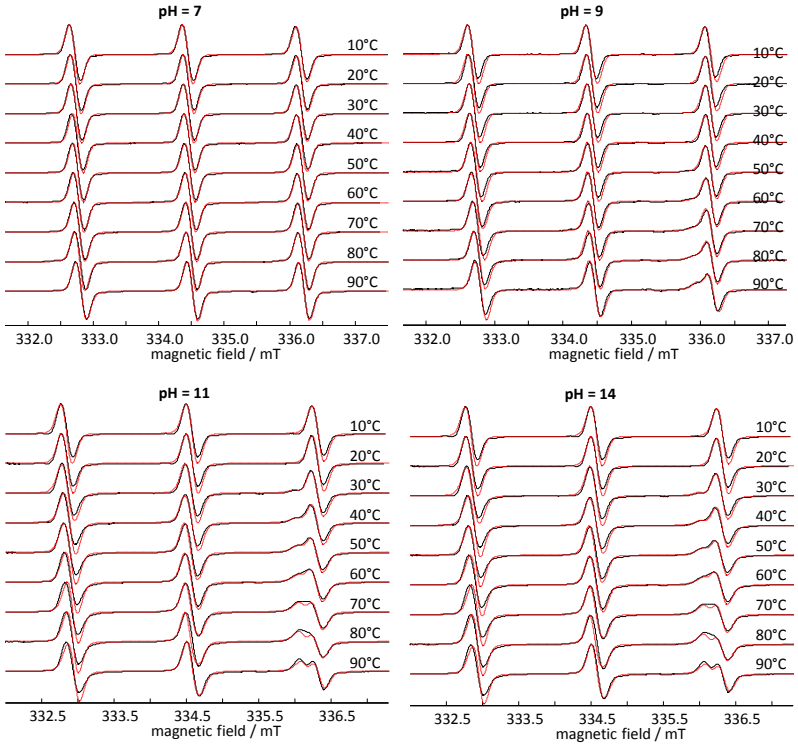

Figure A4.3.4. Experimental CW EPR spectra (black) and corresponding spectral simulations (red) between 10 °C and 90 °C at pH 7, 9, 11 and 14 of PEG-*b*-PDEGA.

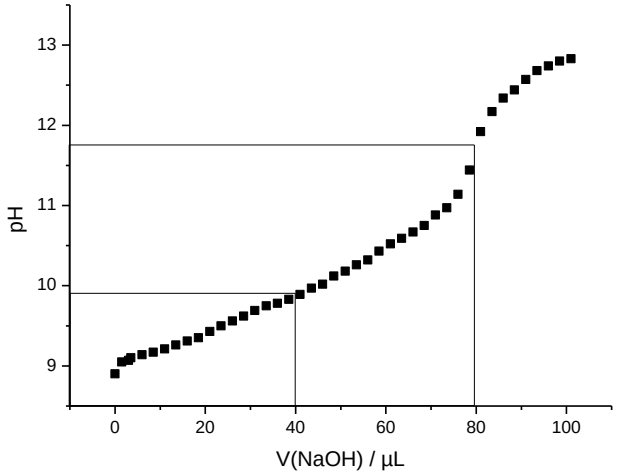

Figure A4.3.5. pH titration profile of PEG-*co*-PDEGA (29 % DEGA) at 5 wt % with 0.1 M NaOH. The pK_a can be estimated to 9.9.

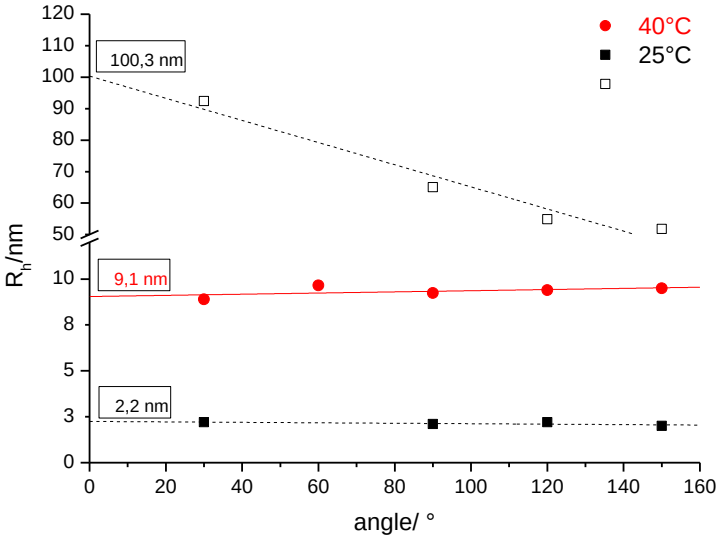

Figure A4.3.6. Scattering-angle dependent hydrodynamic radii, R_H, of PEG-*co*-PDEGA at 25°C (black) and 40°C (red) from dynamic light scattering (DLS) experiments (pH = 14). At 25°C a minor contribution from larger particles (white) were observed.

References and Notes

[1] N. M. Atherton, "*Principles of Electron Spin Resonance*", Ellis Harwood, New York, 1993.
[2] M. J. N. Junk, W. Li, A. D. Schlüter, G. Wegner, H. W. Spiess, A. Zhang, D. Hinderberger, *Angew. Chem. Int. Ed.* **2010**, *122*, 5818.
[3] D. Kurzbach, M. N. Reh, D. Hinderberger, *ChemPhysChem* **2011**, *12*, 3566.
[4] E. Krieger, T. Darden, S. B. Nabuurs, A. Finkelstein, G. Vriend, *Proteins* **2004**, *57*, 678.
[5] U. Essmann, L. Perera, M. L. Berkowitz, T. Darden, H. Lee, L. G. Pedersen, *J. Chem. Phys.* **1995**, *103*, 8577.

A5. The Phase Transition of Genetically Encoded Elastin-Like Polypeptides

A5.1 A Highly Cooperative Phase Transition in Genetically Encoded Polymers Revealed by EPR Spectroscopy

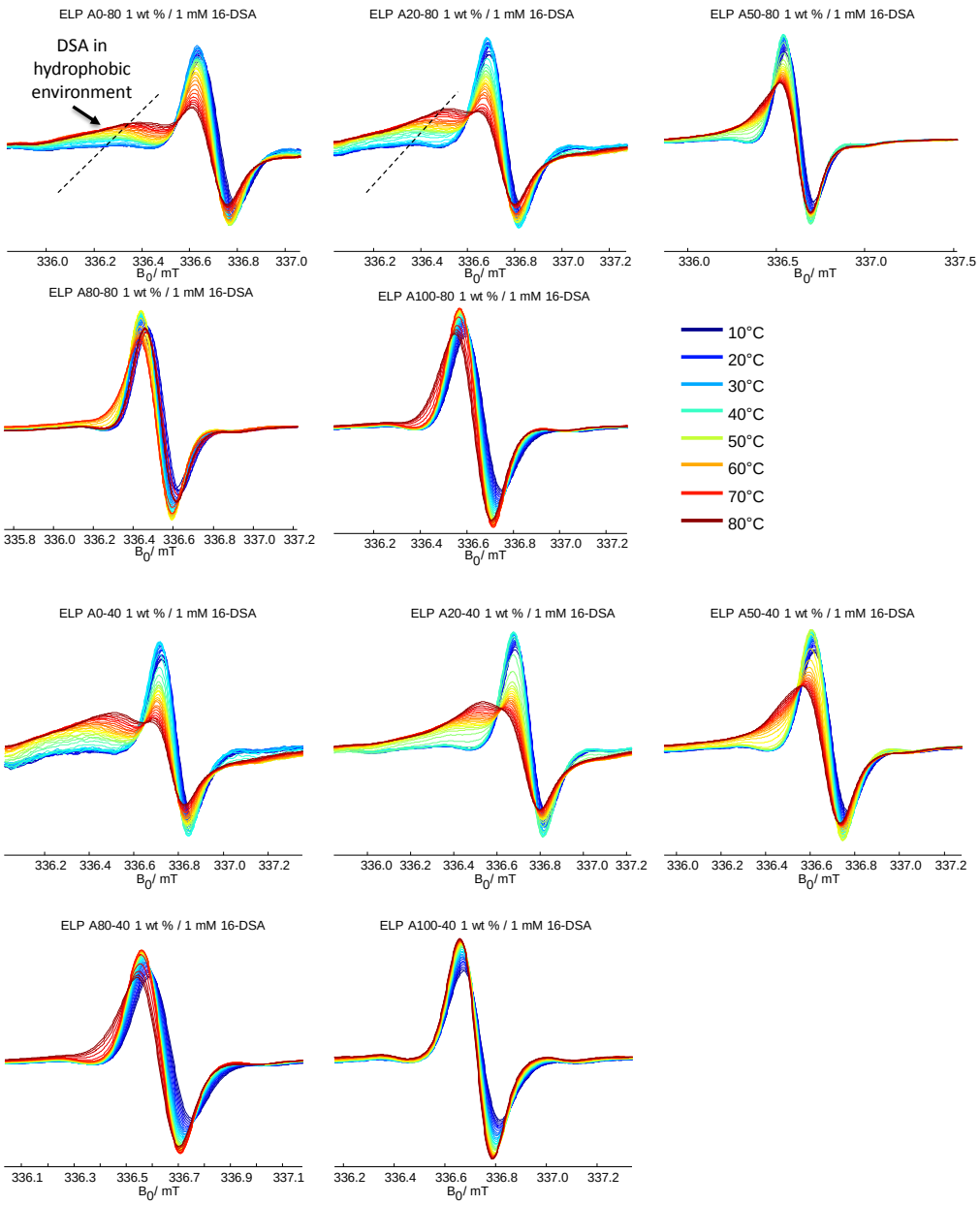

Figure A5.1.1. High-field transitions of experimental CW EPR spectra of 1 mM 16-DSA for solutions of all ELPs under investigation. The temperature range is 10°C to 80°C in steps of 2°C. The color code is shown in the figure.

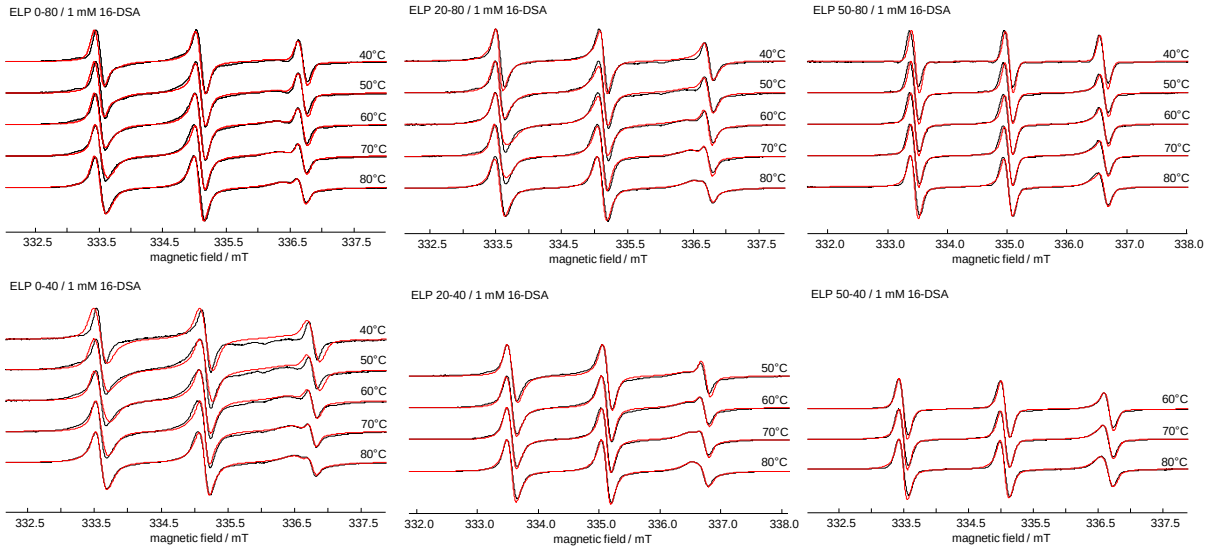

Figure A5.1.2. Experimental spectra (black) and corresponding simulations (red) for selected detected two-component spectra of 1 mM 16-DSA in 1 wt% ELP solutions in temperature intervals of 10°C.

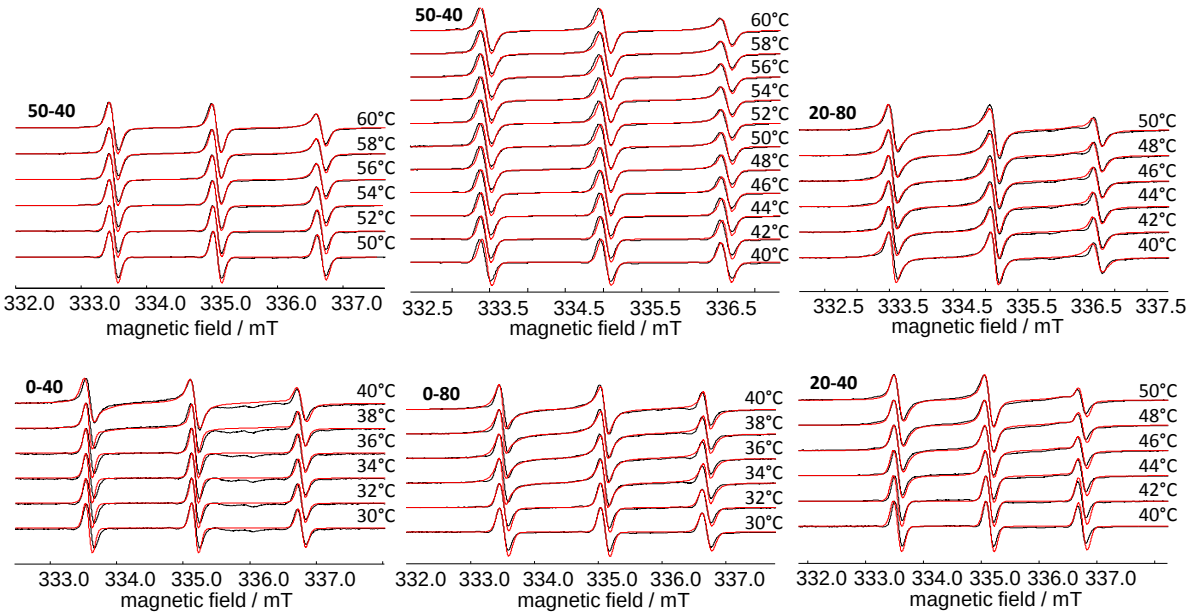

Figure A5.1.3. Experimental spectra (black) and corresponding simulations (red) for selected detected two-component spectra of 1 mM 16-DSA in 1 wt% ELP solutions in temperature intervals of 2°C.

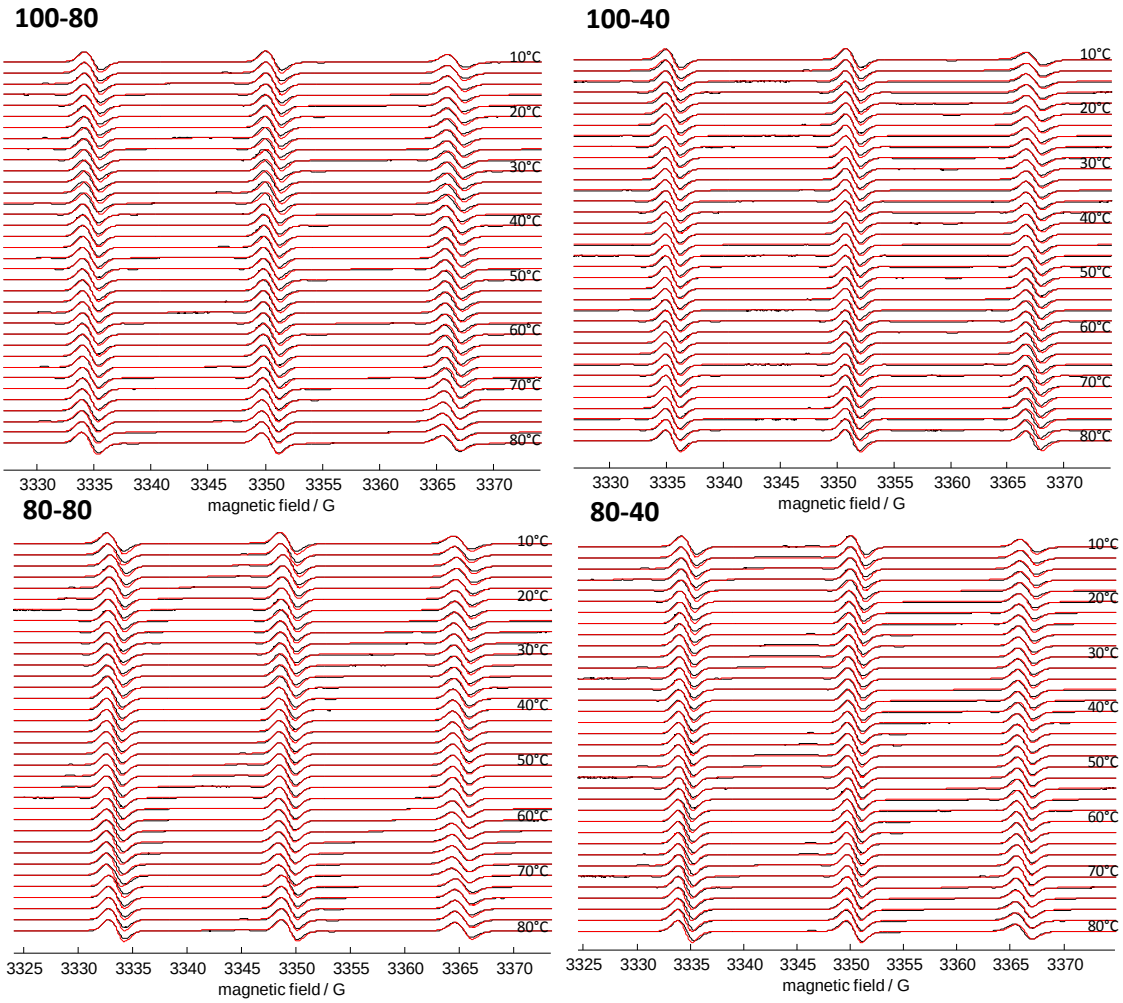

Figure A5.1.4. Experimental spectra (black) and corresponding simulations (red) for one-component spectra of 1 mM 16-DSA in 1 wt% ELP solutions in temperature intervals of 2°C

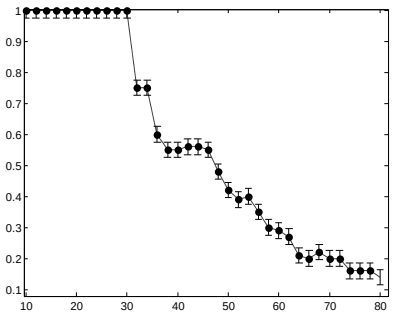

Figure A5.1.5. χ_A for ELP 0-80 at 10 wt %. As can be observed the transition is still broad, like in the case of 1 wt %. Hence, the sharper phase transition of x-40 ELPs is not a consequence of higher molar concentrations at 1 wt % due to lower molecular weight, compared to the x-80 ELPs.

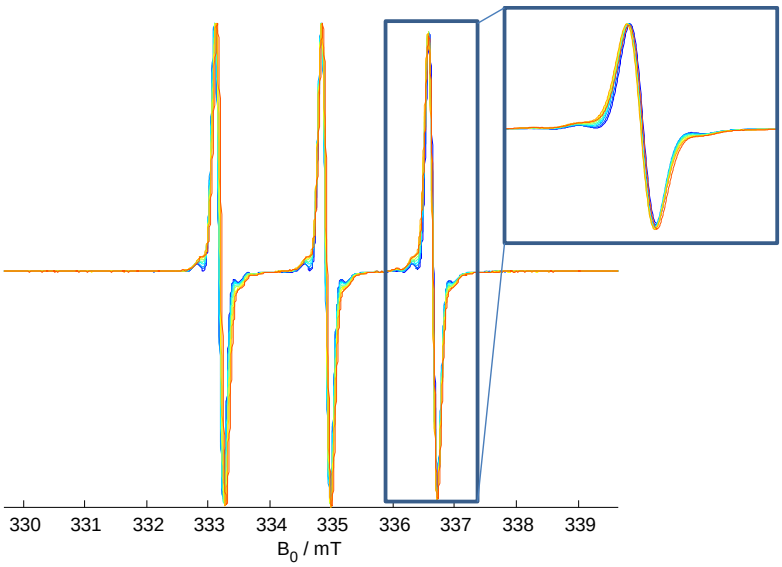

Figure A5.1.6. CW EPR of 1 wt % ELP 0-80 with 0.2 mM TEMPO. Only very weak interaction with the ELP aggregates (incorporation) can be observed.

Sample Preparation: 1 wt % of an ELP was dissolved in PBS, containing 3 mM KCl and 140 mM NaCl at pH = 7.4. Afterwards 1 v/v % of a 100 mM 16-DSA (16-DOXYL stearic acid) ethanol solution was added to the sample to yield a final spin-probe concentration of 1 mM. The samples were subsequently transferred into 3 mM outer diameter quartz tubes for continuous wave (CW) EPR.

EPR Measurements: Field-swept CW EPR spectra at X-band (~9.4 GHz) were measured on a Magnettech (Berlin, Germany) MiniScope MS200 benchtop CW EPR spectrometer with a variable-temperature cooling/heating unit (TC HO2). The temperature was varied in steps of 2°C. After every temperature change the sample was left to equilibrate for 10 min. No changes in the spectra were observed for longer waiting periods. The sample volume was always large enough to fill the complete resonator volume in the probehead (>300 µL).

Spectral Simulations: Typical g-values for the spectral simulation of component A (hydrophilic) were: g_{xx} = 2.0087, g_{yy} = 2.0067, g_{zz} = 2.0030. For species B (hydrophobic): g_{xx} = 2.0088, g_{yy} = 2.0068, g_{zz} = 2.0032. The hyperfine tensor, **A,** was simulated with principle values: A_{xx} = 18.02 MHz, A_{yy} = 16.84 MHz and A_{zz} = 90.00 - 100.00 MHz, depending on the polarity of the probes' environment. Furthermore, an anisotropic rotational diffusion tensor was assumed with principle values for species A: $D_{xx} = 5.0 \cdot 10^9\ s^{-1}$, $D_{yy} = 5.0 \cdot 10^9\ s^{-1}$, $D_{zz} = 4.2 \cdot 10^9 - 8.2 \cdot 10^9\ s^{-1}$. For species B: $D_{xx} = 1.0 \cdot 10^8 - 1.2 \cdot 10^8\ s^{-1}$, $D_{yy} = 1.2 \cdot 10^8\ s^{-1}$, $D_{zz} = 6.0 \cdot 10^7 - 8.0 \cdot 10^7\ s^{-1}$, depending on the temperature with Euler angles of the principle diffusion tensor of $\alpha = 0°$, $\beta = 50°$, $\gamma = 0°$. a_{iso} was calculated as tr(**A**)/3. The rotational correlation time was calculated as: $\tau_c = 6^{-1}(D_{xx}\, D_{yy}\, D_{zz})^{-1/3}$.

A6. The Conformational Space of Intrinsically Disordered Proteins

All protein samples were kind gifts of the group of Prof. Robert Konrat at the MFPL in Vienna.

DEER Experimental

DEER is applied to glassy solids obtained by freeze-quenching the solutions after addition of 30 v/v % glycerole. This is achieved by immersing the sample tube in supercooled iso-pentane. Such, a snapshot representative for the solution at the glass transition temperature is detected. The sample volume was always large enough to fill the complete resonator. The four pulse DEER sequence $\pi/2(\nu_{obs})$ - τ_1 - $\pi(\nu_{obs})$ - (τ_1 + t) - π (ν_{pump}) - (τ_2 - t) - $\pi(\nu_{obs})$ - τ_2 - echo was used to obtain dipolar time evolution data at X-band frequencies (9.2 to 9.4 GHz) with a Bruker Elexsys 580 spectrometer equipped with a Bruker Flexline split-ring resonator ER4118X_MS3. The dipolar evolution time t was varied, whereas τ_2 = 2-4 µs (depending on the sample; see main text) and τ_1 were kept constant. Proton modulation was averaged by the addition of eight time traces of variable τ_1, starting with $\tau_{1,0}$ = 200 ns and incrementing by $\Delta\tau_1$ = 8 ns. The resonator was overcoupled to Q ≈ 100. The pump frequency, ν_{pump}, was set to the maximum of the EPR spectrum. The observer frequency, ν_{obs}, was set to ν_{pump} + 61.6 MHz, coinciding with the low field local maximum of the nitroxide spectrum. The observer pulse lengths were 32 ns for both $\pi/2$ and π pulses, and the pump pulse length was 12 ns. The temperature was set to 50 K by cooling with a closed cycle cryostat (ARS AF204, customized for pulse EPR, ARS,Macungie, PA). The total measurement time for each sample was around 12 h. The raw time domain DEER data were processed with the program package DeerAnalysis2010.[1] The resulting time traces were normalized to t = 0. Background correction was done through dividing by experimental functions gained from DEER on the four single mutants.

A6.1 Cooperatively Folded Conformational Substates in Osteopontin

A6.1.1 Supplementary DEER

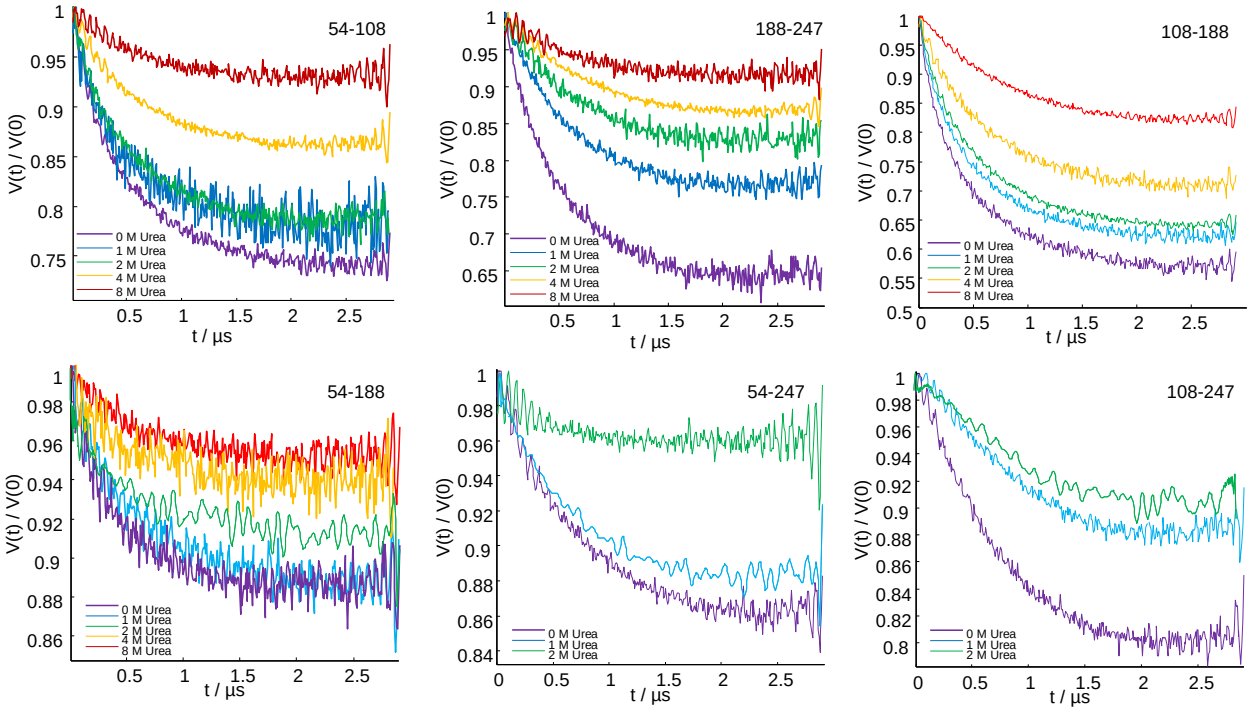

Figure A6.1.1. DEER time domain data for all double mutants for different urea concentrations. Absence of time traces indicates that we observed Δ = 0. Note the different scales of the V(t)/V(0) axes.

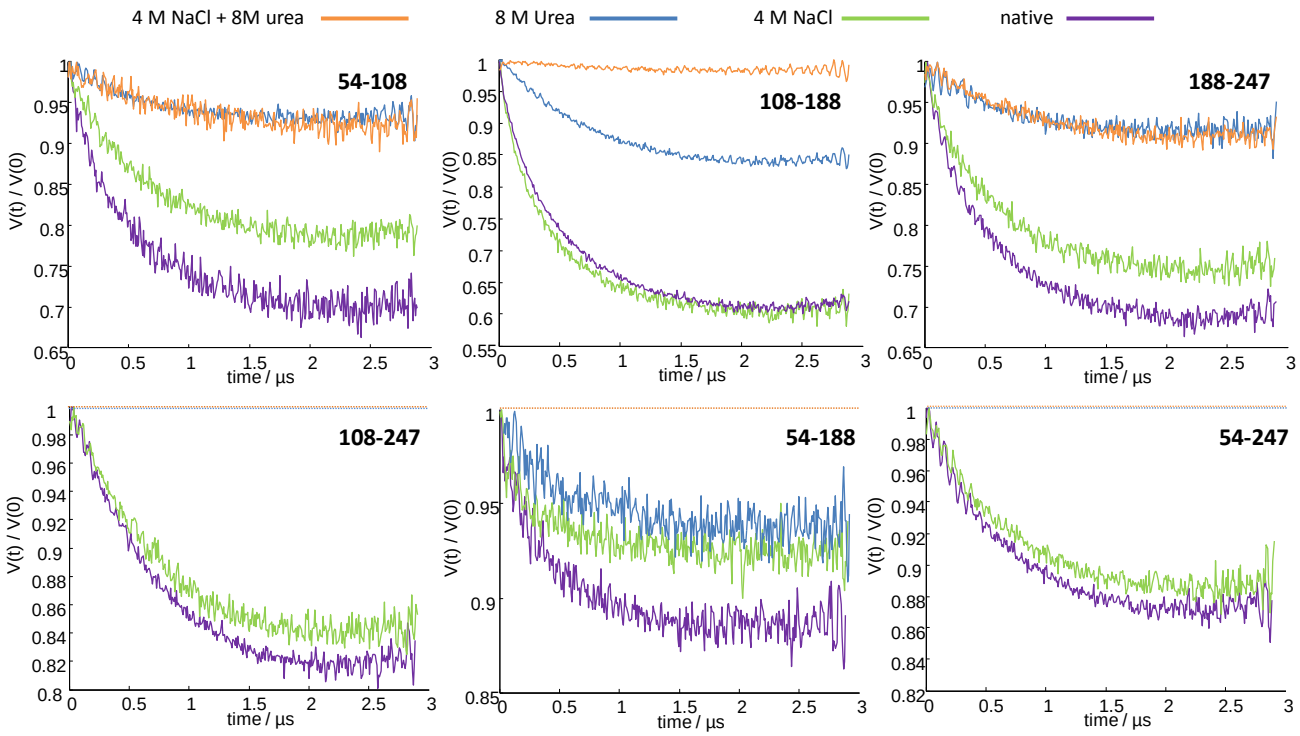

Figure A6.1.2. DEER time domain data for all double mutants for different denaturation conditions. Absence of time traces indicates that we observed Δ = 0. Note the different scales of the V(t)/V(0) axes.

A6.1.2 Details on time domain calculations

All calculations where based on random coil models with:[2]

$$\langle R^2 \rangle = c_\infty n l^2 \quad (A5.3.1)$$

and

$$P(R,n,l) = \left(\frac{3}{2\pi n l^2}\right)^{3/2} \exp\left(-\frac{3(r-R)^2}{n l^2}\right) \quad (A6.1.2)$$

Where $P(R,n,l)$ denotes the distribution of end-to-end vectors (see Figure 4a)). n is the segment number and l the segment length. The latter we assumed as one amino acid. DEER time traces were calculated as (cf. general introduction):[3]

$$V(t) = \sum_R P(\omega_R) V_R(t) \quad (A6.1.3)$$

with

$$V_R(t) = 1 - \int_0^{\pi/2} \lambda(1 - \cos(\omega_R t)) \sin\theta \, d\theta \quad (A6.1.4)$$

λ is an experimental constant (here 0.516) that depends on the experimental pump efficiency (see the Supplementary Material for the DEER pulse sequence), θ is the angle between the external magnetic field and the vector connecting observer and pump spins. $P(\omega_R)$ is a distribution of dipolar coupling frequencies, ω_R, that corresponds to $P(R,n,l)$ as:

$$\omega_R = \frac{\mu_0 g_1 g_2 \mu_B}{4\pi\hbar R^3}(3\cos^2\theta - 1) \quad (A6.1.5)$$

g_1 and g_2 denote the g-values of observer and pump spins. These were assumed to be equal. All other constants have their usual meanings. The contribution of compact conformations to $V(3\ \mu s) = 1 - \Delta_{eff}$ in dependence of $\langle R^2 \rangle$ can be estimated when calculating:

$$1 - \sum_{R_{min}}^{R_{max}} P(\omega_R) V_R(t) \Big/ 1 - \sum_{R_{min}}^{R(x)} P(\omega_R) V_R(t) \quad (A6.1.6)$$

Where x denotes a hypothetic fraction of compact conformations of the overall conformational ensemble. Therefore, $\mathrm{R(x)}$ has to fulfill $\mathrm{x} = \int_{\mathrm{R_{min}}}^{\mathrm{R(x)}} \mathrm{P(R,n,l)dr} / \int_{\mathrm{R_{min}}}^{\mathrm{R_{max}}} \mathrm{P(R,n,l)dr}$ (see Figure 4a)). $\mathrm{R_{min}}$ is depending on the pump pulse length, τP, of a DEER experiment. For τP = 12 ns $\mathrm{R_{min}} = 1.6\ \mathrm{nm}$.[4] $\mathrm{R_{max}}$ is approx. 40 nm as calculated by Jeschke and co-workers.[3] For $\mathrm{x} = 0.05$, that is the cooperatively folded states are estimated to the most compact 5 % of $\mathrm{P(R,n,l)}$ and for $\mathrm{t} = 3\ \mu\mathrm{s}$ eq. A6.1.6 yields the function plotted in Figure A.6.1.3 b).

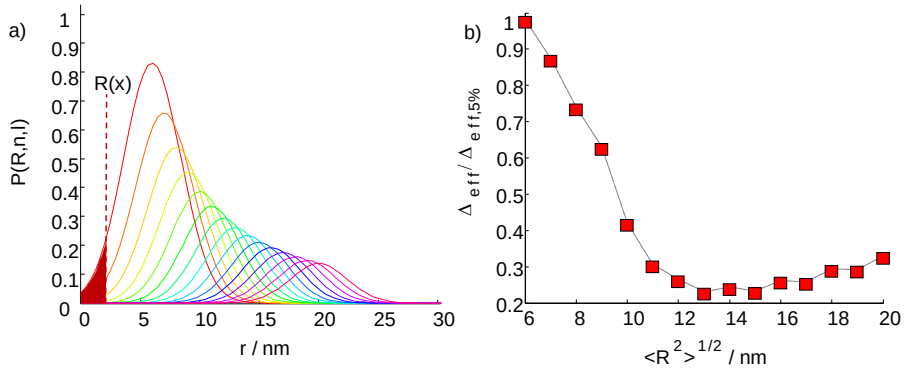

Figure A.3.3. a) End-to-end vector distributions of random coils for different $\langle \mathrm{R^2} \rangle$. $\mathrm{R(x)}$ is defined as the distance at which the integral between $\mathrm{R_{min}}$ and $\mathrm{R(x)}$ matches x% of the total integral of $\mathrm{P(R,n,l)}$. c∞ was assumed as 2. b) Inverse contribution of the most compact 5% of conformations of the distributions in a) to Δeff.

Judging from Figure 4, one can state that with increasing $\langle \mathrm{R^2} \rangle$ the contribution of compact conformations to Δeff increases, as stated in the Results and Discussion section. Yet, we only use this as a qualitative argument, since all the calculations are performed for random coil models and the most compact 5 % of conformations are assumed as the cooperatively folded fraction. For OPN however $\mathrm{P(\omega_R)}$ does not correspond to a random coil and x remains undetermined.

A6.2 Conformational Adaptions of Osteopontin upon Heparin Binding

A6.2.1 Supplementary DEER

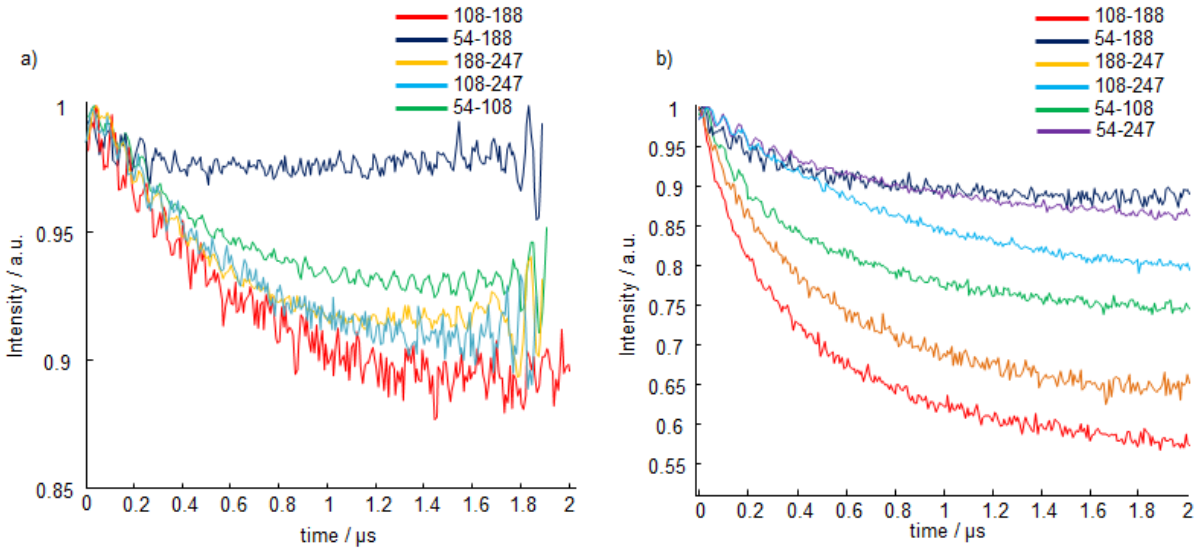

Figure A6.2.1. DEER time traces of the double mutants under investigation a) in the presence and b) in the absence of 0.1 mg/µL heparin. Note the different intensity scales. Missing time traces denote $\Delta_{eff} = 0$.

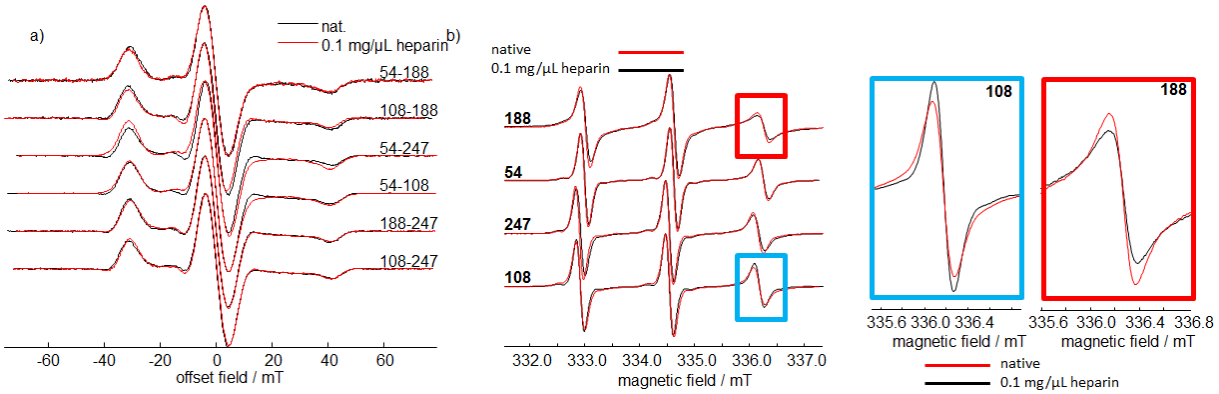

Figure A6.2.2. a) Pseudo modulated low temperature spin echoes of the double-mutants under investigation in the absence (black) and presence (red) of 0.1 mg/µL heparin. The modulation frequency was 3 mT. b) Room temperature CW EPR spectra of the four single-mutants in the absence (red) and presence (black) of 0.1 mg/µL heparin and a zoom on the high-field transitions of C108 (blue) and C188 (red).

A6.3. Structural Response of Intrinsically Disordered BASP1 to pH Variation

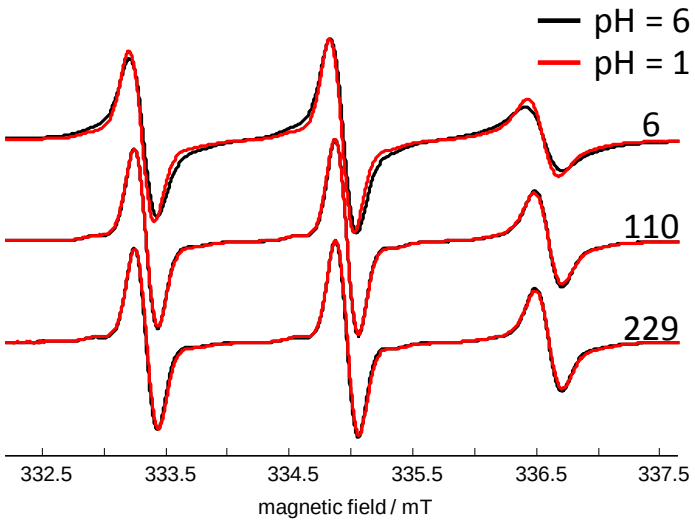

Figure 6.3.1. CW EPR of BASP1 single mutants at pH 6 (black) and pH 1 (red).

References and Notes

[1] G. Jeschke, V. Chechik, P. Ionita, A. Godt, H. Zimmermann, J. Banham, C. R. Timmel, D. Hilger, H. Jung, *Appl. Magn. Reson.* **2006**, *30*, 473.
[2] M. Rubinstein, R. Colby, "*Polymer Physics*", Oxford University Press, New York, 2004.
[3] G. Jeschke, A. Koch, U. Jonas, A. Godt, *J Magn Reson* **2002**, *155*, 72.
[4] Y. D. Tsvetkov, A. D. Milov, A. G. Maryasov, *Russ. Chem. Rev.* **2008**, *77*, 487.